A Novel Highly Accurate Wireless Wearable Human Locomotion Tracking and Gait Analysis System via UWB Radios

Heba A. Shaban

Dissertation submitted to the Faculty of the
Virginia Polytechnic Institute and State University
in partial fulfillment of the requirements for the degree of

Doctor of Philosophy
in
Electrical Engineering

Committee Members:

R. Michael Buehrer, Co-Chair
Mohamad Abou El-Nasr, Co-Chair
Sedki Riad
Sandeep Shukla
Marion R. Reynolds

April 29, 2010
Blacksburg, Virginia

Keywords: Body area networks (BAN), gait analysis, performance analysis, power consumption, sensor-fusion, ultra wideband (UWB) transceivers, and wireless healthcare

A Novel Highly Accurate Wireless Wearable Human Locomotion Tracking and Gait Analysis System via UWB Radios

Heba A. Shaban

(ABSTRACT)

Gait analysis is the systematic study of human walking. Clinical gait analysis is the process by which quantitative information is collected for the assessment and decision-making of any gait disorder. Although observational gait analysis is the therapist's primary clinical tool for describing the quality of a patient's walking pattern, it can be very unreliable. Modern gait analysis is facilitated through the use of specialized equipment. Currently, accurate gait analysis requires dedicated laboratories with complex settings and highly skilled operators. Wearable locomotion tracking systems are available, but they are not sufficiently accurate for clinical gait analysis. At the same time, wireless healthcare is evolving. Particularly, ultra-wideband (UWB) is a promising technology that has the potential for accurate ranging and positioning in dense multi-path environments. Moreover, impulse-radio UWB (IR-UWB) is suitable for low-power and low-cost implementation, which makes it an attractive candidate for wearable, low-cost, and battery-powered health monitoring systems. The goal of this research is to propose and investigate a full-body wireless wearable human locomotion tracking system using UWB radios. Ultimately, the proposed system should be capable of distinguishing between normal and abnormal gait, making it suitable for accurate clinical gait analysis.

To my family:
My parents, sister Heidi, and brother Moumen

Acknowledgments

All Praise be to Allah much good and blessed for everything. All praise be to Allah, who has guided me through this work, and my whole life. First, last, and foremost, thanks to Allah who has granted me patience, health, and strength through the toughest times.

I would like to express my deepest gratitude to my advisors Dr. R. Michael Buehrer and Dr. Mohamad Abou El-Nasr. I would like to thank them for giving me the chance to work on this topic, which would not have been possible if I did not work under their supervision. Also, I would like to thank them for their constructive guidance throughout the work of this dissertation, and for sparing no effort to grant me all the facilities that made me work efficiently on my Ph.D. while being in Egypt.

On behalf of all VT-MENA students, I would like to thank Dr. Yasser Hanafy and Dr. Sedki Riad for everything. They have succeeded in making us all feel like being a one family (VT-MENA family). Their support and encouragement really helped us achieve our goals.

I owe special thanks to Haris I. Volos, Ph.D. candidate at MPRG group, for taking all the UWB measurements. I would also like to thank all my friends and colleagues whose encouragement and prayers made reaching this moment possible. I would like to thank my sister and best friend Heidi, who suffered with me a lot, probably more than I did. Also, I would like to thank my dearest friends Hadeel Badr, Marwa El-Dahshan, May Abd El-Hamid, Nesrine Ramadan, Soha Saleh, and new friends Salma Darwish and Sara Ibrahim. I would like to extend my gratitude to my colleagues and friends at the Arab Academy for Science and Technology and Maritime Transport (AASTMT) for their encouragement. Particularly, I would like to thank Ahmed Abd El-Aziz, Heba Fayed, Maha Hessi, and Marwa Moumen.

I am most thankful and grateful to my lovely and wonderful parents whose invaluable support, love, care, encouragement, and prayers have always been the main source of inspiration to my life. Their presence by my side is the actual and most precious blessing, and key to any success.

Contents

List of Figures

List of Tables

List of Abbreviations

ADC	Analog to Digital Converter
AOA	Angle Of Arrival
ARAKE	Ideal RAKE
AWGN	Additive White Gaussian Noise
BER	Bit Error Rate
BOS	Base Of Support
B	Bandwidth
CCD	Charge Coupled Device
C-MDS	Classical Multidimensional scaling
CRLB	Cramer-Rao Lower Bound
DOF	Degree of Freedom
DTR	Differential Transmitted Reference
EC	Equally Correlated
ED	Energy Detection
EMG	Electromyography
ENOB	Effective Number of Bits

FCC	Federal Communication Commission
FD	Fully Digital
IR	Impulse Radio
LE	Leading Edge
LNA	Low Noise Amplifier
LS	Least Squares
MAE	Mean Absolute Error
MF	Matched Filtering
MGF	Moment Generating Function
ML	Maximum Likelihood
MoCap	Motion Capture
MSE	Mean Square Error
OOK	On Off Keying
PG	Processing Gain
POD	Probability of Detection
PPM	Pulse Position Modulation
PRAKE	Partial RAKE
PDP	Power Delay Profile
PRF	Pulse Repetition Frequency
QAC	Quadrature Analog Correlator
RMSE	Root Mean Square Error

RRcR	Reference Range Correlation
RSSI	Received Signal Strength Indicator
SD	Secure Digital
SNR	Signal to Noise Ratio
TC	Threshold Crossing
TOA	Time Of Arrival
TR	Transmitted Reference
UWB	Ultra Wide-band
WBAN	Wireless Body Area Networks
WWGA	Wireless Wearable Gait Analysis
ZZLB	Ziv-Zakai Lower Bound

Chapter 1

Introduction

1.1 Motivation and Problem Statement

Observational gait analysis, the standard method of evaluating gait, refers to the visual assessment of a patient's gait. Gait analysis by observer assessment does not use any specialized equipment, and is simply used to observe abnormalities in gait. Clinical gait analysis, also termed as quantitative gait analysis, provides a detailed clinical introduction to understanding and treating walking disorders [54], [63]. The identification of gait disorders is commonly assessed by the measurement of the spatial and temporal parameters of gait[1]. However, it is worth noting that the techniques and technologies that work well for measuring normal gait often fail when applied to abnormal gait [11], [88]. Moreover, the criteria valid for clinical research are not necessarily the same as those valid for clinical testing [54], [15]. Accurate measuring systems, e.g., optical tracking systems, are available, but they require that the test subject move inside a dedicated laboratory with multiple charge-coupled devices (CCD-cameras) and require complex settings [63], [36]. Subtle abnormalities are not evident when examined indoors, as when walking is performed in a laboratory with the patients concentrating on what they are doing, since this does not necessarily represent their normal walking [63]. On the other hand, body-fixed-sensors do not require such complex settings or highly skilled operators. Yet, these systems also have their limitations. A possible solution for overcoming these limitations is to use multiple sensors, or what is known as sensor-fusion [11], [10], [24]. However, the overall power consumption and system cost remain as two limiting factors, where sensory systems are commonly expensive.

This work is motivated by the properties of ultra wideband (UWB) technology as a promising candidate for real-time human locomotion tracking with specific application to clinical gait analysis. In particular, wearable wireless body area networks (WBANs) seem to be a promising solution for long-time monitoring of patients without large laboratories or complex measurement setups. Moreover, UWB has the potential for providing accu-

[1]Spatio-temporal parameters of human gait include step-length, stride-length, velocity, etc.

rate ranging and positioning estimates required for the assessment of accurate clinical gait analysis with low-power consumption. However, the design of such a system has many challenges and key factors that need to be addressed. Initially, target ranging accuracy, required signal-to-noise-ratio (SNR), and target sampling rate should be specified. Based on these requirements, calculation of the achievable SNR is necessary for determining the feasibility of the system under investigation. Then, possible receiver structures should be exploited and compared based on both performance and power consumption requirements. Further, possible alternatives for low-power consumption should be conducted. Moreover, arrangement of transceivers (nodes), number of nodes and their locations are important factors that need to be studied, since these factors directly affect motion captured data. Finally, determination of relative positions of nodes during movement based on acquired ranging data and dynamics of human movement is a challenging task, where all-nodes are mobile. Other factors of interest include system performance and sensor-fusion.

1.2 Thesis Statement

In this work, we design the primary components of an on-body human locomotion-tracking system using UWB sensors with a specific application to clinical gait analysis. The design of such a system involves multiple research challenges including the following:

- Time-of-arrival (TOA) estimation techniques which require minimal power (of each node and the overall system) while meeting strict accuracy requirements.
- Determination of the number of sensors and their locations in order to minimize power requirements while providing sufficient information to determine needed body kinematics and/or kinetics.
- Determination of relative positions of nodes using limited (and selectively corrupted) range measurements and collected locomotion biometrics for determining body kinematics.
- Identification of abnormal gait using captured body kinematics based on disease characteristics defined in the literature.
- Development of sensor-fusion techniques to enhance the proposed UWB-based system with additional sensor information including force sensors.
- Addressing general system design issues for such a system.

1.3 Dissertation Scope and Organization

In this dissertation, we address the research challenges mentioned in the previous section. Particularly, we design the principal components of the proposed system, and address the following:

- Propose and investigate a novel highly accurate wireless wearable human locomotion tracking system suitable for clinical gait analysis. Investigation includes the design of key system parameters including the link-budget, transmission frame structure, detailed system initialization, ranging techniques, localization techniques, power consumption, and an evaluation of the overall system performance. More specifically we,
  - Develop a framework for system performance/power consumption evaluation.
  - Apply linear least-squares (LS) and classical multidimensional scaling (C- MDS) with fast Fourier transform interpolation to node localization.
  - Derive theoretical lower bounds on system performance and give closed-form formulas in an additive-white-Gaussian-noise (AWGN) channel, and provide semi-analytic simulations in multi-path channels.
  - Determine system requirements for target accuracy including required ranging accuracy and update rate.
- Propose and evaluate the performance of an accurate reference range correlation-based (RRcR) ranging technique suitable for on-body communications. The achievable accuracy (based on actual analog sliding-correlation implementation proposed in the literature) is 1 mm compared to 1.17 cm inert-marker accuracy reported for current gait analysis and motion tracking systems.
- Propose a short system initialization with high localization accuracy. The provided accuracy is 0.247 mm. Furthermore, develop a core localization procedure with 0.47 mm $\pm$ 52 μm accuracy. The average accuracy reported for current motion tracking and gait analysis systems is $\approx$ 0.8 mm.
- Propose and investigate the integration of foot force sensors with UWB sensors for kinetic data estimation.
- Develop a simulation framework using MATLAB for the evaluation of common communication performance metrics (bit-error-rate (BER), ranging, and localization) based on actual motion capture (MoCap) data files (.C3D, .GCD, .TRC, and .DST). Moreover, the framework further includes the calculation of common gait parameters.

This dissertation proposes and examines the feasibility of the system described above, addresses the challenges associated with the design, and summarizes the obtained results.

The rest of this document is organized as follows. The theoretical background of different disciplines involved in this research is given in Chapter 2. First, a brief overview of gait analysis and human locomotion tracking systems are summarized. Then, different UWB receiver architectures and general power consumption requirements are discussed. Finally, background information on lower-bounds of the common time-of-arrival (TOA) estimators and their performances are provided for ranging and localization estimators.

Chapter 3 introduces the proposed system, proposes a study framework for performance /power consumption, provides an overview of the proposed ranging procedure, gives a summary of the proposed localization procedure, and discusses the possibility of integrating other types of sensors with UWB radios in the proposed system. Then, in Chapter 4 we discuss and analyze some important parameters associated with the design of our proposed system. Chapter 5 derives the theoretical lower bound on system performance, studies and proposes a new ranging technique, and designs a link budget for the proposed system and estimates the receiver power consumption according to the proposed design parameters. Then, Chapter 6 introduces the localization stage, which is composed of two phases, namely the initial and core measurement phases. It further provides simulation results for both phases in the IEEE 802.15.6a channel model based on actual motion capture (MoCap) data. Chapter 7 provides the actual on-body measurements taken for the verification of the proposed system. Particularly, we took multiple measurement sets, namely the knee-to-ankle distance, base-of-support (BOS) distance, RRcR, and system initialization measurement sets. Chapter 8 investigates the integration of UWB sensors with foot force sensors, sensor-fusion, in order to get a complete picture of gait parameters including kinematics and kinetics. Then, it studies the number of bit requirement, and the effect of quantization error on the estimated gait parameters via simulations. It then estimates the overall system performance including memory requirement, power consumption, and battery lifetime. Finally, Chapter 9 provides conclusions and recommendation for future work.

Chapter 2

Background

This chapter provides background related to different aspects of the work presented in this dissertation. Section 2.1 gives an overview of gait analysis and differentiates between observational and quantitative gait analysis. Furthermore, it gives a brief summary of commercially available gait analysis systems and their offered accuracies. Moreover, it highlights the parameters that current systems fail to measure accurately. Then, Section 2.2 gives an overview of ultra wideband (UWB) technology as a promising candidate for health-monitoring systems particularly for human locomotion tracking and gait analysis systems. Furthermore, Section 2.3 discusses the different UWB receiver architectures, and summarizes the advantages and disadvantages of each type. Moreover, Section 2.4 provides a brief summary of theoretical lower bounds on the performance of time-of-arrival (TOA) estimators. Section 2.5 gives a summary of the chapter.

2.1 Gait Analysis

Gait analysis refers to the measurement, description, and assessment of quantities that characterize human locomotion, where musculoskeletal functions are quantitatively evaluated through the measurement of joint kinematics and kinetics [63]. The core part of gait analysis depends on the measurement of joint kinematics and kinetics; depicted in Figure 2.1. Other measurements include, electromyography (EMG), oxygen consumption, and foot pressure. Gait analysis and the construction of a precise body model are important not only for biomechanical research, but also for characterizing diseases that affect mobility [63], [68]. Basically, gait is described as either normal or abnormal gait. Normal gait is the efficient movement of the body, where the expended energy during movement is minimized. Any deviation from the minimal energy expenditure causes abnormal gait [11], [68]. Samples of different abnormal gaits are shown in Figure 2.2[1] [41]. Typically, the evaluation of abnormal

[1]Figure 2.2 is modified based on the materials presented in [104], [61].

gait requires the knowledge of normal movement biomechanics. Commonly, the occurrence of gait abnormalities is due to pain, abnormal range of motion, and leg-length discrepancy [63], [11]. The key to observing abnormal gait is recognizing the symmetry of movement, where the patients should be observed while walking for some distance [63]. It is sometimes necessary to watch patients walking for long distances or even outdoors.

The biomechanical approach to movement analysis can be qualitative, with movement observed and described, or quantitative, by the measurement of different movement aspects [6], [68]. Biomechanical analysis can be conducted from either of two perspectives: namely, kinematic or kinetic analysis. Kinematic analysis involves the description of movement, where position, velocity, and acceleration are the components of interest. Kinetics is the area of study that examines the forces acting on a system, such as the human body, while kinetic movement analysis examines the forces causing movement [63], [11], [68]. Figure 2.3[2] summarizes the different types of movement analysis. Typically, a kinetic movement analysis is more difficult than a kinematic analysis. The examination of both the kinematic and kinetic components is essential to the assessment of all aspects of movement [63], [11], [10].

In locomotion studies, a walking or running cycle is generally defined as the period from

[2]Figure 2.3 is reproduced based on the material presented in [68].

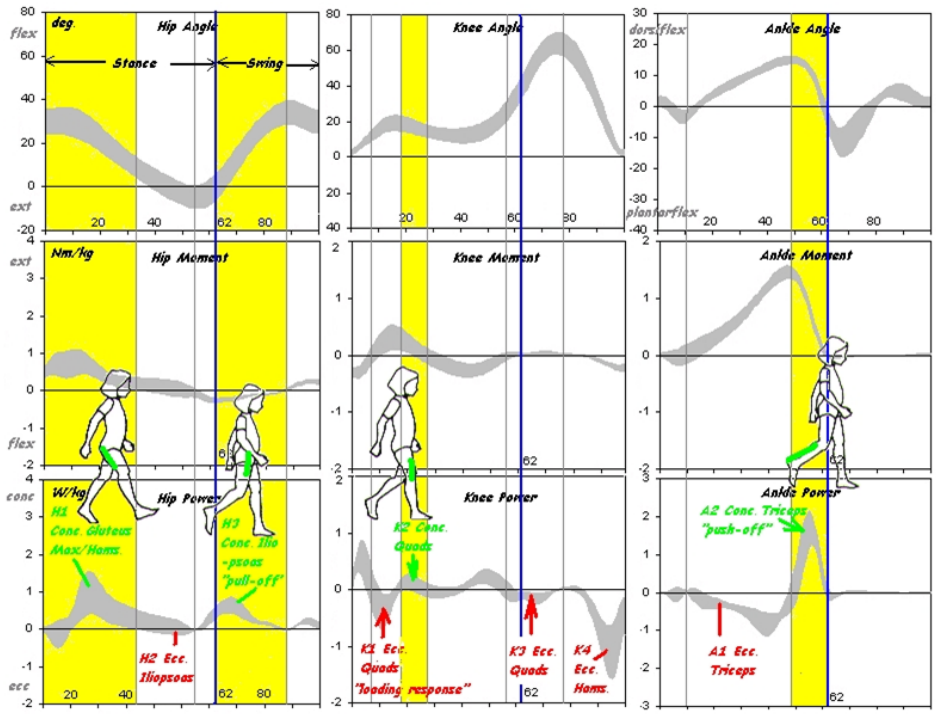

Figure 2.1: Various kinematic and kinetic parameters for normal gait [22]; "*used with permission*".

Figure 2.2: Examples of gait disorders.

the contact of one foot on the ground to the next contact of the same foot. The gait cycle is usually broken down into two phases, referred to as the stance or support phase and the swing phase [13], [15], [68]. In the stance or support phase, the foot is in contact with the ground. The support phase can also be broken down into sub-phases. The first half of the support phase is the braking phase, which starts with a loading or heel-strike phase and ends at mid-support. The second half of the support phase is the propulsion phase, which starts at mid-stance and continues to terminal stance and then to pre-swing as the foot prepares to leave the ground. The swing or non-contact phase is the period when the foot is not in contact with the ground, and it can be further subdivided into initial-swing, mid-swing, and terminal swing sub-phases [68], [88], [78]. Essentially, this phase represents the recovery of the limb in preparation for the next contact with the ground, as shown in Figure 2.4[3]. Furthermore, Table 2.1 summarizes walking speeds of normal walking for different ages.

A reference system is essential for the accurate observation of any type of motion, such as the human movement. The universal method used for the description of the human movement is based on a set of reference planes and axes; shown in Figures 2.5(a) and (b)[4]. Human movement is generated by the muscular system, where the skeletal system represents the levers and axes of rotation about which the movement is generated [68], [78]. The description of a segmental position or joint movement is typically expressed relative to a designated starting position, also termed as zero-position. The starting position is the reference point that is used for the description of most of the joint movements. The ultimate target of human movement capture is to capture the positions of the skeletal system. This is typically performed using either markers in optical tracking systems, or body sensors attached to the body skin in sensory systems [63], [78].

Sophisticated measurement systems employ optical tracking techniques to track the displacement of markers[5] placed at particular anatomical sites on limb segments as shown in

[3]Figure 2.4 is reproduced based on the materials presented in [86], [6], [7], [83], [111].

[4]Figure 2.5 is reproduced based on the materials presented in [67].

[5]Markers are arranged based on well-defined marker-sets. Markers should be placed at specific anatomical

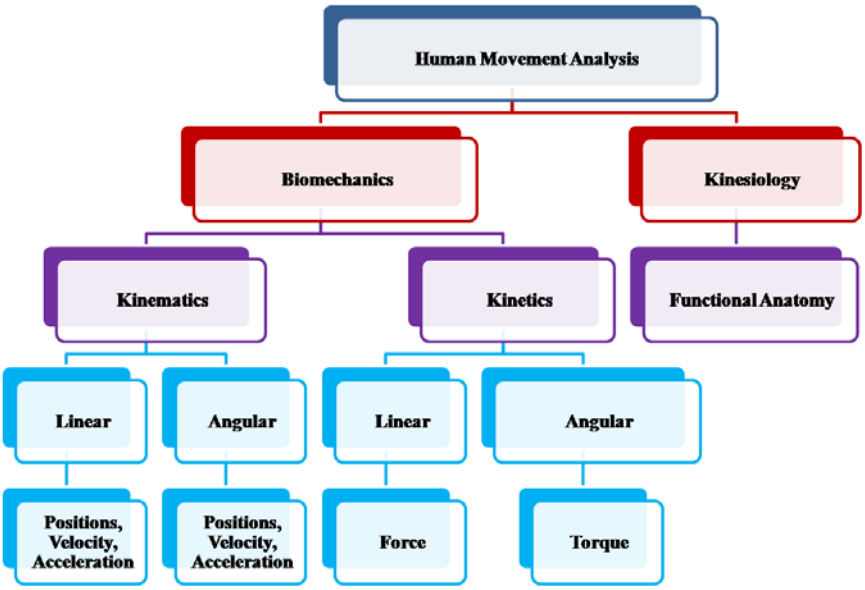

Figure 2.3: Types of movement analysis.

Figure 2.6[6] [13], [11], [88]. Standard gait analysis is based on either optical, magnetic, or ultrasonic motion tracking systems. These systems allow for the assessment of a complete three-dimensional kinematic analysis of human movement [88], [24]. Measurements with quite large random errors can result in meaningful conclusions in clinical research, but are not valid for clinical testing. For instance, for the base-of-support (BOS)[7], the reported mea-

positions, where the objective of data collection is to capture the movement of the underlying skeleton.

[6]Figure 2.6 is reproduced based on the materials presented in [9].

[7]The BOS is defined as the distance from heel-to-heel while walking. It is known to have clinical impor-

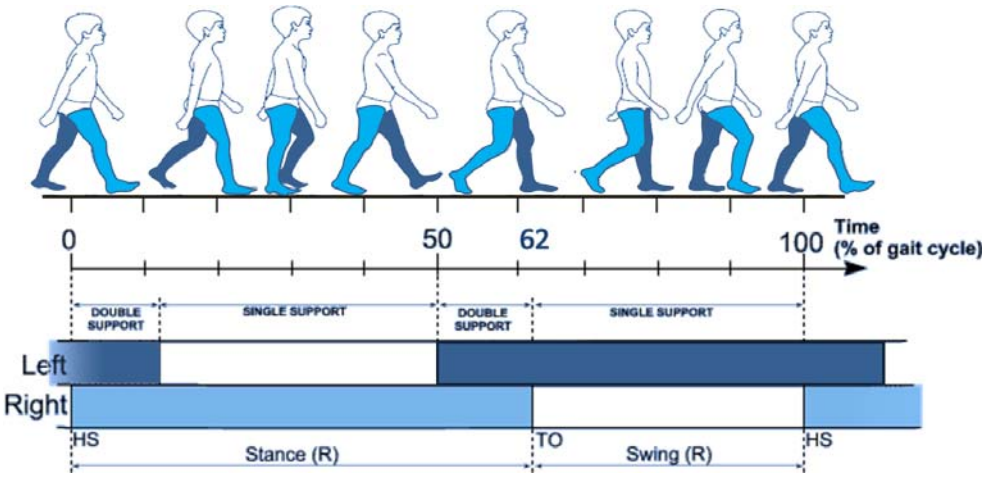

Figure 2.4: Gait cycle of a normal gait.

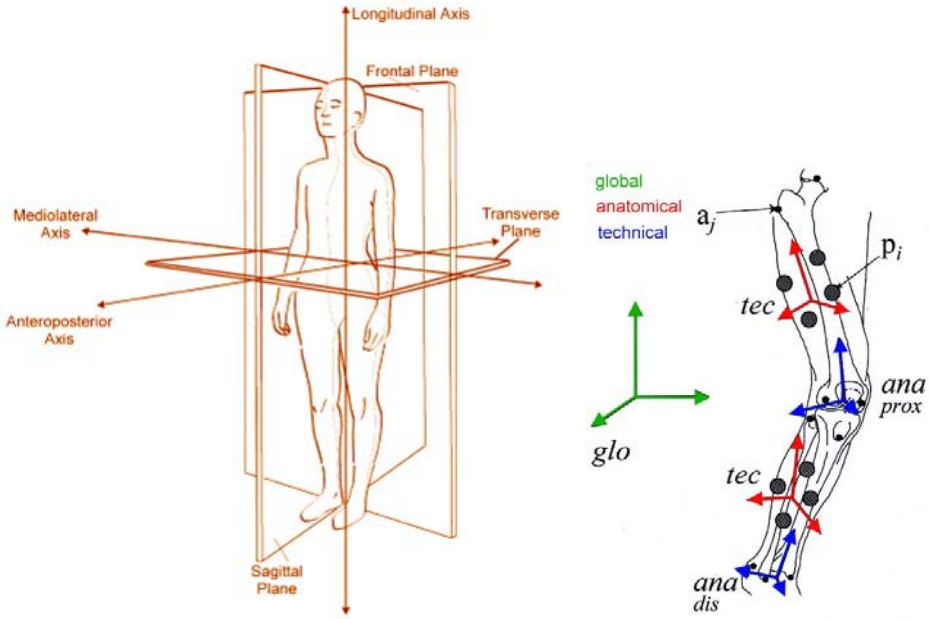

(a) (b)

Figure 2.5: (a) The basic axes definitions of anatomical positions. and (b) The major anatomical planes of motion, and axes of rotation.

surement accuracy is not sufficiently good to be clinically accepted. The BOS is typically equal to 8.5 cm for normal adults with a reported error of 1.17 cm, thus the relative error is ≈ 14.6 % [54], [95]. Abnormalities in the BOS are observed in older people, children with

tance.

Table 2.1: Preferred speed and cadence in terms of age and leg-length [93].

Age (yr)	cadence (st/min)	length (m)	speed (m/s)	stride S/L	Normalized cadence	Normalized velocity
1.00	176	0.32	0.63	1.36	0.53	0.36
1.50	171	0.36	0.71	1.39	0.54	0.38
2.00	156	0.39	0.71	1.41	0.52	0.37
2.50	156	0.41	0.80	1.49	0.53	0.40
3.00	154	0.44	0.86	1.51	0.55	0.41
3.50	160	0.47	0.99	1.59	0.58	0.46
4.00	152	0.49	0.99	1.58	0.57	0.45
5.00	154	0.53	1.08	1.58	0.60	0.47
6.00	146	0.57	1.09	1.57	0.59	0.46
7.00	143	0.62	1.15	1.57	0.60	0.47
adult	111	1.00	1.45	1.57	0.59	0.46

Down's syndrome, and people with Parkinson's disease[8]. In particular, people that suffer from Parkinson's disease have narrower BOS compared to normal people [54], [95], [17]. Snapshots of parkinsonian gait are shown in Figure 2.8[9]. Thus, the accuracy and reliability of the BOS measurement needs to be addressed, as it is one of important parameters to clinicians. Moreover, its measurement requires a certain level of accuracy that is not provided by current measurement systems. A summary of the BOS values in addition to other parameters is provided in Table 2.2 for normal gait. Also, stride-length, step-length, and right-knee (R-knee) flexion-angle are depicted in Figures 2.9(a) and (b) for normal gait.

Table 2.2: Gait parameters for normal subjects [54].

Gait parameter	Young subjects	Older subjects
Step-length, R(cm)	77 cm	65 cm
Step-length, L(cm)	77 cm	63.6 cm
Base-of-support, R(cm)	8.5 cm	8.5 cm
Base-of-support, L(cm)	8.1 cm	8.5 cm

Modern clinical gait analysis traces its origins to the early 1980s, where illuminated retro-

[8]It is a progressive neurological disorder that commonly develops in the range of 55-65 years [41].
[9]Figure 2.8 is reproduced based on the materials presented in [108], [37], [41].

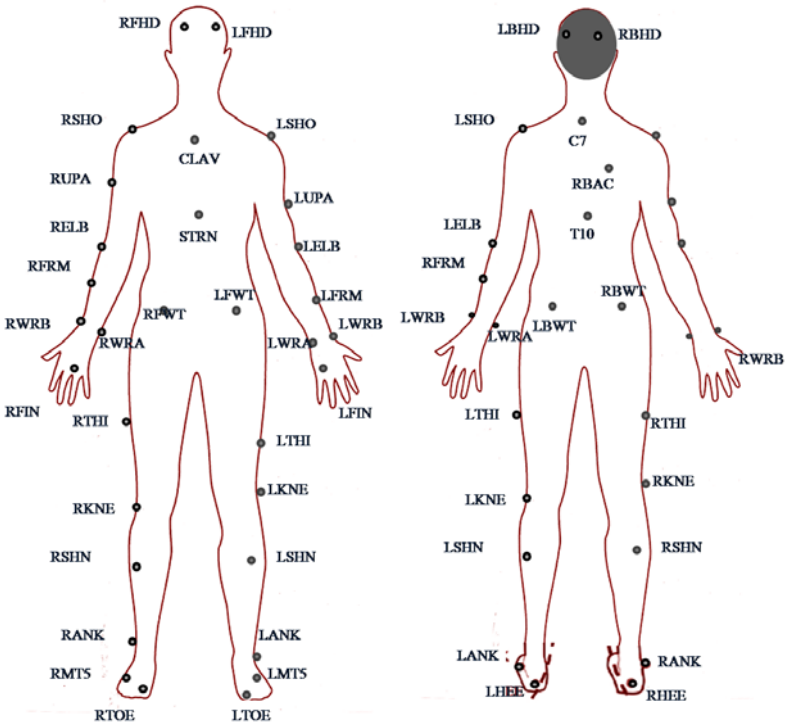

Figure 2.6: Example of diagrammatic definition of a marker-set.

reflective markers were placed on the skin in relation to bony landmarks, and detected by modified video cameras [11], [88]. If two or more cameras detect a marker and the positions and orientations of these cameras are known, then it is possible to detect the three-dimensional position of the marker. These systems are termed optical tracking systems [11], [10]. A simplified description of a gait laboratory equipped with an optical tracking system is shown in Figure 2.7[10]. Other types of motion measurement include the attachment of motion sensors to the patient's body in order to directly acquire motion data. Common types of motion sensors include, inertial, magnetic, and ultrasonic sensors [11], [24].

The choice of a suitable measurement system is controlled by multiple factors, such as accuracy and reliability, cost, and power consumption. Optical tracking systems are based on the use of charge-coupled device CCD-cameras and a set of markers attached to the subject's body, where marker positions are estimated via the triangulation of the position and orientation of two or more cameras [11], [10], [24]. Optical systems are accurate and use high sampling rates, which enable the acquisition of real-time data. The main disadvantage of these systems is that they require dedicated laboratories, complex settings, and highly skilled operators. In addition, they have the line-of-sight (LOS) restriction, where if markers are not detected by at least two-cameras their positions are not recorded [11], [10]. Other systems include motion sensors attached to the human body, which enable direct detection of motion. There are several types of sensory motion tracking systems, such as mechanical, magnetic, and inertial tracking systems. Mechanical systems employ electromechanical transducers attached to the subject's body, where motion is detected through voltage variations, whereas magnetic motion tracking systems use active transducers [11], [88], [24]. These systems are accurate and do not have the LOS restriction. However, the performance of these systems suffer from the interference due to magnetic materials in the surroundings. For inertial tracking systems, they are based on gyroscopes and accelerometers [11], [24]. Inertial sensors have the advantage of being self-contained, can be sampled at high rates, and do not have the LOS restriction. Nevertheless, these systems have the disadvantage of error accumulation over time. A possible solution for a more accurate and reliable tracking is to use hybrid systems [24], [92]. However, current motion tracking systems are expensive, and hybrid systems are expected to be even more expensive.

2.2 Overview of Ultra Wideband (UWB) Technology

UWB signals are characterized by their very large fractional bandwidths. According to the Federal Communications Commission (FCC), UWB systems are systems with fractional bandwidths that exceed 0.20 at -10 dB level. Fractional bandwidth is the ratio of the bandwidth occupied by the signal to the center frequency $B = 2\frac{f_h - f_l}{f_h + f_l}$, where f_h and f_l are the upper and lower frequencies at -10 dB according to the FCC definition for UWB

[10]Figure 2.7 is reproduced based on the materials presented in [30].

systems, and B is fractional bandwidth. Figure 2.10[11] shows indoor and outdoor transmission masks as defined by FCC. Narrowband communication systems have fractional bandwidths < 0.01. Also, according to the FCC, signals are recognized as UWB if the transmitted signal's bandwidth is 500 MHz or more. The band allocated to UWB in the United States is 7.5 GHz, and the frequency band allocated to UWB communications is 3.1 - 10.6 GHz with different emission limits for indoor and outdoor systems. Accordingly, UWB systems have many attractive features as well as many challenges associated with their application. UWB signals have large instantaneous bandwidths that enable fine time resolution and allow for location and tracking applications. Typically, low power-spectral-density (PSD) allows for the coexistence with existing users with low probability of intercept (LPI). According to Shannon's capacity theorem, UWB systems can achieve high data-rates at reasonable SNRs. High data-rates can be traded for low power spectral density and multi-path performance. Typically, UWB pulses are very short, on the order of nanoseconds, which provides robust performance in dense multi-path environments due to the large number of available resolvable paths. Finally, UWB systems are characterized by the low-cost of their hardware components [90], [81].

UWB signals involve two common forms namely, impulse radio UWB (IR-UWB) and multi-carrier UWB (MC-UWB) signals. Impulse radio refers to the generation of a series of very short pulses on the order of hundreds of picoseconds. Impulse radio is essentially a baseband technique. Nevertheless, this type of transmission does not require additional carrier modulation, and is sometimes referred to as carrier-less modulation. The second form of UWB signals is MC-UWB, which is well-suited for avoiding interference because of

[11]Figure 2.10 is reproduced based on [90].

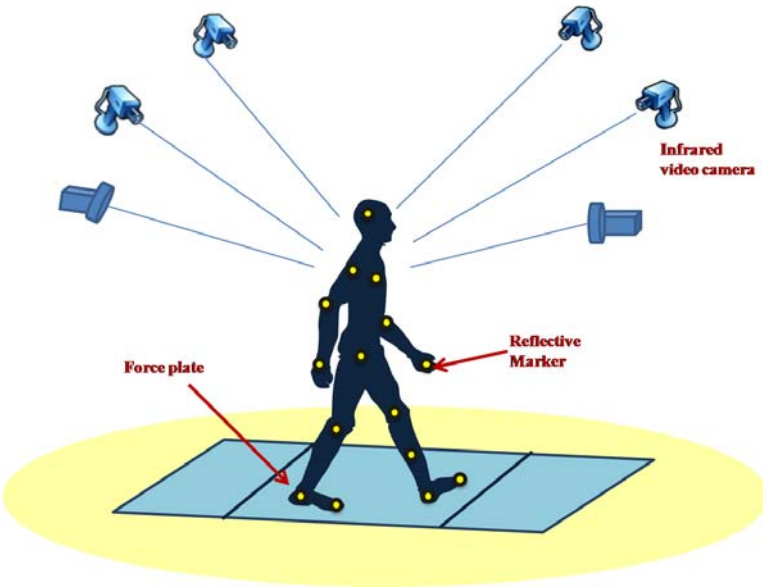

Figure 2.7: Basic configuration of a gait analysis laboratory.

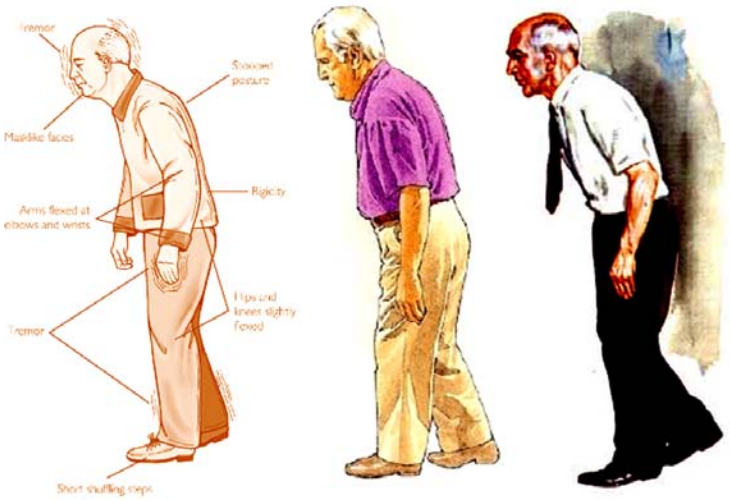

Figure 2.8: Snapshots of Parkinsonian gait.

the precise choice of carrier frequencies for narrowband interference avoidance. In the latter type, high speed FFT processing is necessary, which requires significant processing powers in addition to high peak average power ratios (PAPRs). On the other hand, IR-UWB signals require fast switching times and highly precise synchronization. Furthermore, IR-UWB requires antennas that can cover the ultra wide bandwidths corresponding to pulse durations on the order of nanoseconds with minimum distortion. Ideal UWB antennas should have radiation fields with constant magnitude and phase shift that varies linearly with frequency. Particularly, effects induced from antennas are included in the channel model [60], [90].

Multi-path channels are quantified by their multi-path channel parameters which are determined from the power delay profile. Time dispersive properties of wideband multi-path channels are quantified by their mean excess delay, and the root-mean-square (RMS) delay spread. Typical values of RMS delay spread for outdoor channels are on the order of microseconds and on the order of nanoseconds for indoor channels [89]. Thus, typical channel delay spreads are larger than UWB pulse durations by orders of magnitude, which results in dense multi-path fading channels with many resolvable paths [90], [81].

2.2.1 Pulse Shapes

Pulses employed in UWB systems must satisfy FCC regulations. IR-UWB uses monocycles with pulse shapes that include Gaussian, Rayleigh, and Laplacian pulses. Typically, continuous pulse transmission without signal processing introduces strong spectral lines in the spectrum of the transmitted signal. A common solution is to apply randomizing techniques, such as time-hopping (TH), or direct sequence spread spectrum (DS-SS) techniques. The most common form of IR-UWB is time-hopping pulse-position-modulation (TH-PPM) UWB. An advantage of IR-UWB is the ability of introducing processing gains. Basically,

employing multiple monocycles N per single bit achieves a processing gain $P_{G1} = 10\log(N)$, which combats both noise and interference. Additionally, using low duty-cycles reduces the impact of continuous sources of interference as well as achieving further processing gain $P_{G2} = 10\log\left(\frac{T_f}{T_p}\right)$, where T_f is TH frame duration and T_p is the pulse duration. Moreover, using a short pulse width compared to frame duration reduces inter pulse interference (IPI). The most common form of monocycles employed in IR-UWB is Gaussian pulses, for which the first derivative has a single zero crossing [60], [90].

Typically, the nominal center frequency and bandwidth of the monocycle depend on the monocycle's width. If additional derivatives are considered, the relative bandwidth decreases, and the center frequency increases for the same time constant. UWB antenna differentiates the pulse in the time domain, thus the transmitted pulse is the first derivative of the generated pulse. The potential modulation scheme employed with TH-UWB is PPM scheme, for which increasing the order of pulse derivative leads to a smaller value of the optimum

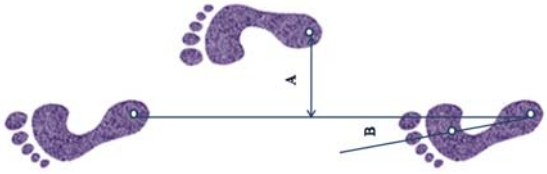

(a)

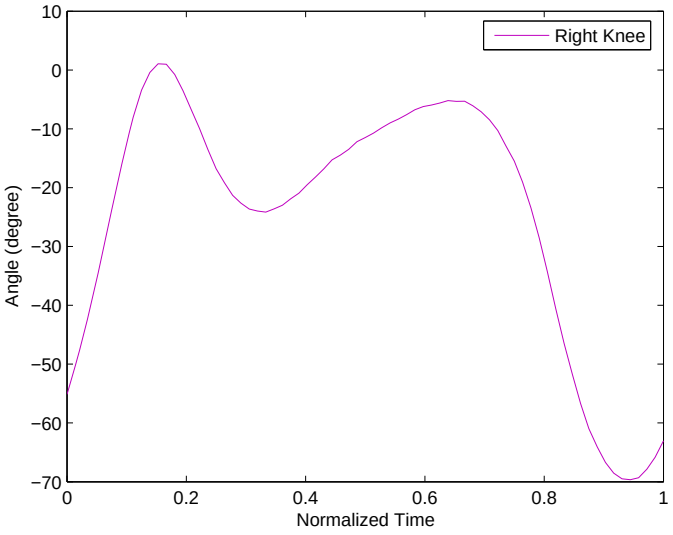

(b)

Figure 2.9: (a) Step-length and stride-length gait parameters. and (b) Simulation of right-knee angle during walking using OpenSim software [4], [33].

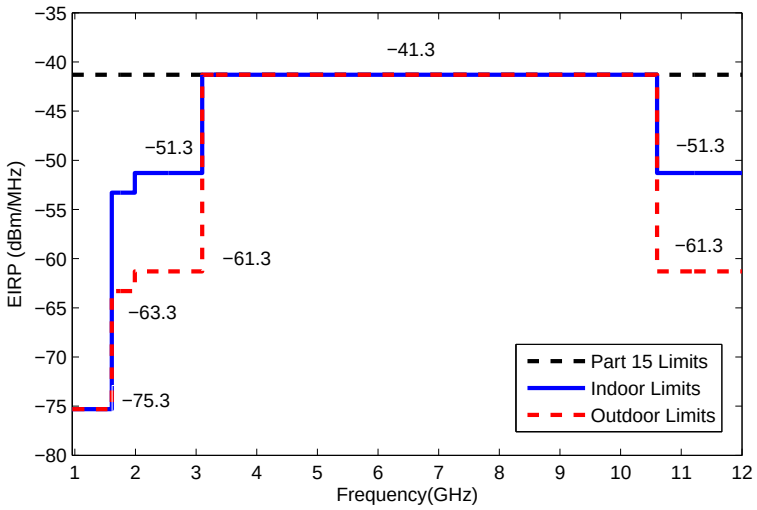

Figure 2.10: Indoor and outdoor limitations as defined by FCC.

modulation index δ, and a consequent better BER performance. This is due to the fact that the behavior is related to the cross-correlation properties of ones and zeros, and thus an optimum value of δ can be selected and fixed for AWGN channel. The achievement of a better BER performance is traded for higher sensitivity to timing jitter. Other common types of modulation schemes include, pulse amplitude modulation (PAM), orthogonal pulse modulation (OPM), and pulse shape modulation (PSM). MC-UWB basically employs orthogonal sub-channels [60]. [90]. Figure 2.11 and Figure 2.12 show various orders of the Gaussian pulse and their autocorrelations, respectively.

2.2.2 Receiver Implementation and Complexity Issues

Digital implementation of UWB systems is directly related to sampling frequency, which could be accomplished via direct sampling or time interleaved sampling approaches. High sampling frequencies put limitations on analog-to-digital-converter (ADC) design including speed and power consumption, which is a very challenging task for UWB systems with direct sampling approach. Figure 2.13 shows ADC power consumption versus number of bits and sampling frequency. Time interleaved approach relaxes the system requirements, and can still attain high sampling frequencies, where the received signal is typically sampled by a number of ADCs operating in parallel. Another receiver implementation issue is the high complexity associated with low-noise amplifiers (LNAs) design. LNAs are scarcely found on chip level designs [90].

Generally, due to the bandwidth requirements of UWB signals, analog UWB receiver designs are considered. In Particular, they can accommodate for the high bandwidth requirement, which comes at the expense of reduced flexibility. Although, the use of digital

approaches provides flexibility in receiver signal processing, they are limited by the resolution of the ADC and digital-to-analog-convert (DAC), and high power consumption requirements [59]. Figure 2.14[12] shows a generic block-diagram of a UWB receiver. A receiver that employs ADC with single bit per sample and a sampling rate that is greater than or equal to the Nyquist rate was introduced in [59]. An ADC based on quantization coefficients that are obtained via the projection of a continuous time signal over a set of basis functions was considered in [57]. Lower sampling rates are traded for an increased system complexity [57]. Moreover, an ADC conversion in the frequency domain yields a relaxation of conversion speed due to the inherently parallel architecture [58].

2.3 UWB Receiver Architectures for Wearable WBANs

Wireless pervasive healthcare has recently received an increased attention in research, where patients can monitor their health and take measurements at home or the office. Wireless

[12]Receiver block diagrams in this chapter are reproduced based on the materials presented in [60].

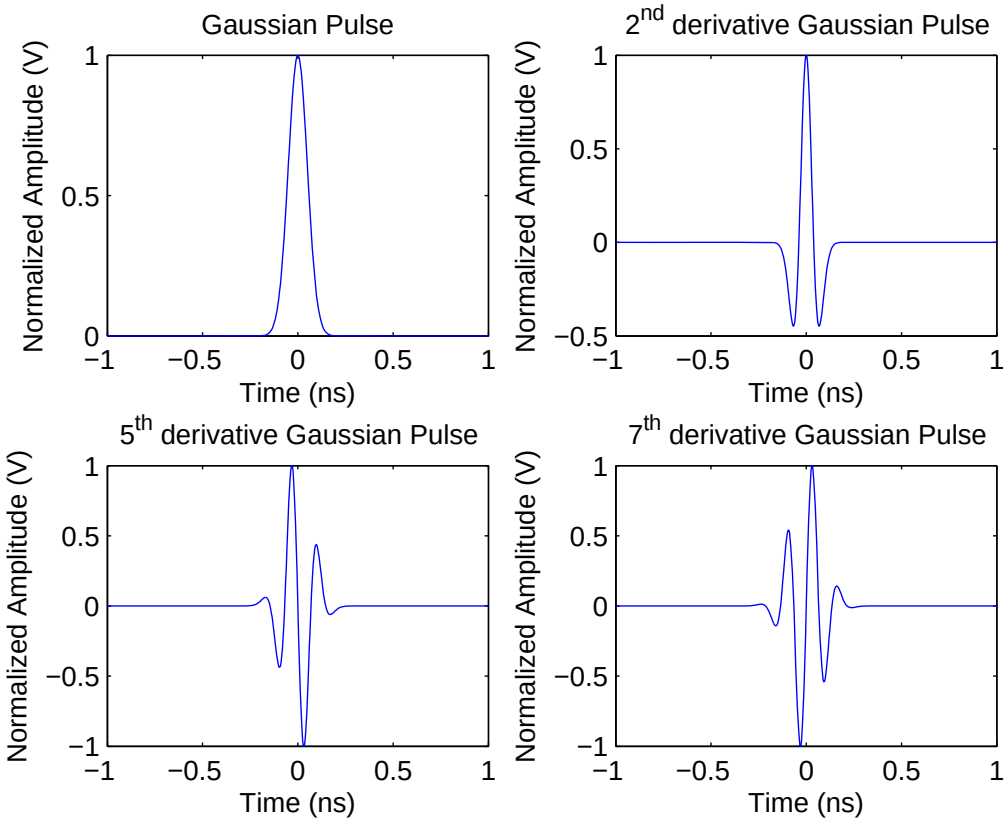

Figure 2.11: zeroth, second, fifth, and seventh order Gaussian pulses.

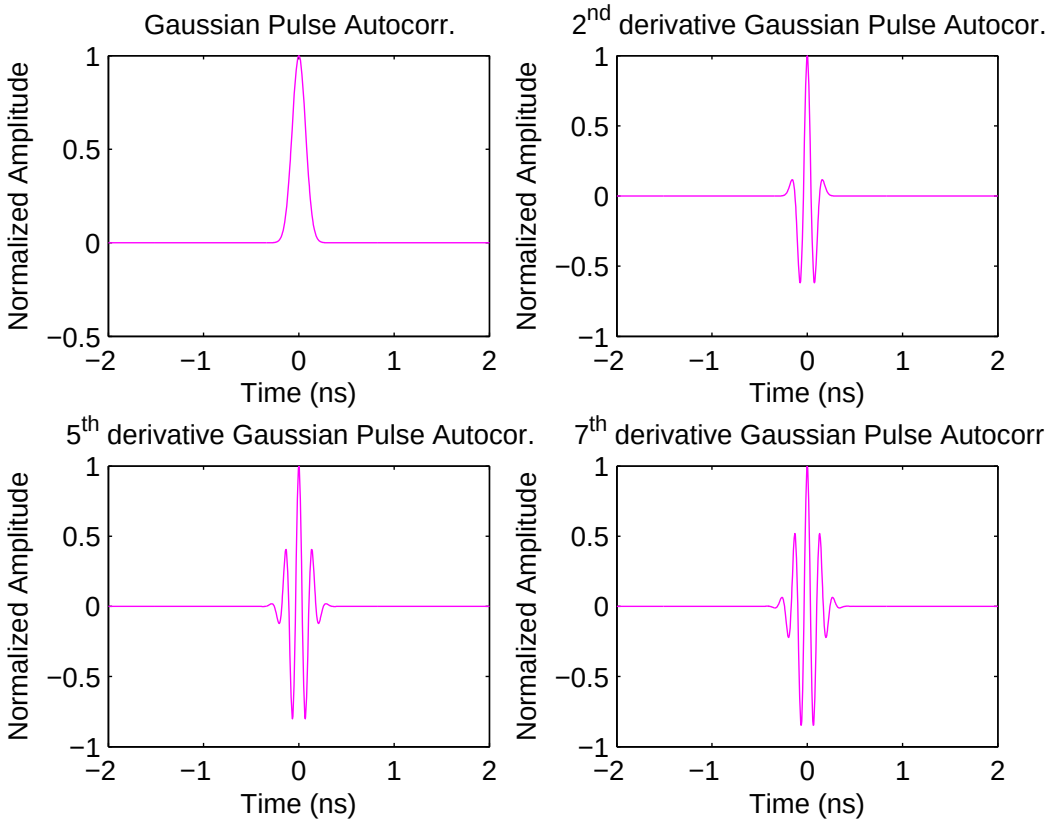

Figure 2.12: Autocorrelation of zeroth, second, fifth, and seventh order Gaussian pulses.

healthcare networks can provide real-time data acquisition via medical sensor nodes attached to human body in the form of a wireless local body area network (WBAN) [16], [123]. Data is then stored in a remote central node. Ultimately, the use of wearable healthcare systems is a promising solution not only for gait analysis, but also for general health-monitoring and early detection of abnormal conditions [39]. UWB pulses are very short, typically on the order of nanoseconds. The ultra-fine time resolution of UWB pulses allows for geo-location and tracking applications. Particularly, the time-of-arrival (TOA) and time-difference-of-arrival (TDOA) range estimation techniques via the arrival time of the first detected path can offer high accurate range estimates [90], [60].

IR-UWB provides robustness in dense multi-path environments [60]. An optimum receiver is fully capable of exploiting the rich multi-path channel diversity. In order to capture the signal energy, All-RAKE (ARAKE) receivers that have a number of fingers equal to the available number of resolvable paths are required, but they are impractical. On the other hand, a single correlator that is matched to one transmission path is very simple, but highly suboptimal [60]. Non-coherent receivers are low-power solutions that do not require channel estimation, and are suitable for low-data rate applications [20]. In these receivers, low-power

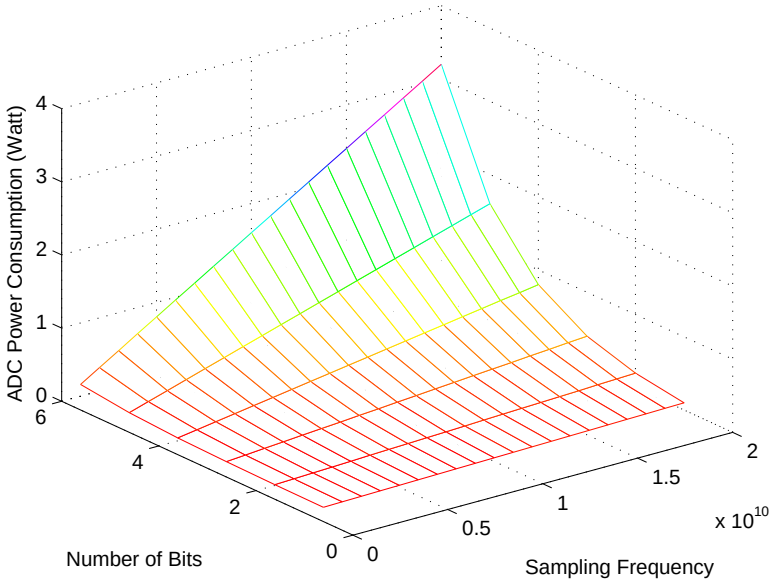

Figure 2.13: ADC dissipation power versus number of bits and sampling frequency.

consumption is traded for a degradation in bit error rate (BER) performance. Non-coherent alternatives include transmitted reference (TR) and energy detection (ED) schemes [106].

Optimum receivers involve the correlation of the received waveform with a locally generated template waveform, and require channel estimation, which adds to the power consumption of the receiver [60]. These requirements are precluded for non-coherent receivers, where the detection process depends solely on the received pulses [60], [20]. Figure 2.15 shows a simplified block-diagram of a correlator receiver.

The TR scheme is based on the transmission of a pair of pulses (one modulated and one unmodulated), where at the receiver, the unmodulated pulse is used to detect the modulated pulse. However, TR correlation receivers, shown in Figure 2.17, suffer from the use of a noisy

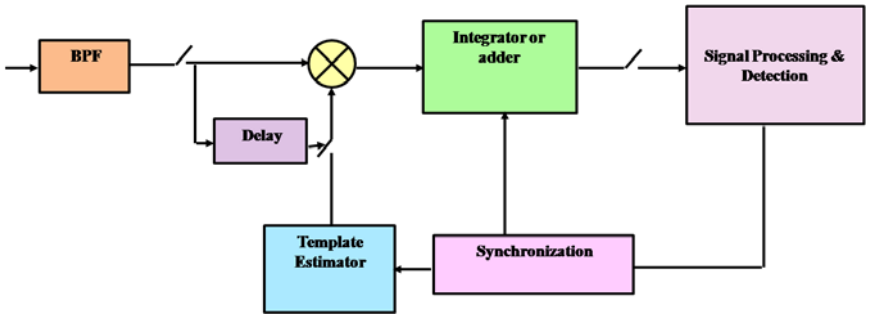

Figure 2.14: Generic block-diagram of UWB receiver.

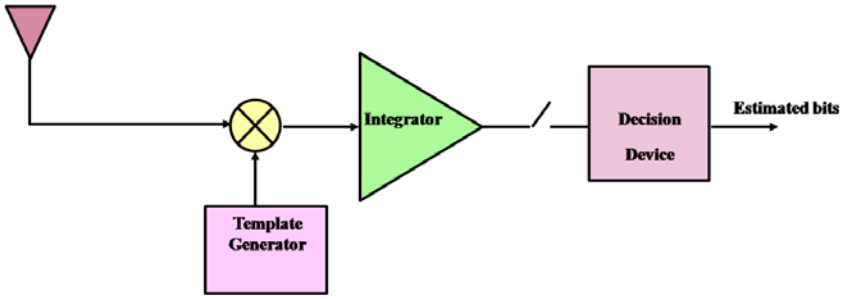

Figure 2.15: Simplified block-diagram of correlator receiver.

template [106]. Instead of sending reference pulses, the differential transmitted reference (DTR) scheme uses the data pulses of previous symbols for the correlation with the received pulses, as depicted in Figure 2.16. Hence, DTR achieves a 3 dB performance gain over TR schemes. On the other hand, DTR requires differential encoding of the transmitted bits, which in turn requires longer delay lines, and higher power consumption [106].

The energy detection (ED) correlation receiver is another non-coherent receiver; depicted in Figure 2.18. In ED correlation receivers, the correlator is replaced by a squaring device. ED IR-UWB receivers can be implemented with on-off keying (OOK) and PPM schemes. However, OOK requires a careful choice of the detection threshold [106].

Typically, there is a tradeoff between the bit-error-rate (BER) performance and receiver complexity. The implementation approaches proposed in the literature for UWB systems include, all-digital, analog, and partially-analog implementations [97], [74]. In the all-digital implementation approach, the complexity is directly related to the sampling frequency. High sampling frequencies put limitations on the analog-to-digital (ADC) design including speed and power consumption, which is a very challenging task for UWB systems based on the direct sampling approach. Generally, due to the bandwidth requirements of UWB signals, analog UWB receiver designs are considered as they can accommodate the bandwidth requirements, which comes at the expense of reduced flexibility. On the other hand, the use of digital approaches provide flexibility in the receiver signal processing, but is limited by the ADC resolution and power consumption [74].

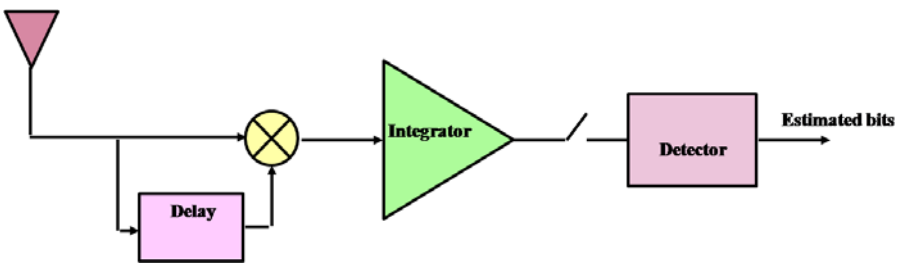

Figure 2.16: Simple TR receiver structure.

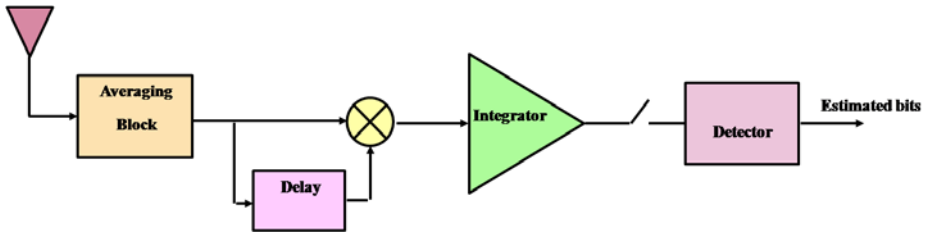

Figure 2.17: DTR receiver structure.

2.3.1 Power Consumption Requirements of UWB Wearable WBANs

Wearable and implanted healthcare applications have strict power consumption requirements, where devices are directly attached to the subject's body. In particular, the IEEE has recently approved the IEEE 802.15 TG6 task group for the standardization of body area networks for short-range, wireless communication in the vicinity of, or inside the human body for the frequency bands approved by the national medical and regulatory authorities including the 3.1 - 10.6 GHz UWB band [16], [123], [120]. More specifically, the goal of this group is to standardize short-range communications via implanted medical devices and on-body sensors with monitoring tools to provide patient-health-data in real-time [39]. However, it is not restricted to medical applications. Initial requirements of the BANs include a coverage distance of 2 to 5m with a power consumption of about 0.1 - 1 mW per node [38]. Furthermore, for on-body sensors, considered power technologies include temperature difference, non-rechargeable (Zinc-air, Lithium and silver-oxide) and Lithium-ion rechargeable. Essentially, the low-power consumption for on-body communications is required to protect the human tissue [16], [39]. Medical application proposals for BANs include swallowable devices for drug delivery and imaging, wearable sensors, such as electroencephalogram (EEG), electrocardiogram (ECG), blood pressure, body temperature, and hearing aids [123].

In IR-UWB receivers, ADCs can be moved almost up to the antenna after the low-noise amplifier (LNA), which moves the signal processing to the digital domain, which is known as the all-digital signal processing approach [90], [74], [65]. This approach puts high constraints on the ADC, where to efficiently sample the incoming signal at the Nyquist rate the sampling frequency is on the order of of several gigahertz. In this approach, the ADC speed and resolution become of utmost importance [74], [65], [114]. Baseband Nyquist sampling of a 2

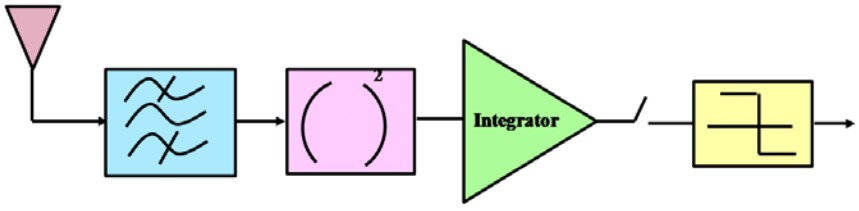

Figure 2.18: Simple energy detection receiver.

GHz UWB signal requires approximately 4 GHz ADC clocking, which has the potential to consume enormous amounts of power. In particular, using a figure of merit of approximately 4e11, the estimated power consumption of a 4-bit and 4 GSa/s ADC is equal to 160 mW. Whereas, a key advantage of UWB radios is the low-power consumption. The ADCs and matched filters, for coherent detectors, represent the bottleneck for achieving a low-power consumption, where they require high sampling rates [74], [114]. Moreover, for coherent detectors, the correlation operation and template generation must be performed at very high speed, which implies a tradeoff between power consumption and template generation accuracy. However, for low-power operation, a simple template is desired [65].

UWB coherent detectors that use windowed sinusoids have been proposed in the literature as an alternative solution for low-power template generation in the analog domain, since windowed sinusoids can approximate the optimal templates and are easily generated in the analog domain [97]. However, this solution suffers from the sensitivity of the correlator output SNR to timing errors. Receiver structures with suboptimal sinusoidal templates are more sensitive to timing errors as compared to optimal receivers [97]. Complex sinusoids were proposed to compensate for the SNR degradation in the presence of timing errors, but this structure requires nearly double the power required for the corresponding structure with real sinusoids [65], [53].

2.4 UWB Time-of-Arrival (TOA) Estimators and Theoretical Lower Bounds

Ranging refers to the process of estimating the distance of a target node from a reference node. Common ranging techniques include received-signal-strength-indicator (RSSI) and time-of arrival (TOA) measurements. In particular, while various approaches can be used for ranging, the most promising approach for UWB signaling is the timebased approach, whose accuracy can be improved by increasing either the SNR at the receiver or the effective signal bandwidth of the transmitted signal. Since UWB signals have very large bandwidths, this property allows for extremely accurate location estimates [36], [60], [35]. The most accurate and frequently used distance measurement approach for accurate indoor positioning is the TOA estimation of the first detected path. In such systems, the detection of the first arriving path in non-line-of-sight (NLOS) multi-path environments is challenging, where the first arriving path, if exists, is not necessarily the strongest path, and can result in a positively biased range estimate [36], [35].

Error bounds are essential for providing a performance limit of any estimator in terms of the mean square error (MSE). The Cramer-Rao lower bound (CRLB) defines the lower bound on the ranging accuracy in terms of the signal bandwidth and SNR [28].

The error of the range estimation $\varepsilon_{\hat{d}}$ is defined as [62]:

$$\varepsilon_{\hat{d}} = \left| d - \hat{d} \right| \tag{2.1}$$

where, d and $\hat{d}$ are the actual and estimated distances, respectively.

From estimation theory, the MSE $\sigma_{\hat{\tau}}^2$ of any unbiased estimate $\hat{\tau}$ of τ is bounded by the CRLB as follows [28]:

$$\sigma_{\hat{\tau}}^2 = \mathrm{E}\left\{ (\hat{\tau} - \tau)^2 \right\} \geq \mathrm{CRLB} \tag{2.2}$$

where, $\varepsilon_{\hat{\tau}} = \hat{\tau} - \tau$ and $\mathrm{E}\{.\}$ denotes the statistical expectation [28].

The CRLB of the ranging error estimate (cm) can be calculated from the relation:

$$\sigma_{\hat{d}} = c\sigma_{\hat{\tau}} \tag{2.3}$$

where, $c = 3.10^8$ m/s is the speed of light [23].

When no-multi-path is present [28]:

$$\mathrm{CRLB} = \frac{N_0/2}{E_p \beta^2} = \frac{1}{2\beta^2 SNR} \tag{2.4}$$

where the pulse-energy-to-noise ratio is represented by $\frac{E_p}{N_0} = SNR$, and β is the second moment of the spectrum $P(f)$ of the pulse shape used $p(t)$ defined by [28]:

$$\beta^2 = \frac{\int_{-\infty}^{\infty} f^2 \left| P(f) \right|^2 df}{E_p} \tag{2.5}$$

Assuming a Gaussian pulse defined in terms of the pulse width T_p and $\tau_p = 0.5 * T_p$ as [28]:

$$p_0(t) = exp\left(-2\pi \left(t^2 / \tau_p^2 \right) \right) \tag{2.6}$$

The n-th order Gaussian pulse has the form [97]:

$$p_n(t) = \frac{d^{(n)}}{dt^n} \left(e^{-2\pi \left(\frac{t^2}{\tau_p^2} \right)} \right) \tag{2.7}$$

Generally, the CRLB provides a loose bound on the TOA estimate which is not realizable in multi-path environments [28]. Another bound that provides more accurate results, and is suitable for multi-path environments is the Ziv-Zakai lower bound (ZZLB). The mean square estimation error is as [28]:

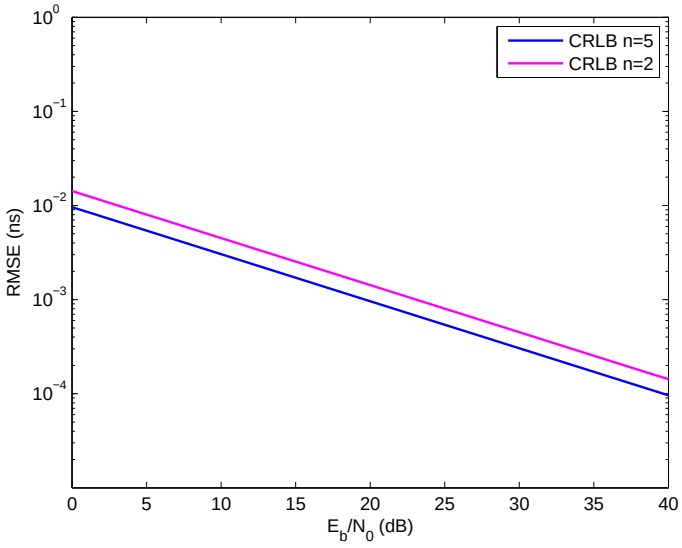

Figure 2.19: CRLB in AWGN assuming second and fifth order Gaussian pulses with $\tau_p = 0.113$ ns, and $T_a = 100$ ns.

$$E\left\{\varepsilon_{\hat{\tau}}^2\right\} = \frac{1}{2}\int_0^{\infty} zP\left\{|\varepsilon_{\hat{\tau}}| \geq \frac{z}{2}\right\} dz \tag{2.8}$$

where the expectation is with respect to τ, and $P_\tau(\tau)$ is the probability density function (pdf) of the TOA in the absence of any information is assumed to be uniformly distributed in the interval $[0, T_a]$. $P\left\{|\varepsilon_{\hat{\tau}}| \geq \frac{z}{2}\right\}$ is equivalent to the probability of a binary detection scheme with equally-probable hypothesis, where T_a is the observation window [28]. Figure 2.19 shows CRLB for second and fifth order Gaussian pulses in AWGN assuming $\tau_p = 0.113$ ns and $T_a = 100$ ns.

The ZZLB for the coherent detection of binary signaling is as given by [28]:

$$\text{ZZLB} = \frac{1}{T_a}\int_0^{T_a} z\left(T_a - z\right) P_{\min}(z) dz \tag{2.9}$$

where, $P_{\min(z)}$ is the minimum attainable probability of error expressed as [28]:

$$P_{\min}(z) = Q\left(\sqrt{\frac{E_p}{N_0}(1 - \rho_{pp}(z))}\right) \tag{2.10}$$

and the pulse autocorrelation $\rho_{pp}(z)$ normalized by the pulse-energy E_p is [28]:

$$\rho_{pp}(z) = \frac{1}{E_p} \int_{-\infty}^{\infty} p(t)p(t-z)dt \tag{2.11}$$

This bound transforms the estimation problem into a binary detection problem, which simplifies the bound estimation in multi-path environments. The derivation of $P_{\min}(z)$ depends on the receiver *a priori* knowledge about the multi-path phenomena [28]. However, the evaluation of the estimator in complex channel models is not analytically tractable [28]. As a result, the ZZLB is typically evaluated using experimentally measured channel impulse responses or Monte Carlo simulations [28].

$$P_{\min}(z) \cong \frac{1}{N_{ch}} \sum_{k=1}^{N_{ch}} Q\left(\sqrt{\frac{SNR}{2} d^2_{k,i(*)}(z)}\right) \tag{2.12}$$

$$P_{\min}(z) \cong Q\left(\sqrt{\frac{SNR}{2} d^2_{\min}(z)}\right) \tag{2.13}$$

where N_{ch} is the number of channel realizations, SNR is the signal-to-noise-ratio, $d_{\min}(z) = \min_k d_{k,i^{(*)}}(z)$ is the minimum normalized distance, $i^{(*)} = \arg\min_i d^2_{k,i}(z)$, and k is the argument of the minimization [28]. Figures 2.20(a) and (b) show ZZLB for second and seventh order Gaussian pulses with $\tau_p = 0.2$ ns and $T_a = 100$ ns for distance in (cm) and TOA in (ns), respectively.

It is worth noting that this bound provides a lower-bound on the TOA of coherent detectors. Whereas for the ED estimator, at high SNR it exhibits a floor equal to $T_s/\sqrt{12}$. On the other hand, the MF estimator performance tends to the CRLB with a behavior depending on the fading of the first-path [26]. Most of the available motion capture and movement tracking systems are based on the acquirement of the absolute positions of the different nodes. These positions are then used for the estimation of the other gait parameters. The relevant approach using UWB radios is the node positioning approach. Typically, UWB positioning-accuracy is based on the ranging accuracy. The CRLB on the positioning accuracy is [84], [47]:

$$\sqrt{\mathrm{var}(\hat{d})} \geq \frac{c}{2\sqrt{2}\pi\sqrt{\mathrm{SNR}}\beta} \tag{2.14}$$

where var() is the variance, $\hat{d}$ is the position estimate, and β is the effective (or root mean square) signal bandwidth. Figure 2.21 shows CRLB on localization (positioning) error for fifth and seventh order Gaussian pulses with $\tau_p = 4$ ns and $T_a = 100$ ns.

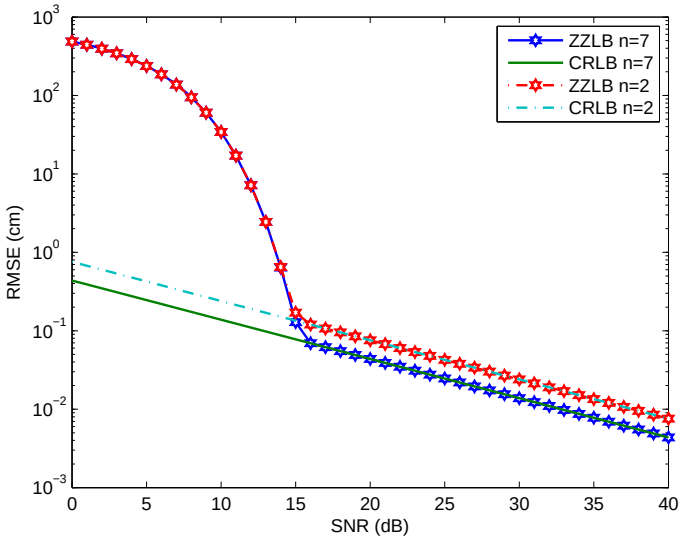

(a)

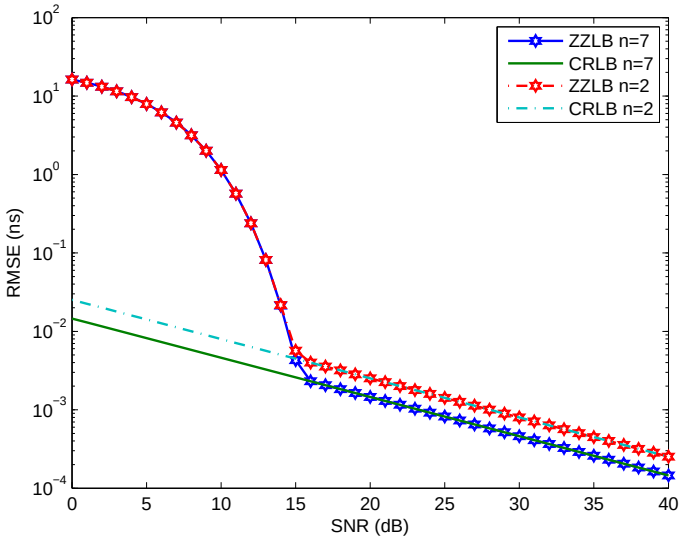

(b)

Figure 2.20: (a) ZZLB for second and sixth order Gaussian pulses AWGN channel in (cm) with $\tau_p = 0.192$ ns, and $T_a = 100$ ns. and (b) ZZLB for second and seventh order Gaussian pulses AWGN channel in (ns) with $\tau_p = 0.2$ ns, and $T_a = 100$ ns.

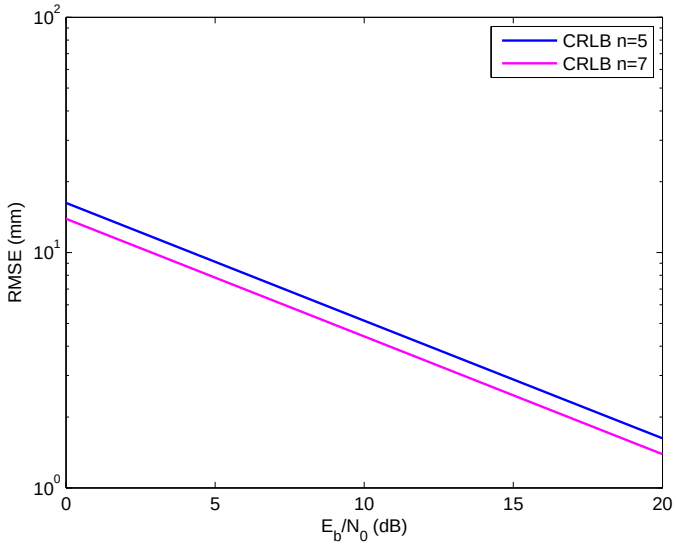

Figure 2.21: CRLB on localization error for fifth and seventh order Gaussian pulses with τ_p = 4 ns and T_a = 100 ns.

2.5 Chapter Summary

In this chapter, we gave an overview of different topics of importance to our proposed system design. Particulary, we summarized different gait analysis systems, and highlighted the advantages and disadvantages of each type. Furthermore, we provided an introduction to UWB technology, pulse shapes, and receiver implementation issues. Moreover, we provided a brief comparative summary of different UWB receiver architectures. Finally, we demonstrated different lower bounds on the performance of TOA ranging and localization estimators. Particularly, we discussed the CRLB and ZZLB for ranging estimators, and CRLB for localization estimators.

Chapter 3

Overview of Proposed System

This chapter introduces the proposed system, proposes a study framework for performance /power consumption, provides an overview of the proposed ranging procedure, gives a summary of the proposed localization procedure, and discusses the possibility of integrating other types of sensors with UWB radios in the proposed system. Section 3.1 gives a brief description of our proposed system. Then, Section 3.2 summarizes the main rules employed in power consumption estimation. Further, Section 3.3 summarizes the system design parameters. Section 3.4 describes the employed transmitter and estimates the power consumption. Then, Section 3.5 provides an overview of the proposed performance/power consumption framework. Section 3.6 provides a brief summary on the proposed ranging approach, and studies the system symbol frame structure. Section 3.7 summarizes the challenges associated with the design of an accurate localization technique for our system, and then gives a description of the proposed approaches. Section 3.8 studies the possibility of employing sensor fusion for our system, and addresses key performance parameters. Finally, Section 3.9 provides a summary of chapter conclusions and contributions.

3.1 Description of Proposed System

The proposed system is based on wearable UWB radios attached to the subject's body, or possibly sewn into clothing specifically designed for this application. The target of the proposed system is to acquire the distances between the different points on the body during movement. A simplified diagrammatic representation of the proposed system's data acquisition approach is shown in Figure 3.1. The data acquisition procedure is divided into two phases, namely the initial phase and the core phase. The initial phase includes the measurement of the subject's height, weight, etc., as shown on the right in Figure 3.1. The aim of the core phase is to acquire the ranging data between the different nodes while the subject is walking through the estimation of the time-of-arrival (TOA) of the first path, which is then converted to a distance estimate, as illustrated by the subject to the left in Figure

3.1. The system is designed based on a target ranging accuracy of ≈ 0.1 cm. This value was particularly chosen for achieving a ranging accuracy that is ten-times better than the inter-marker distance accuracy reported in the literature for current systems. Specifically, the reported accuracy for the inter-marker distance for current systems is equal to 1.17 cm [54], [95].

Our measurement approach is based on LOS links, which have a substantially better performance than NLOS links due to the absence of body shadowing. This could be guaranteed through the predefinition of the sensor groups that have LOS links. An example of this predefinition is depicted in Figure 3.2 assuming the Vicon marker-set [9]. The ultimate goals of our system are as follows.

- High ranging and localization accuracies, and reliability of acquired data.
- Low-power consumption.
- Freedom of movement and ease of use; required to enable our system of taking measurements in indoor and outdoor environments.

Generally, applications that are based on wearable devices have the low-power consumption constraint, as they are placed close to the subject's tissue, and thus cannot consume too much power to avoid overheating or burning human tissue [16], [39]. Additionally, low power is important due to battery life concerns. Moreover, accurate gait analysis, in particular,

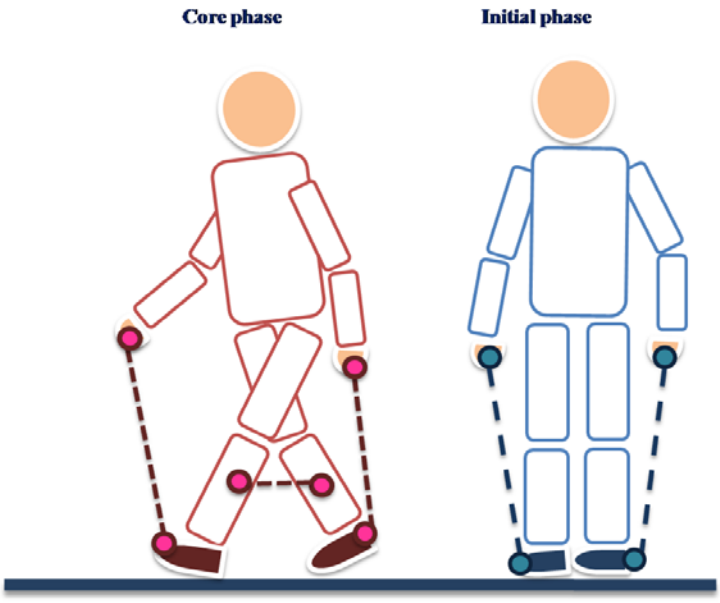

Figure 3.1: Simplified diagrammatic representation of the on-body intersegmental measurements using UWB radios, for the initial and during movement measurements.

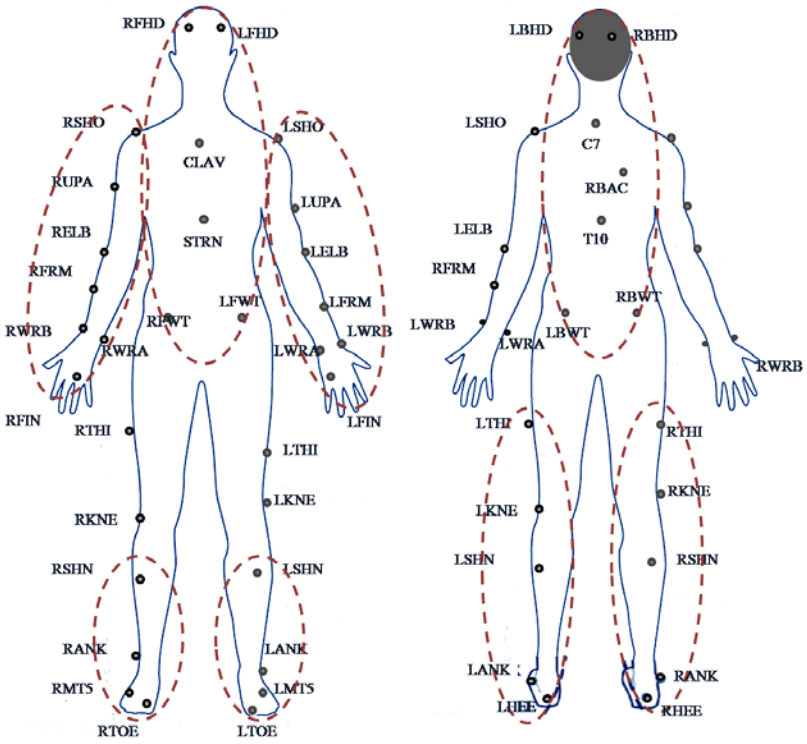

Figure 3.2: Vicon marker-set [9] grouped into regions with LOS markers.

requires a high ranging accuracy. Figure 3.3 shows a simplified representation of a wireless wearable health-monitoring and human locomotion tracking system.

In order to choose a suitable receiver architecture for this application, it should be capable of satisfying the high ranging accuracy and low-power consumption requirements. When transceivers are compared based on the ranging accuracies that they can provide, at high SNR, ED estimators exhibit a floor of $T_s/\sqrt{12}$, where T_s is the integration window. Stored-reference estimators, based on matched-filtering (MF), have performance which approaches the CRLB with a behavior depending on the fading of the first path. Typically, EDs require minimal integration windows equivalent to integer multiples of the pulse width, and in practice multiple pulses are transmitted per bit [26].

Typically, the error-performance and power-consumption tradeoffs have to be carefully studied in order to choose a suitable receiver structure, and the corresponding design parameters that guarantee the achievement of a particular system design target. For this reason, a framework for the characterization of error-performance and power-consumption of UWB receivers was developed, as will be discussed in Section 3.6.

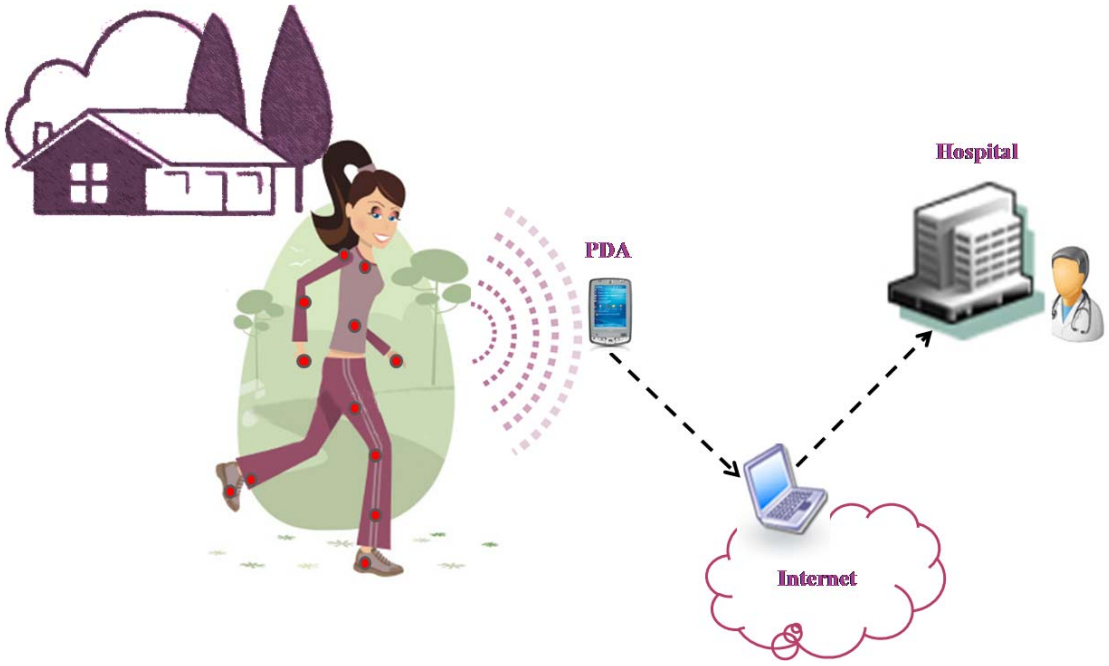

Figure 3.3: Wireless wearable health-monitoring and human locomotion tracking system.

3.2 Power-consumption Approximation

Low power consumption is an important performance metric for wearable, mobile, and healthcare applications. Essentially, power consumption optimization at the algorithmic level has a greater impact on the total power consumption than technological optimization. Figure 3.4[1] shows the common levels of abstraction used in system design. Since mobile, and healthcare systems basically depend on limited battery sources, energy consumption is a fundamental metric for these applications. Current research indicates that the power consumed during memory accesses accounts for a significant percentage of the total power consumption. Furthermore, considering only the computational complexity of an algorithm does not provide accurate estimates of the energy consumed by an algorithm. Moreover, data memory depends on the size of the data being processed and on how often the data memory is being accessed. The general power estimation formula as given in [69], [70] is:

$$P_{av} = \alpha C_{eff} V_{dd}^2 f_s \tag{3.1}$$

where, P_{av} is the average power, V_{dd} is the supply voltage, f_s is the sampling frequency. C_{eff}, is the effective capacitance, which has two components namely, the average capacitance, and the switching activity. For the behavioral level[2] this is equivalent to the number of accesses

[1]Figure 3.4 is reproduced based on the materials presented in [103], [40].

[2]Low-power system design based on the top-down approach includes several levels of abstraction ordered in a hierarchy depending on the level of abstraction. It starts by the highest level of abstraction at the top

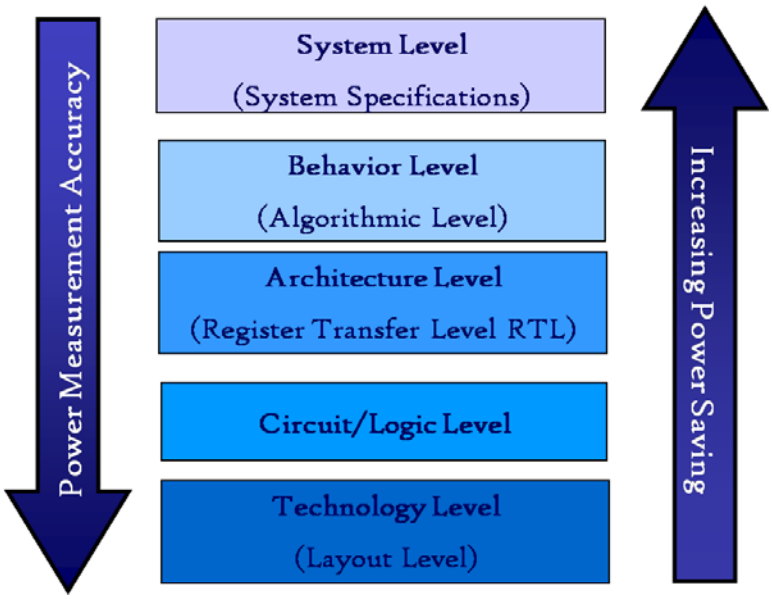

Figure 3.4: Flow of power saving through different levels of abstraction.

to a resource. The factor α represents the switching activity.

The energy consumption is calculated [73]:

$$E_{av} = P_{av}T \tag{3.2}$$

where, E_{av} is the average energy consumption, and T is the run-time.

Typically, a design framework should provide the designer with a flexible and efficient environment to explore the alternatives and trade-offs at the different levels of abstraction. UWB technology has specific challenges associated with its design due to the ultra-wide nature of its spectrum. Specifically, ADCs have to work at the Nyquist frequency. Also, the matched filter digital logic has to work at very high frequency. Since the allocated band to UWB healthcare applications is the 3.1 - 10.6 GHz range, the required sampling frequency is $\approx$ 15 GHz [16], [120]. A main drawback of the all-digital architecture is the high power consumption, which is dominated by ADCs and matched filters. One popular solution to reduce power consumption for UWB transceivers is to move the ADC after the matched filter or correlator block with correlation being performed in the analog domain. As a result, the sampling frequency constraints and consequently the power-consumption are reduced [74], [65].

down to the lowest level of abstraction ordered as, the system level, behavioral level, architectural level, circuit level, and technology level.

3.3 System Design

The initial design parameter of the proposed system is the target ranging accuracy of ≈ 0.1 cm. Furthermore, as specified by the IEEE 802.15 task-group six (TG6), allowable bandwidth for the UWB range is 2 GHz [120]. For the purpose of illustration, seventh-order Gaussian pulse was chosen to satisfy the FCC masks for both indoor and outdoor environments, as shown in Figure 3.5. Assuming the ED detector, and a corresponding pulse width = 0.8 ns, the corresponding B.W. is 2 GHz [85], the maximum achievable ranging accuracy is 6.9 cm for an integration window that is equal to the pulse width. This precludes the choice of ED detectors. Obviously, for such a high target ranging accuracy, the MF seems an appropriate choice, where its performance approaches the CRLB at high SNRs.

3.4 Transmitter Structure and Power Consumption

Typically, pulse correlation properties affect the receiver performance, and pulses should be chosen with parameters that comply to the FCC indoor and outdoor masks [76]. Figure 3.5 shows the PSD of the FCC masks and the corresponding pulses that comply these masks. For the 0 - 960 MHz band, the second order Gaussian pulse with σ= 60 ps covers the band. Whereas, for the 3.1 - 10.6 GHz band, the pulse for indoor systems is the fifth order Gaussian pulse with σ= 51 ps, and the seventh order Gaussian pulse for outdoor systems with σ= 60 ps fits within the spectral mask. As shown, the seventh order Gaussian pulse complies for both indoor and outdoor FCC masks.

Our system is ultimately capable of taking indoor and outdoor measurements, so the selected pulse needs to comply with both environments. Thus, we choose the seventh order Gaussian pulse for our system. The selected bandwidth is 2 GHz from 3.1 - 5.1 GHz. An actual implementation for this pulse generator has been proposed in the literature [85]. The block diagram of the pulse generator is depicted in Figure 3.6[3]. The transmitter is implemented in the analog domain to satisfy the low-power consumption requirement. The corresponding pulse-width is T_p = 0.8 ns [85]. The seventh order Gaussian pulse with T_p = 0.8 ns is shown in Figure 3.7. A summary of the pulse parameters and power consumption is given in Table 3.1. The equivalent power consumption at 50 Mp/s rate is 0.24 mW.

[3]Figure 3.6 is reproduced based on the materials represented in [85].

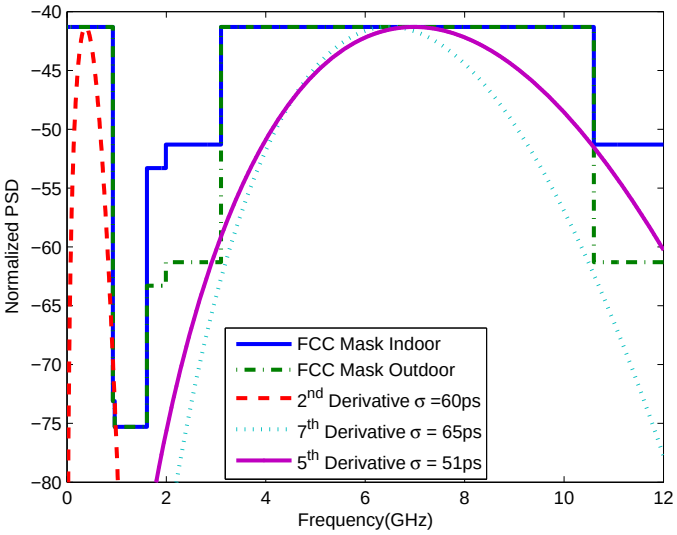

Figure 3.5: PSD of second order, fifth order, and seventh order of Gaussian monocylce and the indoor and outdoor FCC masks for 0 - 960 MHz and 3.1 - 10.6 GHz bands.

Table 3.1: Summary of Transmitter Parameters and Power Consumption [85].

Parameters	Values
Bandwidth	3.1 - 5.1 GHz
Pulse duration	0.8 ns
Energy consumption per pulse	4.9 pJ per pulse

3.5 Overview of Proposed Performance/Power consumption Study Framework with Non-coherent Detectors Case Study

In order to study the power consumption/performance trade-offs, we developed a framework for the estimation of power consumption and performance of the architectures under study. Furthermore, we used this framework for the choice of the optimum hardware architecture for our target application. For instance, the choice of a suitable receiver architecture for our system is crucial. Particularly, our target is to have low power consumption and high ranging and localization accuracy. Since, commonly good performance is traded for higher power consumption, thus combining these two metrics in one architecture choice is a challenging task.

For this reason, our developed framework will take into consideration all possible power consumption and performance parameters without having actually to implement these architectures. Furthermore, in order to have a fair comparison, we assume the same implementation technology based on state-of-the-art components proposed in the literature. The proposed framework in addition to a sample case study will be given in detail in a later chapter.

3.6 Ranging Approach and System Symbol Structure

The primary motivation for using UWB technology (besides the wide spectrum available) is the ability of UWB pulses to provide very accurate distance estimates using TOA measurements [36], [49]. As was shown in a previous section, ranging is the main stage of our proposed system. Typically, the inter-node distance is estimated in real-time based on a TOA estimate of the first arriving path. We divide the measurement procedure into initial and core measurement phases. Typically, our target ranging accuracy (1 mm) is a high accuracy that requires a special type of detectors. The choice of the appropriate receiver for our system is a key parameter, since we require not only high ranging accuracy, but also low-

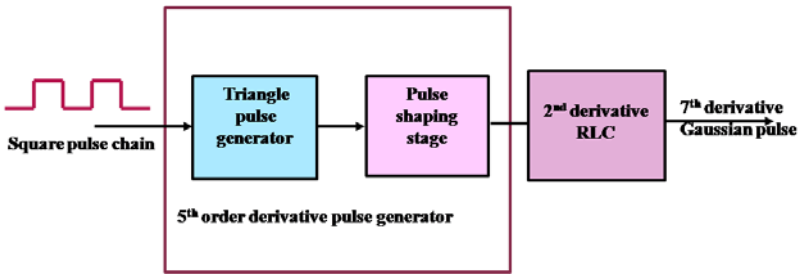

Figure 3.6: Block diagram of pulse generator.

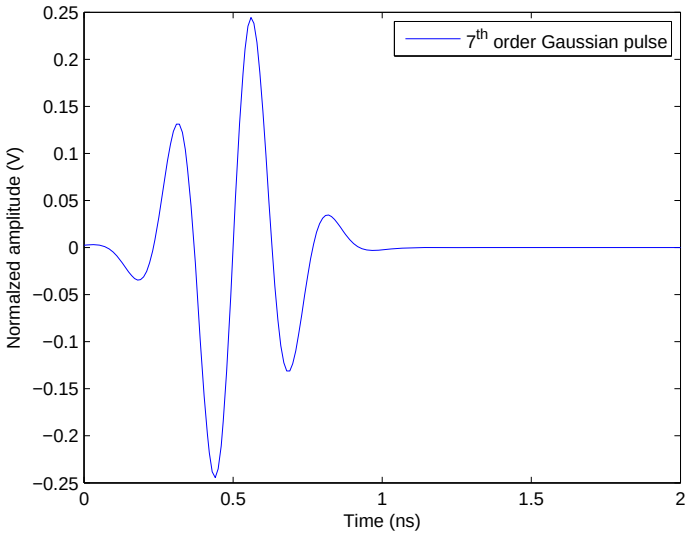

Figure 3.7: Seventh order Gaussian pulse with $T_p = 0.8$ ns.

power consumption. As is well known and previously discussed, there is a common trade-off between accuracy and power consumption. Commercially available UWB TOA estimators achieve ranging accuracies on the order of few centimeters (10 - 15 cm) for operating ranges greater than 50 m [71]. Nevertheless, the selected receiver has to accommodate the special requirements of gait analysis. In other words, the detectors that work well for common sensor network applications, are not necessarily suitable for gait analysis and wearable human locomotion tracking systems. Particularly, on-body communications have special requirements. Moreover, UWB body-area-network (BAN) channels have special characteristics. For instance, [36] suggested that new ranging techniques are required for reliable on-body TOA estimators. We deem that a new ranging technique that is capable of providing a high ranging accuracy, and is suitable for BANs is necessary.

We start our analysis by studying the gait characteristics, setting a frame-rate (range estimate update rate) for our system, and design a symbol frame structure for our system. Human movement is a repetitive movement that occurs at low frequencies. Typically, the normal walking frequency range is 1.7 - 2.3 Hz, 2.0 - 3.5 Hz for running, and 1.8 - 3.4 Hz for jumping [124]. Common optical tracking systems are based on 50, 80, and 120 frame/s frame rates [9], [116]. Recent optical tracking systems provide higher rates, e.g. 240 frame/s (Vicon T-series) [115] and 750 Hz (Optotrak) [82]. Our target system update rate (TOA estimate for all nodes) is 1 kframe/s. We design our system symbol structure based on both gait characteristics and UWB technology properties. The key design parameters and design procedure are as follows:

- Target system update rate is 1 kframe/s

- We assume an initial-frame and subsequent frames.
- We assume a maximum (inter-marker) distance = 1 m ≡ 3.333 ns.
- The corresponding observation interval is 4 ns (sufficient for observing the maximum expected distance).
- Normal walking speed 1.2 m/s [64].
- Fastest man in the world (Usain Bolt) running speed is 37.6 km/hr [118].
- Speed 37.6 Km/hr = 10444.44 mm/s.
- Expected maximum change between successive frames = (10444.44 / 1000) = 10.44 mm.
- This value is equivalent to (10.44 / (3 * 1011)) = 34.8 ps.
- Transmitted pulses are assumed to have a minimum separation that exceeds the channel delay spread equal to 10 ns.
- Assume 20 ns (50 Mpps) spacing to allow for time-hopping.
- For the initial-frame, search all possible 400 time values (4 ns).
- Estimated time-of-arrival (TOA) takes a value of 400 possible values, which requires 9 bits for representation in digital format.

As described above, our system has two measurement phases, namely the initial and core phases. In the initial phase, we search all possible values (4 ns based on our design parameters). In subsequent frames, we limit the search interval to the expected rate of change among successive frames (34.8 ps). The symbol frame structure for the initial and subsequent frames are depicted in Figures 3.8 and 3.9, respectively. Moreover, Figure 3.10 shows a hierarchy diagram of the proposed symbol frame structure for subsequent frames.

As will be addressed in detail in later chapters, the next key design factor is the suitable receiver structure, and the appropriate ranging approach for achieving a 1 mm target ranging accuracy. All assumptions and results will be verified via both simulations and actual measurements. Moreover, we will provide a complete study on the theoretical lower bound of the system performance for the selected receivers.

3.7 Overview of Localization Approach

Localization is another crucial stage for our system, where acquired inter-marker distances are converted to three dimensional coordinates. Nevertheless, localization is another challenging task, and is not like ordinary localization approaches used in common types of wireless

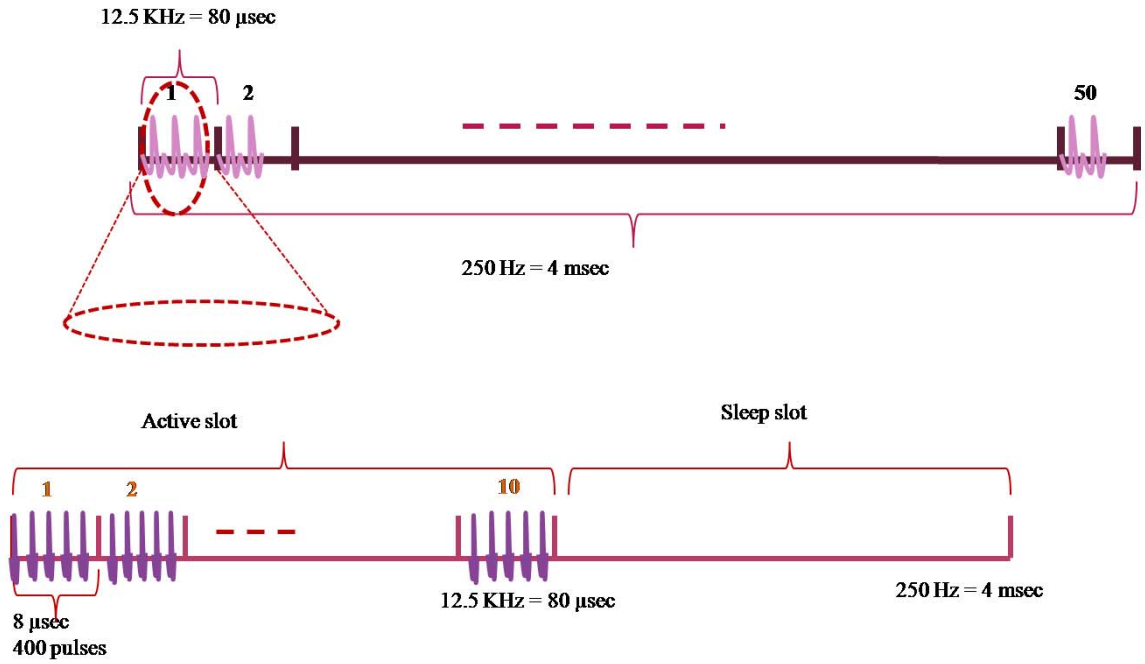

Figure 3.8: Proposed system symbol structure for initialization of the core measurement phase.

sensor networks (WSNs). The main difficulty associated with the design of a localization approach for our system is that all nodes are mobile, and it is hard if not impossible to have reference nodes attached to the test subject's body during movement. Moreover, in order to guarantee freedom of movement, it is also hard to have a fixed reference-node, even if not attached to the subject's body. As, our main target is to give the test subject's freedom, and to overcome the disadvantage of the subject knowing that he/she is being monitored, or limited in movement. As was mentioned before, limiting the movement to a specific path or walkway makes the movement does not necessarily represent the test subject's actual walking, which is a great debate around currently available measurement systems, even the most accurate ones. Again, we need to provide a complete freedom of movement in addition to accurate measurements. Such requirements and limitations make the design of an accurate localization technique a real challenging task for our system. Above all this dominates the low-power consumption requirement for on-body communications.

In order to overcome these difficulties we divide the localization procedure into two main phases, similar to the ranging approach. In the initial phase (system initialization), we can have reference nodes to be able to accurately estimate the initial positions of the nodes. During system initialization, the test subject does not need to start walking or have any movement activity. After initialization is performed, the user is supposed to move freely without any constraints. So, we propose an initial localization phase that requires reference nodes. This initialization stage is followed by a core measurement phase that does not have

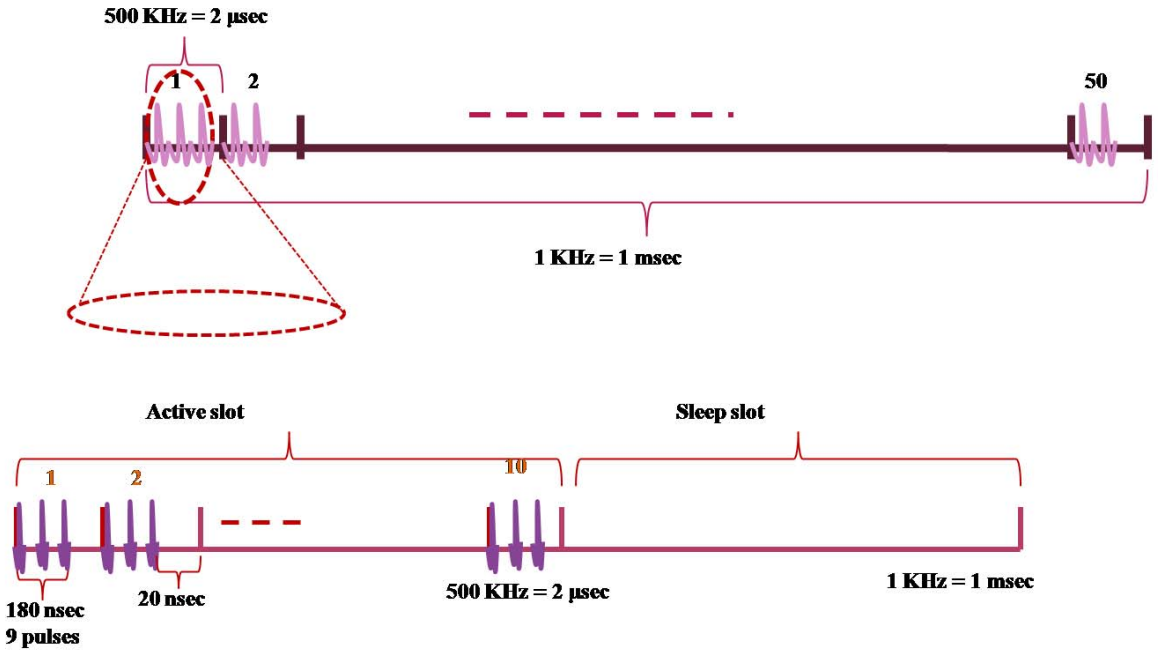

Figure 3.9: Proposed system symbol structure for subsequent frames of the core measurement phase.

any reference nodes, but is required to maintain the attained accuracy during the initial phase.

It is worth mentioning that with all the challenges associated with the design of an accurate localization stage for our system, by dividing the measurements into initial and core phases this ultimately precludes the need for performing localization in real-time (on-body). In other words, real-time acquired ranging data can be stored for sometime, then localization be performed a later time. Definitely, this fact relaxes both memory and power consumption requirements. Moreover, it can facilitate having more complex localization techniques to guarantee high positioning accuracy compared to having to perform localization on-body in real-time.

3.8 Sensor Fusion and System Performance

Essentially, UWB radios are suitable for integration with other motion sensors such as, pressure sensors and accelerometers. Ultimately, acquired data from our proposed system should cover both kinematic and kinetic parameter estimation. Using UWB radios will typically cover kinematic parameter estimation. Thus, in order to be able to estimate kinetic parameters as well, other types of sensors are expected to be integrated with UWB radios. For instance, currently available optical tracking systems use force plates to acquire force

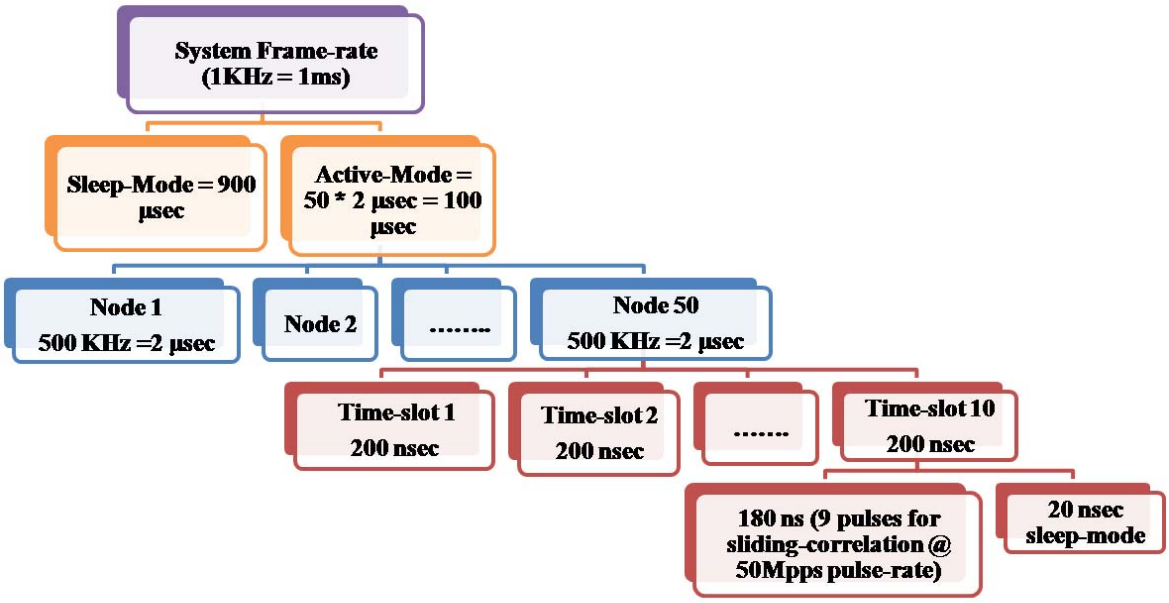

Figure 3.10: Diagrammatic hierarchy of the proposed system symbol structure for initialization of the core measurement phase.

data in addition to the three-dimensional positions of markers to estimate kinetics as well as kinematics. Similarly, in our system we will integrate other types of sensors with UWB radios to estimate both kinematic and kinetic parameters, as will be studied in detail in later chapters of this dissertation.

The integration of other types of sensors with UWB radios also has main requirements and key parameters that need to be addressed. In addition to the choice of the type of sensor, the placement of the sensor is another issue that needs to be considered. Particularly, these sensors need to be integrated with UWB sensors, at the same time they should not affect the performance of UWB sensors. For instance, they can not be placed in such a way that they would interfere with UWB sensors, or obstruct the LOS links needed to guarantee the required accuracy of UWB sensors. Moreover, the power consumption and sampling rate should not put further constraints on the overall power consumption. Furthermore, their update rate needs to cope with the UWB sensor update rate, and not interfere with it. Moreover, typically such sensors often acquire data in the analog form, so this acquired data needs to be converted to the digital form, and be transmitted to the central node in such a way that keeps the accuracy of acquired data. Once again, their connection with the on-body central-node needs to be handled in such a way that it preserves the freedom of movement provided by our system.

There are several key system design parameters that need to be addressed for the system to provide the anticipated accuracies. First of all, since our system is mainly aimed at gait analysis applications, we need to estimate gait analysis parameters kinematics and/or kinetics to verify the validity of our proposed system for the anticipated application. Moreover, we need to compare our system's performance to existing systems in order to verify the claimed gain in performance. Second, preserving the accuracy of the acquired data is essential particularly during the transmission from the body nodes to the central-node, and consequently to the off-body node. Third, we need to study the accuracy and power consumption trade-offs. Like common low-power sensor networks, we consider time-division-multiple-access (TDMA) for our system. Particularly, TDMA is suitable for low-power peer-to-peer networks, where it is suitable for keeping nodes at sleep mode (standby or low-power) while not in operation. Fourth, the battery lifetime is also an important design key parameter. Essentially, we would like to have at least one day of operation without needing to recharge the system, in order to facilitate system use. Finally, we also need to calculate the data storage requirements in order to estimate the required on-body memory. Practically, the frequency of data transfer from the on-body central node to the off-body system should be minimized.

3.9 Chapter Summary and Contributions

In this chapter, we studied the key design and analysis parameters of our proposed system. Furthermore, we gave overviews of different design parameters associated with our system. Particularly, we gave a brief description of our proposed system followed by key design parameters, namely power consumption issues, employed pulse shape, transmitter architecture, and power consumption. Moreover, we gave an overview of the proposed framework for the study of performance/power-consumption. Furthermore, we provided an overview of the proposed ranging stage, and designed the system symbol structure. Moreover, we addressed different challenges related to the design of an accurate localization technique, and gave a brief description of our proposed solution.

The possibility of having sensor-fusion was also addressed in this chapter. We concluded that our system is suitable for the integration of other types of motion sensors with UWB radios for the estimation of kinetic/ kinematic parameters associated with human gait. Particularly, because we need other sensors to provide a complete picture of gait parameters, kinematics/kinetics. Finally, we addressed different system design parameters that need to be precisely chosen in order to achieve the ultimate goals of our proposed system (high accuracy, low-power-consumption, and freedom of movement).

Related Publications:

- H. Shaban, M. Abou El-Nasr, and R.M. Buehrer," Toward a highly accurate ambulatory system for clinical gait analysis via UWB radios," *IEEE Transactions on Information Technology in Biomedicine*, Vol. 14, No. 2, pp. 284-291, Mar. 2010.

Chapter 4

System Analysis

In this chapter we discuss and analyze some important parameters associated with the design of our proposed system. Section 4.1 discusses some UWB BAN channel models proposed in the literature in addition to the IEEE 802.15.3a channel model, which we will use in our proposed system performance/power consumption framework. Furthermore, Section 4.2 proposes a design for our system's link budget. Section 4.3 provides a brief comparative study of power consumption of different UWB receiver alternatives. Section 4.4 provides the proposed performance/power consumption framework, and gives a case study for non-coherent UWB detectors. Then, Section 4.5 briefly describes the different studied gait parameters and methodology of simulation. Finally, Section 4.6 summarizes the chapter conclusions and contributions.

4.1 Channel Models

In this section, we discuss the channel models that are used within our work. First, we discuss the employed BAN channel models. Then, we discuss the IEEE 802.15.3a channel model, which we will use in the analysis of our proposed performance/power consumption framework.

4.1.1 BAN Channel Models

This subsection summarizes some of the UWB-BAN channel models proposed in the literature; particularly the ones that are used in our simulations. Specifically, we consider the models proposed in [12], [44], and [119].

UWB-BAN Channel Simulation Model

According to [44], wave propagation through the body is negligible in the UWB range (3.1-10.6 GHz). This model considers a discrete-time impulse response model for channel characterization, and proposes that energy decays exponentially with time. It also proposes that adjacent bins are correlated up to a factor of 0.8. It assumes two groups of distinct multipath components (MPC), due to scattering waves around the body and reflections from the ground. It also suggests that the second group of MPC decays faster than the first cluster [44]. We implemented this model using MATLAB. Figures 4.1(a) and (b) show impulse response realizations of the side and back scenarios, respectively.

IEEE 802.15.4a BAN Channel Model

This model assumes the presence of two main clusters. The first cluster is due to waves diffracting around the human body, and the second cluster is due to ground reflections. Furthermore, it concludes to that wave arrival bins are correlated following a log-normal distribution. Also, path-loss near the body is dominated by energy absorption from the human tissue leading to exponential decay of power versus distance. The model assumes three different scenarios, namely the front, back, and side scenarios [12].

The path-loss is calculated as [12]:

$$P_{\mathrm{dB}} = \gamma(d - d_0) + P_{0,\mathrm{dB}} \tag{4.1}$$

where $\gamma = 107.8$ dB/m, d is the LOS separation distance, $d_0 = 0.1$ m is the reference distance, and $P_{0,\mathrm{dB}}$ is path-loss in dB at d_0, and is equal to 35.5 dB [12]. Figures 4.2(a) and (b) show impulse response realizations of the front and back scenarios, respectively.

IEEE 802.15.6a UWB-BAN Channel Model

IEEE has recently formed a task group (TG6) for the development of a unified characterization of BAN channels [16]. This model does not assume different body scenarios, instead it assumes a model for the on-body-to-on-body communication (CM3), and on-body-to-off-body scenario, namely CM4, as depicted in Figure 4.3[1].

4.1.2 IEEE 802.15.3a Channel Model

In addition to the BAN models, we consider the IEEE 802.15.3a channel model in our developed framework. Particularly, we consider the time-invariant indoor channel model

[1]Figure 4.3 is reproduced based on [119].

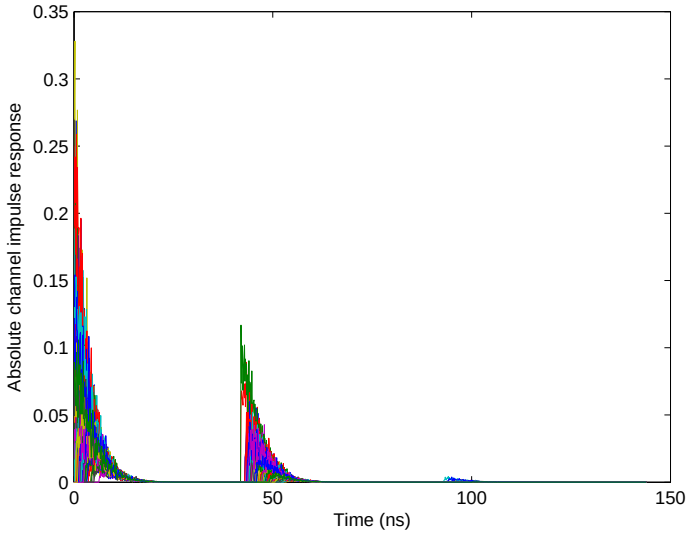

(a)

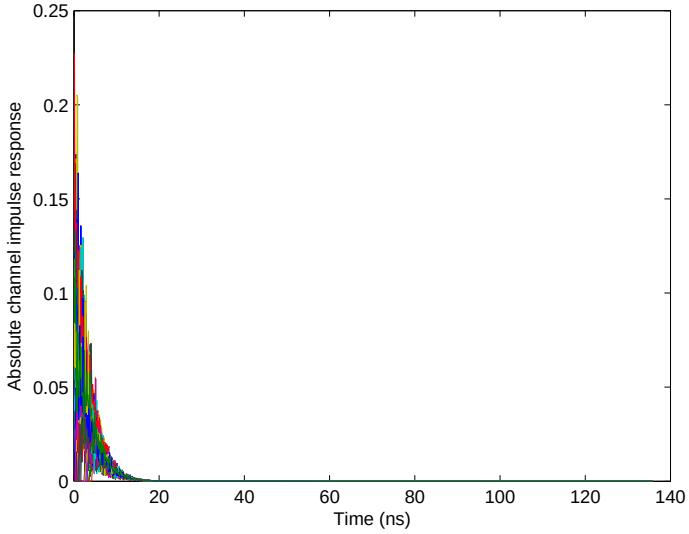

(b)

Figure 4.1: (a) Side scenario impulse response channel realizations for the BAN channel model proposed in [44]. and (b) Back scenario Impulse response channel realizations for the BAN channel model proposed in [44].

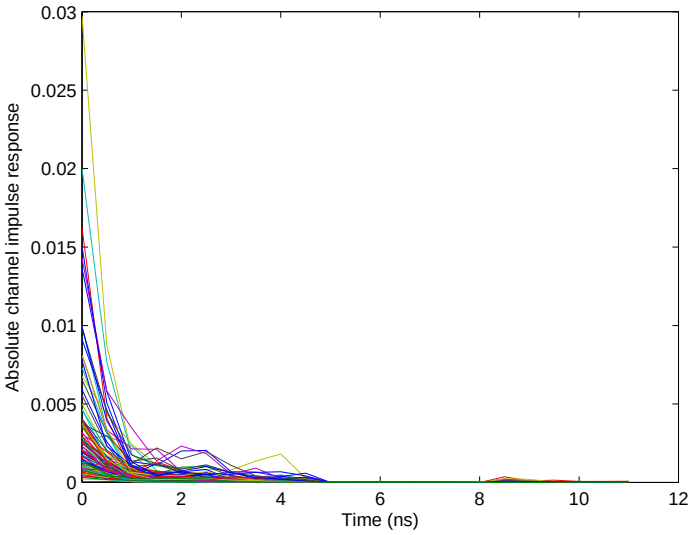

(a)

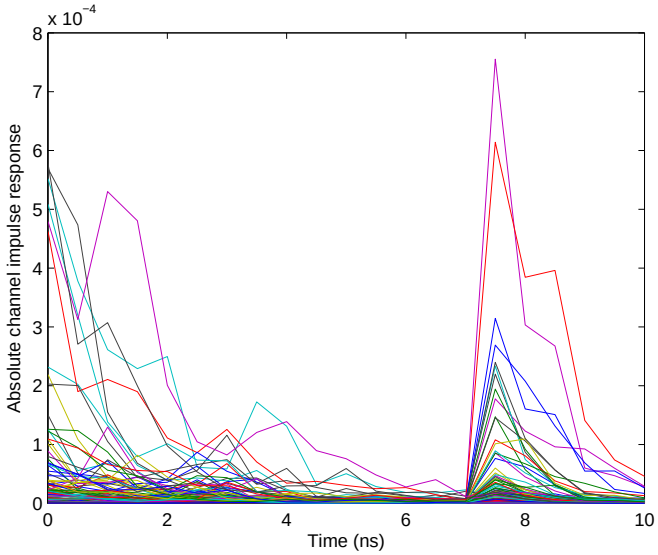

(b)

Figure 4.2: (a) Front scenario impulse response channel realizations for the IEEE 802.15.4a BAN channel model. and (b) Back scenario impulse response channel realizations for the IEEE 802.15.4a BAN channel model.

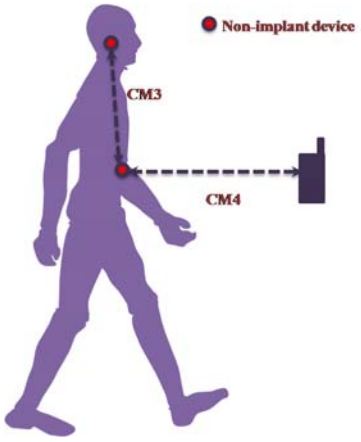

Figure 4.3: IEEE 802.15.6a channel models for non-implant devices.

written as [50]:

$$h(t,\tau) = \sum_k G_k(t)\delta(\tau - T_k(t)) \tag{4.2}$$

where, t and τ are the observation and application times of the impulse response, k denotes the k-th multi-path component, $T_k(t)$ are the time-varying arrivals of the paths, and $G_k(t)$ are the time-varying gains of the impulse [50]. For indoor channels, we consider the time-invariant model [50]:

$$h(\tau) = \sum_k G_k\delta(\tau - T_k) \tag{4.3}$$

The IEEE 802.15.3a channel model is a cluster model, where the paths arrive in clusters with exponentially decaying cluster amplitudes allowing for multiple exponentially decaying sets [55]. Multi-path arrival times T_k are modeled using a random process based on the Poisson point process. Moreover, the multi-path arrivals are grouped into cluster arrivals that are associated with ray arrivals within each cluster [50]. The Measurements in UWB channels indicate that the amplitudes follow a lognormal distribution [50]. The statistics of multi-path arrival times T_k and path gains G_k are specified by the IEEE 802.15.3a model [55], [50].

In [50] and [56], the IEEE 802.15.3a UWB channel model is treated as a two-dimensional point process of pairs (T_k, G_k) with an equivalent representation of the channel response:

$$h(\tau) = \sum_k \phi(T_k, G_k) \tag{4.4}$$

where, $\phi(T_k, G_k) = G_k\delta(\tau - T_k)$, for which the channel response is represented as a sum of a function evaluated at random augments, and is called a shot-noise random variable [56], [50]. If we set $\phi(T_k, G_k) = G_k I_{[0,T_w]}(T_k)$, where $I_{[0,T_w]}(T_k)$ is an indicator function, then the sum represents the path gains that arrive in a time window $[0, T_w]$ and is given by [50], [56]:

$$\Phi_l = \sum_k G_k I_{l[0,T_w]}(T_k) \tag{4.5}$$

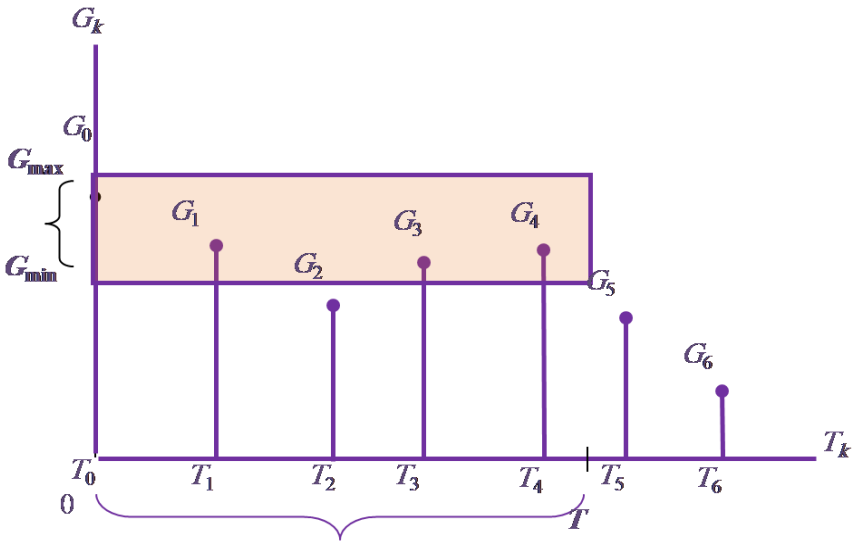

Figure 4.4: IEEE 802.15.3a channel gains G_k versus arrival times T_k with 4 paths that arrive within an observation window $[0, T_w]$ and have gains in the range $G_{min} \leq G_k \leq G_{max}$.

where, the indicator function of the l-th resolvable path within the interval $[0, T_w]$ is $I_{l[0,T_w]}(t)$ =1 for $t \in [0, T_w]$ and is zero elsewhere, and T_w is chosen such that the expected energy in the finite interval $[0, T_w]$ meets a specific fraction of the expected energy in the infinite observation window $[0, \infty)$, e.g. 90% of the expected energy [56].

Generally, point processes can be viewed as counting measures on measurable sets [50]. In the context of multi-path channels, since the multi-path components are now defined as a two-dimensional point process of (T_k, G_k), then the sum of path gains Φ_l can be regarded as a counting measure of the paths that arrive within the measurable set of arrival times and path gains, such that $T_k \in [0, T_w]$ and $G_k \in [G_{min}, G_{max}]$ [50] . Figure 4.4[2] shows a graph of the IEEE 802.15.3a channel that depicts the multi-path components gains versus the arrival times with four paths that occur within the observation window $[0, T_w]$ and that have gains in $[G_{min}, G_{max}]$.

In the IEEE 802.15.3a channel model, each cluster has an initial and non-initial paths, and the initial cluster is assumed to start at a fixed time $T_0 = 0$. For the LOS channel model, the path gains sum the counting processes of the arrival times of the clusters within an observation window $[0, T_w]$ including the initial cluster [50], [56]. The start times of the clusters are assumed to be the occurrences of a homogeneous Poisson process, and the gains are the marks of the Poisson cluster start times, where the marked Poisson process is equivalent to a two-dimensional Poisson process. Furthermore, the arrival times of the non-initial paths are conditioned on the start times of the clusters, and are modeled as independent homogeneous Poisson processes [50], [56]. In the NLOS channel model, the

[2]Figure 4.4 is reproduced based on [50].

initial cluster is omitted [50], [56].

4.2 Preliminary Link Budget Design

In order to guarantee a specific E_p/N_0, a system link budget must be prepared. Commonly, a link budget design includes the choice of pulse width, transmitted power, data rate, and antenna gains for a target E_p/N_0, which in turn is based on a required $E_p/N_0|_{\text{req}}$.

4.2.1 Design Parameters

The link budget signalling design parameters are summarized in Table 5.1. The transmit power is chosen according to the maximum allowed power spectral density (PSD) = -41.3 dBm/MHz, and the bandwidth of interest is 2 GHz.

Another important parameter that defines the loss that the signal exhibits is termed path loss at distance d is defined as [90]:

$$PL_t(d) = PL_0 + 10m\log(\frac{d}{d_0}) \tag{4.6}$$

where, PL_0 is the path loss at the reference distance d_0, and m is the path loss exponent.

The received power P_R at a distance d is [90]:

$$P_R(d) = P_t - PL_t(d) + G_r + G_t \tag{4.7}$$

where P_t is the transmitted power, and G_t and G_r are the transmit and receive antenna gains, respectively. The two-sided noise PSD = $N_0/2$, and N_0 is calculated as:

$$N_0 = 10\log_{10}(kT_0) + N_f = 10 * \log(1.38 * 10^{-23} * 290 * 10^3) + N_f = -174.4\text{dBm/Hz} + \text{N}_\text{F}(\text{dB}) \tag{4.8}$$

Table 4.1: Main Link Budget Parameters.

Parameter	Value
P_t (transmitted power in dB relative to a W)	-8.3 dBm
$B.W._{\text{min}}$ (bandwidth)	2 GHz
PSD(dBm/MHz)	-41.3 dBm/MHz
Receiver Noise Figure (N_F)	10 dB
N_0 (Noise PSD = kT_{sys})	-164.4 dBm/Hz
G_t and G_r (Tx and Rx antenna gains)	0 dBi
Implementation Loss (L_a)	3 dB
Required $E_b/N_0|_{\text{req}}$ (dB)	18 dB

Table 4.2: Path loss values for on-body channel models.

Path Loss PL_0	d_0(m)	Path Loss Exponent m	Channel
82.0dB	1m	3.3	Anechoic Chamber [121]
75.8dB	1m	2.7	Office [121]
109.2dB	1m	4.1	Worst case [121]
82.0dB	1m	2.6	Front side (vertical) [122]
101.0dB	1m	3.7	Front side (horizontal) [122]
86.0dB	1m	2.2	Front side (diagonal) [122]
82.0dB	1m	2.9	Back side (vertical) [122]
93.0dB	1m	2.8	Back side (horizontal) [122]
84.0dB	1m	2.7	Back side (diagonal) [122]
50.5dB	0.1m	7.2	Around Torso [43]
44.6dB	0.1m	3.1	Along Torso [43]

where, k is Boltzman constant $= 1.38 * 10^{-23}$ J/^{0}K, $T_0 = 290^0$K, and N_F is the receiver noise figure. The average noise per pulse P_N in terms of the pulse rate R_p is expressed as:

$$P_N = N_0 + 10 \log R_p \tag{4.9}$$

The link margin L_M is:

$$L_M = P_R(d) - P_N - \left(\frac{E_p}{N_o}|_{\text{req}}\right) - L_a \tag{4.10}$$

where $\left(\frac{E_p}{N_0}|_{\text{req}}\right)$ is the required pulse energy to noise ratio and L_a is the implementation loss. The minimum receiver sensitivity S_r is calculated as:

$$S_r = P_R(d) - L_M \tag{4.11}$$

Effect of Body Shadowing

An important parameter that defines the loss that the signal exhibits is termed path-loss. The received bit energy $E_r = P_r * T_p$ at a distance d in terms of the transmitted bit energy $E_t = P_t * T_p$, T_p is the pulse duration, is [90]:

$$E_r(d)(\text{dBmJ}) = E_t(\text{dBmJ}) - PL_t(d)(\text{dBm}^2) \tag{4.12}$$

To estimate the effect that human body shadowing has on the amount of pulse shape distortion, actual measurements were taken at the Virginia Tech's Mobile and Portable Radio Research Group (MPRG) labs, and the explicit results were presented in [36]. These

Table 4.3: Additional Losses [36].

Measurement	Man (dB)	Woman (dB)
Arm parallel	18.84	12.08
Arm perpendicular	3.35	4.87
Leg inline	20.23	20.31
Leg perpendicular	12.43	5.87
Thigh	14.88	13.88
Torso 45 degree	18.62	20.28
Torso parallel	21.86	18.65
Torso perpendicular	21.60	19.79

measurements showed that the body can introduce a significant attenuation (up to 20 dB) when a body limb blocks the LOS path. A summary of results is given in Table 4.3. These results agree with the results presented in [100]. Moreover, a recent analysis showed that above 2 GHz little to no energy penetrates the body, and that signals transmitted from the antenna diffract around the body and can be reflected from arms and shoulders [100]. This explains the wide variations of the path-loss exponents when the link between nodes is obstructed by the body limbs. Consequently, this fact highlights the importance of the node's placement to guarantee a sufficient number of LOS connections during movement. Also, measurements indicate that there are always a minimum of two clusters of multi-path components, namely a wave diffracting around the body, and a reflection from the ground [100]. Table 4.4 gives preliminary link budget designs for our system assuming a 1 Kb/s bit-rate (TOA update rate per system frame including all non-body nodes) for possible 500 Kp/s, 1 Mp/s, and 50 Mp/s pulse rates. An exact link budget will be presented based on more precise values in later chapters.

4.3 A Comparative Power Consumption Study

UWB technology has specific challenges associated with its design due to the ultra-wide nature of its spectrum. Specifically, ADCs have to work at the Nyquist frequency. Also, the matched filter digital logic has to work at very high frequency. The allocated band to UWB healthcare applications is the 3.1 - 10.6 GHz range. Thus, the required sampling frequency for this band is $\approx$ 15 GHz [16], [120]. Essentially, digital implementation approaches have the advantage of flexibility and accuracy. However, the all-digital architecture suffers from high power consumption. Typically, this power consumption is dominated by ADCs and MFs. An attractive solution to reduce power consumption for UWB transceivers is the partially-analog approach, in which the ADC is moved after the MF or correlator block. Consequently, the correlation is performed in the analog domain. As a result, the sampling frequency constraint and the power-consumption are significantly reduced [65], [74].

This section provides a sample comparative study of power consumption estimation, according to the partially-analog approach for the TR, ED, and correlator receivers based on state-of-the-art implemented UWB components proposed in the literature. The power consumption is estimated assuming 0.18 μm CMOS technology [65].

IR-UWB correlation receivers with analog correlators were proposed in the literature for low-power consumption, where the correlors are placed before the ADC, and hence relaxing the sampling requirements [114]. The correlation operations are assumed to be performed in the analog domain in order to relax the ADCs requirements, and consequently to reduce the overall power consumption [65]. In particular, moving the correlation operation from the digital domain to the analog domain reduces the required sampling frequency from the Nyquist rate to the pulse repetition rate [65]. A possible choice of the number of bits is n is 4 bits. However, the choice of n affects the ADC power consumption, where the power consumption of ADCs is calculated as:

$$P_{ADC} = \frac{2^n f_{\text{ADC}}}{\text{FOM}} \tag{4.13}$$

where FOM is the figure-of-merit, and the quantization noise influences the BER [74]. In [79] it was shown that 4 bits is sufficient for reliable detection of UWB signals.

In order to further reduce the power consumption of correlator receivers, windowed sinusoidal templates have been proposed as an alternative for the generation of optimal Gaussian pulses. Essentially, the template waveform should be matched to the received pulse. Unfortunately, the generation of a Gaussian pulse template is difficult and power consuming. Moreover, generating a sinusoidal wave is straightforward [114], and when windowed it can

Table 4.4: Link Budget for B.W. = 2 GHz.

Pulse rate R_p	500 Kp/s	1 Mp/s	50 Mp/s
$B.W._{\min}$ (bandwidth)	2 GHz	2 GHz	2 GHz
P_t (transmitted power in dB relative to W)	-8.3 dBm	-8.3 dBm	-8.3 dBm
PL_0	44.6 dB	44.6 dB	44.6 dB
$PL(d = 1\text{m})$ (exponent=3.1)	31 dB	31 dB	31 dB
Total path loss PLt(d)	75.6 dB	75.6 dB	75.6 dB
Average noise power per pulse (P_N)	-107.4 dBm	-104.4 dBm	-87.4 dBm
Average power at the receiver (P_R)	-83.9 dBm	-83.9 dBm	-83.9 dBm
Achieved E_p/N_0	23.5 dB	20.5 dB	3.5 dB
Link Margin (L_M)	2.5 dB	-0.5 dB	-17.5 dB
Target bit-rate R_b	1 Kb/s	1 Kb/s	1 Kb/s
Pulses per bit (N_s)	27 dB	30 dB	47 dB
Link Margin (L_M)	29.5 dB	29.5 dB	29.5 dB
Minimum receiver sensitivity (S_r)	-113.4 dB	-113.4 dB	-113.4 dB

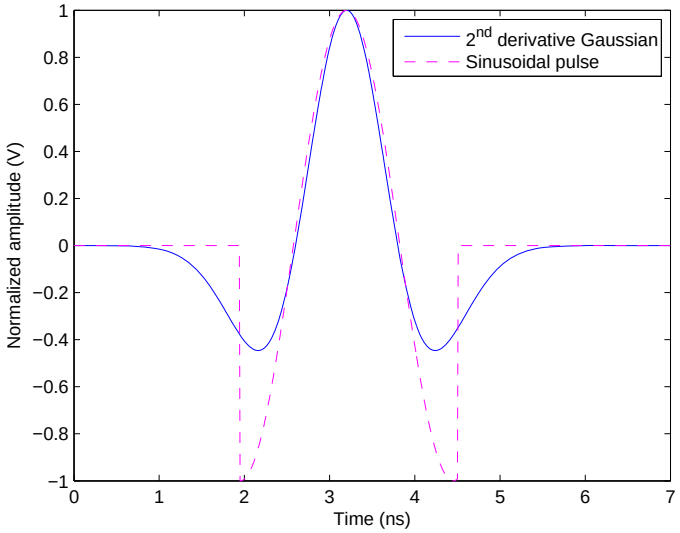

Figure 4.5: Second Order Gaussian pulse and corresponding suboptimal template.

resemble the main pulse form [97]. Figure 4.5 shows the optimal and suboptimal templates assuming the second order Gaussian pulse, and Figure 4.6 shows the corresponding auto-correlation and cross-correlation functions. Suboptimal templates are in the form of either real or complex sinusoids, also known as quadrature analog correlators (QAC). Generally, receivers with complex suboptimal templates lead to less severe SNR degradation, which is traded for more power consumption as compared to receivers with a real template. However, it requires smaller power consumption as compared to the optimum detector [65]. Figure 4.7 shows a comparison of power consumption for the fully-digital (FD) approach with 4 bits and 1 bit, TR, ED, correlator (CR) with a real suboptimal template, and QAC correlator assuming a signal bandwidth = 500 MHz based on the design parameters presented in [65], [113]. As shown, ED detectors has the smallest power consumption followed by correlator-based detector with real suboptimal template and QAC receivers. Thus, CR with suboptimal templates and QAC receivers are worth studying in further details, as they are promising solutions that combine coherent-detection performance and low power requirements associated with non-coherent detectors. A detailed study of the performance of these detectors will be provided in later chapters.

4.4 Proposed Performance/Power-consumption Study Framework with Non-coherent Detectors Case Study

This section provides a sample case-study of power consumption estimation, according to the partially analog approach, for the TR and ED receivers based on state-of-the-art implemented

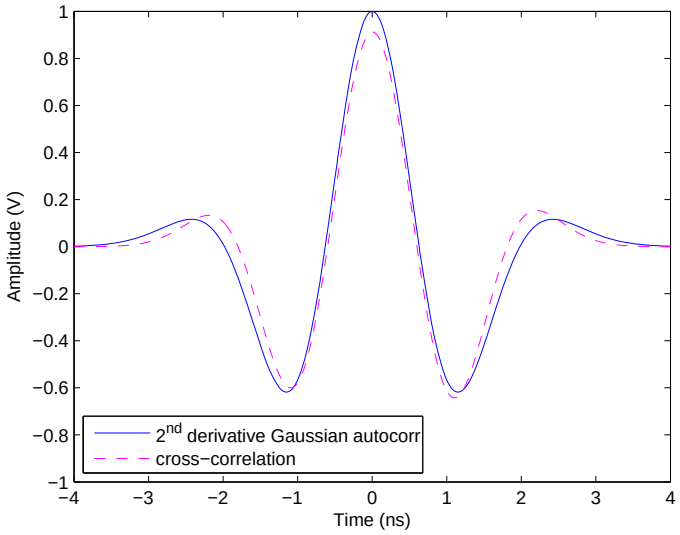

Figure 4.6: Second Order Gaussian pulse autocorrelation and cross-correlation with corresponding suboptimal template.

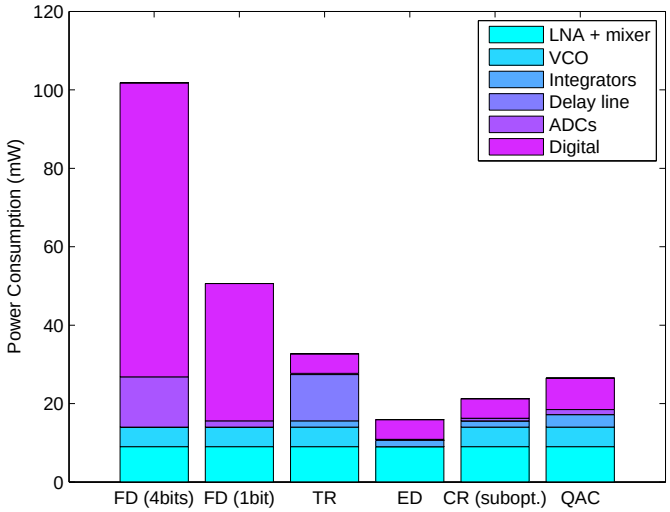

Figure 4.7: Power consumption comparison of six different receivers assuming a 500 MHz bandwidth based on the analysis provided in [65], [113].

UWB components proposed in the literature. The power consumption is estimated assuming 0.18 μm CMOS technology [65].

Non-coherent receivers are low-power solutions that do not require channel estimation, and are suitable for low-data rate applications [20]. In these receivers, low-power consumption is traded for a degradation in bit error rate (BER) performance. Non-coherent alternatives include transmitted reference (TR) and energy detection (ED) schemes [106].

The main modulation scheme employed with time hopping impulse radio TH IR-UWB is the pulse-position modulation (PPM) scheme, for which increasing the order of the pulse derivative leads to a smaller value of the minimal autocorrelation value and a consequently better BER performance. However, the achievement of better BER performance is traded for higher sensitivity to timing jitter. Other common types of modulation include pulse amplitude modulation (PAM) and on-off keying (OOK) modulation [20].

The transmitted reference (TR) scheme with a correlation based receiver is considered a non-coherent receiver. The TR scheme is based on the transmission of a pair of pulses (one modulated and one unmodulated), where at the receiver, the unmodulated pulse is used to detect the modulated pulse. However, TR correlation receivers suffer from the use of a noisy template [106]. Instead of sending reference pulses, the differential transmitted reference (DTR) scheme uses the data pulses of previous symbols for the correlation with the received pulses. Hence, DTR achieves a 3 dB performance gain over TR schemes. On the other hand, DTR requires differential encoding of the transmitted bits, which in turn requires longer delay-lines, and higher power consumption [106].

The energy detection (ED) correlation receiver is another non-coherent receiver. In ED correlation receivers, the correlator is replaced by a squaring device. ED IR-UWB receivers can be implemented with on-off keying (OOK) and PPM schemes. However, OOK requires a careful choice of the detection threshold [106]. The main difference between ED and TR receivers is the reference pulse. Both receiver structures suffer from the use of noisy waveforms at the receiver, and both receivers require a careful choice of the integration window in order to minimize the BER performance [60], [106].

4.4.1 Comparison of Power Consumption of Non-coherent Detectors

This section provides an estimation of the power consumption of TR and ED receivers based on state-of-the-art UWB components proposed in the literature. The power consumption is estimated assuming 0.18 μm CMOS technology [94]. The power consumption comparison of different receiver blocks is given in Table I.

The correlation operations are assumed to be performed in the analog domain in order to relax the ADCs requirements, and consequently to reduce the overall power consumption [94]. In particular, moving the correlation operation from the digital domain to the analog

Table 4.5: Power Consumption Summary.

	TR	ED	Ref.
LNA	9 mW	9 mW	[94]
mixer	10.8 mW	-	[19]
Squarer	-	1.7 mW	[45]
Integrators	10.4 mW	10.4 mW	[99]
Delayline	13.1 mW	-	[74]
PLL	13.5 mW	13.5 mW	[94]
ADC	0.8 mW	0.8 mW	[74]
Digital cct.	2.5 mW	2.5 mW	[74]
Total Power	60.1 mW	37.9 mW	

domain reduces the required sampling frequency from the Nyquist rate to the pulse repetition rate [94]. The ADCs are assumed to have $n = 4$ bits[3] for a signal bandwidth W= 500 MHz, N_s= 10 pulses per bit, a bit-rate of 2 Mbps, and f_{ADC}= 25 MHz [94], [74]. The power consumption of the integrators is based on [99], which requires a power consumption of 5.2 mW for a 100 MHz pulse repetition frequency, or equivalently an energy consumption of 52 pJ and a holding time $>$ 10 ns. Scaling the power consumption to 20 MHz as in [94] gives 1.04 mW. The hold time (integration time) of the integrator is equivalent to half of the clock time [106]. Thus, an integration window of 100 ns would require 10 integrators each with an integration time of 10 ns.

As provided in Table 5.1, ED receivers consume less power as compared to TR receivers. This difference in power consumption is basically because of the analog delay-line used in the TR correlation receiver. Currently, the implementation of analog delay-lines with delays on the order of nanoseconds is challenging [106]. Analog delay-lines can be implemented using the group delay properties of bandpass filters. However, the wide bandwidth nature of UWB signals leads to a high filter implementation complexity, which increases the overall power consumption [106].

[3]The choice of n affects the ADC power consumption $P = \frac{2^n f_{ADC}}{FOM}$, where FOM is the figure-of-merit, and the quantization noise influences the BER [74]. In [79] it was shown that 4 bits is sufficient for reliable detection of UWB signals.

4.4.2 BER Performance

In our estimation for the BER, we consider the IEEE 802.15.3a channel model that was presented in an earlier section. The output signal-to-noise-ratio Λ is proportional to:

$$H_L = \sum_{l=0}^{L} \Phi_l^2 \tag{4.14}$$

where, the random variable H_L is the sum of $L+1$ random variables with different distributions. The Φ_l are uncorrelated but are not statistically independent. The average SNR as a function of number of paths L is [55]:

$$ASNR(L) = E[\Lambda] = SNR \times E[H_L] \tag{4.15}$$

where,

$$\begin{aligned} E[H_L] = \Omega_0\{1 + R\bar{\beta}(T_w, s_0) + C\bar{\beta}(T_w, \tau_0) + RC[s_0\bar{\beta}(T_w, \tau_0) \\ -s_0\bar{\beta}(T_w, s_0\tau_0/(s_0 - \tau_0))e^{-T_w/s_0}]\} \end{aligned} \tag{4.16}$$

$T_w = (L + 1/2)T_\Delta$, $T_\Delta = 1/W$, W is the signal bandwidth,

$$\bar{\beta}(T_w, \mu) = \int_0^{T_w} e^{-t/\mu} dt = \mu \left[1 - e^{-T_w/\mu}\right] \tag{4.17}$$

$E_b = N_s E_p$, is the bit energy, N_s is the number of frames per bit, E_p is the energy per pulse, R is the ray arrival rate, C is the cluster arrival rate, τ_0 is the cluster decay factor, s_0 is the ray decay factor, and Ω_0 is a scale factor, $\Omega_0 = 1/\left[(1 + Rs_0)\,(1 + C\tau_0)\right]$ [55]. In [66] the channel averaged SNR is defined in terms of the integration window $T = L_p T_p$ (T is an L_p integer multiple of the pule duration T_p):

$$ASNR(L_p) = \frac{N_s E_p^2 G^2(L_p)}{N_0 E_p G(L_p) + N_0^2 B L_p T_p/2} \tag{4.18}$$

where B is the one-sided receiver bandwidth, and the average path energy is calculated by enumerating all possible arrival times in the n-th time bin from $G(L_p) \triangleq E\{A_i^{(1)^2}\}$, $E\{A_1^{(v)^2}\} = \Omega_0$, and

$$\begin{aligned} E\{A_n^{(v)^2}\} = \Omega_0 P_c P_r \exp\left[-\frac{nT_\Delta}{s_0} + \frac{T_\Delta}{\tau_0}\right] \frac{\rho^2\,(1 - \rho^{n-2})}{1 - \rho} \\ +\Omega_0 P_c \exp\left[-\frac{(n-1)T_\Delta}{\tau_0}\right] \\ +\Omega_0 P_r \exp\left[-\frac{(n-1)T_\Delta}{s_0}\right] \end{aligned} \tag{4.19}$$

where, $n \geq 2$, N is the number of time bins, P_c is the probability that one cluster occurs with $P_c = CT_\Delta$, given the cluster arrival, P_r is the probability that one ray occurs in a time bin with $P_r = RT_\Delta$, $\rho = exp(\frac{T_\Delta}{s_0} - \frac{T_\Delta}{\tau_0})$, $\bar{E}_c \triangleq E\{\sum_{i=1}^{N} A_n^{(v)^2}\}$, and $\Omega_0 \triangleq \frac{1}{\bar{E}_c\big|_{\Omega_0=1}}$ [66].

The BER of simple TR (STR) receiver for BPAM is [20]:

$$P_b = E\left[Q\left(\left[\frac{2}{N_s}\left(\frac{N_0}{E_b}\right) + \frac{WT}{N_s}\left(\frac{N_0}{E_b}\right)^2\right]^{-\frac{1}{2}}\right)\right] \tag{4.20}$$

where, $E[.]$ is the expected value, W is the real bandpass signal bandwidth, $Q(x) = \frac{1}{\sqrt{2\pi}} \int_x^\infty e^{-z^2/2} dz$, and N_0 is the noise PSD. The BER performance in (4.20) can be evaluated in two ways: (a) using (4.15) to evaluate (4.20) and (b) using (4.18) to evaluate (4.20). As, in multi-path channels, the SNR used in the BER formulas is assumed to be the average SNR. This assumption is valid for non-coherent detectors, where they assume using one receive arm for the detection of the received signal. Thus, calculating the average BER in terms of the channel averaged SNR gives good approximates. A comparison of the BER performance using the aforementioned two ways is shown in Figure 4.8 for $N_s = 2$ and 16. We can see that both methods provide nearly identical results.

The BER of the ED receiver for BPPM (ED-BPPM) is [117]:

$$P_b = \frac{1}{2} erfc\left(\frac{\eta(T)\,(d_0 + d_1 W)\,(E_b/N_0)}{2\sqrt{(TW/p_0) + 2s_0\eta(T)\,(E_b/N_0)}}\right) \tag{4.21}$$

where, $\eta(T)$ is the ratio of the energy captured to the total energy available, T denotes the integration window, d_0, d_1, and s_0 are IEEE 802.15.3a channel parameters [117]. The ED-BPPM receiver achieves a similar BER performance to the TR-BPAM receiver as shown in Figure 4.9.

The BER of DTR receiver for BPAM (DTR-BPAM) is [20]:

$$P_b = E\left[Q\left(\left[\frac{2N_s - 1}{N_s^2}\left(\frac{N_0}{E_p}\right) + \frac{WT}{4N_s}\left(\frac{N_0}{E_p}\right)^2\right]^{-\frac{1}{2}}\right)\right] \tag{4.22}$$

A BER performance comparison of DTR-BPAM and TR-BPAM correlation receivers in the IEEE 802.15.3a CM4 is given in Figure 4.10. The performance of the TR-BPAM receiver, and DTR-BPPM and ED-BPPM receivers are similar as shown in Figure 4.11. For the ED correlation receiver, due to the squaring device it is unable to detect binary antipodal signaling. Moreover, BPPM is more sensitive to timing mismatch when compared to BPAM scheme. The DTR-BPAM receiver outperforms TR-BPAM and ED-BPPM receivers.

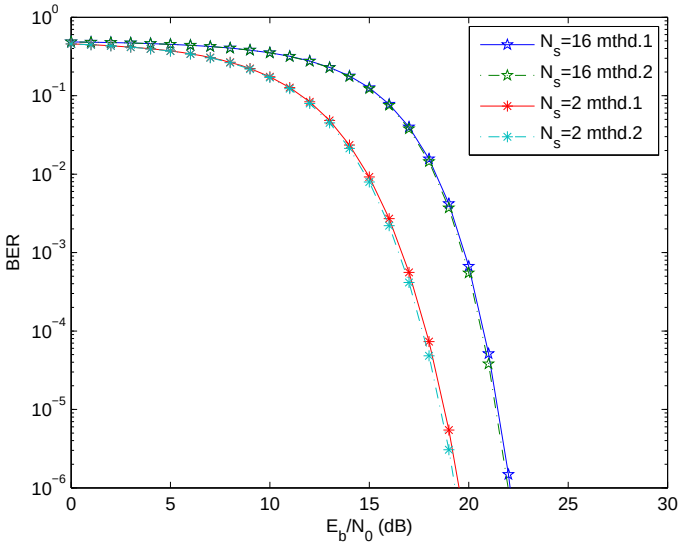

Figure 4.8: BER performance of TR-BPAM receiver in the IEEE 802.15.3a CM1 using two ways: (a) mthd.1 [55] and (b) mthd.2 [66] for N_s= 2 and 16.

4.4.3 Relationship between BER and Power-Consumption

This subsection describes the framework in detail and discusses the relationship between the BER and power consumption of the receivers under investigation. In order to maintain a

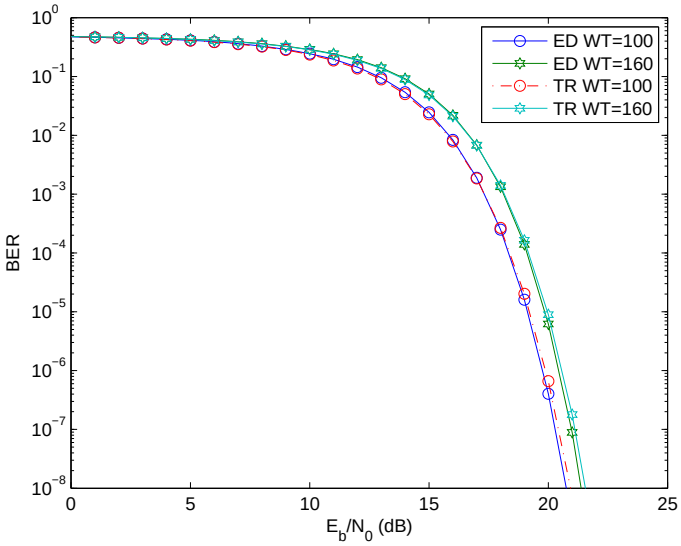

Figure 4.9: BER performance comparison of ED-BPPM and TR-BPAM receivers in the IEEE 802.15.3a CM4 for WT= 100, and 160.

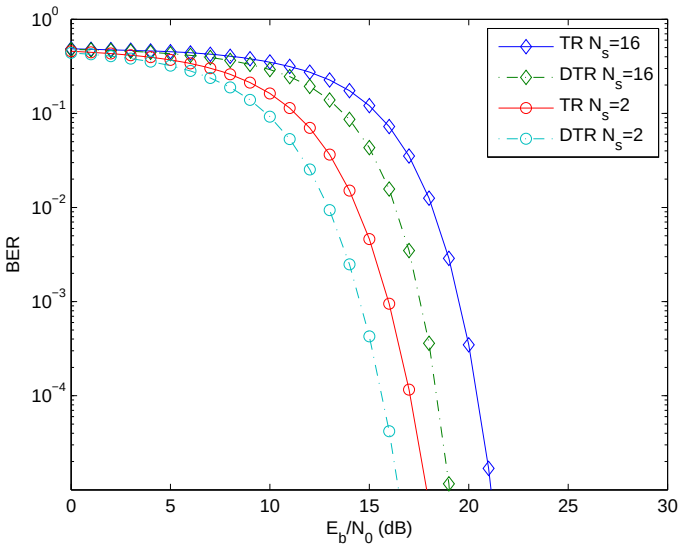

Figure 4.10: BER performance comparison of TR-BPAM and DTR-BPAM receivers in the IEEE 802.15.3a CM1 for N_s= 2 and 16.

fair comparison, both the implementation and performance parameters were fixed. From an implementation point of view, ED receivers consume less power than TR receivers. The difference in power consumption is mainly caused by the analog delay-line required for the correlation operation in the TR receivers, as depicted in Figure 4.12(a). Further, the use of

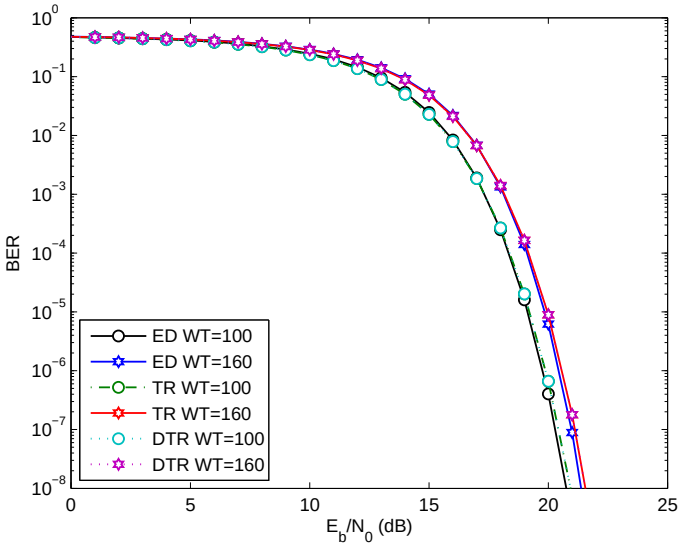

Figure 4.11: BER performance comparison of ED-BPPM, DTR-BPPM, and TR-BPAM receivers in the IEEE 802.15.3a CM4. for WT= 100 and 160.

analog delay-lines not only leads to higher power consumption, but the design of accurate analog delay-lines for UWB signals is challenging. The performance of the studied receivers suffer from the use of noisy templates, and the achievement of a better BER performance requires the averaging of multiple received pulses.

TR-BPAM, DTR-BPPM and ED-BPPM receivers have the same BER performance for the same parameters, including n (when the effect of quantization noise is considered), W, N_s, and T, as shown in Figure 4.12(b). However, the choice of these parameters is essential for both the BER performance and power consumption. Since the channel $ASNR$ depends on the channel model and T_w, W in turn affects the amount of energy captured by the receiver. Further, T is chosen such that it minimizes the BER for a specific channel model and a specific value of T_w. Moreover, N_s affects E_b/N_0 and the BER performance. When the power consumption is the main constraint, it is more convenient to fix the power consumption, and to compare the equivalent BER performance. For the same pulse repetition frequency (PRF) and P_{ADC}, the number of required N_s for W= 500 MHz and 1 GHz are 10 and 20 pulses/bit respectively. The BER performance is plotted versus T in Figure 4.13(a) for W = 500 MHz and 1 GHz, and N_s = 10 and 20 in CM1 and CM4. Accordingly, one integrator (10 ns) is chosen for minimum power consumption and BER performance, and the BER versus the corresponding change in power consumption ΔP is depicted in Figure 4.13(b). Typically, increasing the integration window increases power consumption. However, it does not necessarily enhances the performance, as there is an optimal value after which increasing the window results in adding more noise, which causes the performance to degrade. From the power consumption point of view, W affects the sampling frequency, T determines the number of integrators, and N_s and n influence the amount of relaxation of the ADC sampling frequency, where the correlation is performed in the analog domain before the ADC. To summarize, the ED-BPPM receiver achieves the same BER as TR-BPAM and DTR-BPPM correlation receivers with much less power consumption for the same parameters.

4.5 Studied Gait Parameters

As a part of studying different gait parameters, we developed multiple MATLAB simulation scripts for the extraction and calculation of various gait parameters based on actual motion capture (MoCap) files. Particularly, we extracted and estimated gait parameters from ".C3D" files associated with the Plug In Gait software of the Vicon optical system [115], ".GCD" and ".DST" associated with GaitLab (GaitCd) software [112], and ".TRC" associated with OpenSim software [4], [33].

In order to estimate gait parameters, first raw marker data was extracted from MoCap files, and then processed using MATLAB. Generally, ".C3D" files were obtained from the human locomotion database available at [1], [2]. Figures 4.14(a) and (b) show the heel-to-heel and base-of-support (BOS) distances for normal gait, respectively. Furthermore, Figure

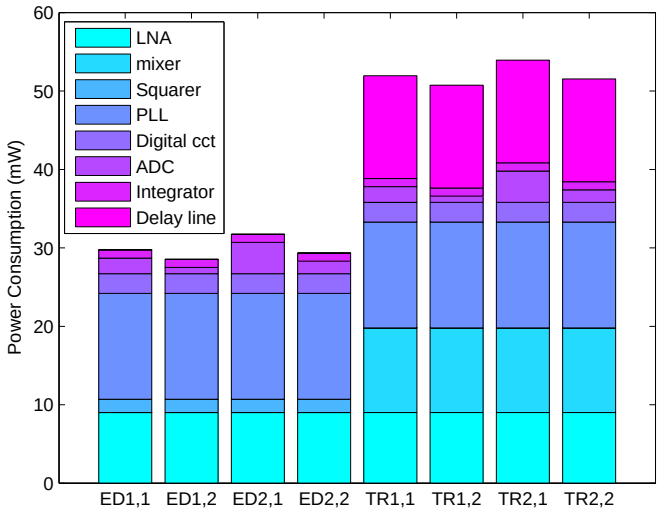

(a)

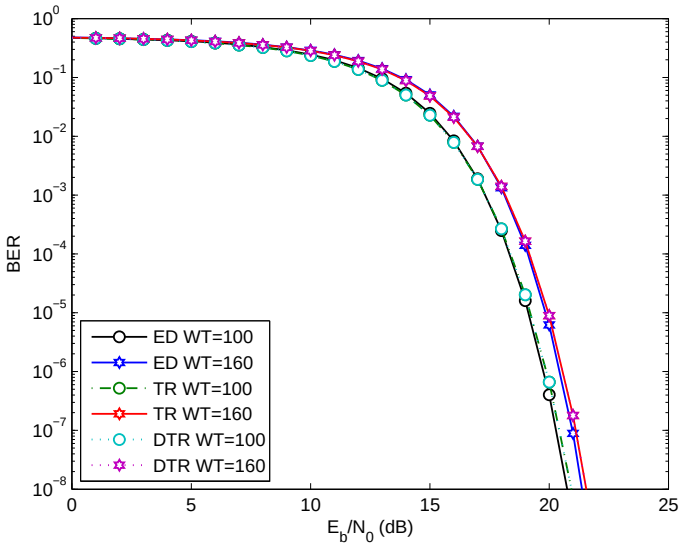

(b)

Figure 4.12: (a) Power-consumption comparison of $\mathrm{ED}_{\mathrm{W_i,N_{si}}}$ and $\mathrm{TR}_{\mathrm{W_i,N_{si}}}$ Rxs for $W_{1,2}$= 500 MHz and 1 GHz, and $N_{s1,2}$= 10 and 20. and (b) BER performance comparison of ED-BPPM, DTR-BPPM, and TR-BPAM receivers in the IEEE 802.15.3a CM4.

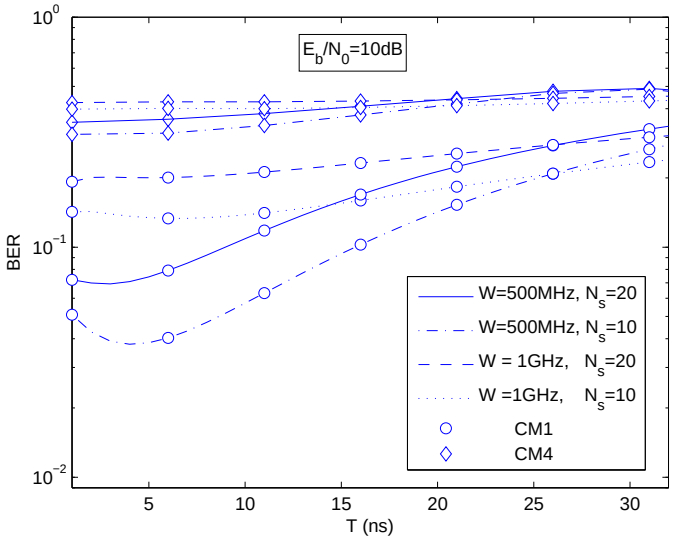

(a)

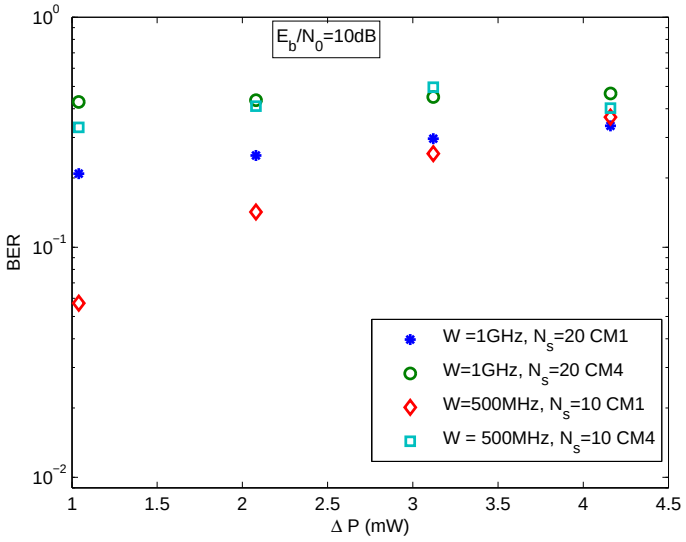

(b)

Figure 4.13: (a) BER of TR-BPAM Rx. versus $T(ns)$ for various W and N_s in CM1 and CM4. and (b) BER vs ΔP, with same parameters as in (a), in CM1 and CM4.

4.15(a) shows the right-knee flexion angle for normal gait. Similarly, Figure 4.15(b) shows the right-ankle angle. Moreover, Figures 4.16(a) and (b) depict the angular velocity and acceleration of the right-knee for normal gait, respectively.

4.6 Chapter Summary and Contributions

This chapter discussed and studied some important parameters related to our system design, namely the channel model, the link budget, and the important estimation of gait parameters to be studied. Also, it gave a comparative study of power consumption considering six different receiver architectures. Specifically, three different channel models employed in our simulation were discussed including the recent industrially accepted IEEE 802.15.6a channel model. Then, link budget design parameters were discussed and estimated for our target system TOA update rate for different pulse repetition frequencies (PRF). Moreover, we proposed a framework for the study of performance/power-consumption, and gave a case study for non-coherent UWB receivers. Furthermore, a brief comparative power consumption study was provided for the comparison of power consumption of different receiver architectures. Moreover, the employed estimation methodology of gait parameters was explained. Particularly, we do not use motion capture specialized software for the simulation of gait parameters, as we will further need to integrate these parameters in our communication system simulations starting from the raw marker data.

Related Publications:

- H. Shaban, M. Abou El-Nasr, and R.M. Buehrer, " A Framework for The Power Consumption and BER Performance of Ultra-low Power Wireless Wearable Healthcare and Human Locomotion Tracking Systems via UWB Radios ",*The 9th IEEE International Symposium on Signal Processing and Information Technology (ISSPIT 2009)*, Dec.-14 Dec. 17 2009, pp. 322-327.

- H. Shaban, M. Abou El-Nasr, and R.M. Buehrer,"Toward a highly accurate ambulatory system for clinical gait analysis via UWB radios," *IEEE Transactions on Information Technology in Biomedicine*, Vol. 14, No. 2, pp 284- 291, Mar. 2010.

- H. Shaban, M. Abou El-Nasr, and R.M. Buehrer,"A highly accurate wireless wearable UWB-based full-body motion tracking system for gait analysis in rehabilitation ," *Submitted to IEEE Transactions on Information Technology in Biomedicine.*

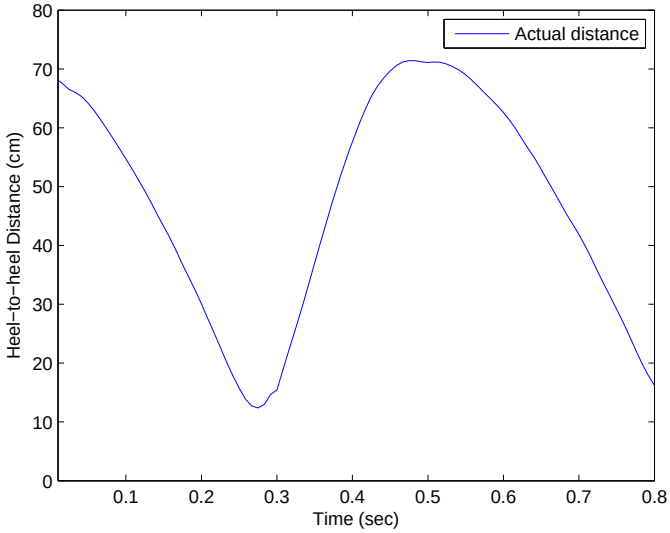

(a)

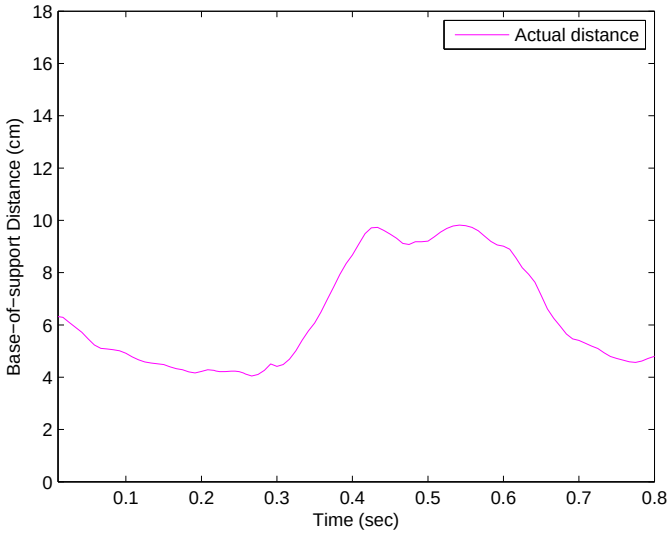

(b)

Figure 4.14: (a) Heel-to-heel distance for normal gait extracted from actual MoCap file. and (b) Base-of-support (BOS) distance for normal gait extracted from actual MoCap file.

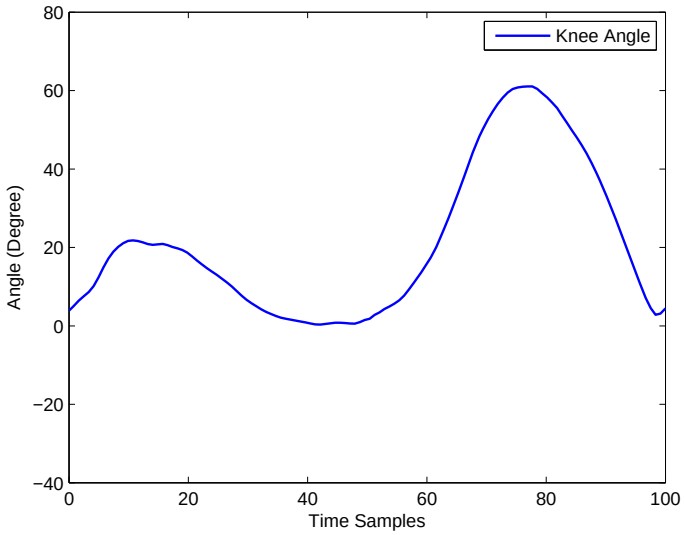

(a)

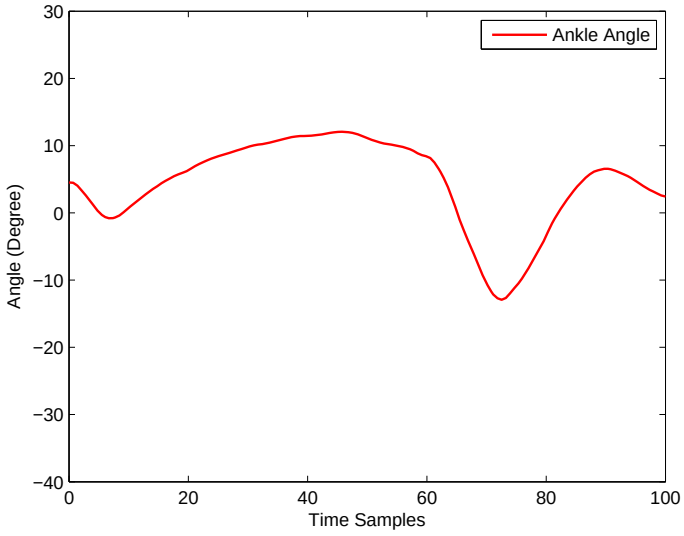

(b)

Figure 4.15: (a) Right-knee flexion angle for normal gait extracted from actual MoCap file. and (b) Right-ankle angle extracted from actual MoCap file.

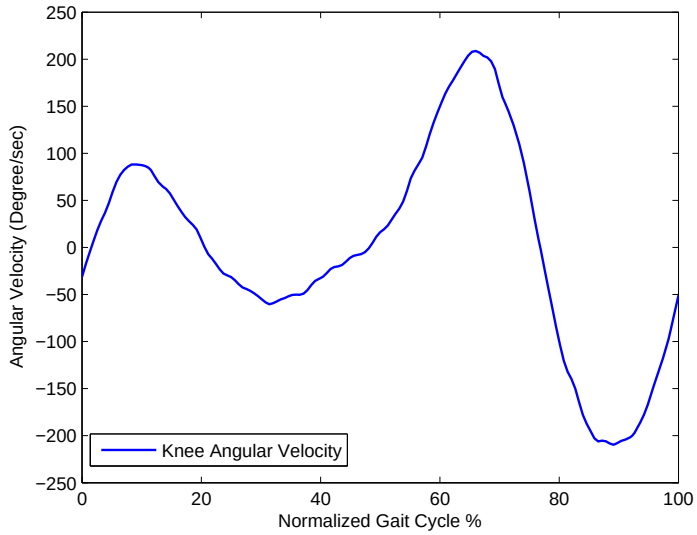

(a)

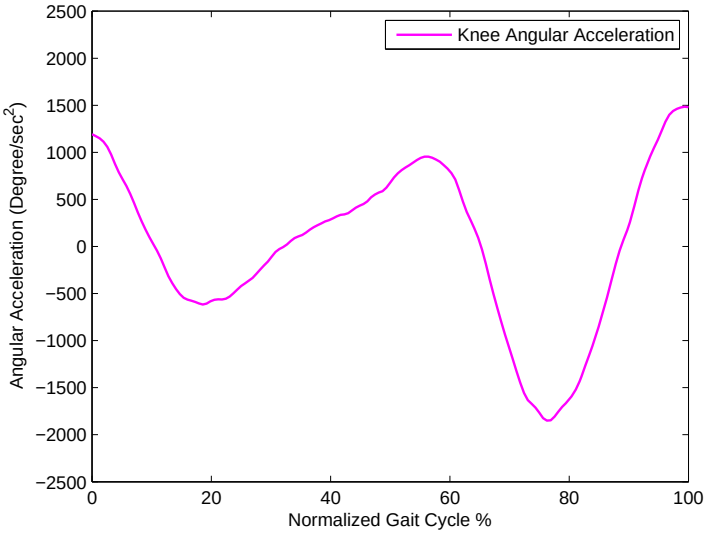

(b)

Figure 4.16: (a) Angular velocity of right-knee joint extracted from actual MoCap file. and (b) Angular acceleration of right-knee joint extracted from actual MoCap file.

Chapter 5

Ranging and Theoretical Lower Bounds

This chapter derives the theoretical lower bound on ranging performance, studies and compares ranging approaches proposed in the literature, and proposes a new ranging technique for on-body communications. Moreover, it provides link and power budgets for the proposed system. In particular, Section 5.1 studies the structure of the employed receiver based on state-of-the-art implementation parameters proposed in the literature. Furthermore, Section 5.2 studies the template design, BER in AWGN and multi-path channels, and SNR degradation. Moreover, Section 5.3 studies the theoretical lower bound on system performance and provides closed-form formulas. The proposed ranging approach is introduced in Section 5.4. Then, a comparison of the performance of the proposed approach with other TOA estimators is provided in Section 5.5. The link and power budgets for the proposed approach are given in Section 5.6. Finally, chapter conclusions and contributions are given in Section 5.7.

5.1 Analog Correlator Receiver Architecture

In our design, we assume the analog sliding-correlator proposed in [31]. In this receiver, incoming pulses are multiplied by a series of template pulses generated at the pulse repetition rate (PRR) with a predetermined phase offset increment added to each generated template pulse. Target time-of-arrival (TOA) is determined from the receiver clock phase when the output energy of multiplied incoming and template signals is maximum. This value is set to correspond to the TOA of the incoming signal. In more detail, the analog sliding-correlator is composed of a multiplier and buffer stages. The TOA of the incoming signal is determined by sweeping the phase of reference clock with a predetermined one-degree-per-step value, and the TOA is set to correspond to the maximum detected cross-correlation energy. Time-step is calculated as $\Delta t = \frac{1}{\mathrm{CLK_{RX}}.360^{o}}$ in s/1^{o}, where $\mathrm{CLK_{RX}}$ is the reference clock frequency [31].

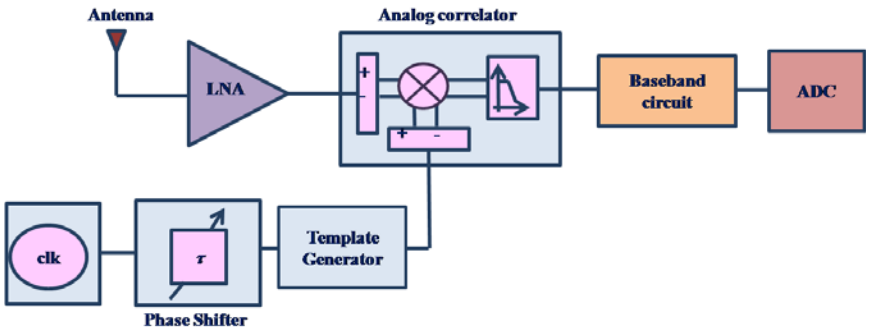

Figure 5.1: Sliding-correlator block-diagram based on the receiver architecture in [31] [32].

A simplified block-diagram of the correlator is shown in Figure 5.1[1]. Furthermore, Figure 5.2[2] shows how the incoming signal and template pulses are aligned with a 10 ps incremental phase step. It also shows the multiplier output which resembles the cross-correlation of the incoming and template signals. This procedure is verified using MATLAB simulations assuming a PRF = 50 MHz, as shown in Figure 5.3, where the incoming and template signal trains are showed. Moreover, Figure 5.4 depicts the output correlation function.

Even though the multiplier output pulses are spaced by the pulse-repetition frequency (PRF), this spacing is transformed to clock sweeping step when estimating the TOA [31] [32]. Obviously, in order to be able to determine the maximum energy, which corresponds to the TOA, an ADC placed after the buffer stage is required. It needs to have a sampling frequency equivalent to PRF. For the proposed gait analysis system, initially we assume 400 possible positions of the correlation pulse peaks, which correspond to the maximum expected 4 ns delay divided by the 10 ps step. Thus, for this stage, an ADC with 9 bit resolution and a sampling frequency equivalent to PRF = 50 MHz is sufficient. According to [29], an ADC with 9.7 effective number of bits (ENOF) and 80 Msample/s sampling frequency requires a 10 mW. Thus, for a 50 Msample/s PRF, the ADC power consumption is approximately 6.25 mW.

In our calculations, as was shown in earlier chapters, we further perform TOA estimation ten-times, and take the average of these estimates. Essentially, averaging provides values that are not limited to the 10 ps resolution assumption. For instance, averaging 10 ps and 20 ps gives 15 ps, a value that would not have been attained by solely using the 10 ps limit.

[1]Figure 5.1 is reproduced based on the receiver provided in [31], [32].
[2]Figure 5.2 is reproduced based on the figure presented in [110].

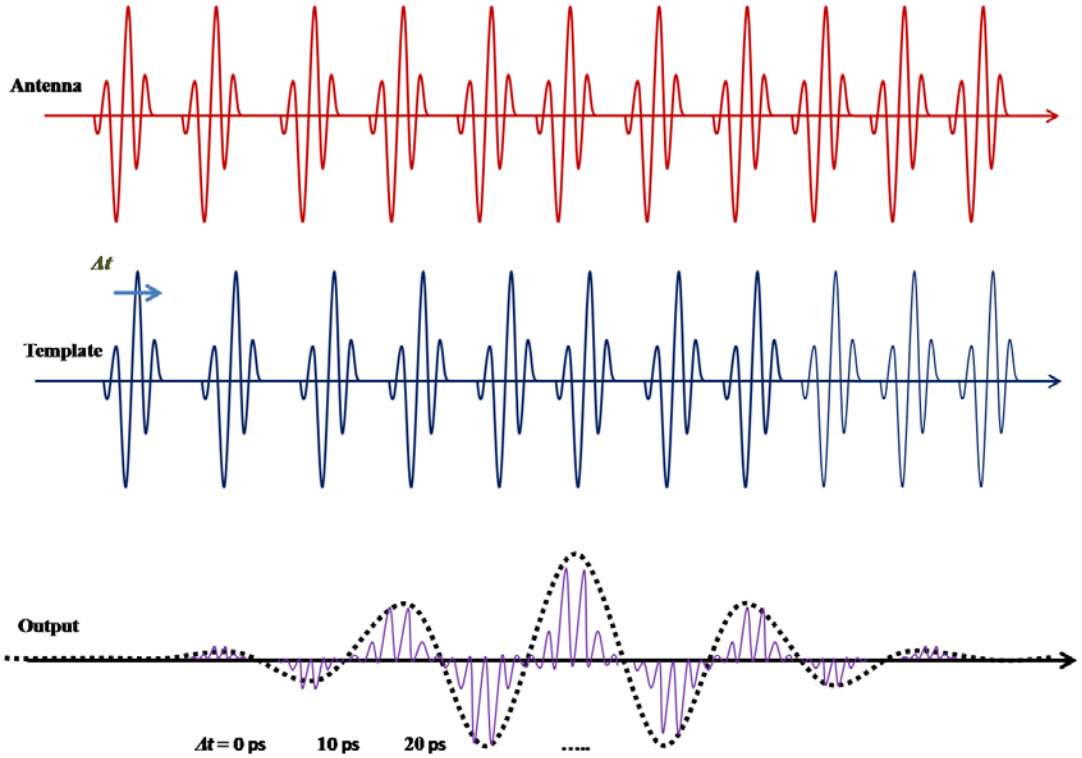

Figure 5.2: Sliding-correlator signal flow.

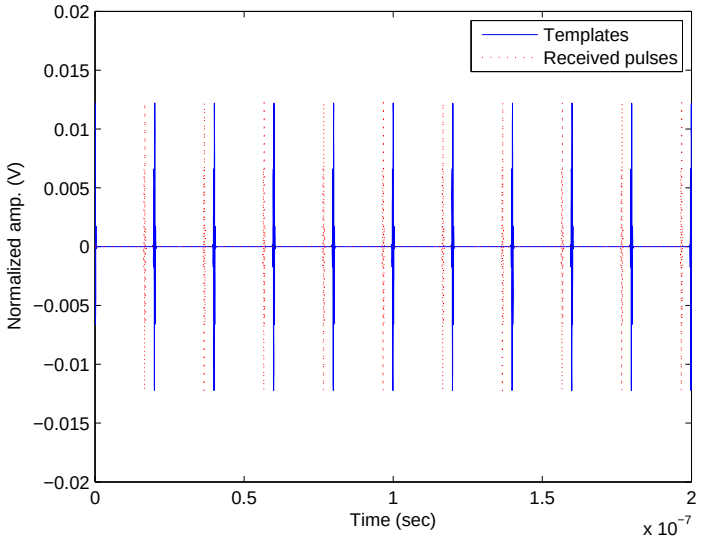

Figure 5.3: Received and template pulse streams.

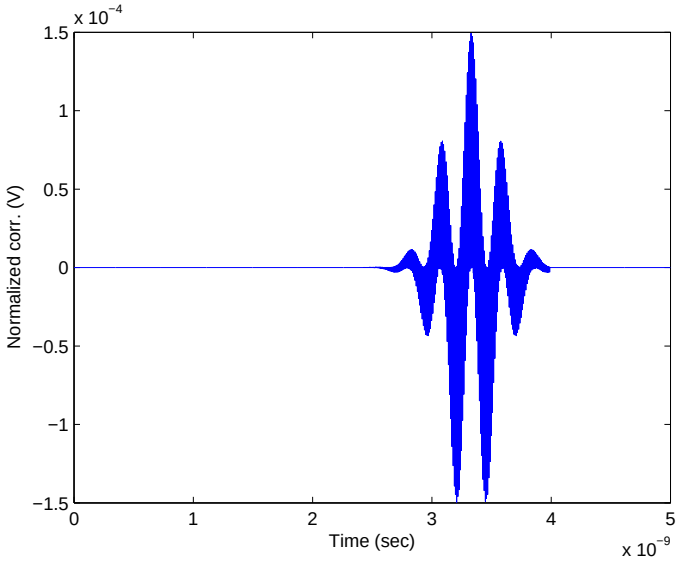

Figure 5.4: Output of the multiplier stage.

5.2 Template Pulses and BER Performance in AWGN and Multi-path Channels

The n-th order Gaussian pulse $p_0(t)$ in terms of $\sigma^2 = T_p/2\pi$, and the pulse duration T_p, has the form [97]:

$$p_n(t) = \frac{d^{(n)}}{dt^n}\left(\frac{1}{\sqrt{2\pi\sigma^2}} e^{\frac{-t^2}{2\sigma^2}}\right) \tag{5.1}$$

Assuming a correlation receiver, the optimal template $v(t)$ should be matched to the received pulse $p(t) = p_n(t)$, where the pulse parameters are chosen to meet the specified FCC allowable emission limits. When using a suboptimal windowed sinusoidal template, $v(t) = \cos(\omega_c(t))$ for a window-length T and carrier frequency ω_c, the oscillator frequency should be chosen to maximize the output SNR [97]:

$$SNR = \frac{E_s}{N_0}\frac{\rho_{pv}^2(\tau_e)}{\rho_{pp}(0)} \tag{5.2}$$

where, E_s is the bit energy, N_0 is the noise PSD, $\rho_{pv}(.)$ is the normalized cross-correlation of the received pulse and the template waveform, τ_e is the timing error, and $\rho_{pp}(.)$ is the normalized auto-correlation of the received pulse.

5.2.1 BER Performance in AWGN Channel

In this subsection, we derive the BER assuming the PPM scheme, which will be used later in the estimation of the ZZLB. Considering binary Pulse Position Modulation (BPPM), with

a transmitted pulse $p(t)$, the optimal template is [14]:

$$v(t) = p(t) - p(t - \delta) \tag{5.3}$$

where, δ is the PPM modulation parameter. In the case of the optimum receiver, the BER can be minimized by choosing δ to minimize the autocorrelation [91]:

$$\delta_{opt} = \arg\left\{\min_{\delta} \rho_{pp}(\delta)\right\} \tag{5.4}$$

For equally correlated (EC) M-ary PPM, the transmitted signal is composed of N_s time shifted pulses with $2 \leq M < N_s$, where each signal is identified by a sequence of cyclic shifts of an m-sequence of length N_s [91]. The union bound on the bit error probability of EC M-ary PPM assuming an optimum receiver is [91]:

$$U_{BPb} = \frac{M}{2} Q\left(\sqrt{\frac{E_s}{2N_0}(1 - \rho_{pp\,\min})}\right) \tag{5.5}$$

$$\rho_{pp}(\tau) = \frac{1}{E_p} \int_{-\infty}^{\infty} p(t)p(t-\tau)dt \tag{5.6}$$

where, $Q(.)$ is the Gaussian tail function [91], [102]. The alternate representation for the tail function is expressed as $Q(x) = \frac{1}{\pi}\int_0^{\pi/2} exp\left(-\frac{x^2}{2sin^2\theta}\right) d\theta$ [102], $\rho_{pp\,\min} \triangleq \rho_{pp}(\delta_{opt})$, and E_p is the pulse energy.

Real Suboptimal Template

The normalized cross-correlation function of the received pulse and windowed sinusoidal template (where T is the window-length and ω_c is the carrier frequency) can be calculated as [97]:

$$\rho_{pv}(\tau) = \frac{1}{\sqrt{E_p}\sqrt{E_v}} \int_{-T/2}^{T/2} p(t)\cos(\omega_c(t-\tau))dt \tag{5.7}$$

where, E_v is the template energy. Without loss of generality we assume that the received pulse is the Gaussian pulse $p(t) = p_0(t)$, from which all derivatives could be obtained, this gives:

$$\rho_{pv}(\tau) = \frac{1}{4\sqrt{E_p}\sqrt{E_v}} \left[erf\left(\frac{1}{2\sqrt{2}\sigma}\Phi\right) + erf\left(\frac{1}{2\sqrt{2}\sigma}\Phi^*\right)\right] \left[\exp\left(\frac{-\omega_c}{2}\Lambda\right) + \exp\left(\frac{-\omega_c}{2}\Lambda^*\right)\right] \tag{5.8}$$

where, $\Phi = T + 2i\omega_c\sigma^2$, $\Lambda = \sigma^2\omega_c + 2i\tau$, $i = \sqrt{-1}$, ω_c is the oscillator angular frequency in rad/s, T is the window duration, and τ is the time-shift. To minimize BER, we wish to choose the value of δ that minimizes the correlation $\rho_{pv\,\min}(\delta_{opt})$. Further, at the receiver we

choose a sample time μ to maximize the correlation between the suboptimal template and the generated pulse:

$$\mu_{opt} = \arg\left\{\max_{\mu} \rho_{pv}(\mu)\right\} \tag{5.9}$$

with $\rho_{pv\,\max} = \rho_{pv}(\mu_{opt})$, the union bound on the bit error probability for equally correlated signals is defined as:

$$U_{BPb} = \frac{M}{2} Q\left(\sqrt{\frac{E_s}{2N_0}(\rho_{pv\,\max} - \rho_{pv\,\min})}\right) \tag{5.10}$$

Complex Suboptimal Template

The quadrature analog correlation (QAC) receiver uses two branches for correlation, namely the in-phase I-branch and quadrature-phase Q-branch [65]. The I-branch uses a template signal similar to the real suboptimal template-based receiver. Whereas, the Q-branch uses a template $v(t) = \sin(\omega_c t)$. The resulting correlation from the Q-branch is expressed as:

$$\rho_{pvQ}(\tau) = \frac{1}{\sqrt{E_p}\sqrt{E_v}} \int_{-T/2}^{T/2} p(t) \sin(\omega_c(t-\tau))dt \tag{5.11}$$

The corresponding closed-form correlation is written as:

$$\rho_{pvQ}(\tau) = \frac{i\sqrt{2\pi}\sigma}{4\sqrt{E_p}\sqrt{E_v}} \left[erf\left(\frac{1}{2\sqrt{2}\sigma}\Phi\right) + erf\left(\frac{1}{2\sqrt{2}\sigma}\Phi^*\right)\right] \left[-\exp\left(\frac{-\omega_c}{2}\Lambda\right) + \exp\left(\frac{-\omega_c}{2}\Lambda^*\right)\right] \tag{5.12}$$

Also, The cross-correlation function could be further simplified to:

$$R_{pvQ}(\tau) = \frac{-i\sqrt{2\pi}\sigma}{2\sqrt{E_p}\sqrt{E_v}} \left[erf\left(\frac{1}{2\sqrt{2}\sigma}\Phi\right) + erf\left(\frac{1}{2\sqrt{2}\sigma}\Phi^*\right)\right] \sin\left(\frac{\omega_c}{2}\Theta\right) \tag{5.13}$$

where, $\sin\left(\frac{\omega_c}{2}\Theta\right) = -i0.5\left(\exp\left(i\frac{\omega_c}{2}\Theta\right) - \exp\left(i\frac{\omega_c}{2}\Theta\right)\right)$. The resulting cross-correlation function is plotted versus ω_c for various values of τ and T in Figure 5.5. The resulting correlation from the I-branch and Q-branch is expressed as:

$$\rho_{pv_{QAC}} = \rho_{pvI} + i\rho_{pvQ} \tag{5.14}$$

and from Eq. (5.8) and (5.13), the resulting cross-correlation function is expressed as:

$$\rho_{pv_{QAC}}(\tau) = \frac{\sqrt{2\pi}\sigma}{2\sqrt{E_p}\sqrt{E_v}} \left[erf\left(\frac{1}{2\sqrt{2}\sigma}\Phi\right) + erf\left(\frac{1}{2\sqrt{2}\sigma}\Phi^*\right)\right] \exp\left(\frac{-\omega_c}{2}\Lambda\right) \tag{5.15}$$

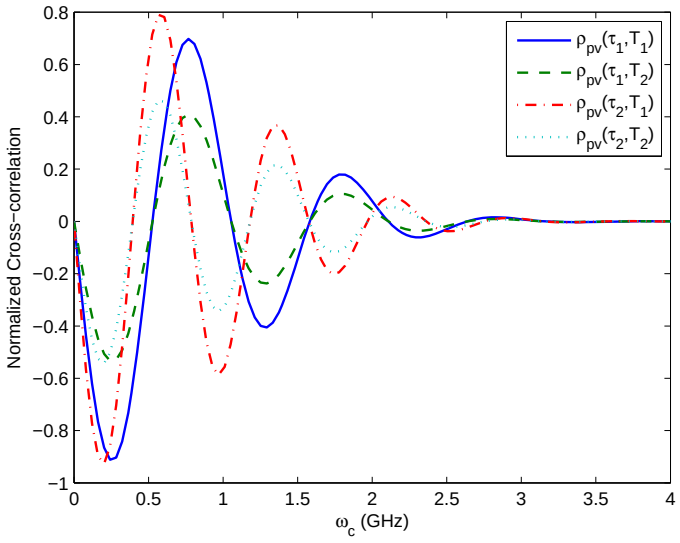

Figure 5.5: Normalized cross-correlation function $R_{pvQ}(\tau)$ of the Gaussian pulse and suboptimal sinusoidal pulse from the Q-branch versus the frequency of the suboptimal template for various values of τ, and T, $\tau_1 = 1.9192$ ns, $\tau_2 = 5.9596$ ns, $T_1 = 1.9$ ns, and $T_2 = 0.9$ ns.

5.2.2 Signal to Noise Ratio Degradation

The SNR degradation at the output of the correlator could be calculated according to Eq. (5.2) for the real and complex suboptimal templates based on Eq. (5.8) and (5.15), respectively. Figure 5.6 shows the SNR degradation versus timing error for the optimal template, real and complex suboptimal templates for various values of ω_c and T. Obviously, both parameters affect the SNR degradation. Moreover, receivers with complex suboptimal templates exhibit less severe SNR degradation, which is traded for more power consumption compared to receivers with real templates. However, it requires smaller power consumption compared to optimum detectors [65].

5.2.3 BER Performance in Dense Multi-path Channels

The BER of low complexity partial RAKE (PRake) receivers [87], assuming PPM modulation and optimal templates in terms of the moment generating function (MGF), M_{η_l}, over a Nakagami-m channel with uniform power delay profile (PDP), and $L_{\rm p}$ independent identically distributed (*i.i.d.*) paths is [87]:

$$P_{b,\rm PRake} = \frac{1}{\pi}\int_0^{\pi/2}\left(M_{\eta_l}\left(-\frac{(1-\rho_{pp\,\rm min})}{4m\sin^2\theta}\right)\right)^{L_{\rm p}} d\theta \tag{5.16}$$

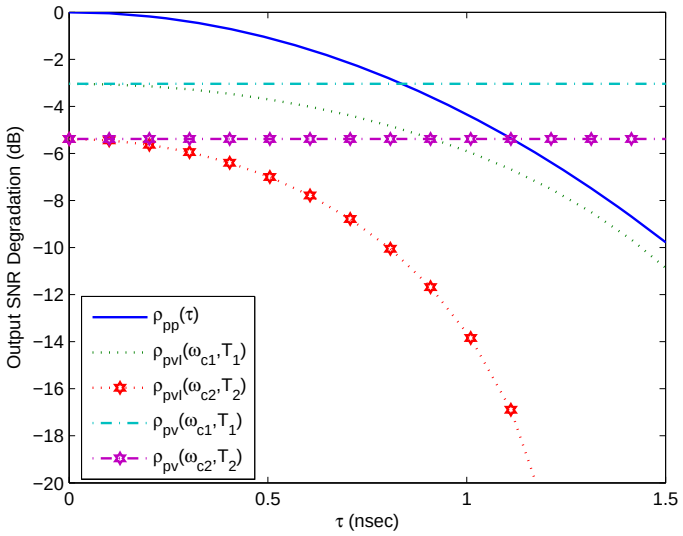

Figure 5.6: Output SNR degradation of the correlation receiver output for the Gaussian pulse and suboptimal templates versus the timing error for various values of ω_c, and T, $\omega_{c1} = 0.7677$ GHz, $\omega_{c2} = 1.1717$ GHz, $T_1 = 1.9$ ns, and $T_2 = 2.9$ ns.

where, $\bar{\eta} = E_s/LN_0$. Ideal Rake (ARake) receivers capture all the energy in all L paths, i.e., $L_\mathrm{p} = L$ [87]. Substituting with the MGF $M_{\bar{\eta}}(s) = \left(1 - \frac{s\bar{\eta}}{m}\right)^{-m}$ gives:

$$P_{b,\mathrm{PRake}} = \frac{1}{\pi}\int_0^{\pi/2}\left(\frac{4m\sin^2\theta}{4m\sin^2\theta + \bar{\eta}(1-\rho_{pp\,\min})}\right)^{mL_\mathrm{p}} d\theta \tag{5.17}$$

The probability of bit error of PRake receivers for PPM modulation with a suboptimal template is:

$$P_{b,\mathrm{PRake}} = \frac{1}{\pi}\int_0^{\pi/2}\left(\frac{4m\sin^2\theta}{4m\sin^2\theta + \bar{\eta}(\rho_{pv\,\max} - \rho_{pv\,\min})}\right)^{mL_\mathrm{p}} d\theta \tag{5.18}$$

The MGF for correlated Nakagami-m fading is:

$$M_{\bar{\eta}}(s) = \prod_{l=1}^{L}\left(\frac{1-s\bar{\eta}_l}{mL}\right)^{-m}\left[\det[\mathrm{c_{uj}}]\right]^{-m} \tag{5.19}$$

where,

$$c_{uj} = \begin{cases} 1 & u = j \\ \sqrt{\rho_{uj}}\left(1 - \frac{mL}{s\bar{\eta}_j}\right)^{-1} & o.w. \end{cases} \tag{5.20}$$

where ρ_{uj} is the fading power correlation between sub-bands u and j [102]. The corresponding error probability is:

$$P_{b,\mathrm{PRake}} = \frac{1}{\pi} \int_0^{\pi/2} \prod_0^{L_p} \left(\frac{4m \sin^2\theta + \bar{\eta}(\rho_{pv\,\max} - \rho_{pv\,\min})}{4m^2 L_{\mathrm{p}} \sin^2\theta} \right)^{-m} . \left[\det[\mathrm{c_{uj}}]\right]^{-m} d\theta \tag{5.21}$$

and,

$$c_{uj} = \begin{cases} 1 & u = j \\ \sqrt{\rho_{uj}} \left(1 + \frac{4m^2 L_{\mathrm{p}} \sin^2\theta}{(\rho_{pv\,\max} - \rho_{pv\,\min})\bar{\eta}_j}\right)^{-1} & o.w. \end{cases} \tag{5.22}$$

Template Design and Numerical Results

In this sub-section, we use the analysis provided above to compare the performance of IR-UWB correlation receivers with optimal and suboptimal templates in AWGN and dense multi-path channels.

Using windowed sinusoids was proposed in the literature as an alternative solution for low-power template generation in the analog domain, since windowed sinusoids can approximate the optimal templates and are easily generated in the analog domain [97]. However, this solution suffers from the sensitivity of the correlator output SNR to timing errors. As will be shown later, this is an advantage for our system since we are interested in estimating the TOA rather than the BER. Receiver structures with suboptimal sinusoidal templates are more sensitive to timing errors as compared to optimal receivers [97]. Complex sinusoids were proposed to compensate for the SNR degradation in the presence of timing errors, but this structure requires nearly double the power required for the corresponding structure with real sinusoids [53], [65].

Suboptimal template design requires the appropriate choice of the sinusoidal wave frequency, and the integration window-length [97]. Figure 5.7(a) shows the optimal and suboptimal templates assuming the seventh order Gaussian pulse, and Figure 5.7(b) shows the corresponding autocorrelation and cross-correlation functions. Figure 5.8 shows the cross-correlation function of the Gaussian pulse and the sinusoidal template versus the frequency of the sinusoidal template at different time samples, and correlation window-lengths using Eq. (5.15). As shown, the cross-correlation function is highly sensitive to both the sinusoidal template frequency and the integration window. The normalized cross-correlation coefficient can be > 0.9 for appropriate choice of sinusoidal templates. For M-ary PPM modulation, the performance loss caused by sinusoidal templates with appropriately chosen parameters is $<$ 0.2 dB, as depicted in the simulation results in Figure 5.9. Furthermore, the simulated BER performance of ARake receivers is shown in Figure 5.10 for BPPM and 4-PPM schemes in IEEE 802.15.4a outdoor NLOS channel, for the seventh order Gaussian pulse, and sinusoidal templates. Finally, Figure 5.11 shows a BER comparison between simulated BPPM and 4-PPM schemes in IEEE 802.15.6a for the seventh order Gaussian pulse, assuming optimal, suboptimal, and complex suboptimal sinusoidal templates.

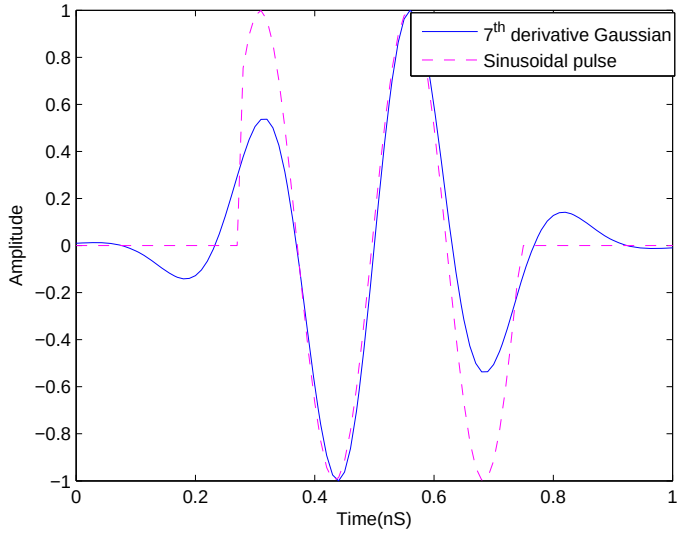

(a)

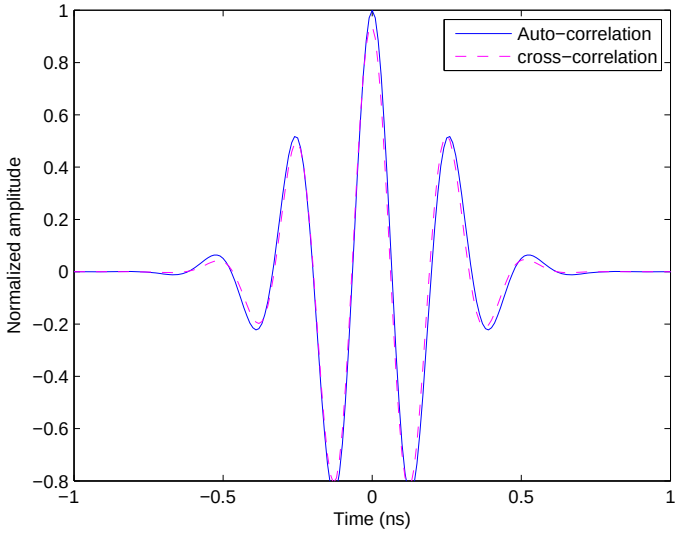

(b)

Figure 5.7: (a) Seventh Order Gaussian pulse and corresponding suboptimal template. and (b) Seventh order Gaussian pulse autocorrelation and cross-correlation with corresponding suboptimal template.

5.3 Derivation of TOA Theoretical Lower Bounds

The primary motivation for using UWB technology (besides the wide spectrum available) is the ability of UWB pulses to provide very accurate distance estimates using Time-of-Arrival

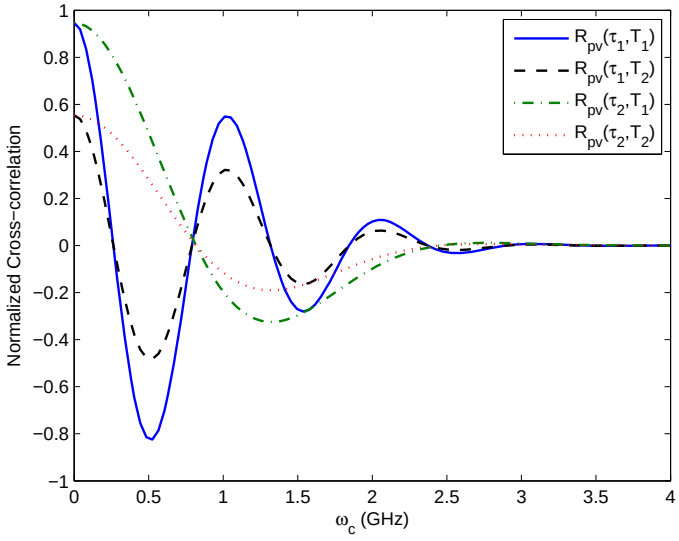

Figure 5.8: Normalized cross-correlation function $\rho_{pv}(\tau)$ of the Gaussian pulse and suboptimal sinusoidal pulse versus the frequency of the suboptimal template for various values of τ, and T, $\tau_1 = 1.9192$ ns, $\tau_2 = 5.9596$ ns, $T_1 = 1.9$ ns, and $T_2 = 0.9$ ns.

(TOA) measurements [36], [49]. In general, the accuracy can be improved by increasing either the SNR at the receiver or the effective signal bandwidth of the transmitted signal [60]. Error bounds are essential for providing a performance limit of any estimator in terms

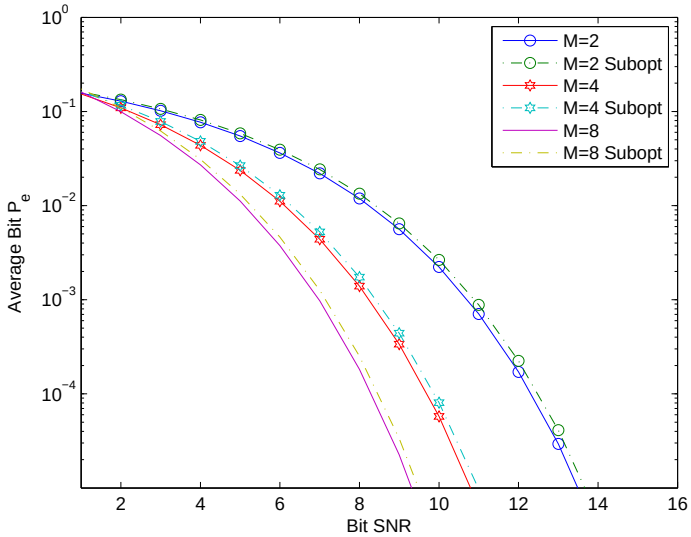

Figure 5.9: BER performance comparison of M-ary PPM modulation in AWGN channel for the second order of the Gaussian pulse with optimal and suboptimal templates.

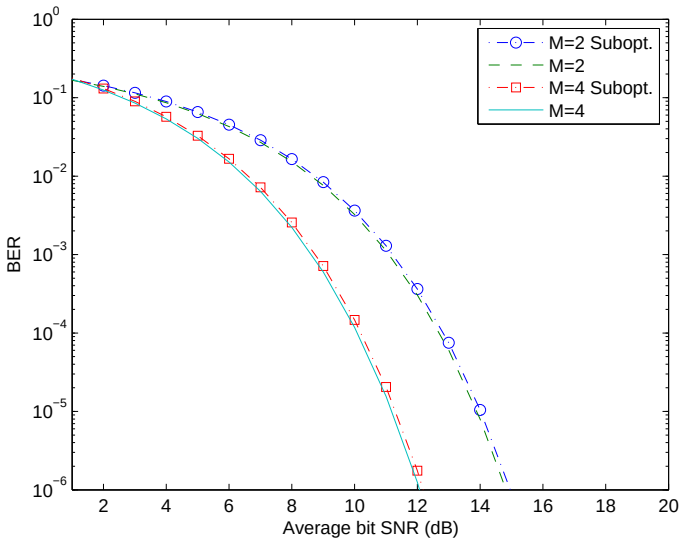

Figure 5.10: BER performance comparison of M-ary PPM modulation in NLOS IEEE 802.15.4a channel for the seventh order of the Gaussian pulse with optimal and suboptimal templates.

of the mean square error (MSE) [36]. From estimation theory, the mean square error (MSE) $\sigma_{\hat{\tau}}^2$ of any unbiased estimate $\hat{\tau}$ of the time-of-arrival τ is under-bounded by the Cramer-Rao Lower Bound (CRLB) [28]:

$$\sigma_{\hat{\tau}}^2 = \mathrm{E}\left\{(\hat{\tau} - \tau)^2\right\} \geq \mathrm{CRLB} \tag{5.23}$$

where the measurement error is $\varepsilon_{\hat{\tau}} = \hat{\tau} - \tau$ and $\mathrm{E}\{.\}$ denotes the statistical expectation [28].

5.3.1 CRLB and ZZLB TOA Lower-Bounds

The CRLB for the ranging error estimate can be calculated from the relation:

$$\sigma_{\hat{d}} = c\sigma_{\hat{\tau}} \tag{5.24}$$

where, $c = 3 \times 10^8$ m/s is the speed of light [23]. When no-multi-path is present [28]:

$$\mathrm{CRLB} = \frac{N_0/2}{E_p \beta^2} = \frac{1}{2\beta^2 SNR} \tag{5.25}$$

where, the pulse-energy-to-noise ratio is represented by $\frac{E_p}{N_0}$, and β^2 is the second moment of the spectrum $P(f)$ of the pulse shape used $p(t)$ defined by [28]:

$$\beta^2 = \frac{\int_{-\infty}^{\infty} f^2 \left|P(f)\right|^2 df}{E_p} \tag{5.26}$$

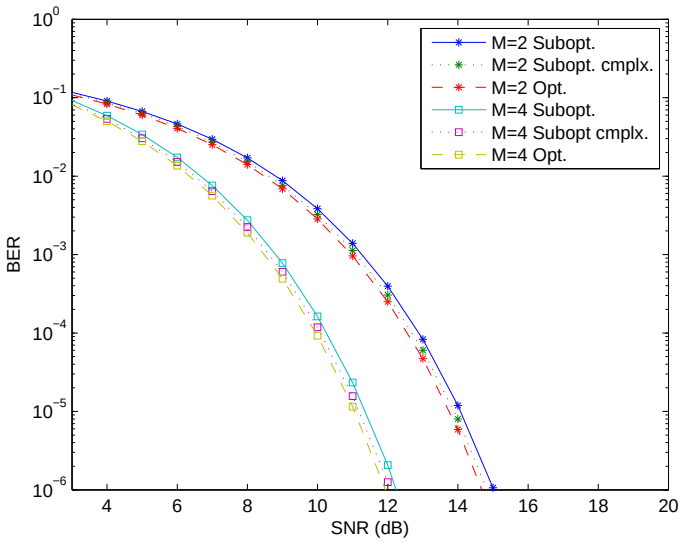

Figure 5.11: BER performance comparison of M-ary PPM modulation in IEEE 802.15.6a channel for the seventh order Gaussian pulse assuming coherent detectors with optimal, and real and complex suboptimal templates.

Another representation of the Gaussian pulse defined in terms of pulse-width T_p and $\tau_p = 0.5 * T_p$ as [28] is:

$$p_0(t) = exp\left(-2\pi\left(t^2/\tau_p^2\right)\right) \tag{5.27}$$

The n-th order Gaussian pulse has the form [97]:

$$p_n(t) = \frac{d^{(n)}}{dt^n}\left(\frac{1}{\sqrt{2\pi\sigma^2}}e^{\frac{-t^2}{2\sigma^2}}\right) \tag{5.28}$$

In order to estimate the ZZLB, we need to find the mean square error. The mean square estimation error is [28]:

$$E\left\{\varepsilon_{\hat{\tau}}^2\right\} = \frac{1}{2}\int_0^\infty zP\left\{|\varepsilon_{\hat{\tau}}| \geq \frac{z}{2}\right\}dz \tag{5.29}$$

where the expectation is with respect to τ and $r(t)$. $P\left\{|\varepsilon_{\hat{\tau}}| \geq \frac{z}{2}\right\}$ is equivalent to the probability of a binary detection scheme with equally-probable hypotheses, where T_a is the observation window [28]. It is assumed that the probability density function (pdf) of the TOA in the absence of any information is uniformly distributed in the interval $[0, T_a]$.

The TOA ranging approach is based on the estimation of the arrival time of the first detected path. Typically, optimum detection involves the correlation of the received wave-

form with a locally generated template waveform, which adds to the receiver complexity [60]. However, this requirement is precluded for non-coherent receivers, where the detection process depends solely on the received pulses [60], [20]. One promising low-power non-coherent receiver is the energy detection (ED) correlation receiver, where the correlation is replaced by a squaring device. Generally speaking, EDs consume smaller amounts of power as compared to coherent stored-reference receivers since they do not require template generation. However, this simplification is traded for a degradation in the estimation performance. Assuming the ED detector, and a corresponding pulse-width 0.8 ns, the corresponding B.W. is 2 GHz for the seventh-order Gaussian pulse[3] [85], the maximum achievable ranging accuracy is 6.9 cm for an integration window that is equal to the pulse-width. This is because the ED estimator exhibits a maximum achievable accuracy equal to $T_s/\sqrt{12}$, where T_s is the integration window. This precludes the choice of ED detectors. Obviously, for such a high target ranging accuracy, required for accurate human locomotion tracking, the MF seems an appropriate choice, where its performance approaches the CRLB at high SNRs.

Generally, the CRLB provides a loose bound on the TOA estimate which is not realizable in multi-path environments [28]. Another bound that provides more accurate results suitable for multi-path environments is the Ziv-Zakai lower bound (ZZLB). The improved ZZLB for the coherent detection of binary signaling is as given by [28]:

$$\text{ZZLB} = \frac{1}{T_a} \int_0^{T_a} z\,(T_a - z)\, P_{\min}(z) dz \tag{5.30}$$

where, $P_{\min}(z)$ is the minimum attainable probability of error expressed as [28]:

$$P_{\min}(z) = Q\left(\sqrt{\frac{E_p}{N_0}(1 - \rho_{pp}(z))}\right) \tag{5.31}$$

where E_p is the pulse energy and $\rho_{pp}(z)$ is the pulse autocorrelation. For the suboptimal template, the corresponding minimum attainable probability of error is:

$$P_{\min}(z) = Q\left(\sqrt{\frac{E_p}{N_0}(\rho_{pv}(0) - \rho_{pv}(z))}\right) \tag{5.32}$$

This bound transforms the estimation problem into a binary detection problem, which simplifies the bound estimation in multi-path environments. The derivation of $P_{\min}(z)$ requires the *a priori* knowledge of the multi-path phenomena [28].

The evaluation of the estimator in complex channel models is not analytically tractable [28]. As a result, the ZZLB is typically evaluated using experimentally measured channel impulse responses or Monte Carlo simulations [28].

[3]Seventh-order Gaussian pulse was chosen to satisfy the FCC masks for both indoor and outdoor environments

$$P_{\min}(z) \cong \frac{1}{N_{ch}} \sum_{k=1}^{N_{ch}} Q\left(\sqrt{\frac{SNR}{2} d^2_{k,i(*)}(z)}\right) \tag{5.33}$$

$$P_{\min}(z) \cong Q\left(\sqrt{\frac{SNR}{2} d^2_{\min}(z)}\right) \tag{5.34}$$

where N_{ch} is the number of channel realizations, SNR is the total signal-to-noise-ratio, $d_{\min}(z) = \min_k d_{k,i^{(*)}}(z)$ is the minimum normalized distance between the symbols used for the representation of the PPM scheme, $i^{(*)} = \arg\min_i d^2_{k,i}(z)$, and k is the argument of the minimization [28].

Assuming a correlation receiver, the optimal template $v(t)$ should be matched to the received pulse $p(t) = p_n(t)$, where the pulse parameters should be chosen to meet specified FCC system's allowable emission limits. Since the human locomotion tracking system under investigation should work in indoor and outdoor environments, we chose the seventh derivative Gaussian pulse to satisfy the FCC masks for both environments. The corresponding ZZLB for the optimal and suboptimal templates are shown in Figures 5.12(a) and (b) for TOA and distance bounds, respectively. In order to obtain results for the TOA bounds using realistic BAN channels, the ZZLB was determined using a semi-analytic simulation approach in the BAN channel model described in [44]. The ZZLB was calculated for the simulated channels and the average is depicted in Figures 5.13(a) and (b) for the distance and TOA bounds, respectively assuming the back, side, and front channel models. Further results for the TOA bounds using industrially accepted BAN channels were obtained by simulating the ZZLB using a semi-analytic simulation approach in the IEEE 802.15.6a channel model [119] and in Section 4.1. The resulting ZZLB is depicted in Figures 5.14(a) and (b) for the distance and TOA bounds, respectively. As seen from the results, an accuracy of 0.11 cm is achievable at an $E_p/N_0 = 18$ dB, which defines the target E_p/N_0. Different link budget calculations for low-power and low-cost detectors for BAN applications showed that the achievable E_p/N_0 is greater than 18 dB with appropriate link margins [101], [80]. We will discuss the link budget in detail in Section 5.6. Figures 5.15(a) and (b) show a comparison of the ZZLB in the IEEE 802.15.6a assuming optimal, real suboptimal, and complex suboptimal template-based detectors for the TOA and distance bounds, respectively.

5.3.2 Effect of Timing Misalignment on The ZZLB

In this subsection, we will study the effect of timing-misalignment on the ZZLB, which results from of error in the position of the template relative to what the clock. For the suboptimal template, the effect of timing-misalignment τ_e on the BER performance of PPM scheme is:

$$P_{\min}(z) = Q\left(\sqrt{\frac{E_p}{N_0} \frac{\left[\rho_{pvI}(\tau_e) - \rho_{pvI}(z-\tau_e)\right]^2}{\rho_{pvI}(0) - \rho_{pvI}(z)}}\right) \tag{5.35}$$

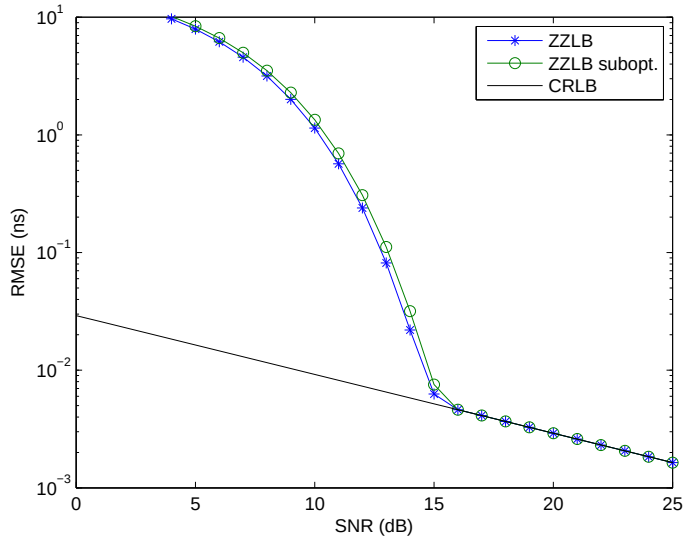

(a)

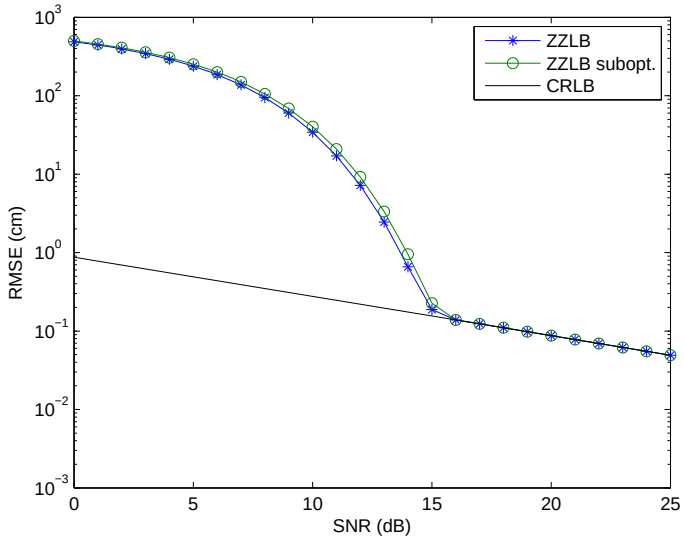

(b)

Figure 5.12: (a) ZZLB and CRLB (ns) for range estimation in AWGN channel for a seventh order Gaussian pulse. and (b) ZZLB and CRLB (cm) for range estimation in AWGN channel for a seventh order Gaussian pulse.

where $\rho_{pvI}(.)$ is the normalized cross-correlation of the received pulse and the template waveform, and τ_e is the timing error.

The ZZLB with the effect of timing misalignment for suboptimal template is given in Eq.

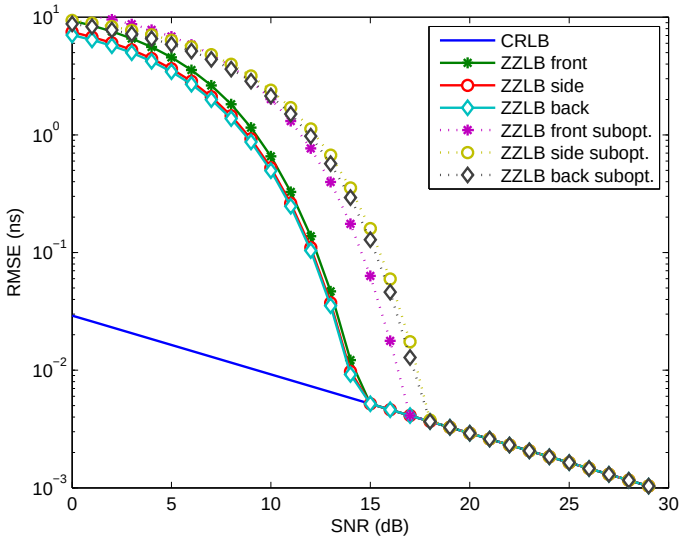

(a)

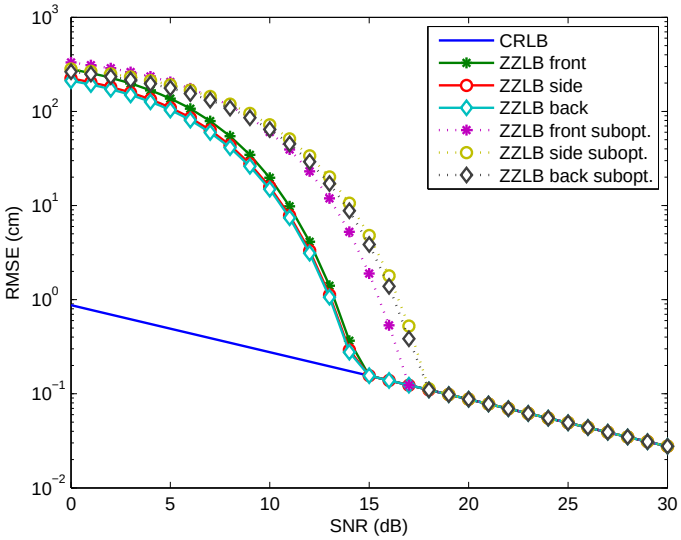

(b)

Figure 5.13: (a) CRLB along with a comparison of ZZLB (ns) for optimal, suboptimal, and QAC receivers in the IEEE 802.15.6a channel for a seventh order Gaussian pulse. and (b) CRLB along with a comparison of ZZLB (cm) for optimal, suboptimal, and QAC receivers in the IEEE 802.15.6a channel for a seventh order Gaussian pulse.

(5.36).

$$\text{ZZLB}_{\tau_e} = \frac{1}{T_a}\int_0^{T_a} z\,(T_a - z)\,Q\left(\sqrt{\frac{E_p}{N_0}\frac{\left[\rho_{pvI}(\tau_e) - \rho_{pvI}(z-\tau_e)\right]^2}{\rho_{pvI}(0) - \rho_{pvI}(z)}}\right)dz \tag{5.36}$$

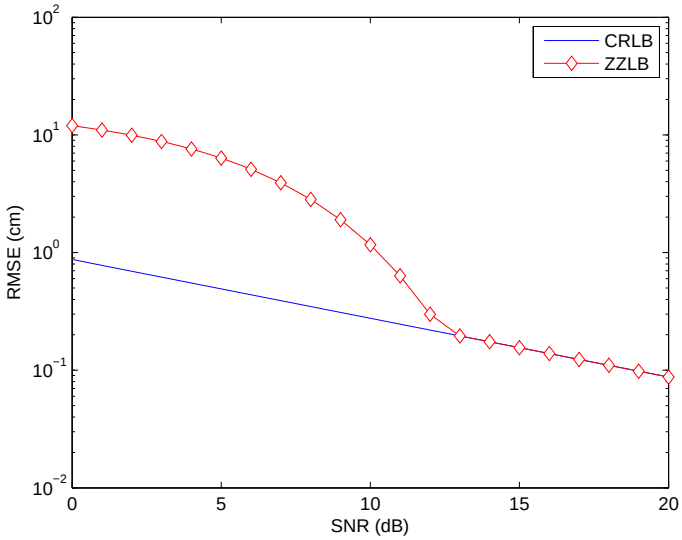

(a)

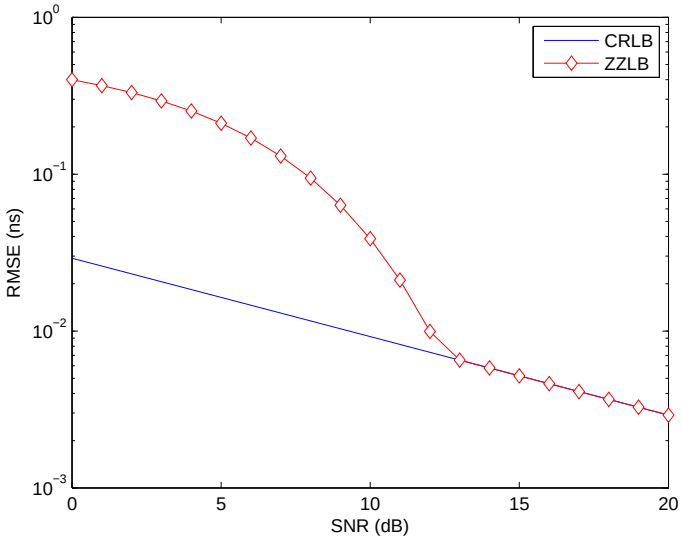

(b)

Figure 5.14: (a) ZZLB and CRLB (cm) for range estimation in a BAN channel for seventh order Gaussian pulse. and (b) ZZLB and CRLB (ns) for range estimation in a BAN channel for seventh order Gaussian pulse.

In order to obtain results for the TOA bounds using realistic BAN channels, the ZZLB was simulated using a semi-analytic simulation approach with the IEEE 802.15.6a UWB BAN channel model. The resulting ZZLB for suboptimal template is shown in Figures 5.16(a) and (b) for $\tau_e = 10$ and 30 ps for distance and TOA bounds, respectively. Since the target SNR

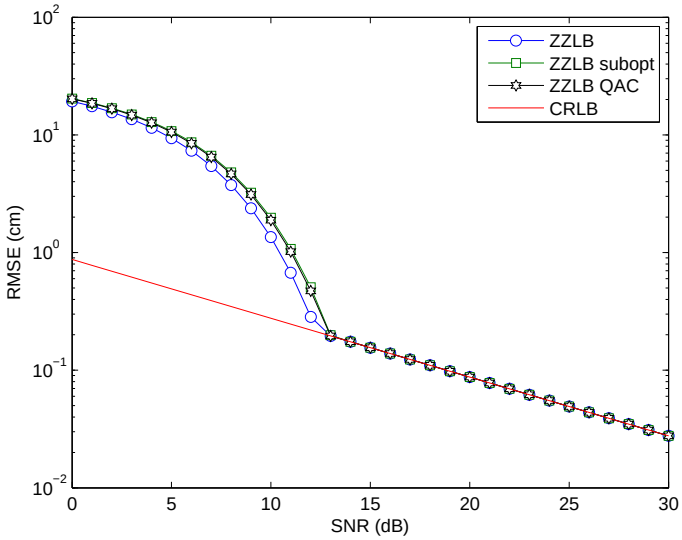

(a)

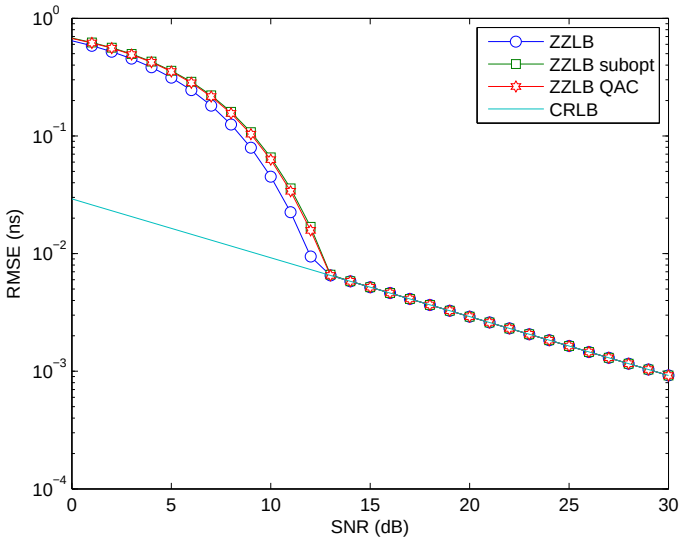

(b)

Figure 5.15: (a) ZZLB and CRLB (cm) for range estimation in a BAN channel for seventh order Gaussian pulse. and (b) ZZLB and CRLB (ns) for range estimation in a BAN channel for seventh order Gaussian pulse.

is within the high SNR region (at which performance approaches the CRLB), the effect of the allowable timing misalignment (10 ps) has no effect on the target SNR. More specifically, since our system is based on a 10 ps accuracy, as explained in Section 5.1, the simulated results for 10 ps represent the maximum expected template timing-misalignment. Even for

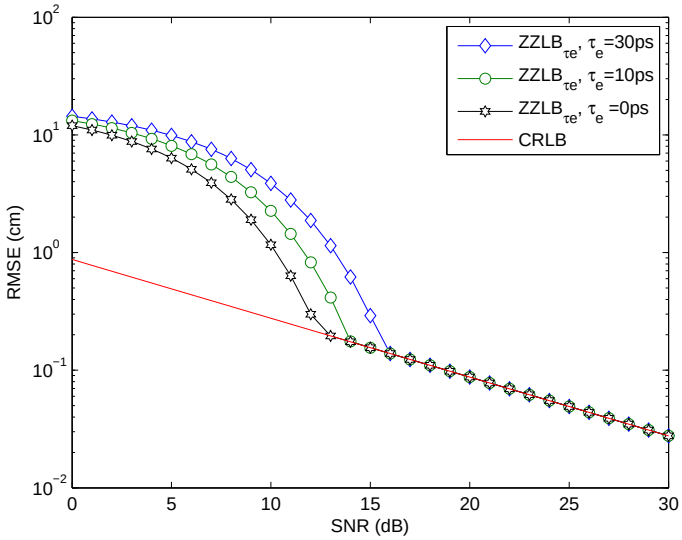

(a)

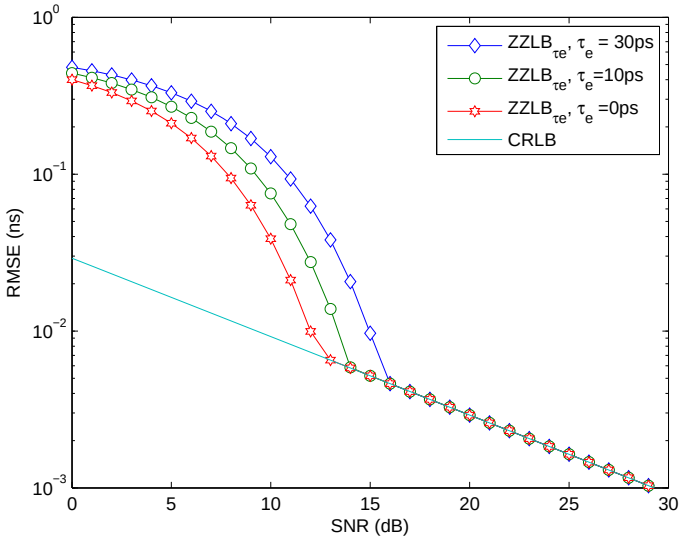

(b)

Figure 5.16: (a) ZZLB$_{\tau_e}$ (cm) for various values of timing mismatch τ_e in the IEEE 802.15.6a, assuming suboptimal template and seventh-order Gaussian pulse. and (b) ZZLB$_{\tau_e}$ (ns) for various values of timing mismatch τ_e in the IEEE 802.15.6a, assuming suboptimal template and seventh-order Gaussian pulse.

the 30 ps case, which exceeds the maximum expected timing misalignment, the 18 dB SNR requirement is sufficient for achieving a 1 mm target ranging accuracy. It is worth noting that even though the expected misalignment is 10 ps, which corresponds to 3 mm ranging

accuracy, by averaging ten successive TOA readings we obtain more accurate TOA estimates, where averaging works as interpolation. In [98], we show that for a 2 GHz seventh order Gaussian pulse with a transmit power P_t = - 8.3 dBm, 75.6 dB path-loss, and bit-rate R_b = 10 Kb/s, the achievable SNR is 40.5 dB. Thus, for a 10 Kb/s gait analysis system with a 2 GHz transmit pulse, and considering an additional 3 dB implementation loss, the 18 dB SNR requirement is achieved with a 19.5 dB link-margin [98].

5.4 Proposed Reference Range Correlation-based (RRcR) Technique

IR-UWB is a good candidate for low-power wireless sensor network applications. UWB systems have the potential for providing high ranging and positioning accuracies. However, the design of a highly accurate ranging system with low-power consumption is a challenging task, and has many implications. Particularly, ranging is based on determining the time-of-arrival (TOA) of the first-path. UWB channels are dense multi-path channels, in which the first-path is not necessarily the strongest, or may not be sufficiently separated from later-arriving paths, which makes the TOA estimation a challenging task.

Basically, TOA estimation is either performed by threshold-crossing (TC), also known as leading-edge (LE) detectors, or matched filtering-based (MF) estimators. In threshold-based approaches, the determination of the optimum threshold is critical, as it highly affects the system performance. A small threshold leads to increasing the probability of false alarm (detecting noise as the TOA), and large thresholds increase the probability of missing the direct-path. Both cases provide erroneous TOA estimates [75]. Typically, threshold design is based on the channel statistics, and due to the large number of available multi-path components and channel variations, this makes accurate and fast channel estimation a challenging task [27].

On the other hand, MF estimators determine the maximum value of the cross-correlation of the received pulse and a pre-stored template pulse. In absence of multi-path, a MF-based TOA estimator is the optimal estimator. In multi-path channels, the MF requires *a priori* knowledge of the received pulse. In that case, the maximum (MAX) selection criteria could be applied to determine the maximum output within a selected window. Absence of *a priori* channel knowledge makes the performance of MF-estimators suboptimal. Another concern related to MF-estimators is that they require very high-sampling rates for resolving the large number of available multi-path associated with UWB channels [27], [52], [105]. This requirement could be overcome by implementing the MF using a sliding-correlator, which reduces the sampling requirement to the pulse repetition frequency (PRF). Generally, ranging applications can have low PRFs compared to communication systems [34]. Transmitter receiver synchronization requirement of TOA-based ranging approaches adds another implication to the system design. Moreover, clock jitter is an important performance metric that needs to be considered while evaluating the accuracy of UWB ranging and positioning systems [75],

[96]. However, this should not be an issue in our system since they are all ultimately tied to the same on-body clock. From the achievable ranging accuracy point of view, energy detection (ED) estimators exhibit an error floor of $T_s/\sqrt{12}$ at high signal-to-noise ratio (SNR), where T_s is the integration window. On the other hand, stored-reference estimators, based on the MF, have a performance that approaches the Cramer-Rao lower bound (CRLB) at high SNRs [27].

There have been recent research trials trying to overcome the above mentioned implications associated with the design of highly accurate, but less-complex, UWB ranging systems. For instance, some techniques proposed using a piece of the received signal as the correlation template [72]. However, there is still a crucial need for new approaches suitable for emerging UWB applications (such as gait analysis), that are capable of providing high ranging accuracy at low-complexity and low power consumption [36].

This section proposes a reference range correlation (RRcR) technique for our proposed locomotion tracking system. This technique is ultimately suitable for on-body communications, and should be able to provide a higher ranging accuracy as compared to MF TOA estimators. Assuming a suboptimal template (windowed sinusoid) $v(t)$ in terms of the carrier frequency ω_c and window length T is defined as $v(t) = \cos(\omega_c t)$, where $-T \leq t \leq T$ [97].

The assumed transmit signal $s(t)$ with N_s time-hopping (TH) pulses $p(t) = p_n(t)$ is given by:

$$s(t) = \sum_{k=1}^{N_s} p\left(t - kT_f - c_k T_c\right) \tag{5.37}$$

where T_f and T_c are the frame and hop durations, respectively, and $c_k \in \{1, 2, 3, ..., N_s\}$ is the time-hopping code. The multi-path fading channel impulse response is represented as a series of impulses as:

$$h(t) = \sum_{l=1}^{L} \alpha_l \delta\left(t - \tau_l\right) \tag{5.38}$$

where, L is the number of paths, α_l and τ_l are the gains and delays, respectively, and $\tau_1 < \tau_2 < ... < \tau_L$ and $\sum_{l=1}^{L} \alpha_l^2 = 1$. The received signal after the effect of multi-path is $r_{mp}(t) = s(t) \bigotimes h(t) = \sum_{l=1}^{L} \alpha_l p_l\left(t - \tau_l\right)$, where $p_l(t)$ is the normalized received pulse at the l-th tap, and $\bigotimes$ denotes convolution. Received signal $r(t)$ at a distance $d = c.\tau_{toa}$, where c is the speed of light = 3.10^8 m/s [23], is:

$$r(t) = \sum_{k=1}^{N_s} r_{mp}\left(t - kT_f - kT_c - \tau_{toa}\right) + n(t) \tag{5.39}$$

where $n(t)$ is two-sided AWGN with variance $\sigma_n^2 = N_0/2$, and N_0 is noise power spectral density. The delay τ_{toa} is the TOA at the receive node. The correlator output in terms of

the template signal $v(t)$[4] with a sampling interval t_s [27]:

$$z_s = \int_{(n-s)t_s}^{(n-1)t_s+N_sT_f} r(t)v(t-(n-1)t_s)dt \tag{5.40}$$

Obviously, the sampling interval affects the output of the correlator, and consequently the TOA estimate. Considering power consumption constraints, we assume the use of an analog sliding-correlator as proposed in [31]. The sampling interval in analog correlation is represented as time-shift. In our system, we assume a sampling interval (time-shift) = 10 ps, similar to [31]. Sliding-correlator determines the TOA of the signal of the strongest path [27]:

$$r_s(t) = \sum_{k=1}^{N_s} r_{mp}(t - kT_f - c_kT_c - \tau_{peak}) \tag{5.41}$$

where, τ_{peak} is the TOA of the strongest path. It is worth noting that the strongest path does not necessarily represent the direct-path.

Generally, the UWB BAN channel is characterized by two clusters, with the first cluster due to the diffraction of propagating waves, and the second due to reflections from the ground [109]. These clusters are statistically independent, and typically the second cluster occurs between 7 and 10 ns after the first cluster [42]. Figures 5.17(a) and (b) shows two received on-body pulses at 6 in and 12 in spacings from the transmit antenna placed on the same side of the body, respectively. When transmit and receive antennas are placed on different sides of the body, ground reflections tend to be dominant [109], [42]. Intuitively, this is because of the presence of body parts that obstruct the line-of-sight (LOS) link between the transmit and receive antennas. According to [36], when a body limb obstructs the direct LOS link, an attenuation of up 20 dB occurs depending on the amount of first Fresnel zone obstruction. This obstruction causes the propagation wave to diffract around the obstructing body limb causing a pulse shape distortion. When the link is LOS, with no Fresnel zone obstruction, there is no pulse shape distortion [36]. In order to guarantee accurate TOA estimates for clinical gait analysis, target nodes, among which the distances are measured, need to have LOS links [98].

Inspired by the above mentioned properties of UWB BAN channel, and the high ranging accuracy required for accurate gait analysis, we propose a reference range correlation-based (RRcR) ranging algorithm, as depicted in Figure 5.18(a). We assume LOS links between target nodes guaranteed through the predefinition of LOS node regions [98]. The proposed algorithm assumes the presence of three nodes, namely transmit, receive and reference nodes. The reference range node (RRN) has a predetermined and fixed range. This node is used as a reference for the measured node. Assuming that both RRN and the node with unknown range exhibit the same channel (at least when considering paths arriving within the first $2T_p$ seconds), the RRN can be used for correcting the difference between the determined τ_{peak}

[4]Optimally, the template pulse $v(t)$ should be a clean version of the transmitted pulse $p(t)$. Another low-power alternative, is to use suboptimal templates, sinusoidal templates, that resemble the original pulse [97].

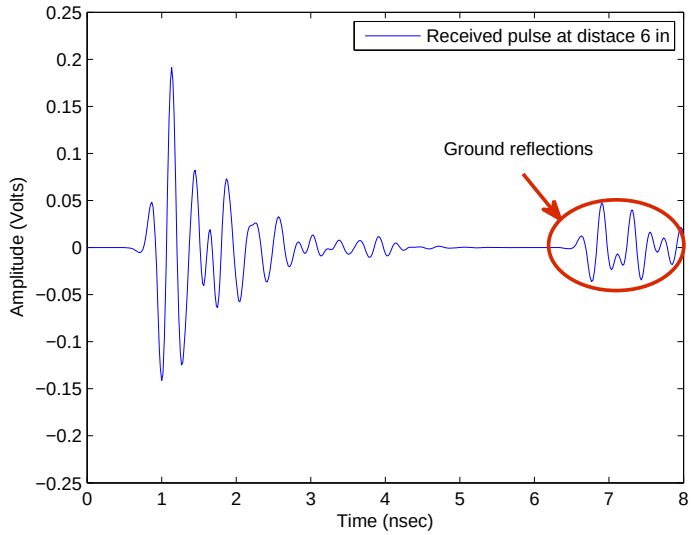

(a)

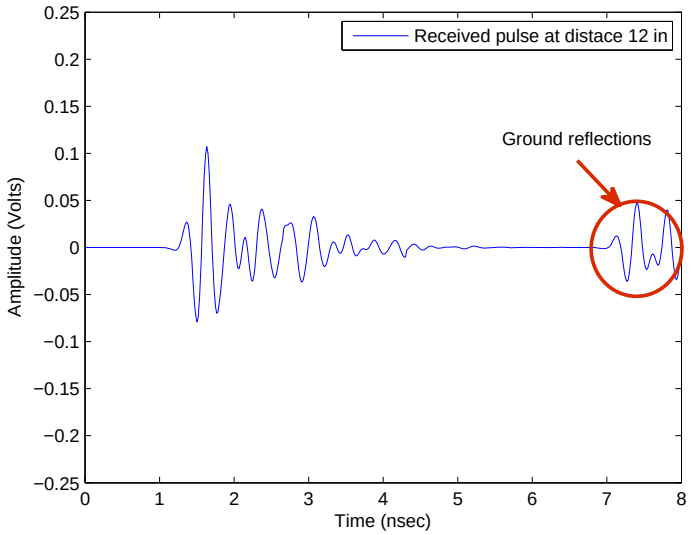

(b)

Figure 5.17: (a) Received on-body pulse at 6 in tx.-rx. antenna separation distance indicating ground reflections based on replicated measurement data. (b) Received on-body received pulse at 12 in tx.-rx. antenna separation distance indicating ground reflections based on replicated measurement data.

and the actual τ_{toa} of the direct-path. Figure 5.18(b) shows the output of an analog sliding-correlator based-on actual measurements taken at the MPRG labs[5]. It also shows τ_{peak} and

[5]Actual on-body measurements were taken at the Mobile and Portable Radio Research Group (MPRG)

τ_δ determination at the RRN node. The TOA estimation procedure of the proposed RRcR is as follows:

1. Calculate the matched-filter (MF) output at the RRN.
2. Estimate the corresponding $\tau_{peak_{ref}}$.
3. From the known d_{ref}, calculate the corresponding $\tau_{toa_{ref}}$.
4. Calculate $\tau_\delta = \tau_{peak_{ref}} - \tau_{toa_{ref}}$.
5. At the unknown range node, also calculate the MF output.
6. Determine the corresponding $\tau_{peak_{ij}}$.
7. Use the calculated τ_δ from the RRN to estimate the actual $\tau_{toa_{ij}}$ for this node.
8. Calculate $\tau_{toa_{ij}} = \tau_{peak_{ij}} - \tau_\delta$.

Figures 5.19(a) and (b) show the performance of RRcR compared to MF-estimator for both no-*a priori* channel information and perfect channel knowledge cases along with the corresponding ZZLB and CRLB for the case of optimal template (noise free Gaussian pulse) for TOA and distance estimators, respectively. As can be seen, RRcR shows substantial improvement over MF estimator with no-*a priori* channel knowledge, and approaches the performance of MF with perfect channel knowledge at high SNR. Same results are shown for the suboptimal template (windowed sinusoid) in Figures 5.20(a) and (b). Also, RRcR is studied and compared to the MF for actual clinical gait parameter, particularly for the heel-to-heel distance in Figure 5.21. A motion capture (MoCap) data file representing normal walking movement was obtained from [2]. This file was processed using MATLAB to extract the raw-marker data, and estimate the heel-to-heel distance in the IEEE 802.15.6a channel. Simulated results (along with the actual distances) are plotted for multiple gait cycles. From the plots we can see that RRcR closely approximates the true distance, and provides substantial improvement over MF estimator. Figures 5.22(a) and (b) show the histograms of mean-absolute-error (MAE) of RRcR and MF with suboptimal templates in the IEEE 802.15.6a channel at SNR = 21 dB. As shown, RRcR provides a 1 mm ranging accuracy compared to 3.76 cm for MF estimator, the latter agrees with the accuracy reported in [71] for MF estimator (120 ps accuracy = 3.6 cm).

It is worth noting that the performance gain achieved by the proposed RRcR is traded for having an extra reference node per body segment. According to the IEEE 802.15.6a, the power consumption should be 0.1 - 1 mW per node [38], so the extra reference node does not contradict with the power consumption constraints. Typically, the extra node will have an influence on the overall power consumption of the system if all nodes are assumed to be fed by a common battery source.

labs. Detailed measurement setup and results are presented in [98].

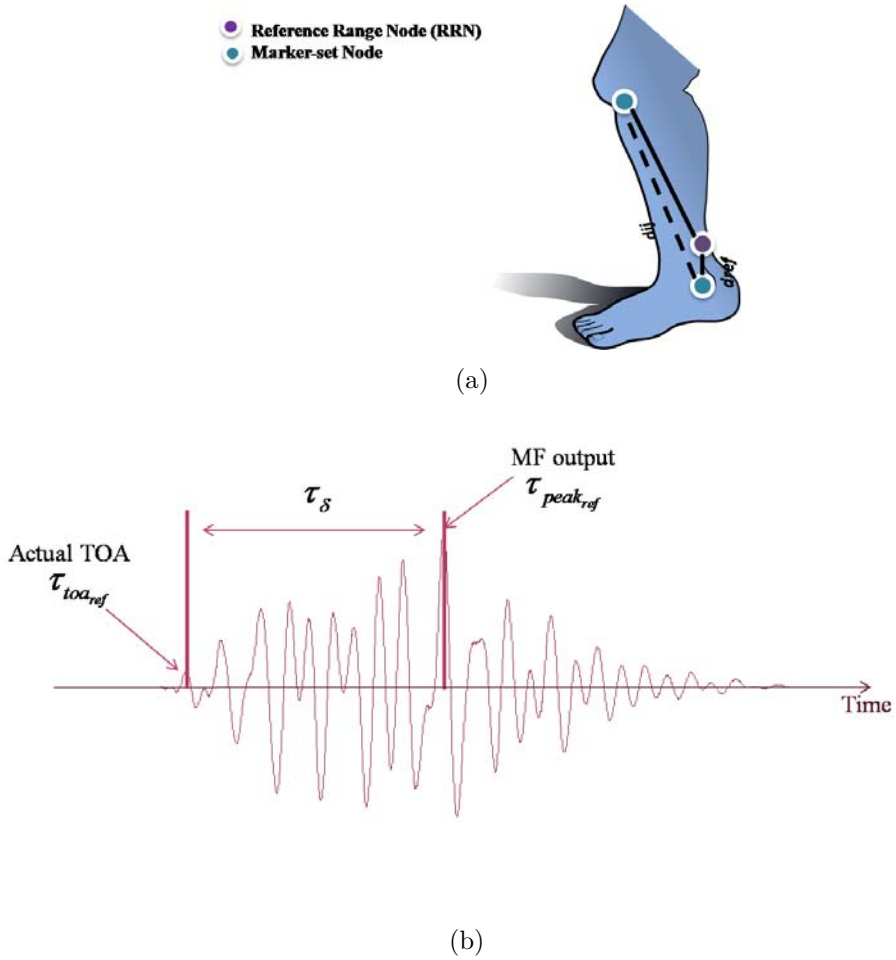

Figure 5.18: (a) Simplified schematic diagram of RRcR measurement setup. and (b) MF output depicting TOA estimation at RRN based on actual measurements.

5.5 Performance Comparison of Practical TOA Estimators

This section compares different TOA estimators provided in the previous sections. Figure 5.23 compares the performance of QAC and MF with real suboptimal templates in the IEEE 802.15.6a channel. According to the plots, the MF with real suboptimal template outperforms the corresponding QAC TOA estimator. Figure 5.24 extends the comparison to include MF with optimal templates. Clearly, the performance of MF with real suboptimal template approaches the performance of MF with optimal templates for all SNR values. The comparison is further extended to include the proposed RRcR approach. Figures 5.26(a) and (b) compare the performance of the proposed RRcR assuming optimal and suboptimal templates for the TOA and distance estimators, respectively. As shown, at low SNR both techniques approximately achieve the same performance. Whereas, at high SNR RRcR with

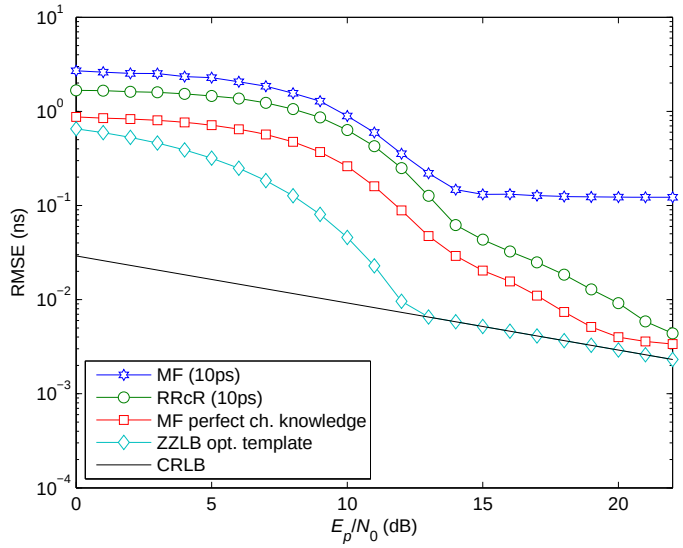

(a)

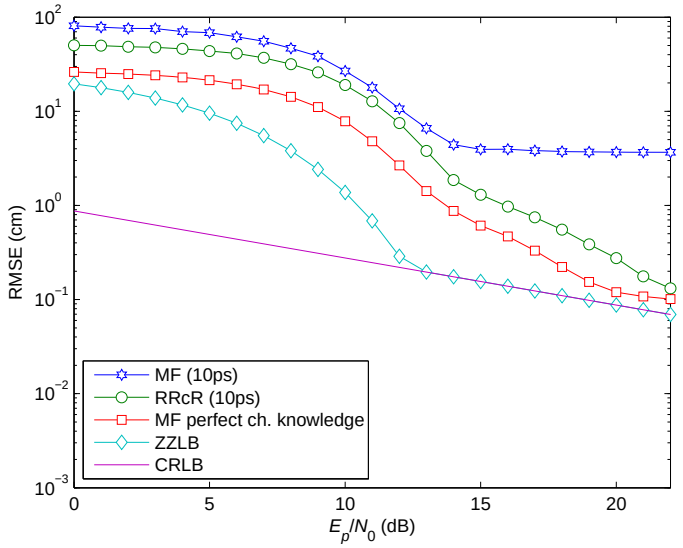

(b)

Figure 5.19: (a) Performance of proposed RRcR compared to MF without and with perfect channel knowledge, ZZLB, and CRLB (ns) in the IEEE 802.15.6a channel assuming optimal template pulse. and (b) Performance of proposed RRcR compared to MF without and with perfect channel knowledge, ZZLB, and CRLB (cm) in the IEEE 802.15.6a channel assuming optimal template pulse.

optimal template outperforms the corresponding RRcR with suboptimal template. Figure 5.25 depicts a comparison of different TOA estimators plotted along with the corresponding ZZLB bounds. Mainly, this figure compares the performance of QAC based detectors to

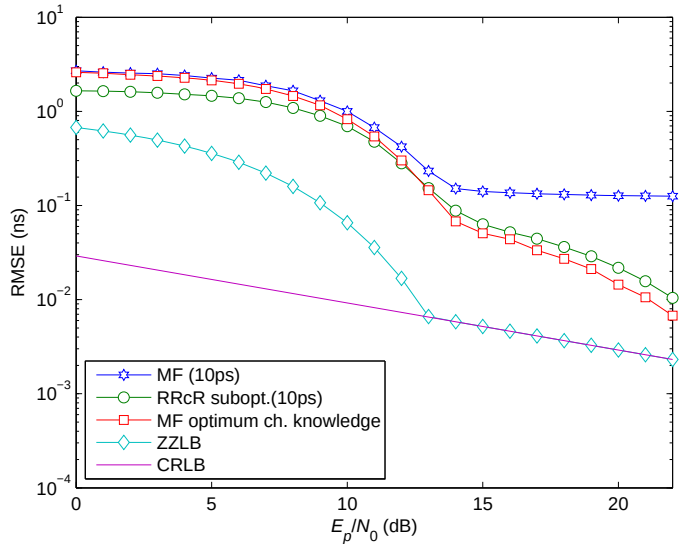

(a)

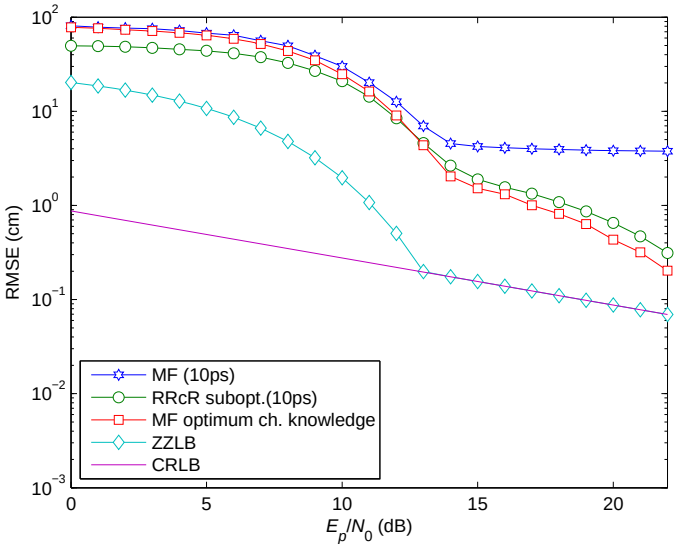

(b)

Figure 5.20: (a) Performance of proposed RRcR compared to MF without and with perfect channel knowledge, ZZLB, and CRLB (ns) in the IEEE 802.15.6a channel assuming suboptimal template pulse. and (b) Performance of proposed RRcR compared to MF without and with perfect channel knowledge, ZZLB, and CRLB (cm) in the IEEE 802.15.6a channel assuming suboptimal template pulse.

our proposed RRcR technique. Particularly, the QAC is compared to the proposed RRcR with real and complex suboptimal templates. As can be seen, the RRcR with complex suboptimal template substantially outperforms the corresponding QAR. Moreover, RRcR

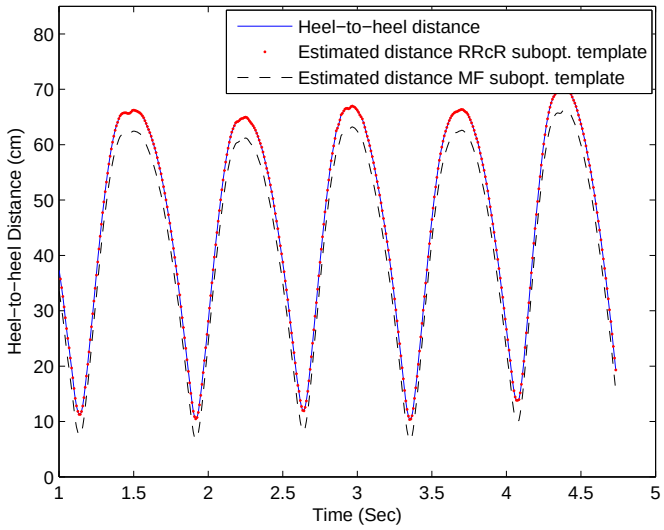

Figure 5.21: Heel-to-heel distance using RRcR and MF assuming suboptimal template in the IEEE 802.15.6a channel compared to actual distance obtained from Mocap file.

with real suboptimal template outperforms both estimators.

5.6 Link and Power Budgets Revisited

This section calculates the link and power budgets for our system based on actual design and implementation parameters. Now, almost all main design parameters related to performance and power of our system have been set, so it is quite convenient to estimate the link and power budgets based on these parameters.

5.6.1 Proposed System Link Budget

Generally, in our link and power budget calculations we choose the maximum expected values, and sometimes even higher values in order to have an upper bound on the expected values rather than exact values. For instance, in our link budget calculation we assume a path loss = 75.6 dB, where based in our assumed LOS links the path loss is expected to be $\approx$ 10 dB better than the selected value.

In order to be able to determine the available link margin (LM), we need to accurately estimate the effective bit-rate. This comes from the fact that even though our system's update rate is 1 Kb/s, we assume sleep time-slots in order to save power. So, we need to estimate the active time slot, and consequently the effective bit-rate. Table 5.1 summarizes

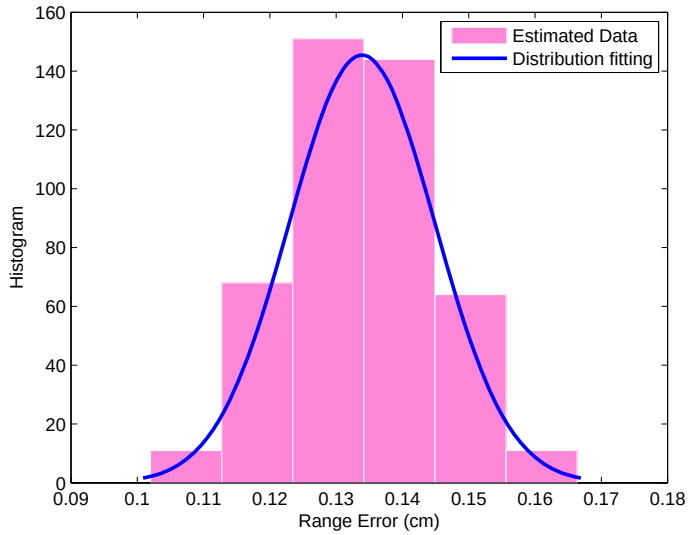

(a)

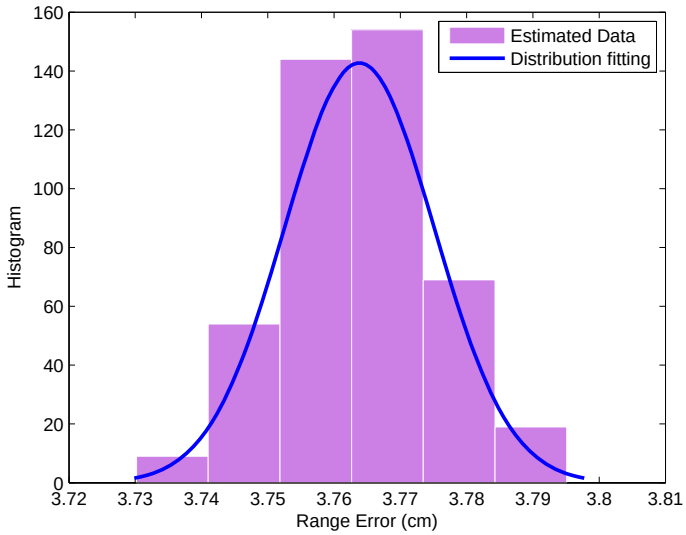

(b)

Figure 5.22: (a) Histogram of MAE of RRcR ranging approach with suboptimal template in the IEEE 802.15.6a at SNR = 21 dB. and (b) Histogram of MAE of MF approach with suboptimal template in the IEEE 802.15.6a at SNR = 21 dB.

the main link budget design parameters.

Now, we need to estimate the effective bit-rate in order to be able to estimate the available link margin. According to the above parameters, the received power is calculated as:

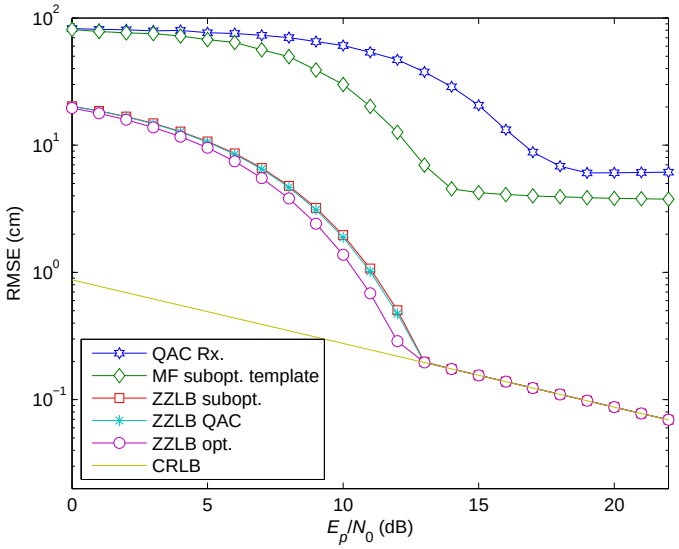

Figure 5.23: ZZLB along with performance comparison between QAC and MF with real suboptimal template in the IEEE 802.15.6a channel assuming seventh order Gaussian pulse.

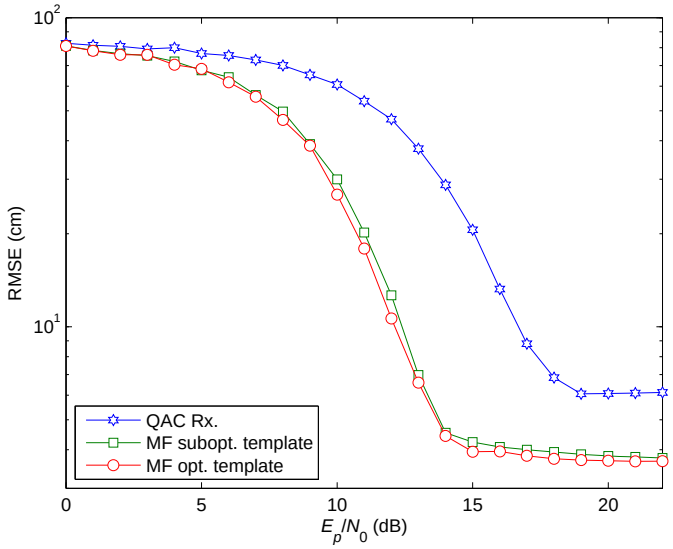

Figure 5.24: Performance comparison between QAC and MF with optimal and real suboptimal templates in the IEEE 802.15.6a channel assuming seventh order Gaussian pulse.

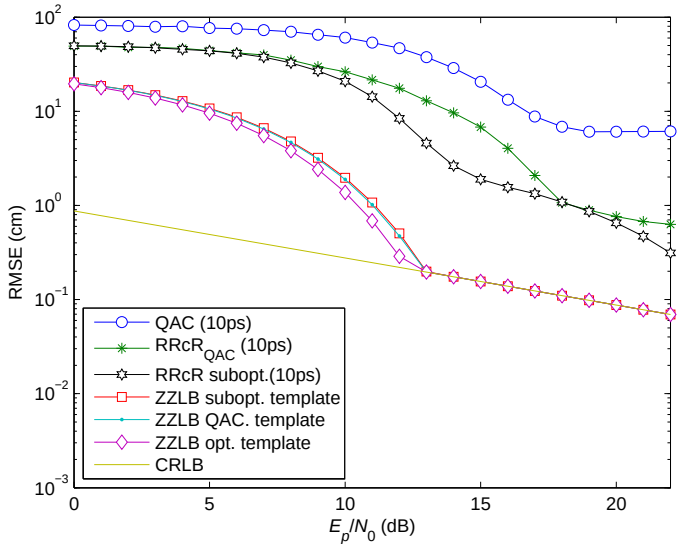

Figure 5.25: Performance comparison of different TOA estimators, namely QAC, RRcR with complex and real suboptimal templates, and ZZLB lower bounds in the IEEE 802.15.6a channel assuming the seventh order Gaussian pulse.

Table 5.1: Main Link Budget Parameters.

Parameter	Value
Pulse Rate (R_p)	50 Mp/s
P_t (transmitted power in dB relative to a W)	-8.3 dBm
$B.W._{\min}$ (bandwidth)	2 GHz
PSD(dBm/MHz)	-41.3 dBm/MHz
Receiver Noise Figure (N_F)	10 dB
N_0 (Noise PSD = kT_{sys})	-164.4 dBm/Hz
PL_0(path loss at reference distance (d_0))	44.6 dB
$PL(d)$(path loss at distance (d))	31 dB
PL_t(total path loss)	75.6 dB
G_t and G_r (Tx and Rx antenna gains)	0 dBi
Implementation Loss (L_a)	3 dB
Required $E_b/N_0\|_{\text{req}}$ (dB)	18 dB

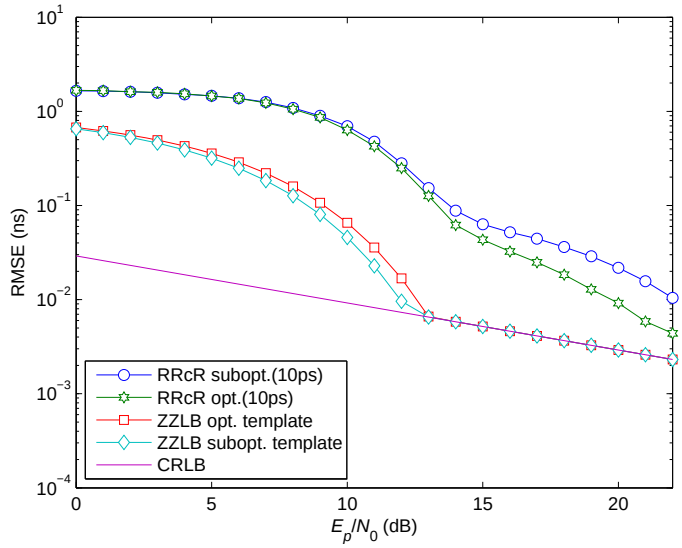

(a)

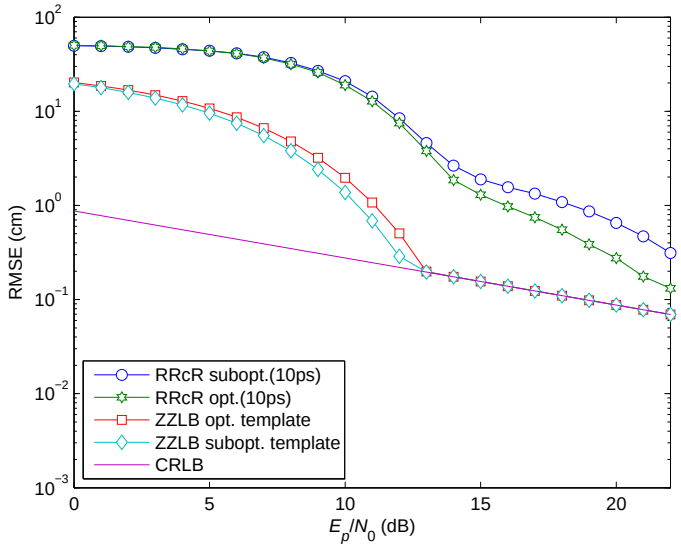

(b)

Figure 5.26: (a) ZZLB along with RRcR with optimal and suboptimal templates for the TOA estimator in the IEEE 802.15.6a channel assuming the seventh order Gaussian pulse. and (b) ZZLB along with RRcR with optimal and suboptimal templates for the distance estimator in the IEEE 802.15.6a channel assuming the seventh order Gaussian pulse.

$$P_R(d) = P_t - PL(d) + G_r + G_t = -8.3 - 75.6 + 0 + 0 = -83.9\text{dBm} \tag{5.42}$$

Noise power spectral density N_0 is:

$$N_0 = 10\log(kT_0) + N_F = -174.4 + 10 = -164.4\text{dBm/Hz} \tag{5.43}$$

Hence, the average noise power is calculated as:

$$P_N = N_0 + 10\log(R_b|_{\text{effective}}) \tag{5.44}$$

The corresponding link margin LM is calculated as:

$$LM = P_R(d) - P_N - \left(\frac{E_b}{N_0}\right)_{\text{req}} - L_a \tag{5.45}$$

$$LM = 59.5 - 10\log\left(R_b\right)_{\text{effective}} \tag{5.46}$$

The effective bit-rate is calculated as:

$$R_b|_{\text{effective}} = \left(\frac{\text{Active} - \text{Transmission} - \text{Slot}}{\text{frame} - \text{time}}\right) * R_p \tag{5.47}$$

Link margin in terms of the effective active transmission slot is calculated as:

$$LM = 59.5 - 10\log\left(\left(\frac{\text{Active} - \text{Transmission} - \text{Slot}}{\text{frame} - \text{time}}\right) * R_p\right) \tag{5.48}$$

Figure 5.27 shows the link margin calculation per node for our system. The link margin per node is 10 dB. Again, this value is calculated for a path loss = 75.6 dB. Typically, our system is expected to have a 10 dB performance gain compared to this value, which corresponds to 20 dB link margin. The link budget is summarized in Table 5.2 for an effective bit-rate = 90 Kb/s, based on a system range update-rate = 1 Kb/s.

5.6.2 Receiver Power Consumption

For the proposed gait analysis system, initially we assume 400 possible positions of correlation pulse peaks, which correspond to the maximum expected 4 nsec delay divided by the 10 ps step. Thus, for this stage, an ADC with 9 bits resolution and sampling frequency equivalent to PRF = 50 MHz is sufficient. The estimated power consumption is 98.45 mW, as summarized in Table 5.3.

In our calculations, we further perform TOA estimation ten-times, and take the average of these estimates. Essentially, averaging provides values that are not limited to the 10 ps resolution assumption. For instance, averaging 10 ps and 20 ps gives 15 ps, that would not have been attained by solely using the 10 ps limit. Thus, for our frame estimate, we need a higher resolution ADC compared to the one used after the sliding-correlator. Based on our simulations, the required number of bits is 16 bits. Since our design is based on sampling each node at a 500 KHz, the power consumption of a 16 bits ADC at 500 ksample/s rate is equal

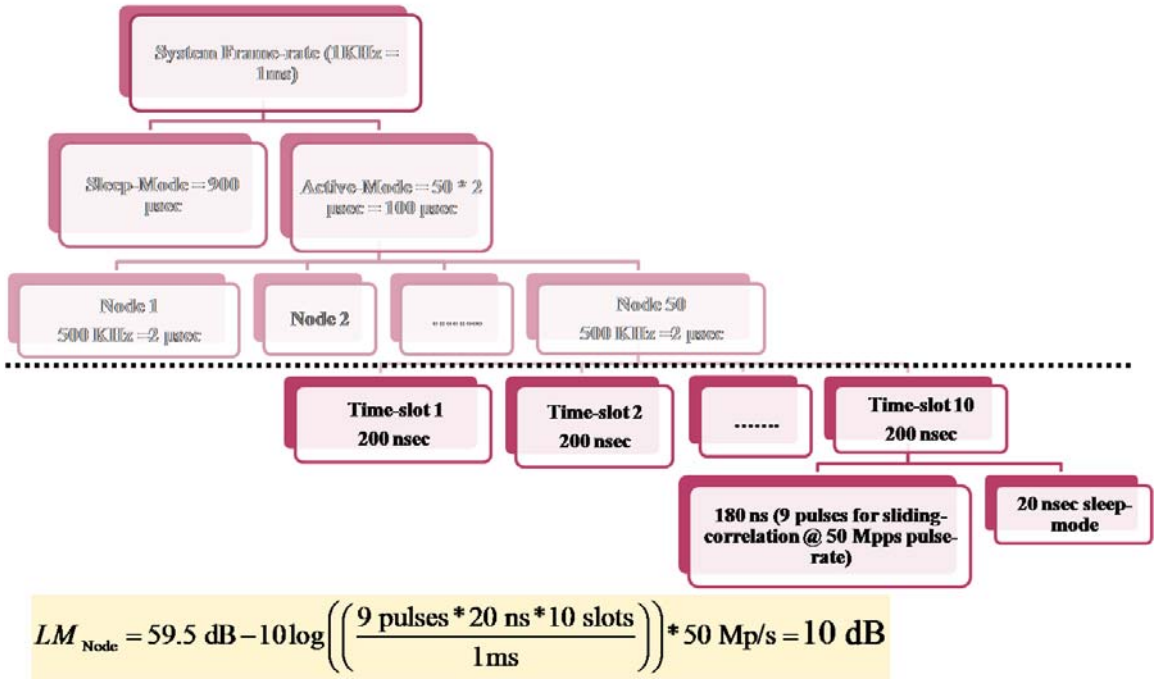

Figure 5.27: Link margin of the proposed system per node.

to 6.25 mW; based on the design provided in [29]. Adding this value to the estimated 98.45 mW, this gives 103.35 mW. Further assuming a 1% duty-cycle transmission, this corresponds to a 1.03 mW power consumption, which satisfies the target power consumption range. As was previously mentioned, we put an upper bound on the power consumption estimate. For instance, the second ADC (at 500 ksample/s) is not required to be an ADC, as the signal is already represented in the digital form.

5.7 Chapter Summary and Contributions

This chapter studied and compared different ranging approaches, proposed a ranging technique for our proposed system, derived theoretical lower bounds, and provided link and power budgets for the prosed system. Basically, different MF TOA estimators were studied and compared. Particularly, MF with optimal, real suboptimal, and complex suboptimal templates were studied and compared. MF with real suboptimal templates were shown to achieve a performance that approaches the performance of MF with optimal templates while saving power. These estimators were also shown to outperform the corresponding MF with complex suboptimal templates, or commonly known as QAC. Furthermore, the ZZLB on the system performance was derived for both real and complex suboptimal template-based estimators

Table 5.2: Link Budget for The Proposed System.

Parameter	Value
$B.W._{\min}$ (bandwidth)	2 GHz
P_t (transmitted power in dB relative to a W)	-8.3 dBm
PL_0(path loss at reference distance (d_0))	44.6 dB
$PL(d)$(path loss at distance (d))	31 dB
PL_t(total path loss)	75.6 dB
G_t and G_r (Tx and Rx antenna gains)	0 dBi
Receiver Noise Figure (N_F)	10 dB
Pulse Rate (R_p)	50 Mp/s
Implementation Loss (L_a)	3 dB
Average received power at the receiver (P_R)	-83.9 dBm
Average noise power (P_N)	-114.9 dBm (Eff. bit-rate $R_b = 90$ kb/s)
Achieved E_b/N_0	31 dB
Required $E_b/N_0\|_{\text{req}}$ (dB)	18 + 3 = 21 dB
Link Margin (LM)	10 dB
Receiver Sensitivity (S_r)	-93.9 dBm

Table 5.3: Power Consumption Summary.

	Power consumption	Ref.
LNA	12.6 mW	[94]
Correlator	31 mW	[31]
VCO+ PLL	7.6 mW	[94]
ADC	6.25 mW	[29]
Digital cct.	14 mW	[74]
Buffers	27 mW	[31]
Total Power (100% duty-cycle)	98.45 mW	
Total Power (1% duty-cycle)	< 1 mW	

in AWGN channel, and semi-analytic simulations were presented in realistic BAN channels. Moreover, the effect of timing-misalignment on the ZZLB was also studied, and was shown to be negligible on our proposed system for the expected 10 ps timing misalignment. Then, the proposed RRcR technique was studied, and was shown to provide substantial improvement over MF-TOA estimators without *a priori* channel knowledge, and approaches the performance of MF estimators with perfect channel knowledge. Performance comparisons supported the performance enhancement provided by our proposed ranging approach.

In order to be able to design a link budget for our proposed system, and estimate the link margin, it was necessary to estimate the effective bit-rate of our system. Investigation showed that for our target 1 Kb/s system update-rate, the effective bit-rate per node is 90 Kb/s. The corresponding link margin is 10 dB. We further showed that the estimated link margin is an underestimate, as we selected an upper bound for the path loss. Practically, our system is expected to have a 10 dB better path loss, and consequently the link margin is expected to be $\approx$ 20 dB at the target 1 mm ranging accuracy. Effective power consumption was shown to be $\approx$ 1 mW, which satisfies the IEEE 802.15.6a power consumption limit per node (0.1 - 1 mW per node).

Related Publications:

- H. Shaban, M. Abou El-Nasr, and R. M. Buehrer, "Performance of ultralow-power IR-UWB correlator receivers for highly accurate wearable human locomotion tracking and gait analysis systems," *IEEE Global Telecommunications Conference, GLOBECOM '09*, pp. 1–6, 30 Nov. - 4 Dec. 2009.
- H. Shaban, M. Abou El-Nasr, and R.M. Buehrer," Reference range correlation-based (RRcR) ranging for highly accurate wearable UWB motion tracking and movement analysis systems," *Submitted to IEEE Global Telecommunications Conference, GLOBECOM '10*.

Chapter 6

Localization

This chapter introduces the localization stage. Specifically, the proposed localization stage is divided into initial and core phases. The initialization stage is based on the linear least-squares (LS) localization approach, and assumes the presence of reference-nodes. Then, the core phase is based on classical multidimensional scaling (C-MDS) localization, where on-body communication starts to take place, and is performed without reference-nodes.

The organization of this chapter is as follows. Section 6.1 gives an overview of both the initialization and core measurement phases. Then, Section 6.2 introduces the proposed system initialization stage. Then, the arrangement of nodes is given in Section 6.3. The core measurement phase is presented in Section 6.4. Then, chapter conclusions and contributions are provided in Section 6.5.

6.1 Overview of Localization Stage

As was previously mentioned, in our system we assume two measurement phases, namely the initial and core phases. In the initial phase, we assume a low-complexity localization approach, linear least-squares (LS) with reference-nodes. Whereas for the core phase, we assume a more complex localization approach, namely the classical multidimensional scaling (C-MDS) localization approach with no reference-nodes. This is typically because at the initial stage we can have reference nodes, whereas at the core phase all nodes are mobile with no reference nodes. This makes it require a more complex localization technique for providing a high localization accuracy. Each localization stage is preceded by a ranging stage with a ranging accuracy dependant upon the system requirements at that stage, as will be described in further details later. Figure 6.1(a) shows a simplified schematic representation of the proposed system, and Figure 6.1(b) shows a block diagram of the ranging and localization stages. Specifically, we assume that the localization data processing is performed at an off-body centralized node (typically a PC).

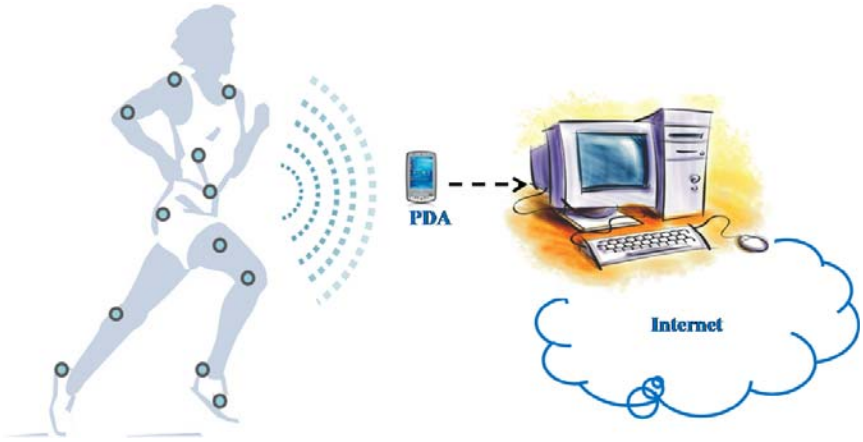

(a)

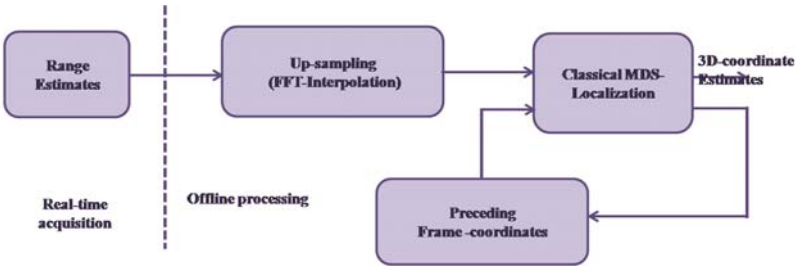

(b)

Figure 6.1: (a) Schematic representation of the proposed system. and (b) Block diagram of the ranging and localization procedures of the proposed system.

6.2 Initial Measurement Phase

For our system's initialization stage, we assume averaging multiple range measurements in order to obtain a high ranging accuracy, and consequently a high positioning accuracy. Furthermore, during system initialization we assume that the subject does not move, so that the initial coordinates of all nodes are accurately determined. After initialization, the subject is allowed to move, where on-body range measurements start to take-place. In order to accurately determine the coordinates of the initial-frame, we further assume the presence of eight reference-nodes grouped into two node groups with four nodes (rectangles) in each group with fixed and predetermined dimensions. The initialization setup of is depicted in Figure 6.2. We assume that each of the two groups of nodes is fixed on a pad with fixed dimensions, and the test subject stands on the mid-point between the two groups. This approach guarantees an accurate system setup, as well as direct LOS links between on-body nodes and each of the reference-nodes. Particularly, each of the two four-node groups is responsible for one side of the body, and each of the on-body nodes transmits signals to each of the four reference off-body nodes to measure the TOA at a preassigned time-slot. Typically, the on-body nodes are synchronized through wire connections. We assume a

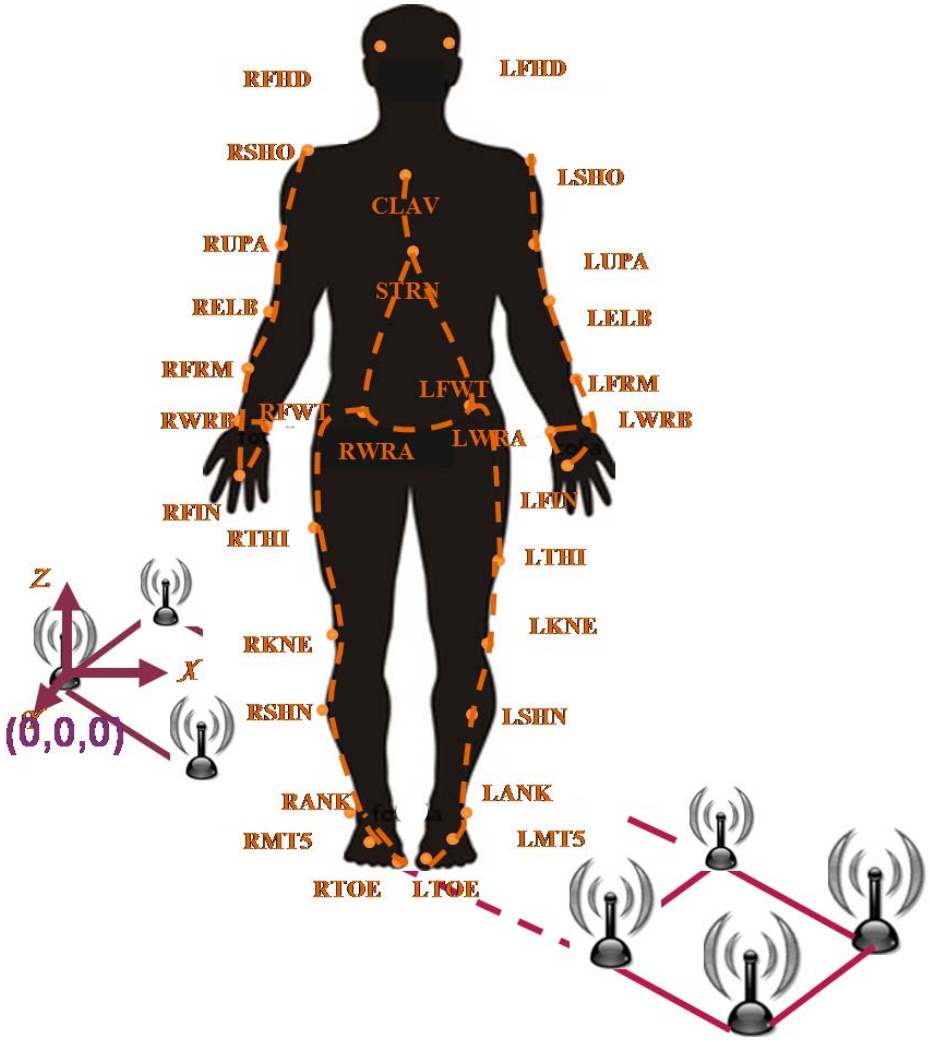

Figure 6.2: Schematic representation of the nitial measurement phase of the proposed UWB-WWGA system.

minimal number of wires to guarantee freedom of movement, as illustrated in Figure 6.3. Similarly, reference nodes are synchronized through wire connections. In order to synchronize on-body nodes and reference-nodes, we assume a wire connection between the pad, where the reference nodes are fixed, and the on-body nodes through a plug. This plug is connected during the system initialization, and is removed afterwards.

The structure of the symbol super-frame of the initial phase is illustrated in Figure 6.4. As can be seen, we assume that the system initialization is subdivided into initial and subsequent frames. The initial frame requires 0.14 seconds and 2e4 subsequent frames each of which is 1 ms. This leads to an overall system initialization of 20.14 seconds. In the initial-frame of the system initialization procedure, depicted in Figure 6.5, we assume an active time per node of 2.8 ms, which is subdivided into ten time-slots. At each time slot, twenty pulses

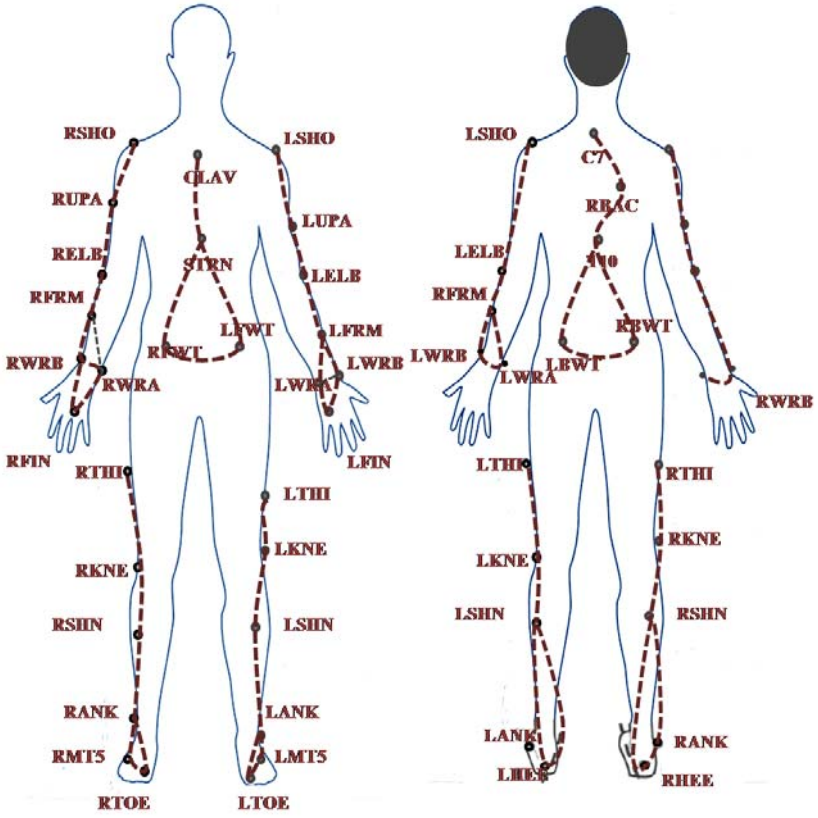

Figure 6.3: Wire connection of nodes to guarantee synchronization while maintaining freedom of movement.

are averaged in order to obtain a processing gain, as well as higher ranging and positioning accuracies. Then, these ten time slots are averaged in order to obtain a finer range estimate. This initial-frame is followed by 2e4 subsequent-frames, as shown in Figure 6.6. After the acquisition of the TOA of the initial-frame, subsequent-frames do a fine tracking of acquired TOA values. Particularly, at each subsequent-frame we search over five samples around the previous TOA to determine the current peak. This provides us with the TOA offset w.r.t. the preceding value. We also assume averaging of twenty pulses per TOA estimate for subsequent-frames. The resulting ranging error of the system initialization stage is depicted in Figure 6.7. These obtained ranges are further employed in a linear least-squares (LS) localization approach, which is typically performed at an off-body centralized node.

Generally when precise localization is required, linear-LS localization could be used for obtaining an initial value for initializing the high accuracy localization system [46]. So, we use linear LS as an initial solution to a more complicated approach, the C-MDS localization approach. As mentioned above, we assume four reference nodes, and the target is to estimate the three-dimensional positions of the on-body nodes. Based on the acquired TOA estimates d_{ij}, the linear-LS technique is as follows [46], [35], [51]:

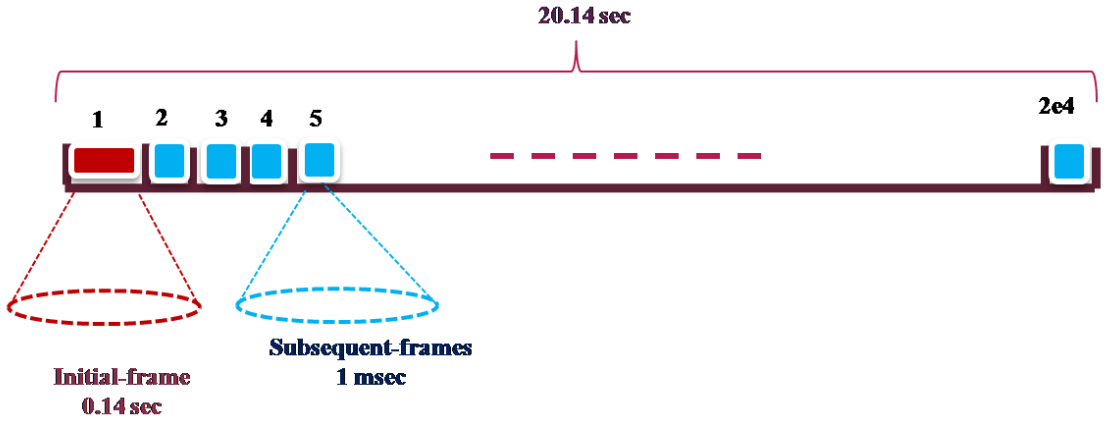

Figure 6.4: Super-frame symbol structure of the initial measurement phase.

$$d_{ij}^2 = \sqrt{(x_i - x_j)^2 + (y_i - y_j)^2 + (z_i - z_j)^2} \tag{6.1}$$

$$\mathbf{AX} = \frac{1}{2}\mathbf{p} \tag{6.2}$$

where, $\mathbf{X_i} = \begin{bmatrix} x_i & y_i & z_i \end{bmatrix}^T$

$$\mathbf{A} = \begin{bmatrix} x_1 - x_k & y_1 - y_k & z_1 - z_k \\ x_2 - x_k & y_2 - y_k & z_2 - z_k \\ \vdots & \vdots & \vdots \\ x_N - x_k & y_N - y_k & z_N - z_k \end{bmatrix} \tag{6.3}$$

$$\mathbf{p} = \begin{bmatrix} d_{1i}^2 - d_{ki}^2 - x_1^2 + x_k^2 - y_1^2 + y_k^2 - z_1^2 + z_k^2 \\ d_{2i}^2 - d_{ki}^2 - x_2^2 + x_k^2 - y_2^2 + y_k^2 - z_2^2 + z_k^2 \\ \vdots \\ d_{Ni}^2 - d_{ki}^2 - x_N^2 + x_k^2 - y_N^2 + y_k^2 - z_N^2 + z_k^2 \end{bmatrix} \tag{6.4}$$

The position of the target-node is estimated as [46], [51]:

$$\hat{\mathbf{X}} = \frac{1}{2}\left(\mathbf{A}^T\mathbf{A}\right)^{-1}\mathbf{A}^T\mathbf{p} \tag{6.5}$$

The mean-square-error (MSE) on the estimated coordinate is given by [51]:

$$\text{MSE} = \text{Tr}\left\{\text{Cov}(\hat{\mathbf{X}})\right\} \tag{6.6}$$

where, $\text{Tr}(\mathbf{X})$ is the trance of a matrix $\mathbf{X}$ and $\text{Cov}(\hat{\mathbf{X}})$ is the covariance.

In the absence of ranging error, the linear-LS technique finds a unique solution and an exact position estimate [46], [35], [51]. Figure 6.8(a) shows triangulation in the absence

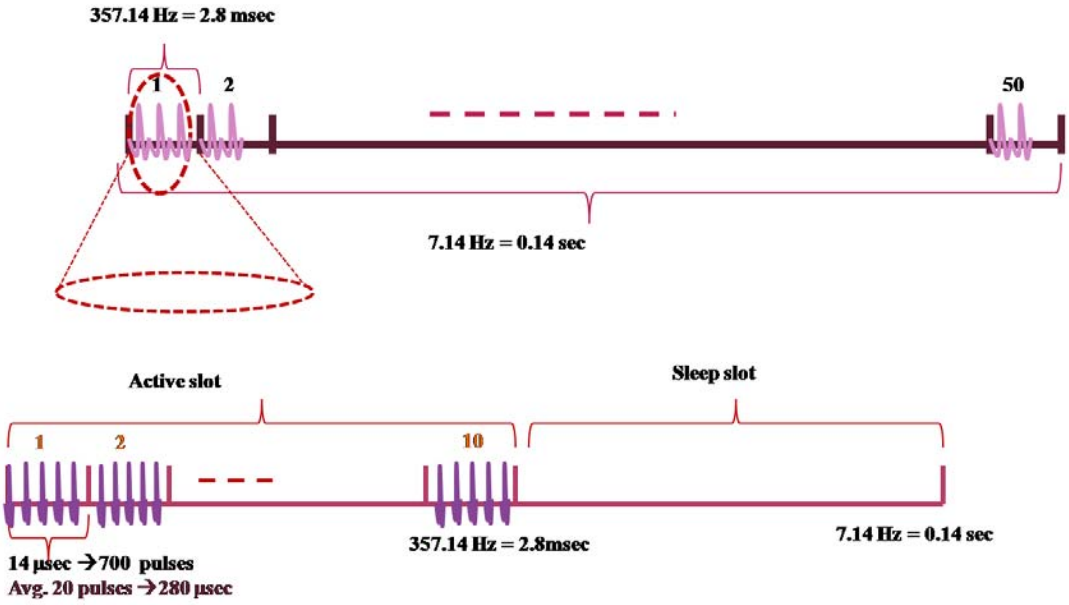

Figure 6.5: Initial-frame symbol structure of the initial measurement phase.

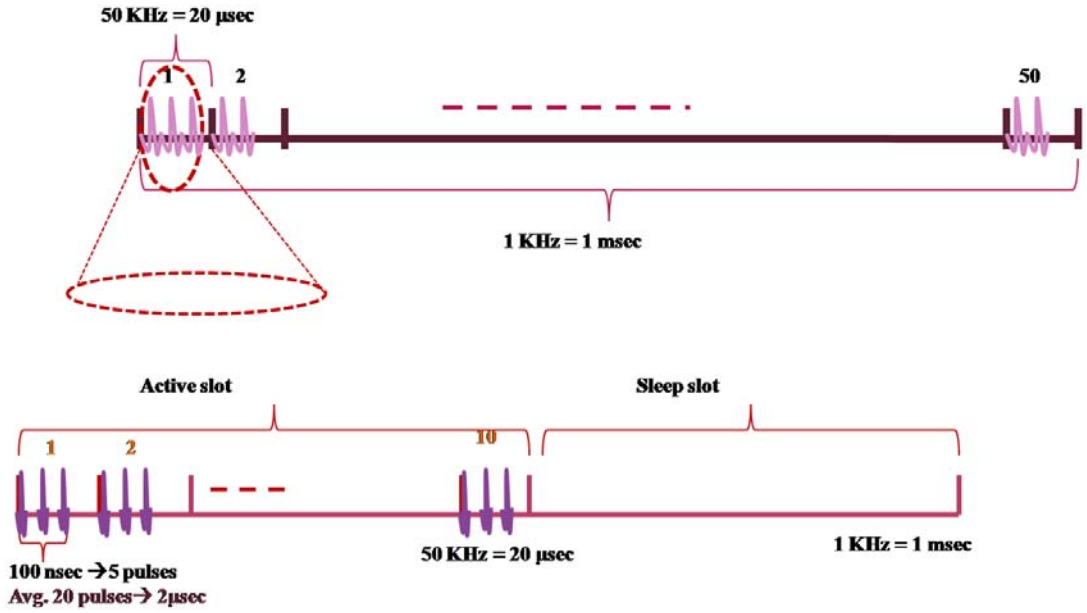

Figure 6.6: Subsequent-frames symbol structure of the initial measurement phase.

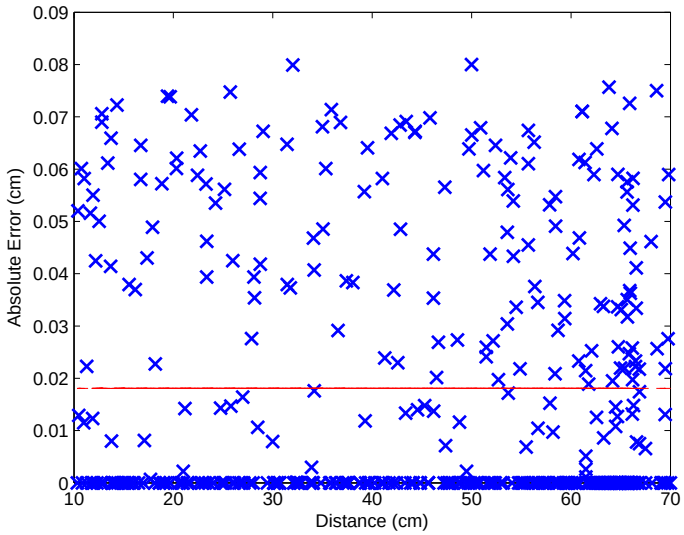

Figure 6.7: Absolute error versus distance for our proposed system initialization stage.

of ranging error, which leads to an accurate determination of target-node location. In the presence of ranging error, triangulation leads to multiple intersections of reference nodes' circles. The LS technique finds the solution which minimizes the distance to the different ranging circles, which leads to erroneous estimated position in the presence of ranging error, as depicted in Figure 6.8(b).

The proposed system initialization procedure is summarized in Figure 6.9. The achievable localization accuracy of our proposed system initialization is 0.247 mm. Figures 6.10 (a) and (b) show the estimated positions plotted along with the actual node positions for MoCap data files representing normal-walking and boxing, respectively.

6.3 Node Arrangement

Generally, gait analysis is based on markers located according to a standard arrangement, termed marker-set. There are several standardized marker-sets like Helen Hayes, modified Helen Hays, and Vicon marker-sets. These marker sets are typically based on substantial work for developing sets that track each segment taking into consideration the degrees of freedom (DOF) associated with the movement of each segment [8].

We assume using standardized marker-sets. In order to guarantee LOS links during movement, we predetermine the groups of nodes that have this property, as depicted in Figure 6.11 assuming the Vicon marker-set. Typically, we need four nodes in order to be able to determine the three dimensional positions. So, we use the three nodes that are typically using per segment in addition to a node from a neighboring body segment, such

(a)

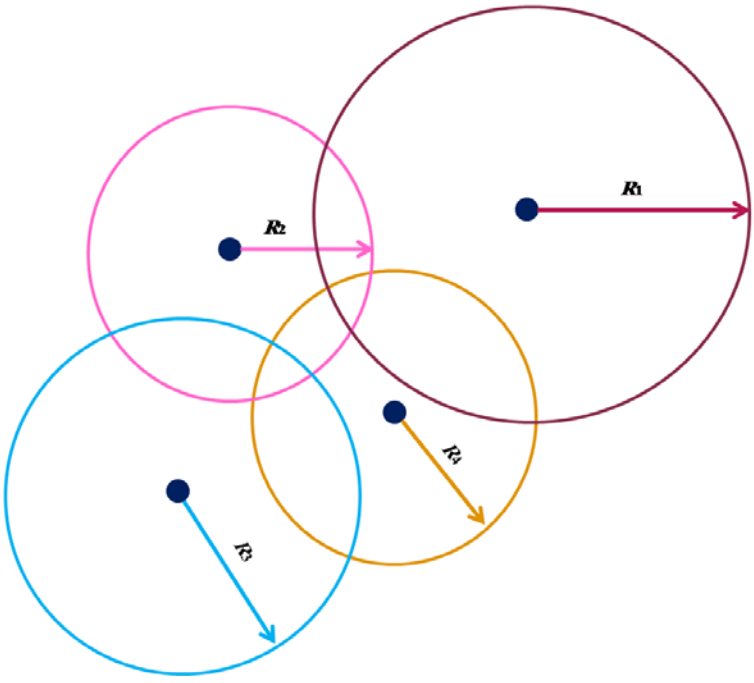

(b)

Figure 6.8: (a) Triangulation in absence of ranging error. and (b) Triangulation in the presence of ranging error.

Proposed Initialization Procedure

- Use two fixed squares of four nodes with known relative locations.
- One square is for the front-side and the other for the back-side of the body.
- The separation distance between the two squares is also fixed, and the subject stands on the midway point.
- Transmit nodes are the body attached nodes (markers), and the receive nodes are the off-body nodes.
- Use least-squares (LS) localization for obtaining the initial positions of all nodes (one at a time) calculated w.r.t the reference-nodes.
- Once the initial-frame coordinates are obtained, the reference nodes are removed.
- Subsequent-frames use classical multidimensional scaling (C-MDS), and the preceding frame as a reference-frame

Figure 6.9: Proposed system initialization procedure.

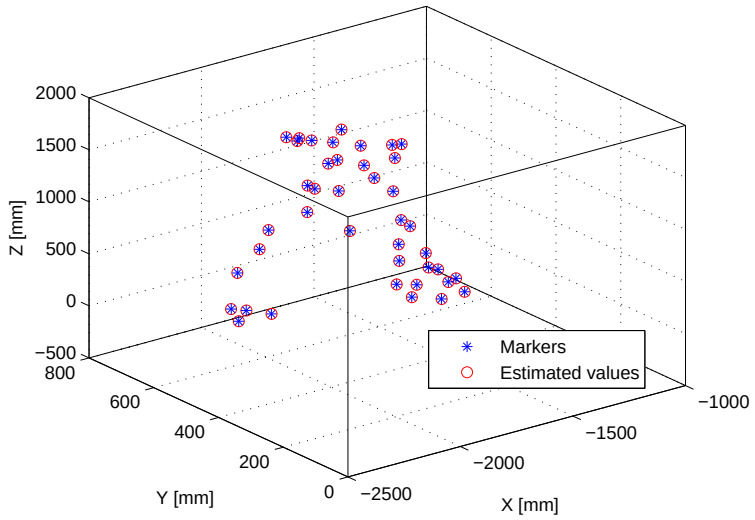

(a)

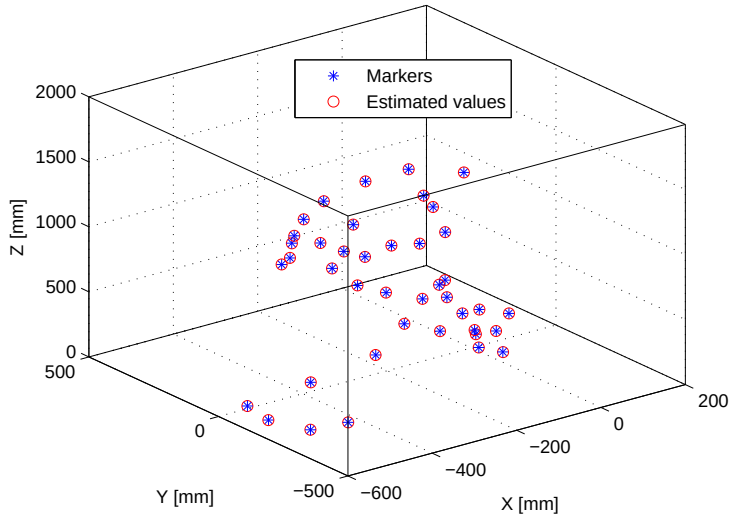

(b)

Figure 6.10: (a) Actual markers (Vicon marker-set) compared to the estimated node positions using linear-LS localization for a normal-walking MoCap file. and (b) Actual markers (Vicon marker-set) compared to the estimated node positions using linear-LS localization for a boxing MoCap file.

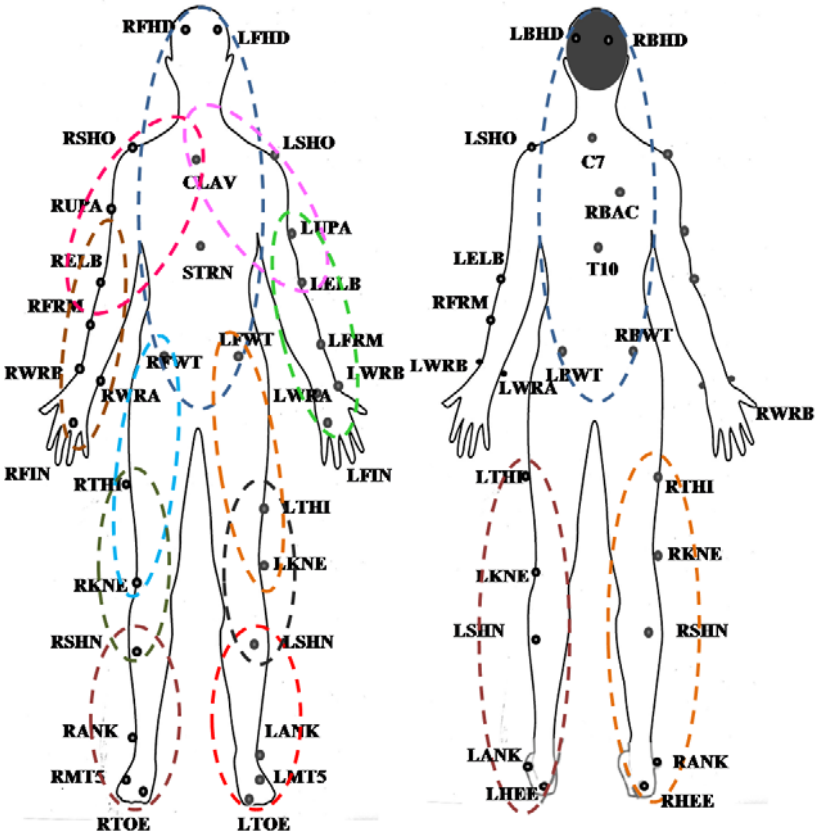

Figure 6.11: Illustration of node grouping into LOS regions assuming the Vicon marker-set.

that the node on this segment has a LOS link with the node of interest during movement. For instance, the nodes attached the the leg-calf have LOS connections with the corresponding nodes on the thigh segment of the same leg.

6.4 Core Measurement Phase

Multidimensional scaling (MDS) includes a family of methods. Scaling refers to the methods that construct a configuration of points in a target metric space from the information about the inter-point distances, and is referred to as MDS when the target space is Euclidean. C-MDS is the simplest form of MDS, and when the reference absolute frame is available it gives a unique solution for the estimated coordinates. Otherwise, the result from MDS could be a translated, rotated, and scaled version of the actual set, as depicted in Figure 6.12. This is essentially because of the absence of the absolute coordinate reference [21].

An $m \times m$ matrix $\mathbf{D}$ consisting of squared distances d_{ij}^2, where $m = 4$ nodes for a three-dimensional absolute coordinate system. To recover the $m \times d$ matrix $\mathbf{X}$ of positions in

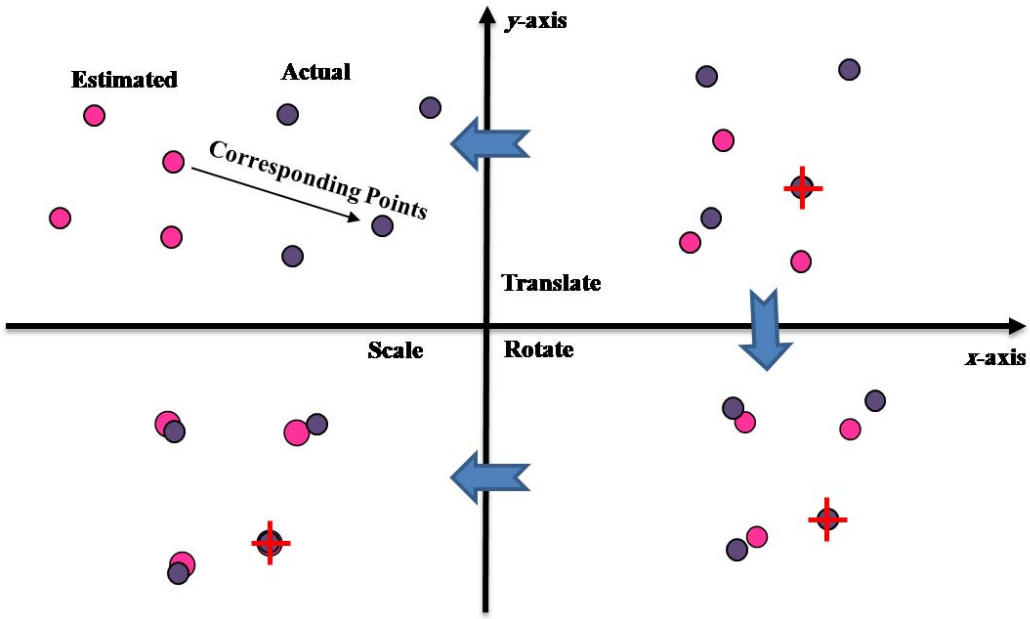

Figure 6.12: Mapping points using translation, rotation, and scaling.

d-dimensional space; three-dimensional space in our case, $\mathbf{D}$ is expressed as [21]:

$$\mathbf{D} = \begin{pmatrix} 0 & d_{12}^2 & d_{13}^2 & d_{14}^2 \\ d_{21}^2 & 0 & d_{23}^2 & d_{24}^2 \\ d_{31}^2 & d_{32}^2 & 0 & d_{34}^2 \\ d_{41}^2 & d_{42}^2 & d_{43}^2 & 0 \end{pmatrix} \tag{6.7}$$

where, d_{ij} is defined in terms of the absolute coordinates x_i and x_j as [21]:

$$d_{ij}^2 = (x_i - x_j)^2 = x_i^2 - 2x_i x_j + x_j^2 \tag{6.8}$$

The elements b_{ij} of the dot-product matrix $\mathbf{B} = \mathbf{X}\mathbf{X}'$ are defined as follows [21]:

$$b_{ij} = d_{ki} d_{kj} \cos(\alpha) \tag{6.9}$$

where α is the angle between d_{ki} and d_{kj}, as shown in Figure 6.13. Singular Value Decomposition (SVD): the scalar products matrix $\mathbf{B}$ formed from the elements b_{ij} is a symmetric matrix. The SVD of $\mathbf{B}$ gives [21]:

$$\mathbf{B} = \mathbf{U}\mathbf{V}\mathbf{U}' \tag{6.10}$$

where, $\mathbf{V} = \text{diag}\{\lambda_1, \lambda_2, ..., \lambda_n\}$ is a diagonal matrix of eigenvalues of $\mathbf{B}$ with $\lambda_1 \geq \lambda_2 \geq ... \geq \lambda_n \geq 0$, and $\mathbf{U} = [u_1, u_2, ..., u_n]$ is an orthogonal matrix with columns equivalent to the eigenvectors [21]. Since, $\mathbf{B}$ is a symmetric positive definite matrix, the rank of $\mathbf{B}$ is equal to the dimensionality of $\mathbf{D}$ (i.e., the number of positive eigenvalues) [21]. Hence,

$$\mathbf{X} = \mathbf{U}\mathbf{V}^{1/2} \tag{6.11}$$

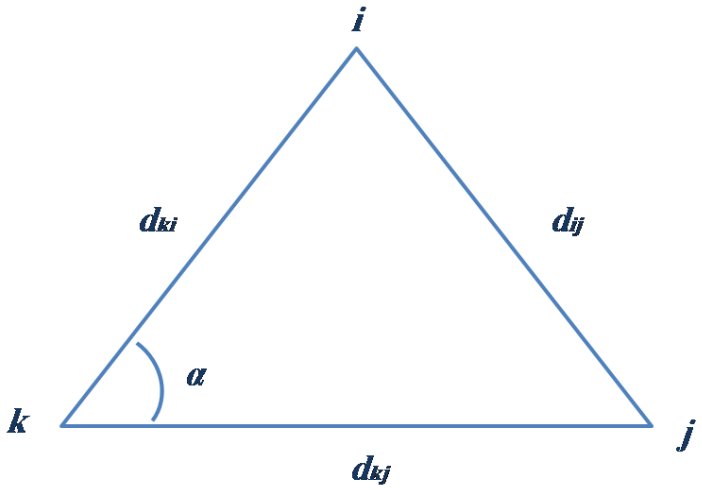

Figure 6.13: Law of cosines.

In our system, we consider C-MDS, and overcome the problem of the missing reference coordinates by using preceding frames as reference-frames, and obtain the initial-frame coordinates from the initial range measurement phase of our system [98]. We further increase the accuracy of estimated coordinates by using FFT interpolation after the ranging stage. This interpolation is performed in time (frame-to-frame). The detailed procedure of the localization stage associated with our system is depicted in Figure 6.14. The localization approach was also investigated based on real MoCap data obtained from [112] in the IEEE 802.15.6a channel using Monte Carlo simulations. Particularly, the ranges obtained from the preceding stage, with 1 mm ranging error, were applied to the localization procedure described in Figure 6.14 for various motion speeds and types. Specifically, it was applied to normal and abnormal walking, running, boxing, and ballet dancing. The resulting mean absolute three-dimensional (3D) localization error was 0.47 mm with $\pm$ 52 μm variations among the different files. This accuracy is better than the accuracy for current technologies, with millimeter and sub-millimeter of up to $\approx$ 0.8 mm accuracies reported for the latter [9], [82]. The estimated positions are plotted along with the actual node positions in Figures 6.15 (a) and (b) for an arbitrary sample frame for MoCap data files representing boxing and normal-walking, respectively. Furthermore, the absolute error of the estimated positions of the node with the poorest results is plotted in Figure 6.16. Moreover, Figures 6.17(a) and (b) show the mean absolute error MAE of localization error plotted versus time frames obtained via simulations in the IEEE 802.15.6a channel for a boxing Mocap data file and the corresponding histogram, respectively. As can be seen, the MAE among the different frames follows a normal distribution.

C-MDS localization with FFT-interpolation

Initial-frame

1. Obtain ranges acquired through the initial-range-measurement phase.
2. Construct the initial-frame spatial coordinates with respect to a chosen on-body reference-point, and set other points according to this point.

Subsequent-frames

1. Compute the distance matrix **D** from the ranges acquired in the ranging stage.
2. Up-sample data using FFT interpolation.
3. Calculate the dot-product matrix **B**.
4. Find SVD of **B**.
5. Use the preceding-frame to current-frame as a reference-frame.
6. Apply basic transformations, rotation, translation, and scaling w.r.t reference nodes to obtain normalized absolute coordinates.

Figure 6.14: Application procedure of C-MDS localization with FFT-interpolation to the proposed system.

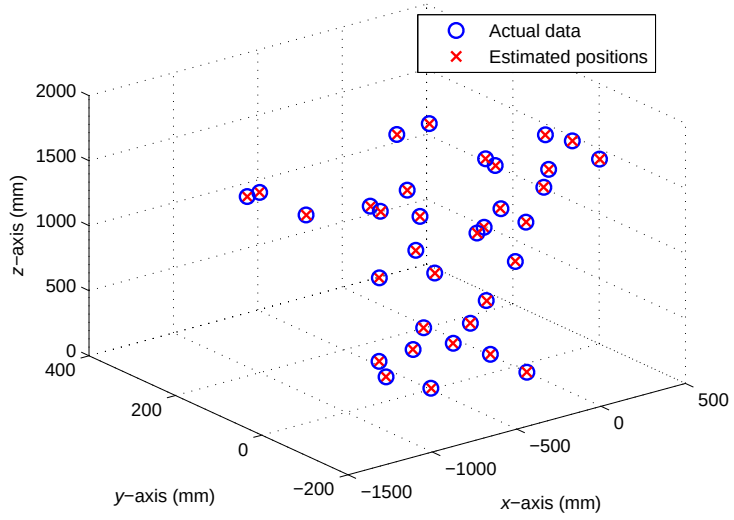

(a)

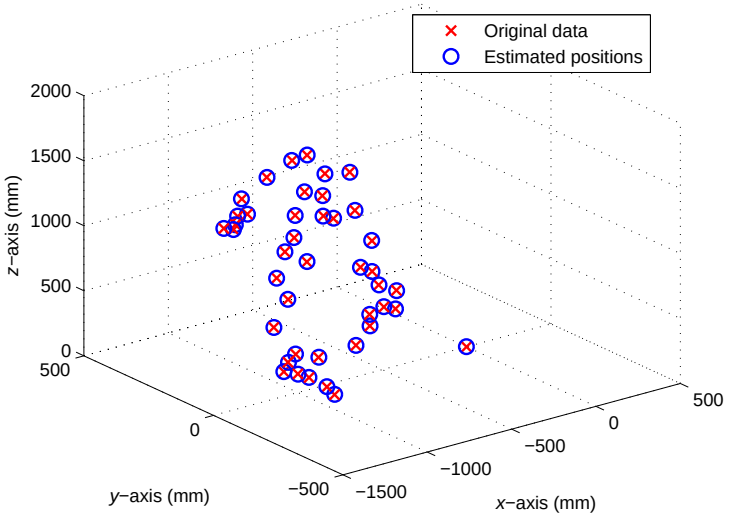

(b)

Figure 6.15: (a) Arbitrary sample-frame of a boxing MoCap file showing the actual markers (Vicon marker-set) compared to the estimated node positions using C-MDS localization with FFT-interpolation. and (b) Arbitrary sample-frame of a normal-walking MoCap file showing the actual markers (Vicon marker-set) compared to the estimated node positions using C-MDS localization with FFT-interpolation.

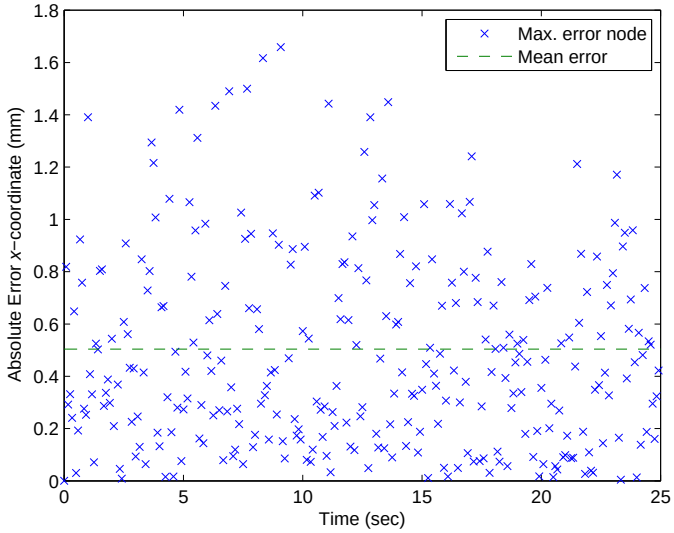

Figure 6.16: Absolute error for the maximum-error node in the x-direction.

6.5 Chapter Conclusions and Contributions

This chapter introduced the localization stage, and studied the employed localization techniques. It was shown that system initialization requires 20.14 seconds for a complete setup. The localization technique used at the system initialization stage is the linear-LS, and was

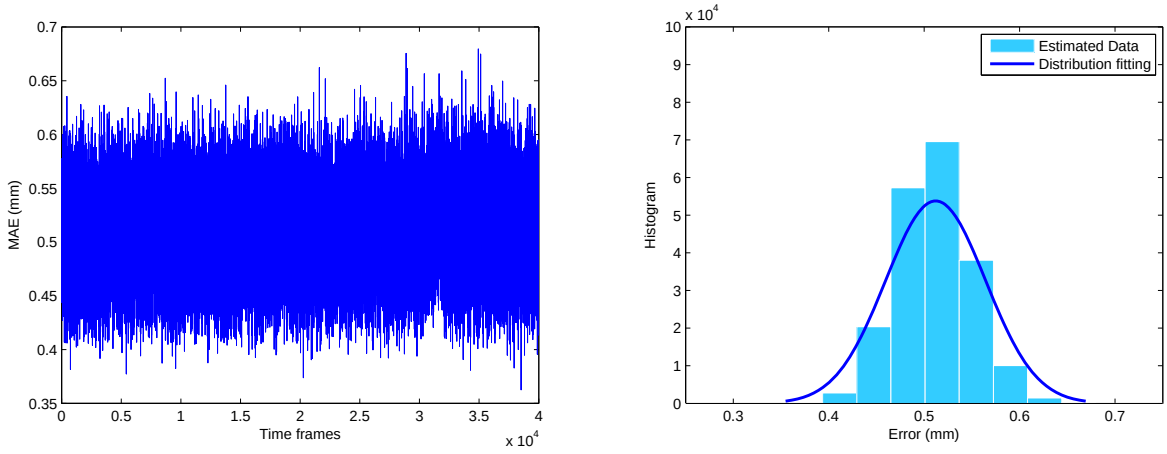

(a) (b)

Figure 6.17: (a) Mean absolute error versus time frames based on simulations for boxing MoCap data in the IEEE 802.15.6a channel. and (b) Histogram of mean absolute error over different time frames based on simulations for boxing MoCap data in the IEEE 802.15.6a channel.

shown to achieve an average positioning accuracy equal to 0.247 mm. The node arrangement and grouping of nodes into LOS regions were then provided. Then, the core measurement phase was studied. In this stage, we assumed using C-MDS localization approach preceded by an FFT interpolation. The achieved accuracy of acquired data during this stage was shown to be 0.47 mm $\pm$ 52 μm. Results were obtained via simulations in the IEEE 802.15.6a channel based on actual acquired MoCap data. Further results based on actual UWB measurements will be given in the following chapter.

Related Publications:

- H. Shaban, M. Abou El-Nasr, and R.M. Buehrer," A highly accurate wireless wearable UWB-based full-body motion tracking system for gait analysis in rehabilitation," *Submitted to IEEE Transactions on Information Technology in Biomedicine*.

Chapter 7

Ranging and Localization Measurements

This chapter provides the actual on-body measurements taken for the verification of the proposed system. Particularly, we took multiple measurement sets, namely the knee-to-ankle distance, base-of-support (BOS) distance, RRcR, and system initialization measurement sets. In our measurements we considered the verification of both ranging and localization measurement accuracies, as well as the investigation for the capability of our proposed system of the extraction of gait parameters.

In the knee-to-ankle measurement set, we investigate the ranging accuracy provided by the proposed system. Furthermore, in the RRcR measurement set we verify the accuracy of the proposed RRcR ranging technique. Moreover, in the BOS measurement set we investigate the capability of the proposed system for the extraction of gait parameters. Finally, in the system initialization measurement set we investigate the localization accuracy provided by the proposed system.

This chapter is organized as follows. Section 7.1 gives an overview of the four measurement sets and equipments. The first measurement set, the knee-to-ankle distance measurement set, is given in Section 7.2 along with numerical results based on the measurements. Section 7.3 describes the RRcR measurement set with further results. The third measurement set, the base-of-support measurement set, is provided in Section 7.4. The system initialization measurement set, fourth measurement set, is given in Section 7.5. Finally, chapter conclusions and contributions are provided in Section 7.6.

(a) (b)

Figure 7.1: (a) UWB antennas manufactured by the Virginia Tech Antenna Group (VTAG). and (b) UWB antennas from Time Domain Corporation.

7.1 Overview of Measurement Sets

In order to evaluate the system performance based on actual-data, on-body UWB measurements were taken at the MPRG labs[1]. The following equipments were used: HP33120A function generator, Tektronix CSA8000B Digital Sampling Oscilloscope, Geozondas pulser (GZ1106DL1, GZ1117DN25), and two antennas manufactured by the Virginia Tech Antenna Group and from Time Domain Corporation, as depicted in Figures 7.1(a) and (b), respectively.

As was previously mentioned, we considered four distinct measurement sets, as depicted in Figure 7.2 and Figure 7.3. The first measurement set is the knee-to-ankle measurement set; shown in Figure 7.2(a). The second set is the RRcR measurement set; depicted in Figure 7.2(b). The third measurement set is the BOS set, shown in Figure 7.2(c). The fourth measurement set is the system initialization set; depicted in Figure 7.3. In the first measurement set, we used the UWB antennas depicted in Figure 7.1(a). Whereas, for the other three sets we used the second UWB antenna, shown in Figure 7.1(b).

7.2 Knee-to-Ankle Distance Measurement Set

The target of this measurement set is to investigate the ranging accuracy of the proposed system, and compare it to the accuracy provided by commercial systems. In this set, two UWB transmit and receive antennas were attached to the knee and ankle of the test subject

[1]We determined the measurement sets with all related requirements, and Haris Volos, Ph.D. candidate at Wireless at Virginia Tech research group, took the measurements at the MPRG labs.

in order to estimate the inter-spacing distance based on the TOA of the received pulses. This parameter was chosen because it directly reflects the effect of both ranging accuracy and the effect of antenna displacement due to body movement. In this measurement set, the test subject was allowed to walk forward and backward, and the received pulses were recorded and stored. The length of the pulses was 4000 samples. The reference pulse is shown in Figure 7.4 along with an example received pulse; both pulses are normalized to unit energy. The measured data was further used in postprocessing simulations in order to estimate the TOA and the corresponding distances. Figures 7.5(a) and (b) show performance comparisons between the MF with optimal and real-suboptimal templates and QAC estimators for the TOA and distance estimates, respectively. As can be seen, the performance of MF-TOA estimator with suboptimal template approaches the performance of the corresponding estimator with optimal template. Moreover, on the contrary to the BER performance, the performance of QAC-TOA estimator is much worse then the performance of the MF estimator with real optimal and suboptimal templates.

7.3 RRcR Measurement Set

This measurement set was taken in order to verify the accuracy of the proposed RRcR ranging technique based on actual measurements, and to take the effect of antenna displacement due to movement into consideration. In gait analysis systems, since the main target of the system is to acquire the distances among the sensors during movement, the effect of the probable antenna displacement due to subject movement needs to be considered. For this reason, measurements were taken of the distance between the knee and ankle sensors, and the acquired pulses were further used in postprocessing simulations. This was done in order to estimate the TOA of the received pulses, and to obtain the corresponding Euclidean distance. The actual measurement setup is shown in Figure 7.6. Furthermore, the normalized received

Figure 7.2: (a) Knee-to-ankle measurement set. (b) RRcR measurement set. and (c) Base-of-support measurement set.

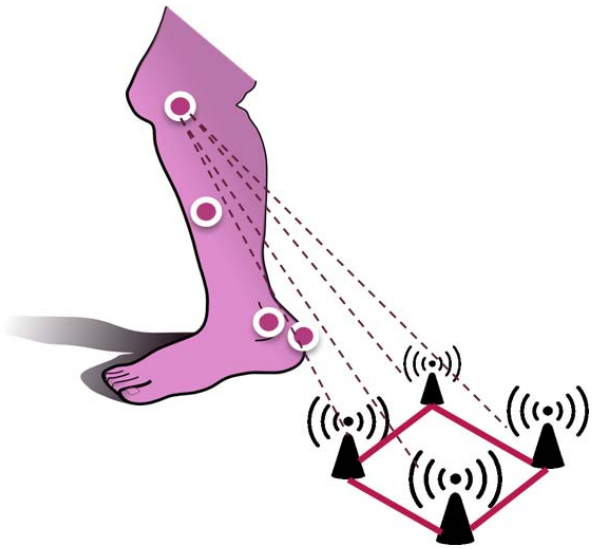

Figure 7.3: System initialization measurement setup.

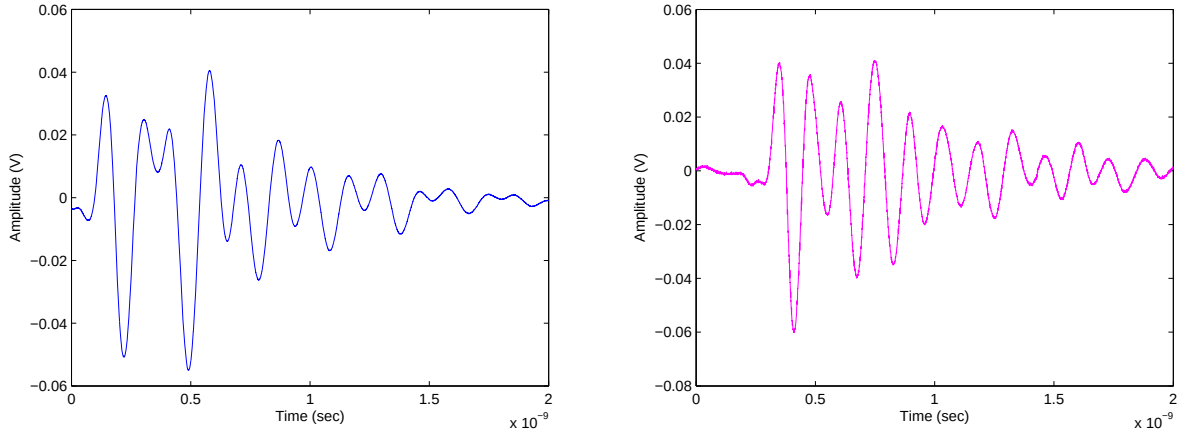

(a) (b)

Figure 7.4: (a) Normalized reference pulse of measurement set 1. and (b) Normalized received pulse for measurement set 1.

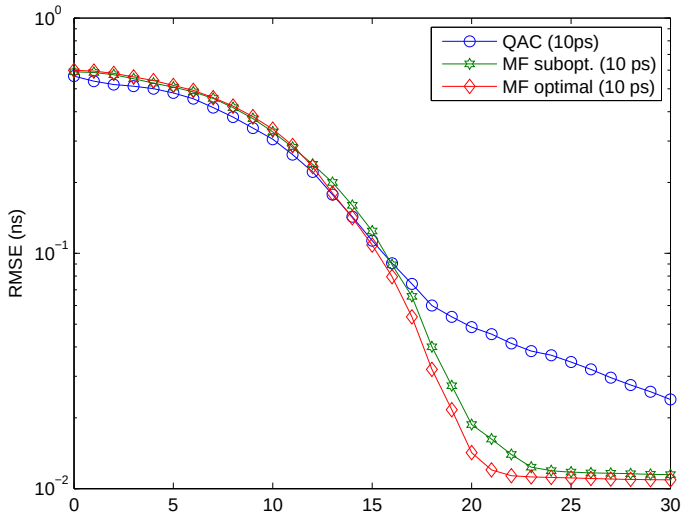

(a)

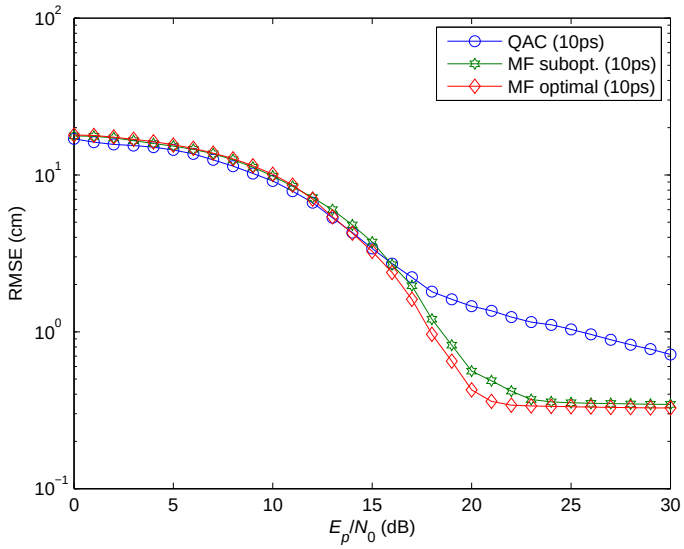

(b)

Figure 7.5: Comparison between measured knee-to-ankle distance using MF with optimal and suboptimal templates, and QAC detector based on actual measurements for the TOA estimator. and (b) Comparison between measured knee-to-ankle distance using MF with optimal and suboptimal templates, and QAC detector based on actual measurements for the distance estimator.

Figure 7.6: RRcR measurement setup.

pulses at the two receive nodes, nodes ♯ 1 and 2, are depicted in Figures 7.7 (a) and (b), respectively. The results are plotted and compared to a commercial optical tracking system in Figure 7.8. As can be seen, the proposed system achieves obvious improvement as compared to the commercial system providing an average ranging accuracy of 1 mm compared to 11 mm for the commercial optical tracking system.

RRcR is further evaluated and compared for optimal and suboptimal based detectors as shown in Figure 7.9. Results show that RRcR is capable of achieving a 1 mm ranging accuracy at 20 dB and 22 dB SNR for optimal and suboptimal templates, respectively. Moreover, the performances of RRcR with optimal and suboptimal templates, and QAC are compared in Figures 7.10(a) and (b) for the TOA and distance estimators, respectively. As can be seen, the proposed RRcR with optimal and suboptimal templates outperform the performance of MF estimators with optimal and suboptimal templates. Similar to the MF estimator, the performance of the proposed RRcR estimator with suboptimal template approaches the performance of the same estimator with optimal template. Moreover, based on practical RRcR estimators, a target 1 mm ranging accuracy is achievable at 19 dB and 20 dB for the optimal and suboptimal template based estimators, respectively.

7.4 Base-of-Support Distance Measurement Set

After the investigation of the ranging accuracy of the proposed system, it was more convenient to investigate the capability of the proposed system of the extraction of specific gait parameters. In particular, the parameters that are known to be of clinical importance, such as the BOS, were examined. In this measurement set, we measure the BOS distance for normal gait. The actual measurement set is depicted in Figure 7.11. An example received

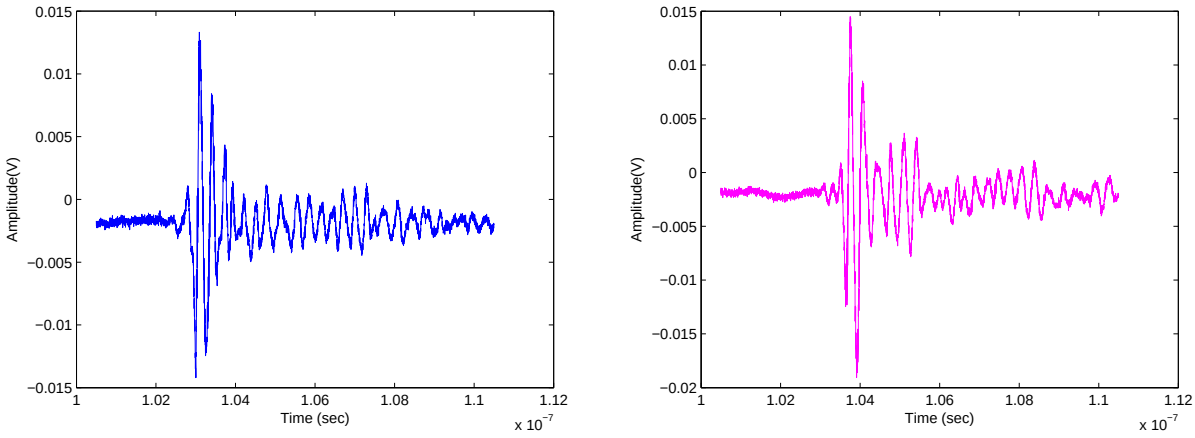

(a) (b)

Figure 7.7: Normalized received pulse for the RRcR measurement set at (a) Node ♯ 1. and (b) Node ♯ 2.

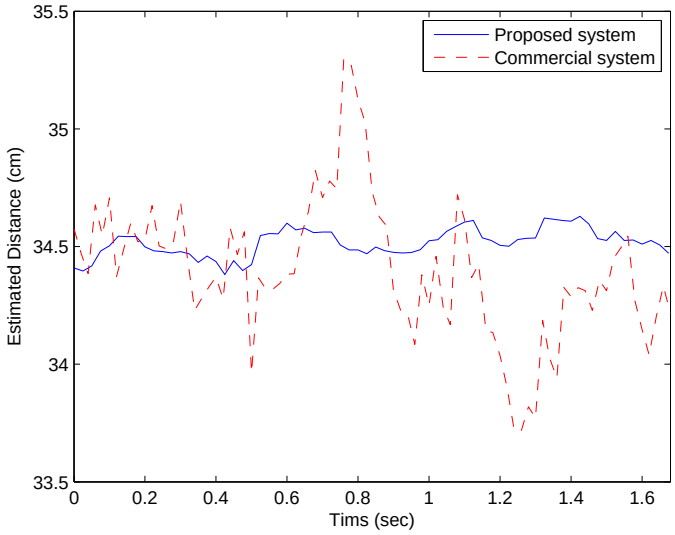

Figure 7.8: Comparison between the measured knee-to-ankle distance using the proposed RRcR technique, and using optical tracking system.

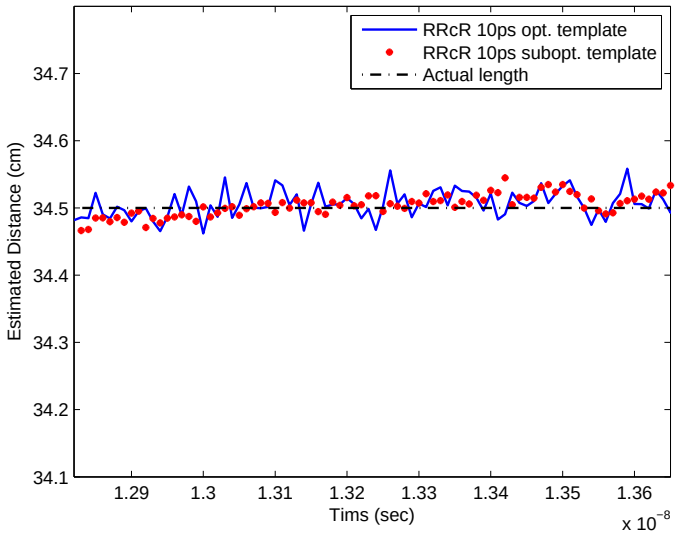

Figure 7.9: Comparison between measured knee-to-ankle distance using RRcR with optimal and suboptimal templates based on actual measurements.

pulse normalized to unit energy is depicted in Figure 7.12. The measured BOS is shown in Figure 7.13 for normal gait. Moreover, Figure 7.14 shows the BOS distance for normal gait using a commercial optical tracking system. As can be seen, the measured BOS using the proposed system resembles the BOS curve for normal gait with an average distance of 8.5 cm, which agrees with the value reported in the literature for normal adults.

7.5 System Initialization Measurement Set

System initialization is an important procedure for our proposed system, where in subsequent frames we assume that the C-MDS is based on the preceding frames. Thus, the system initialization, particularly the estimation of the initial-frame node coordinates is crucial for our system. For this reason, we verify the proposed initialization procedure using actual measurements. Particularly, we consider four nodes attached to the lower right-leg of the test subject attached to the knee, leg calf, ankle, and heel. Also, we assume the use of four reference-nodes, and take TOA measurements between each of the on-body nodes and the four reference-nodes. The results are shown in Figure 7.15. Measurement results show that the proposed system initialization procedure achieves a 0.247 mm localization accuracy, which agrees with the simulation results presented in Chapter 6.

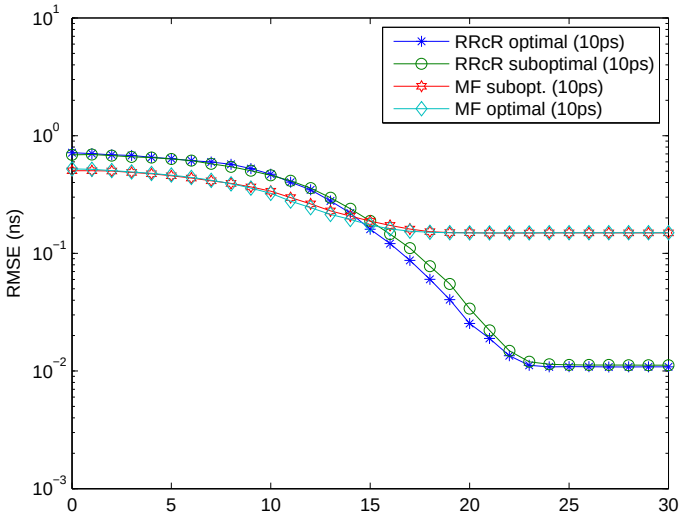

(a)

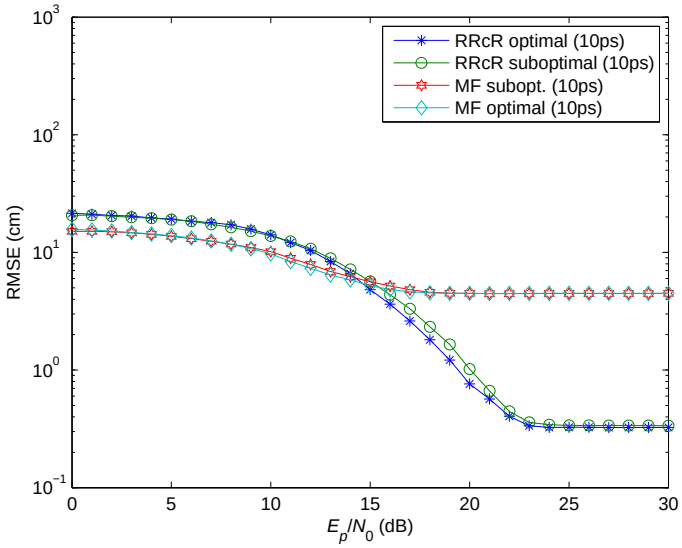

(b)

Figure 7.10: (a) Comparison between measured knee-to-ankle distance using RRcR and MF with optimal and suboptimal template-based estimators based on actual measurements for the TOA estimate. and (b) Comparison between measured knee-to-ankle distance using RRcR and MF with optimal and suboptimal template-based estimators based on actual measurements for the distance estimate.

Figure 7.11: BOS measurement setup.

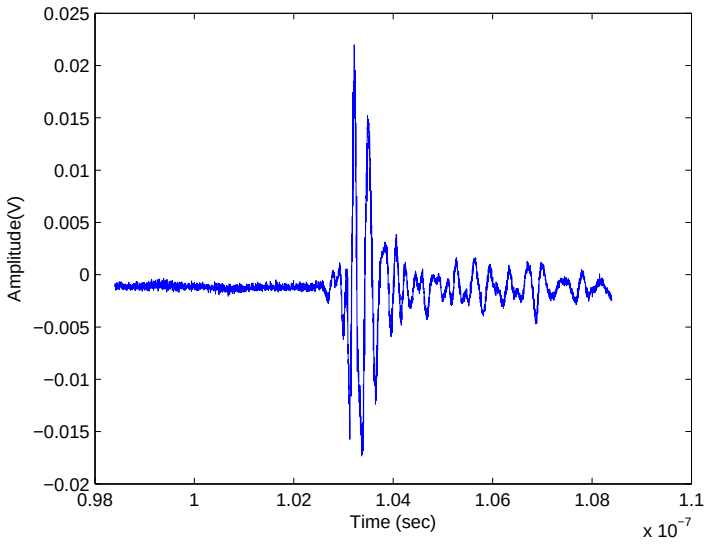

Figure 7.12: Normalized received pulse for the BOS measurement set.

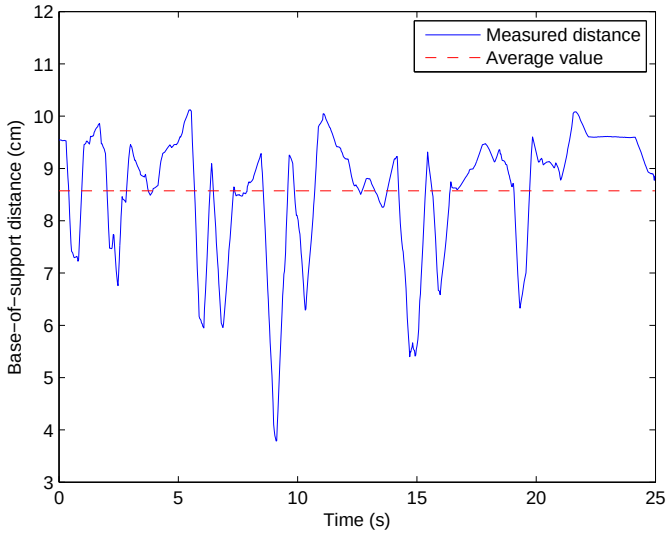

Figure 7.13: BOS distance for normal gait measured using the proposed UWB system.

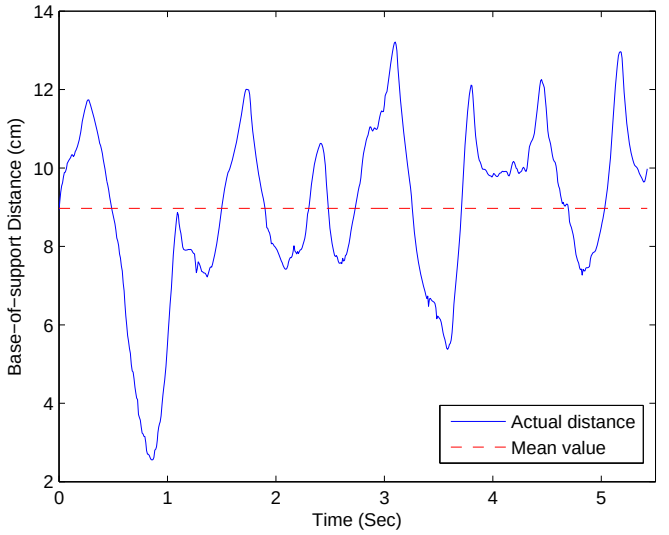

Figure 7.14: BOS distance for normal gait measured using commercial optical tracking system.

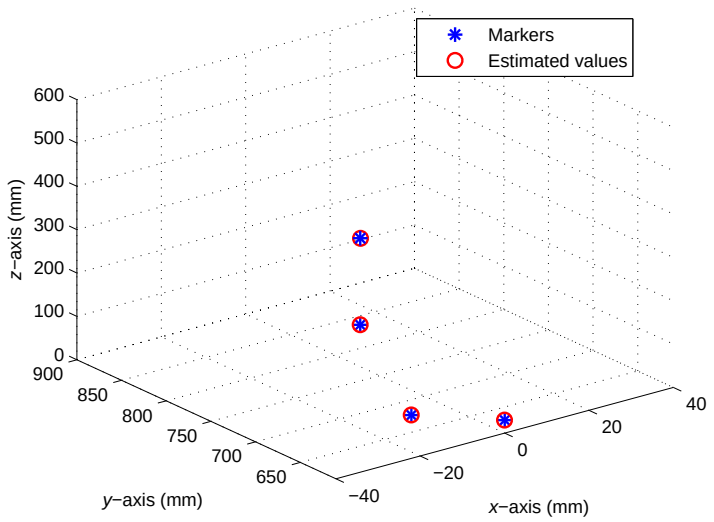

Figure 7.15: Results of system initialization measurement set.

7.6 Chapter Conclusions and Contributions

This chapter provided the actual measurements taken at the MPRG labs for the verification of the ranging and localization accuracies provided by our proposed system. Furthermore, it included the investigation of the capability of extraction of actual gait parameters based on actual measurements using UWB radios. Particularly, we took four different measurement sets for the investigation of ranging and localization accuracies, verification of the accuracy provided by the proposed RRcR ranging technique, and the extraction of actual gait parameters.

The results presented in Section 7.3 showed that the proposed system is capable of providing a 1 mm ranging accuracy using optimal template at an SNR = 20 dB and 22 dB using suboptimal real sinusoidal template, respectively. This accuracy is compared to a 1.17 cm accuracy reported for current tracking systems. Furthermore, the extracted BOS was shown to have the same shape as the BOS extracted using optical tracking system with average BOS = 8.5 cm. This value agrees with the average BOS reported for normal adults. Moreover, the proposed system initialization procedure was also verified using actual measurements.

Related publications:

- H. Shaban, M. Abou El-Nasr, and R.M. Buehrer,"Toward a highly accurate ambulatory system for clinical gait analysis via UWB radios," *IEEE Transactions on Information Technology in Biomedicine*, Vol. 14, No. 2, pp 284- 291, Mar. 2010.

- H. Shaban, M. Abou El-Nasr, and R.M. Buehrer," Reference range correlation-based (RRcR) ranging for highly accurate wearable UWB motion tracking and movement

analysis systems," *Submitted to IEEE Global Telecommunications Conference, GLOBECOM '10*.

Chapter 8

Sensor-Fusion and Overall System Performance

This chapter investigates the integration of UWB sensors with other sensors, i.e., sensor-fusion, in order to be able to get a complete picture of gait parameters including kinematics and kinetics. Specifically, we consider the integration of UWB sensors with foot force sensors, which is analogous to using force-plates in commercial optical tracking systems. Then, we study the number of bits required, and the effect of quantization error on the estimated gait parameters via simulations. Also, we compare the performance of our proposed system to commercial optical tracking systems considering several gait parameters. Particularly, we consider the parameters that are known to be of clinical importance for the characterization of abnormal gait. Finally, we estimate the overall system performance including power consumption and battery lifetime.

The organization of this chapter is as follows. First, Section 8.1 studies the senor-fusion and gives numerical results. Then, Section 8.2 investigates the number of bits required for UWB and force sensors. Section 8.3 provides some of the important gait parameters to characterizing abnormal gait, and highlights the promise of our proposed system for providing a more reliable gait analysis. Then, Section 8.4 compares the capability of normal/abnormal gait identification of our system to commercial optical tracking systems. Moreover, Section 8.5 gives comparisons between our proposed system and optical tracking systems for various gait parameters. Then, Section 8.6 estimates the overall power consumption, memory requirements, and battery lifetime. Finally, chapter conclusions and contributions are provided in Section 8.7.

8.1 Sensor-Fusion

One of the advantages of UWB radios is their suitability for the integration with other motion sensors. With UWB sensors and inherent ranging and localization approaches, our system is capable of accurately estimating the gait kinematics. Ultimately, our system should be capable of estimating both kinematic and kinetic parameters associated with gait analysis. Thus, we further propose the use of force sensors placed under the test subject's feet. The analog data, force sensor data, is first converted into the digital form, and transferred to the on-body central-node. This is typically analogous to the force plate used in optical tracking systems. It is worth noting that the fusion of data may not be directly obvious, as both kinetics and kinematics are used for obtaining a complete picture of the gait. So, fusion here means using more than one type of sensors for obtaining the data required by one system, the gait analysis system. However, some gait parameters do require the data obtained from both kinetics and kinematics, such as the moments, which is equal to the force (kinetics) multiplied by the distance (kinematics) [5].

In order to examine sensor integrability and accuracy of the proposed system for actual gait parameters, gait data files acquired via force sensors were obtained from [48]. These files were processed using MATLAB to extract the gait data. The data was first converted to the binary format using a 12-bit ADC, as will be justified in later sections, and then used in a simulation which was used as binary data in the IEEE 802.15.6a channel model. The detected bits were then reconverted and compared to original data in Figures 8.1(a) and (b) for normal gait and Parkinson's gait, respectively. Figure 8.2 shows the BER assuming energy detection in the IEEE 802.15.6a CM3 and CM4 channel models. The achieved BER is 7e-5 at $E_p/N_0 = 28$ dB in the IEEE 802.15.6a on-body channel model. This is equivalent to $E_b/N_0 = 18$ dB with 10 pulses-per-bit. As can be seen from figure, when adding the effect of CM4 (on-body to off-body communication), the effect of body shadowing becomes dominant. As, for the 0^o body angle, the BER approaches the performance in the CM3 model alone, whereas considering other body rotation angles causes significant degradation in the BER. This means that for our system we should ultimately consider the 0^o transmission scenario. This would require storing the acquired data for sometime on the on-body central-node. The memory and battery lifetime constraints will be studied in detail in a later section.

8.2 Number of Bits for Force and Range Data and ADC Power Consumption

In addition to ranging and localization accuracies, the number of bits is an important parameter for our system that needs to be estimated. This includes the number of bits required for the transmission of acquired data, including force and range data. For the force sensor acquired data, in Figure 8.3 we consider a 6-bit ADC reconstructed data as compared to an infinite number of bits. As shown, six bits are insufficient for accurate reconstruction of

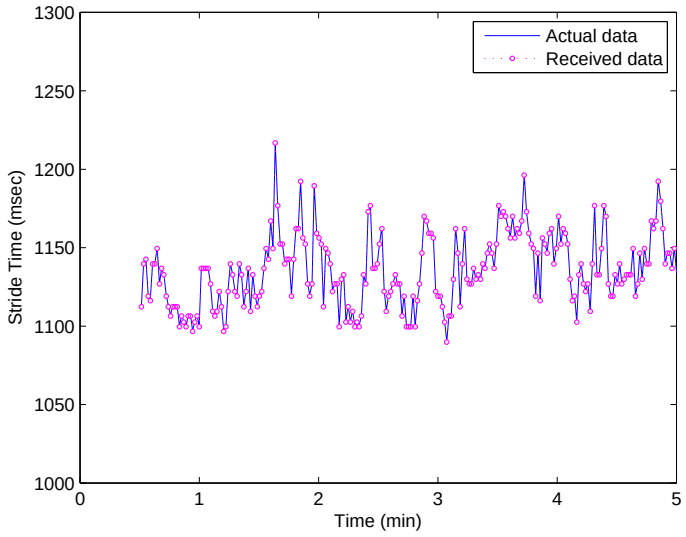

(a)

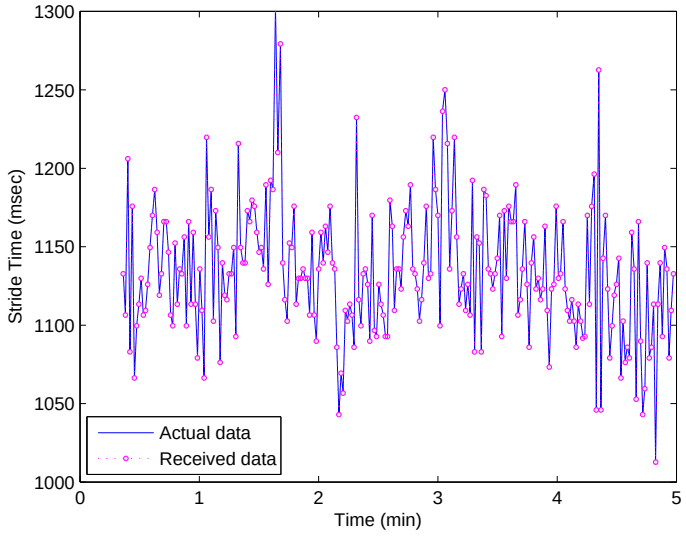

(b)

Figure 8.1: (a) Comparison between stride time gait parameter extracted from force sensors [48] and simulated data in IEEE 802.15.6a using UWB radios for normal gait. and (b) Comparison between stride time gait parameter extracted from force sensors [48] and simulated data in IEEE 802.15.6a using UWB radios for Parkinson's gait.

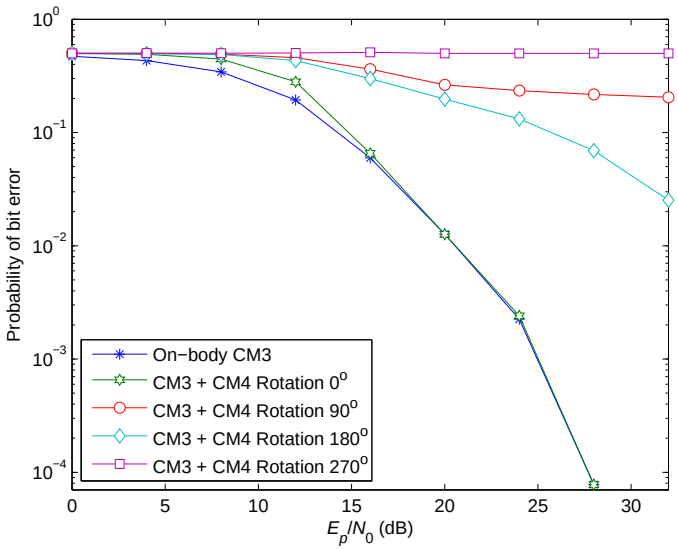

Figure 8.2: BER performance comparison in the IEEE 802.15.6a CM3 and CM4 UWB channel models.

data. Typically, force sensor data needs to be accurately represented, as when used in the estimation of gait parameters, it greatly affect the estimated data, such as the gait moments. Then, in Figure 8.4 we increase the number of bits to eight bits. Also, this number provides insufficient accuracy. Figure 8.5 shows the reconstructed stride time using a 12-bit ADC along with the infinite bit data. As can be seen, the 12-bit ADC provides sufficient accuracy for accurate reconstruction of gait data. A rate of 300 Hz is sufficient for the force sensor data transmission to the on-body central-node. The corresponding ADC power consumption is 2.5 μW, based on the FOM given in [29].

We further consider the estimation of number of bits for the gait parameters estimated via UWB sensors' acquired data. In Figure 8.6 we present a reconstructed knee-flexion angle using a 10-bit ADC compared to the original data for an adult with cerebral palsy. As can be seen, the reconstructed curve requires more bits for a more accurate gait parameter estimate. We consider increasing the number of bits to 14 bits in Figure 8.7, but this is also insufficient. Figure 8.8 shows the reconstructed angle for a 16-bit ADC along with the infinite bit knee-flexion angle. As can be seen, the 16-bit ADC provides the required accuracy. Thus, we assume a 16-bit ADC. For a signal bandwidth W = 2 GHz, and f_{ADC} = 20 KHz, and n = 16 bits, the power consumption of the ADC is 2.6 mW.

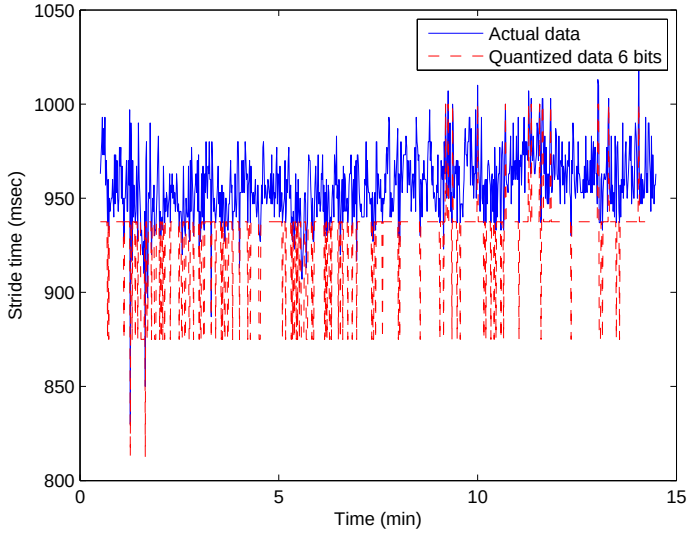

Figure 8.3: Stride time gait parameter extracted from force sensor data [48] assuming a 6-bit ADC compared to infinite-bits.

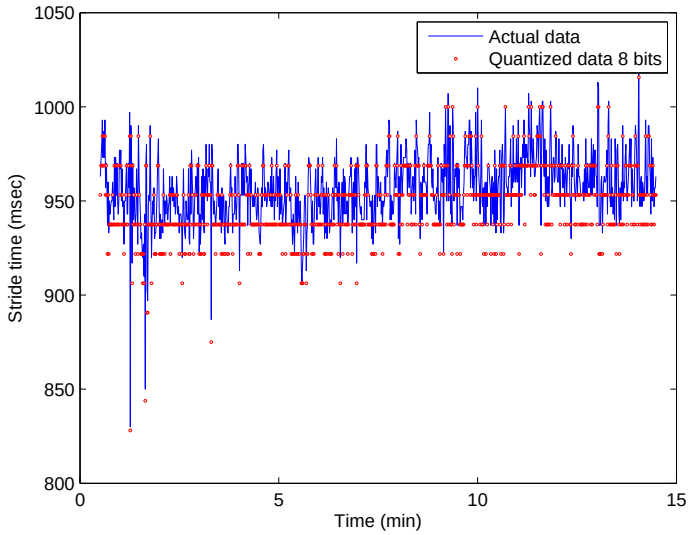

Figure 8.4: Stride time gait parameter extracted from force sensor data [48] assuming a 8-bit ADC compared to infinite-bits.

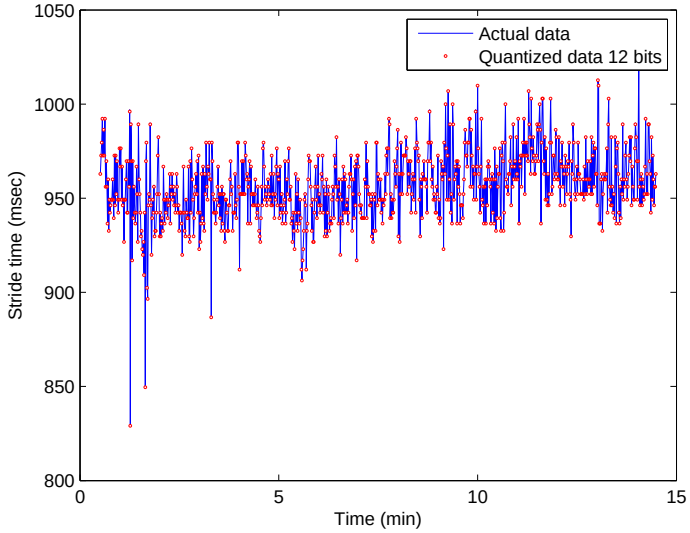

Figure 8.5: Stride time gait parameter extracted from force sensor data [48] assuming a 12-bit ADC compared to infinite-bits.

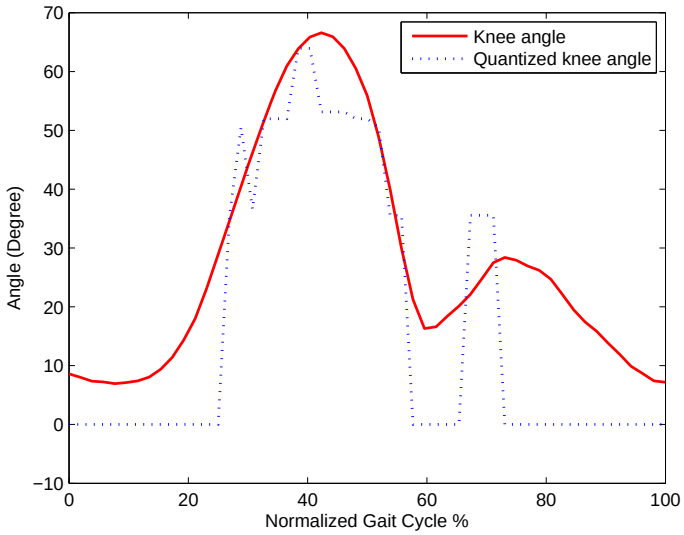

Figure 8.6: Knee-flexion angle for an adult with cerebral palsy (CP) assuming a 10-bit ADC compared to infinite-bits.

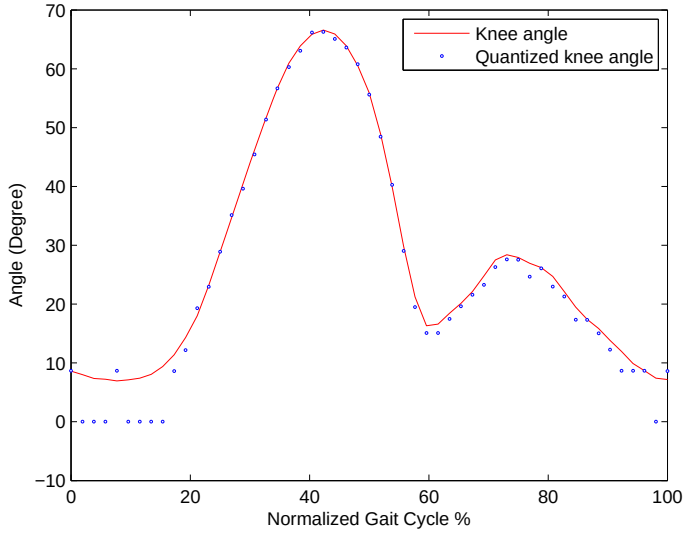

Figure 8.7: Knee-flexion angle for an adult with cerebral palsy (CP) assuming a 14-bit ADC compared to infinite-bits.

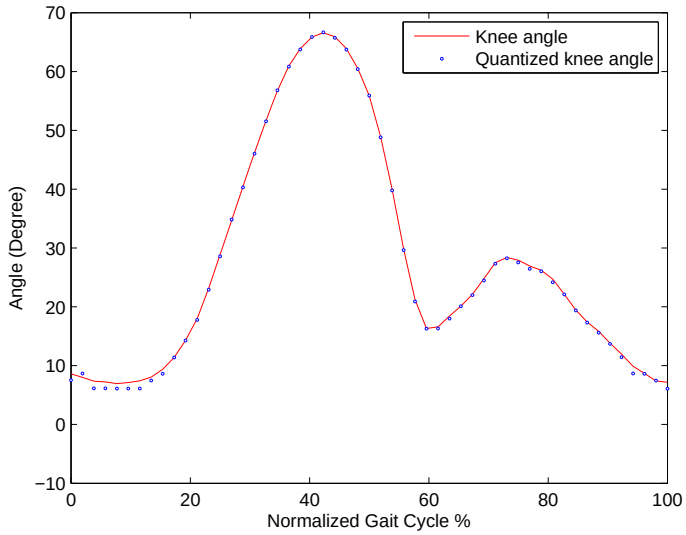

Figure 8.8: Knee-flexion angle for an adult with cerebral palsy (CP) assuming a 16-bit ADC compared to infinite-bits.

8.3 The Promise for a More Reliable Gait Analysis

In this section, we consider the parameters that are known to be measured with less reliability using current technologies. In addition to the BOS gait parameter that was studied in previous chapters, there are other parameters that are of clinical importance, and are known to be unreliably measured using current systems. Due to the insufficient accuracy provided by current systems, differentiation between normal and abnormal gait may not be possible. Some of these parameters are as follows.

- Inter-marker distance (linear displacement) reported error = 11.7 mm.
  - BOS measurement, equal to 8.5 cm for normal gait. Reported accuracy leads to $\approx 14\%$ error.
  - Average leg-length discrepancy reported in the literature differs from 3 mm up to 10 mm [25]. Obviously, this would fail to be accurately characterized with the reported accuracy (11.7 mm).
- Knee-flexion angle measurement error up to 4^{o} for commercial systems [10], [77].
- Toe IN/OUT angle is known to be inaccurately measured [10].
- Inter-session measurement inconsistency [10].

Our proposed system's linear displacement accuracy (1 mm) seems to have a promising accuracy for a better reliability in detecting leg-discrepancy and BOS, and consequently for characterizing abnormal gait. Figure 8.9[1] shows a simplified diagram of leg discrepancy. Figure 8.10 shows the difference for the step-length between normal and Parkinson's gait. Furthermore, the $\approx 1^{o}$ angular displacement accuracy of our system also seems to provide a more accurate knee-flexion angle measurement. Figure 8.11 shows the knee-flexion angle measurement. This accuracy also provides a more reliable measurement for the toe IN/OUT angle measurement. In general, most of the gait parameters are expected to be measured with higher accuracies as compared to current systems, but we decided to concentrate on some of the parameters that are known to be of clinical importance, and are less reliably measured.

8.4 Normal/Abnormal Gait Identification

In this section we compare our proposed system to commercial tracking systems based on the ability to automatically identify normal/abnormal gait. We assume a hypothetical artificial test implemented via simulations. We estimate the leg-length for normal MoCap gait for

[1]Figure 8.9 is reproduced based on the materials presented in [18], [107].

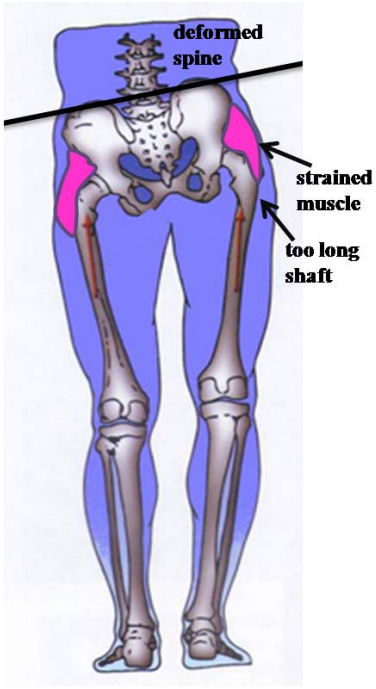

Figure 8.9: Schematic diagram showing leg-discrepancy.

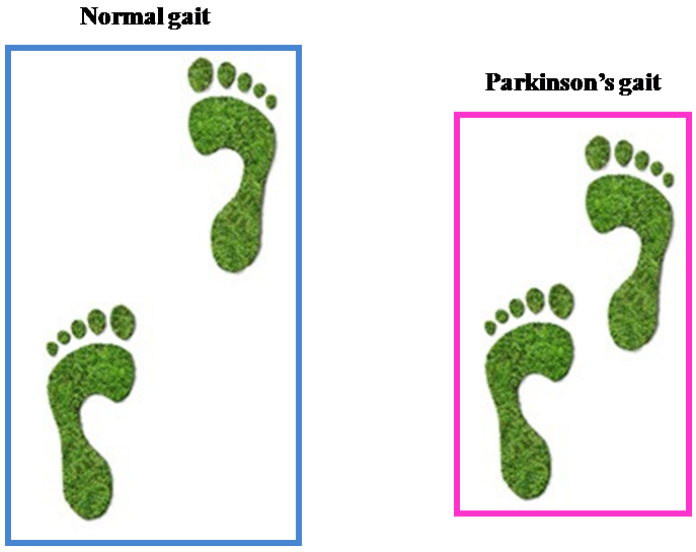

Figure 8.10: Comparison between step width for normal gait and Parkinson's gait.

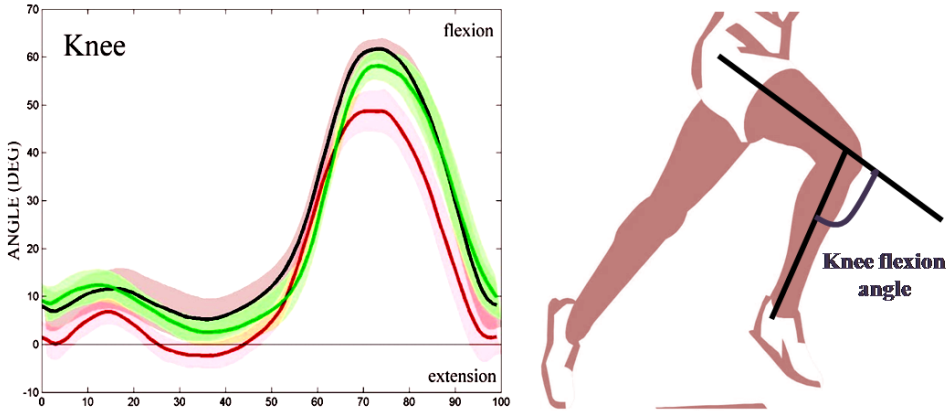

Figure 8.11: Definition of knee-flexion angle.

Table 8.1: Artificial test results.

	Commercial System	Proposed System
Probability of detection (POD)	56.3%	100%

the left and right legs. Typically, for normal gait, they should be the same, as shown in Figure 8.12 for the leg-segment measurement during walking. The variations in leg-length is due to soft-tissue (skin) movement while walking in addition to the measurement accuracy. In this simulation, we add the ranging error associated with the commercial system and our proposed system, and estimate the probability of detection (POD) of normal gait. The POD is the probability that the system identifies the data as normal gait. For this test, we set a threshold of 3 mm for the definition of abnormal gait. If the detected difference is greater that 3 mm, then the data is characterized as abnormal gait. Otherwise, it is correctly identified as normal gait. The results are summarized in Table 8.1. As can be seen, our system substantially outperforms the corresponding optical tracking system. The POD for our system is 100% for normal gait tests applied 1e5 times. Whereas, for the optical tracking system, the POD is 56.3%.

8.5 Comparison of Gait Parameters using the Proposed System and Commercial Systems

This section gives results for some gait parameters of the proposed system using simulation. Moreover, it compares these parameters for the proposed system and commercial gait analysis system (accurate commercial optical tracking system) based on real-data captured using the commercial system. In order to examine and compare the ranging accuracy of the proposed system to the commercial system for actual gait parameters, particularly for the heel-to-heel

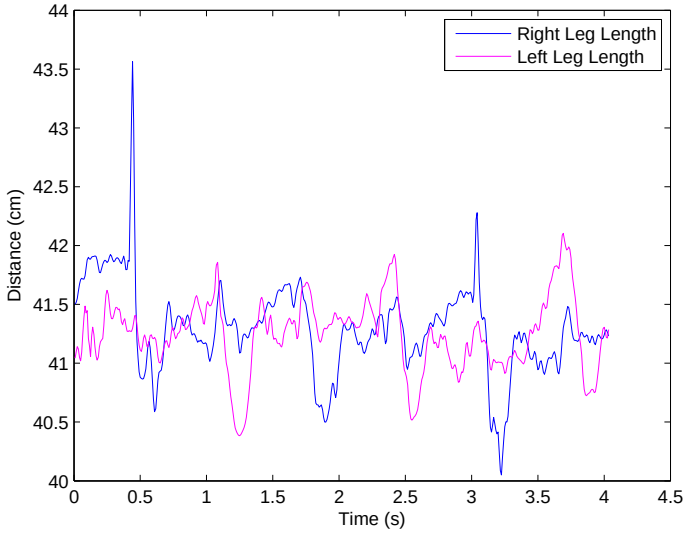

Figure 8.12: Comparison between the length of left and right leg segments.

distance parameter, a motion capture data file representing normal walking movement was obtained from [2], [112], [3]. This file was processed to extract the raw-marker data, and estimate the heel-to-heel distance. The data was then used in a simulation which mimicked the heel-to-heel measurement. The simulated results (along with the actual distances) are plotted for multiple gait cycles in Figure 8.13(a), and the simulated results for the proposed system and the actual distances are plotted for multiple gait cycles in Figure 8.13(b).

Furthermore, the same comparisons are shown in Figures 8.14(a) and (b) for the base-of-support (BOS). As can be seen from the plots, the simulated measurements of our proposed system closely approximate the true distance for both the heel-to-heel and BOS distances. It outperforms the commercial system for both results. The proposed system shows a clear advantage over the commercial system for the BOS distance.

A similar comparison for the knee-flexion angle is presented in Figures 8.15(a) and (b). The simulated results in the IEEE 802.15.6a channel model (along with the actual distances) are plotted in Figure 8.15(a) for a commercial optical tracking system, and Figure 8.15(b) for our system for an adult with cerebral palsy (CP). The results show that the proposed system closely approximates the true angle. From the simulated linear-displacement (ranging), the attainable ranging accuracy of our proposed system in the IEEE 802.15.6a is 1 mm at an SNR = 20 dB (assuming the sub-optimal template) using the proposed RRcR technique, as depicted in Figure 5.22. Moreover, the corresponding achievable angular-displacement accuracy is less than 1^{o}.

The MoCap data was also used in a simulation of the right-knee angular-velocity for a normal adult and plotted in Figure 8.16(a) for the commercial system, and for the system under investigation in Figure 8.16(b). The results show that the proposed system closely ap-

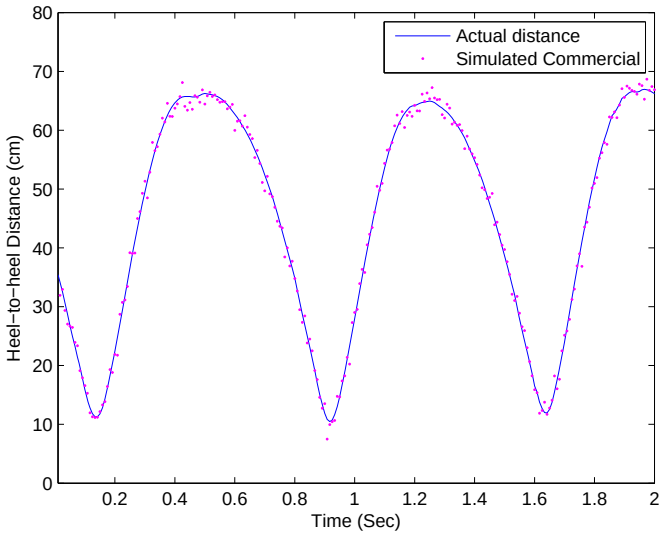

(a)

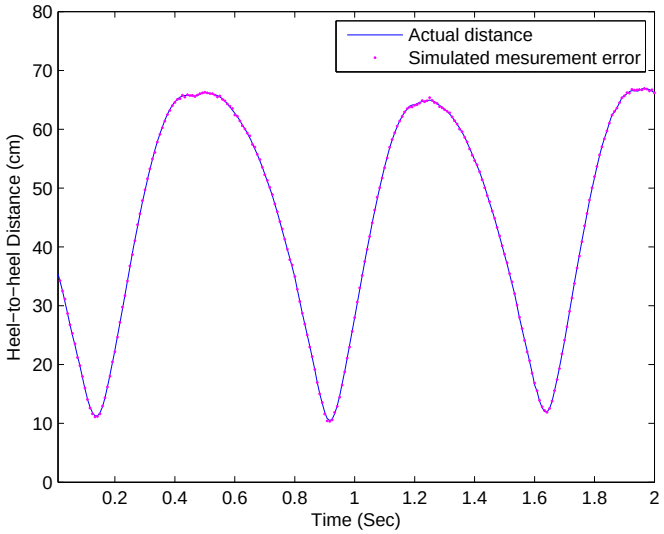

(b)

Figure 8.13: (a) Comparison between the heel-to-heel distance from measurements [2] (actual) and simulation of the commercial system. and (b) The actual system and proposed system via simulation.

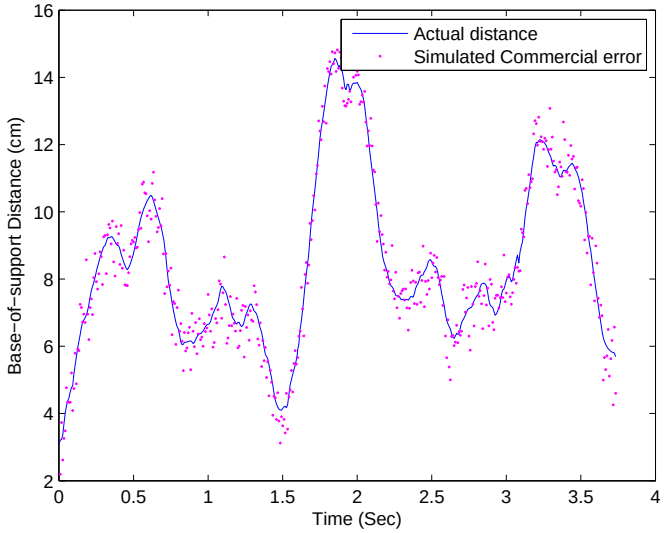

(a)

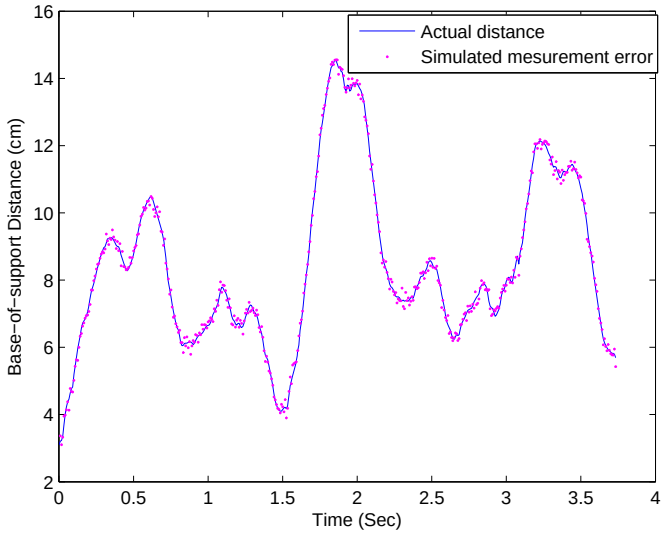

(b)

Figure 8.14: (a) The base-of-support distance of the actual system and simulation of a commercial system, and b) The actual system and the proposed system via simulation.

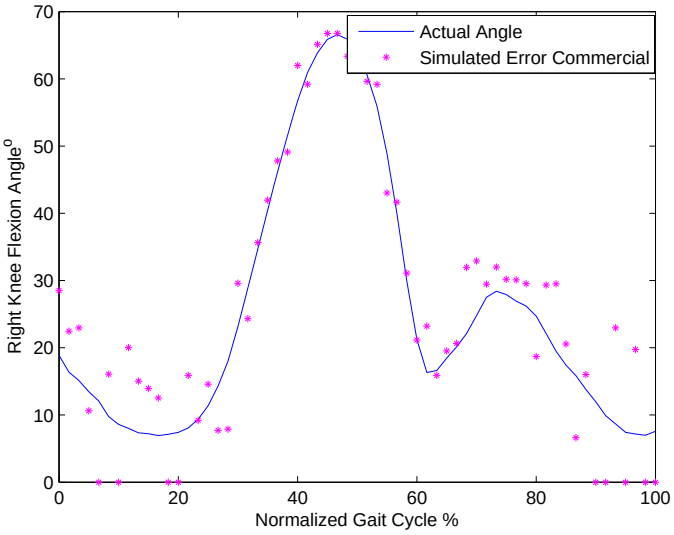

(a)

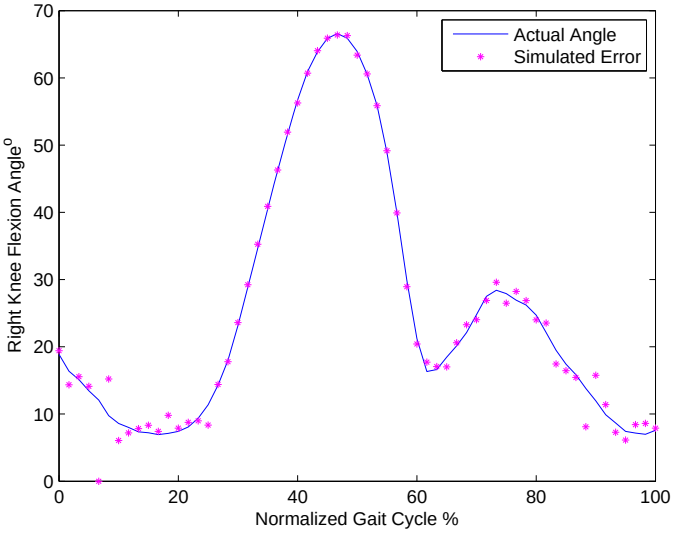

(b)

Figure 8.15: (a) Comparison of right-knee flexion angle from measurements [112] and a commercial system simulation. and (b) A comparison of right knee flexion angle from measurements [112] and proposed system simulation.

proximates the true angular-velocity (represented by the solid-line curve). The toe IN/OUT angle gait parameter comparisons were also considered in Figures 8.17(a) and (b) for the commercial and proposed systems, respectively. The proposed system outperforms the corresponding commercial optical tracking system.

8.6 Overall Power Consumption and Battery Lifetime Estimation

This section studies the memory and battery lifetime requirements based on the design parameters presented in previous chapters. We start by estimating the memory requirement as follows.

- Assuming 16 bits per range estimate, this gives 2 bytes per frame per node.
- For all 50 nodes, it gives an overall data per frame = 100 bytes.
- Memory requirements for all UWB nodes per day = 24*60*60/1 s * 100 bytes = 8.64e9 bytes/day.
- Considering also force-sensors at a 300 Hz rate, 2*24*60*60*300 = 51.84e6 bytes/day.
- Overall memory requirements = 8.69e9 bytes/day = 8.09 Gigabytes/day.
- A 64 Gigabyte micro-Secure Digital (SD) memory card is sufficient for storing approximately 8 days of acquired data.

Moreover, the overall power consumption and battery lifetime are estimated as follows.

- Duty-cycle per node= 2 μs / 1 ms = 2e-3.
- Estimated average power consumption for 100% duty-cycle $\approx$ 100 mW.
- Hence, the average power consumption for a 0.2% duty-cycle = 100 mW * 2e-3 = 0.2 mW.
- If the system is considered to have one battery, thus considering all 50 nodes, the average power consumption = 10 mW.
- Roughly considering a common 1.5 V voltage source, this gives 6.667 mA.
- Considering a common battery (AAA battery) source (750 mAh), the average battery-life is 750 mAh / 6.667 mA = 112.5 hrs/24 = 4.6 days.

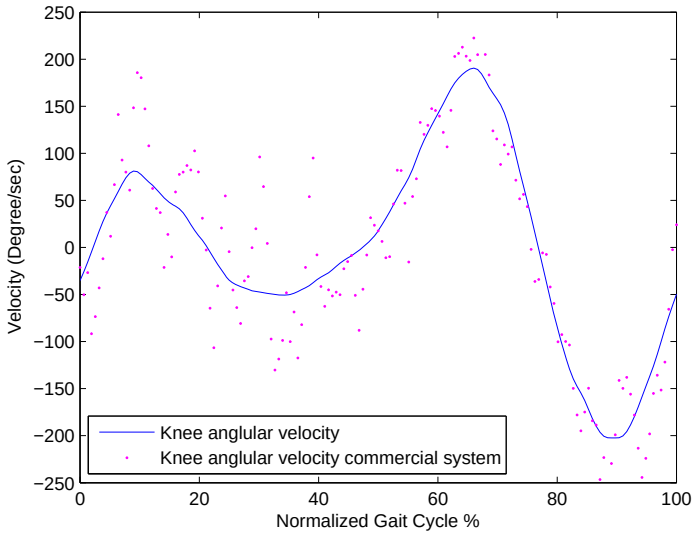

(a)

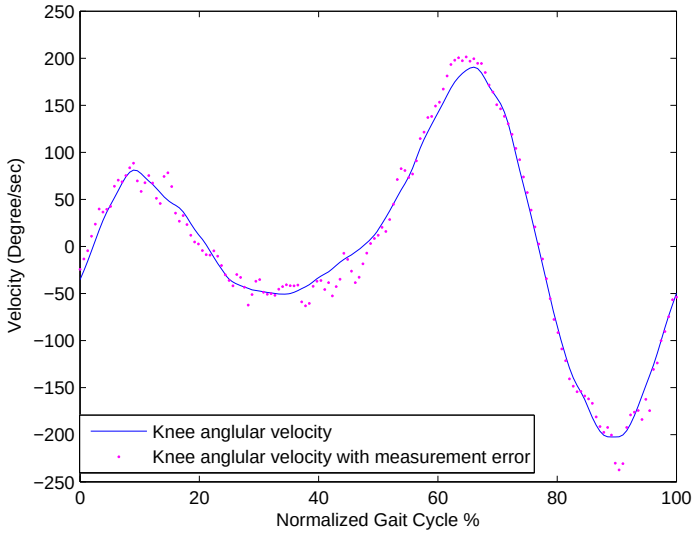

(b)

Figure 8.16: (a) Comparison of the knee angular velocity of a commercial motion tracking systems. and (b) Comparison of the knee angular velocity of the proposed UWB.

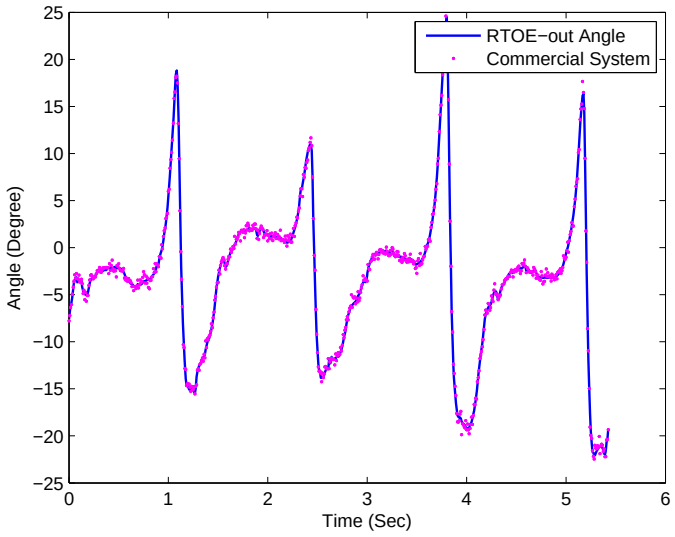

(a)

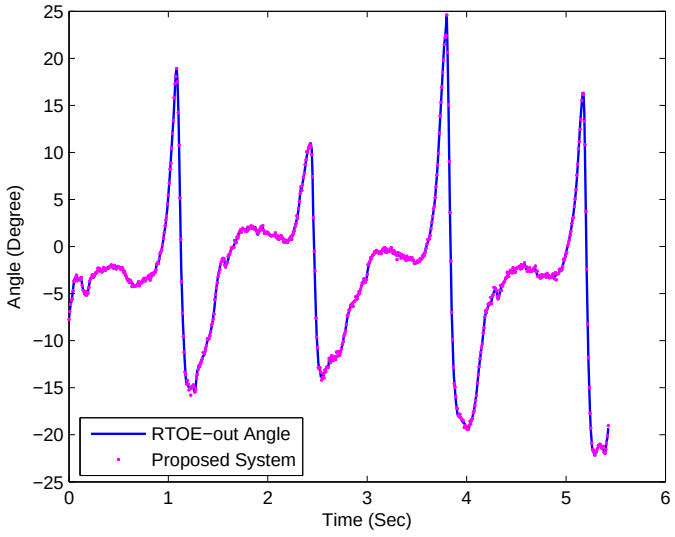

(b)

Figure 8.17: (a) Comparison of toe IN/OUT angle from measurements [2] and a commercial system simulation. and (b) A comparison of toe IN/OUT angle angle from measurements [2] and proposed system simulation.

8.7 Chapter Conclusions and Contributions

This chapter studied multiple key design parameters related to the evaluation of the overall system performance. Particularly, we studied the integration of UWB sensors with foot force senors in the form of sensor-fusion for the evaluation of gait kinematics and kinetics. Furthermore, we summarized some of the important parameters that are known to be of clinical importance, and that current systems fail to provide sufficient accuracy for their measurements. Particularly, we considered the BOS, knee-flexion angle, leg-discrepancy, and toe IN/OUT angle gait parameters. We further provided an artificial test for comparing the gait normality/abnormality identification capability of our proposed system to the commercial optical tracking system. This test showed that our system has a 100% gait identification capability compared to 56.3% for the optical tracking system for leg-discrepancy. Then, the performance of our system was compared to the optical tracking systems considering various gait parameters via simulations based on actual MoCap data. Finally, the overall system power consumption, battery lifetime, and memory requirements were estimated. Our system is capable of storing data on the on-body central-node using a 64 Gigabytes SD memory card for $\approx$ 8 days without needing to transfer data to the off-body node. Moreover, the system can work up to 4.6 days without needing to recharge the batteries, assuming two common AAA battery sources supplying the whole system.

Related publications:

- H. Shaban, M. Abou El-Nasr, and R.M. Buehrer," A highly accurate wireless wearable UWB-based full-body motion tracking system for gait analysis in rehabilitation," *Submitted to IEEE Transactions on Information Technology in Biomedicine.*

Chapter 9

Conclusions and Recommendation for Future Work

In this dissertation, we proposed a full-body wearable wireless UWB human locomotion tracking system with high ranging and positioning accuracies. The proposed system is capable of achieving a ranging accuracy that is ten times better than the ranging accuracy provided by the commercially available systems. Results showed that the proposed system is a promising solution for providing accurate measurements of important clinical parameters, such as the BOS, which is known to be insufficiently accurate when measured using current technologies. In particular, the proposed system is capable of providing a ranging accuracy of 1 mm for intersegmental distance measurements, which exceeds the accuracy of current technologies. The proposed system is also capable of providing a high localization accuracy, which also exceeds the accuracy provided by current locomotion tracking systems. In addition, this system can take both indoor and outdoor measurements, which is suitable for the long-term monitoring and assessment of mobility diseases.

In order to achieve the ultimate goals of this system, there have been multiple challenges that have been handled. Mainly, the system performance and the overall power consumption of the system needed to be investigated. Moreover, the proposed system did not only need to provide accurate ranging and localization accuracies, but also needed to provide accurate motion capture data in a sense that does not affect or alter the measured motion data. This goal is absolutely dependent upon the nature of human locomotion, and the dynamics of human movement. Essentially, the specific acquired parameters, either kinematics or kinetics, and their measurement requirements as dictated by clinical gait analysis, are the main controllers of this task. The investigation of available ranging and localization techniques, as well as the proposal of new techniques have been considered. Also, low-power alternatives have been studied. Furthermore, important factors that affect performance, such as synchronization errors have been addressed. Moreover, actual measurements have been provided for the verification of the proposed system. Additionally, the integration of UWB sensors with other sensors has been investigated.

The system design and implementation issues of the system were discussed and simulations were provided based on realistic environments. Furthermore, it was proven that the required E_p/N_0 for the target ranging accuracy is achievable for an adequate number of transmitted pulses per bit. This in turn relaxes the synchronization constraints. As for a large number of bits, synchronization becomes a complicated and a challenging task. Moreover, the ranging accuracy was investigated, and simulation results were presented. It was shown from simulations as well as actual measurements that the high ranging accuracy of the proposed system approaches the optimal curves (the original curves) of the investigated gait parameters. Typically, the proposed system provides high ranging and localization accuracies at low-complexity implementation requirements. Moreover, it is suitable for taking continuous real-time measurements required for clinical gait analysis.

Chapters 1 and 2 provided an introduction and the necessary background for the work presented in this dissertation, respectively. In Chapter 3, we studied the key design and analysis parameters of our proposed system. We gave a description of our proposed system followed by key design parameters, namely the power consumption, employed pulse shape, transmitter architecture, proposed ranging stage, and designed the system symbol structure. Moreover, we addressed the different challenges related to the design of an accurate localization technique, and gave a brief description of our proposed solution.

Chapter 4 discussed and studied some important parameters related to our system design, namely the channel model, link budget, estimation of gait parameters, and gave a comparative study of power consumption considering six different receiver architectures. Furthermore, it introduced our proposed framework for the study of performance/power-consumption, and provided a case study for non-coherent UWB receivers.

Chapter 5 studied and compared different ranging approaches, proposed a ranging technique for our proposed system, derived theoretical lower bounds, and provided link and power budgets for the proposed system based on the performance of the ranging system. Moreover, it studied the effect of timing-misalignment (error in template position w.r.t. the received signal) on the ZZLB. Then, it proposed a ranging technique, the RRcR technique. The proposed technique was shown to provide substantial improvement over MF-TOA estimators without *a priori* channel knowledge, and approaches the performance of MF estimators with perfect channel knowledge. In this chapter, we also designed the link budget. We showed that the link margin is expected to be equal to 10 dB at the target 1 mm ranging accuracy using the proposed RRcR technique with suboptimal low-power template alternative. The 10 dB link margin is calculated w.r.t. the 18 dB SNR requirement based on the ZZLB. The corresponding link margin based on the 22 dB (based on actual measurements) SNR requirement is 6 dB based on the effective power consumption was also estimated. It was shown to be $\approx$ 1 mW, which satisfies the IEEE 802.15.6a power consumption limit per node (0.1 - 1 mW per node).

Chapter 6 investigated the localization stage, and studied the employed localization techniques. It showed that the proposed system initialization requires 20.14 seconds for a complete setup. The localization technique used at the system initialization stage is the linear-LS

(as it is a low-complexity solution that could provide us with the required high positioning accuracy), and was shown to achieve an average positioning accuracy equal to 0.247 mm. The core measurement phase was also studied. In this stage, we assumed using C-MDS localization approach preceded by an FFT interpolation. The achieved accuracy of acquired data during this stage was shown to be 0.47 mm $\pm$ 52 μm. Results were obtained via simulations in the IEEE 802.15.6a channel based on actual acquired MoCap data. This chapter also investigated the node arrangement, and proposed grouping the nodes in LOS links guaranteed regions that guarantee LOS links during movement.

Theoretical and simulation results were further justified via actual measurements. Chapter 7 provided the actual measurements taken at the MPRG labs for the verification of the ranging and localization accuracies provided by our proposed system. Furthermore, it included the investigation of the extraction of actual gait parameters based on actual measurements using UWB radios. In Particular, we took four different measurement sets for the investigation of ranging and localization accuracies, verification of the accuracy provided by the proposed RRcR ranging technique, and the extraction of actual gait parameters. The results presented in this chapter showed that the proposed system is capable of providing a 1 mm ranging accuracy using an optimal template at an SNR = 20 dB and 22 dB using a suboptimal real sinusoidal template.

Chapter 8 investigated sensor-fusion, and evaluated the overall system performance. Specifically, we studied the integration of UWB sensors with foot force senors for the evaluation of gait kinetics. Then, we summarized some of the important parameters that are known to be of clinical importance, and that current systems fail to measure with sufficient accuracy. In Particular, we considered the BOS, knee-flexion angle, leg-discrepancy, and toe IN/OUT angle gait parameters. Furthermore, we provided an artificial test for comparing the gait normality/abnormality identification capability of our proposed system to the commercial optical tracking systems. This test showed that our system has a 100% gait identification capability (based on 1e5 attempts) compared to 56.3% for the optical tracking system for leg-discrepancy. Then, the performance of our system was compared to the optical tracking system considering various gait parameters via simulations based on actual MoCap data. Also, in this chapter we evaluated the overall system power consumption, battery lifetime, and memory requirements. Results showed that our system is capable of storing data on the on-body central-node using a 64 Gigabyte SD memory card for $\approx$ 8 days without needing to transfer data to the off-body node. It also showed that, the system can work up to 4.6 days without needing to recharge the batteries, assuming two common AAA battery sources supplying the whole system.

9.1 Contributions

A detailed list of contributions of this work is as follows.

- Proposed and investigated a novel highly accurate wireless wearable human locomotion tracking system suitable for clinical gait analysis.
- Designed and investigated the primary components of the proposed system, and proposed novel approaches when necessary.
- Studied human locomotion biomechanics. Defined a target ranging accuracy based on studied gait properties and limitations of current technologies. Our selected system's target ranging accuracy is 1 mm. This value was particularly chosen to achieve an accuracy that is ten-times better than the reported accuracy for current technologies, 1.17 cm. On the other hand, this accuracy has been reported in the literature for UWB technology based on actual low-power implementations.
- Developed a study framework for performance/power consumption evaluation. The optimum receiver architecture for the proposed system was selected based on the developed framework.
- Studied and compared low-power receiver alternatives.
- Studied theoretical lower bounds on time-of-arrival (TOA) ranging estimate. Particularly, we studied the Ziv-Zakai lower-bound (ZZLB) performance of coherent detection with suboptimal (real and complex windowed sinusoid) templates, and derived closed-forms in AWGN channel. Furthermore, we evaluated the ZZLB in the IEEE 802.15.6a body-area-network (BAN) channel model. Accordingly, we defined the target signal-to-noise-ratio SNR based on target ranging accuracy.
- Further studied the effect to timing-misalignment on ZZLB, and provided closed-forms in AWGN. Moreover, extended the evaluation in the IEEE 802.15.6a via semi-analytic simulations.
- Designed key parameters of our system's performance including the link-budget and the frame structure.
- Defined LOS regions that guarantee preserving LOS links during movement based on human movement dynamics and available motion capture marker sets.
- Proposed a short-time system setup (initialization) process that achieves 0.247 mm localization accuracy within 20.14 seconds.
- Proposed a reference range correlation-based (RRcR) ranging technique suitable for on-body communications.
- Verified simulation results based on actual on-body measurements.
- Proposed using classical multidimensional scaling (C-MDS) along with fast-Fourier-transform (FFT) for subsequent frame localization. The proposed procedure provides 0.47 mm 3D localization accuracy in indoors and outdoors; compared to 1 mm average accuracy reported for current systems.

- Studied gait parameters, particularly those of clinical importance. Defined the parameters for which the proposed system is expected to provide more accurate results in comparison to current technologies.
- Developed a simulation framework using MATLAB for the extraction of marker data and estimation of most gait parameters from motion capture (MoCap) data associated with common motion capture systems and software programs, namely Vicon Plug In Gait, OpenSim, and GaitLab (associated with GaitCD).
- Compared the performance of the proposed system to the commercially available gait analysis and motion capture systems based on simulations in the IEEE 802.15.6a channel.
- Proposed the integration of UWB sensors with foot force sensors for the estimation of gait kinetics. Further evaluated the proposed system performance (BER) in the IEEE 802.15.6a channel and verified the proposed link-budget.
- Evaluated the overall system performance, including transmission of acquired TOA data to central on-body node (on-body to on-body), and from on-body central node to off-body node in the IEEE 802.15.6a CM3 and CM4, respectively.
- Developed simulations for all studied aspects, and investigated all proposals on actual motion capture data in realistic on-body multi-path channels.
- Estimated system's overall power consumption and battery lifetime.

9.2 Recommendation for Future Work

This research included the design and analysis of the components associated with the proposed system. The natural next phase of this project would be the implementation of the proposed system. The implementation would essentially include the choice of the most suitable implementation technology. Other low-power alternatives could also be developed for further power consumption reduction. Furthermore, a detailed study of the MAC layer design would also be required.

Bibliography

[1] *The 3d biomechanics data standard*, [available online]: http://www.c3d.org, 2010.

[2] *Cmu graphics lab motion capture database*, [available online]: http://mocap.cs.cmu.edu, 2010.

[3] *International society of biomechanics*, [available online]: http://isweb.org, 2010.

[4] *Opensim software*, https://simtk.org/home/opensim, 2010.

[5] *A microcomputer-based video vector system for clinical gait analysis*, Journal of Biomedical Engineering **12** (1990), no. 5, 383 – 388.

[6] *Biomechanics*, http://www.sportspodiatry.co.uk, 2009.

[7] *Momentum sports: The running website*, http://momentumsports.co.uk/, 2009.

[8] *A six degrees-of-freedom marker set for gait analysis: Repeatability and comparison with a modified helen hayes set*, Gait & Posture **30** (2009), no. 2, 173 – 180.

[9] *Vicon motion systems preparation*, [Available Online] http://www.udel.edu/PT/Research/MAL/, 2009.

[10] A. Leardini L. Chiari A. Cappozzo, and U. Della Croce, *Human movement analysis using stereophotogrammetry part 2: instrumental errors*, Gait and Posture **21** (Feb. 2005), no. 2, 197–211.

[11] A. Leardini L. Chiari A. Cappozzo, and U. Della Croce, *Human movement analysis using stereophotogrammetryc part 1: theoretical background*, Gait and Posture **21** (Feb. 2005), no. 2, 186–196.

[12] D. Cassioli et al. A. F. Molisch, and K. Balakrishnan, *IEEE 802.15.4a channel model-final report*, Tech. rep., 2005, doc: IEEE 802.15-04-0662-02-004a.

[13] E. Pavan, C. Frigo, D. Bettinelli, M. Rabuffetti, P. Crenna A. Leardini, A. Ferrari, and M. Grazia Benedetti, *Quantitative comparison of five current protocols in gait analysis*, Gait and Posture **28** (August 2008), no. 2, 207–216.

[14] B. Hu and N. C. Bueaulieu, *Pulse shapes for ultra wideband communication systems*, IEEE Trans. On Wireless Comm **4** (2005), no. 4, 1789–1797.

[15] L. D'Astous and B. MacWilliams, *Current challenges in clinical gait analysis*, ASB 29th Annual Meeting, Aug. 2002, p. 946.

[16] A. Bindra, *Medical info-communications signals an era of body area networking*, RF Design (Feb. 2008), 10–14.

[17] I. Carpinella, P. Crenna, E. Calabrese, M. Rabuffetti, P. Mazzoleni, R. Nemni, and M. Ferrarin, *Locomotor function in the early stage of parkinson's disease*, Neural Systems and Rehabilitation Engineering, IEEE Transactions on **15** (2007), no. 4, 543–551.

[18] H. -M. Chai, *The pelvic girdle*, [Online]: http://www.pt.ntu.edu.tw, Dec. 2004.

[19] F. -C. Chang, P. -C. Huang, S. -F. Chao, and H. Wang, *A low power folded mixer for UWB system applications in 0.18-mum CMOS technology*, Microwave and Wireless Components Letters, IEEE **17** (May 2007), no. 5, 367–369.

[20] Y.- L. Chao and R. A. Scholtz, *Optimal and suboptimal receivers for ultra-wideband transmitted reference systems*, Global Telecommunications Conference, 2003. GLOBECOM '03. IEEE **2** (1-5 Dec. 2003), 759–763 Vol.2.

[21] Z. -X. Chen, H. -W. Wei, Q. Wan, S. -F. Ye, and W. -L. Yang, *A supplement to multidimensional scaling framework for mobile location: A unified view*, Signal Processing, IEEE Transactions on **57** (2009), no. 5, 2030–2034.

[22] C. Kirtley, *CGA normative gait database*, Available Online: http://www.univie.ac.at/cga/data/index.html, 2010.

[23] W. C. Chung and D. Ha, *An accurate ultra wideband (UWB) ranging for precision asset location*, Ultra Wideband Systems and Technologies, 2003 IEEE Conference on (2003), 389–393.

[24] J. A. Corrales, F. A. Candelas, and F. Torres, *Hybrid tracking of human operators using IMU/UWB data fusion by a kalman filter*, HRI '08: Proceedings of the 3rd ACM/IEEE international conference on Human robot interaction (New York, NY, USA), ACM, 2008, pp. 193–200.

[25] S. Curran, *Relationship of Functional Leg-Length Discrepancy to Abnormal Pronation: Commentary*, J Am Podiatr Med Assoc **96** (2006), no. 6, 505–506.

[26] D. Dardari, C. -C. Chong, and M. Z. Win, *Threshold-based time-of-arrival estimators in UWB dense multipath channels*, IEEE Transactions on Communications, **56** (2008), no. 8, 1366–1378.

[27] D. Dardari, C. -C. Chong, and M. Z. Win, *Threshold-based time-of-arrival estimators in UWB dense multipath channels*, Communications, IEEE Transactions on **56** (2008), no. 8, 1366–1378.

[28] D. Dardari, C. -C. Chong, and M. Z. Win, *Improved lower bounds on time-of-arrival estimation error in realistic UWB channels*, Ultra-Wideband, The 2006 IEEE 2006 International Conference on (2006), 531–537.

[29] A. K. Das, H. Bhasin, and S. S. R. Giduturi, *A 10mW 9.7ENOB 80Msps pipeline adc in 65nm CMOS process without any special mask requirement and with single 1.3V supply*, sept. 2009, pp. 165 –168.

[30] P. DeLuca, M. Romness, D. Davis, and S. Ounpuu, *Clinical gait analysis and its role in treatment decisionmaking. medscape general medicine*, Medscape (2002).

[31] J. Dederer, B. Schleicher, F. De Andrade, Tabarani Santos, A. Trasser, and H. Schumacher, *FCC compliant 3.1-10.6 GHz UWB pulse radar system using correlation detection*, Microwave Symposium, 2007. IEEE/MTT-S International, June 2007, pp. 1471–1474.

[32] J. Dederer, B. Schleicher, A. Trasser, T. Feger, and H. Schumacher, *A fully monolithic 3.1-10.6 GHz UWB Si/SiGe HBT impulse-UWB correlation receiver*, Ultra-Wideband, 2008. ICUWB 2008. IEEE International Conference on, vol. 1, Sept. 2008, pp. 33–36.

[33] S. L. Delp, F. C. Anderson, A. S. Arnold, P. Loan, A. Habib, C. T. John, E. Guendelman, and D. G. Thelen, *Opensim: Open-source software to create and analyze dynamic simulations of movement*, Biomedical Engineering, IEEE Transactions on **54** (2007), no. 11, 1940–1950.

[34] C. Desset, M. Badaroglu, J. Ryckaert, and B. van Poucke, *UWB search strategies for minimal-length preamble and a low-complexity analog receiver*, Signal Processing Advances in Wireless Communications, 2006. SPAWC '06. IEEE 7th Workshop on, July 2006, pp. 1–5.

[35] M. -G. Di -Benedetto and G. Giancola (eds.), *Understanding ultra wide band radio fundamentals*, Prentice Hall, USA, 2004.

[36] M. Di Renzo, R. Buehrer, and J. Torres, *Pulse shape distortion and ranging accuracy in UWB-based body area networks for full-body motion capture and gait analysis*, Global Telecommunications Conference, 2007. GLOBECOM '07. IEEE (26-30 Nov. 2007), 3775–3780.

[37] The Free Dictionary, *Disease*, Online: http://medical-dictionary.thefreedictionary.com/disease, 2010.

[38] Stefan Drude, *Tutorial on body area networks*, Tech. report, July 2006, doc: IEEE 802.15-06-0331.

[39] C. Otto, P. Groen E. Jovanov, A. Milenkovic, *A wireless body area network of intelligent motion sensors for computer assisted physical rehabilitation.*, J. Neuroengineering Rehabil, no. 1.

[40] J. Erickson and M. Munsey, *How to achieve predictable front-end power closure*, CommsDesign (2007), 1–1.

[41] F. Bloom, M. Beal, and D. Kupfer (ed.), *The dana guide to brain health. a practical family reference from medical experts*, Dana Press, Washington, 2006.

[42] A. Fort, C. Desset, J. Ryckaert, P. De Doncker, L. Van Biesen, and S. Donnay, *Ultra wide-band body area channel model*, vol. 4, May 2005, pp. 2840 – 2844 Vol. 4.

[43] A. Fort, C. Desset, P. Wambacq, and L. Van Biesen, *Body area UWB rake receiver communication*, Communications, 2006. ICC '06. IEEE International Conference on **10** (June 2006), 4682–4687.

[44] A. Fort, J. Ryckaert, C. Desset, P. De Doncker, P. Wambacq, and L. Van Biesen, *Ultra-wideband channel model for communication around the human body*, Selected Areas in Communications, IEEE Journal on **24** (2006), no. 4, 927–933.

[45] A. Gerosa, M. Soldan, A. Bevilacqua, and A. Neviani, *A 0.18 μm CMOS squarer circuit for a non-coherent UWB receiver*, Circuits and Systems, 2007. ISCAS 2007. IEEE International Symposium on (27-30 May 2007), 421–424.

[46] S. Gezici, I. Guvenc, and Z. Sahinoglu, *On the performance of linear least-squares estimation in wireless positioning systems*, May 2008, pp. 4203 –4208.

[47] S. Gezici, Z. Tian, G. B. Giannakis, H. Kobayashi, A. F. Molisch, H. V. Poor, and Z. Sahinoglu, *Localization via ultra-wideband radios: a look at positioning aspects for future sensor networks*, Signal Processing Magazine, IEEE **22** (2005), no. 4, 70–84.

[48] A. L. Goldberger, L. A. N. Amaral, L. Glass, J. M. Hausdorff, P. Ch. Ivanov, R. G. Mark, J. E. Mietus, G. B. Moody, C. -K. Peng, and H. E. Stanley, *PhysioBank, PhysioToolkit, and PhysioNet: Components of a new research resource for complex physiologic signals*, Circulation **101** (2000 (June 13)), no. 23, e215–e220.

[49] A. A. Goulianos and S. Stavrou, *UWB path arrival times in body area networks*, Antennas and Wireless Propagation Letters, IEEE **6** (2007), 223–226.

[50] J. A. Gubner, *The ieee 802.15.3a UWB channel model as a two-dimensional augmented cluster process*, IEEE Transactions on Information Theory (submitted Mar. 2006), [Online]:http://eceserv0.ece.wisc.edu/ gubner/GubnerHaoITuwb2col.pdf.

[51] I. Guvenc, C. C. Chong, and F. Watanabe, *Analysis of a linear least-squares localization technique in LOS and NLOS environments*, April 2007, pp. 1886–1890.

[52] I. Guvenc and Z. Sahinoglu, *Multiscale energy products for toa estimation in IR-UWB systems*, Global Telecommunications Conference, 2005. GLOBECOM '05. IEEE, vol. 1, Nov.-2 Dec. 2005, pp. 5 pp.–.

[53] J. Zhu, H. Huang, and H. Yin, *The structure and performance on an orthogonal sinusoidal correlation receiver of impulse radio*, Proc. of IEEE 60th Vehicular Technology Conference VTC2004-Fall, vol. 2, 2004, pp. 1192– 1196.

[54] A. Tiedemann, M. Kwan, S. Lord, H. Menz, and M. Latt, *Reliability of the gaitrite walkway system for the quantification of temporo-spatial parameters of gait in young and older people*, Gait and Posture **20** (Aug. 2004), no. 1, 20–25.

[55] K. Hao and J. A. Gubner, *Performance measures and statistical quantities of rake receivers using maximal-ratio combining on the IEEE 802.15.3a UWB channel model*, Wireless Communications, IEEE Transactions on (submitted 2005), 1–7.

[56] K. Hao and J. A. Gubner, *The distribution of sums of path gains in the IEEE 802.15.3a UWB channel model*, Wireless Communications, IEEE Transactions on **6** (March 2007), no. 3, 811–816.

[57] S. Hoyos and B. M. Sadler, *Ultra-wideband analog-to-digital conversion via signal expansion*, Vehicular Technology, IEEE Transactions on **54** (2005), no. 5, 1609–1622.

[58] S. Hoyos and B. M. Sadler, *Frequency-domain implementation of the transmitted-reference ultra-wideband receiver*, Microwave Theory and Techniques, IEEE Transactions on **54** (2006), no. 4, 1745–1753.

[59] S. Hoyos, B. M. Sadler, and G. R. Arce, *Monobit digital receivers for ultrawideband communications*, Wireless Communications, IEEE Transactions on **4** (2005), no. 4, 1337–1344.

[60] Z. N. Chen, H. Arslan, and M.-G. Di Benedetto (eds.), *Ultra wideband wireless communication*, Wiley Interscience, New Jersey, 2006.

[61] Health Grades Inc, *Gait propulsive*, Online: www.wrongdiagnosis.com/symptoms, 2010.

[62] Z. Irahhauten, G. Bellusci, G. J. M. Janssen, H. Nikookar, and C. Tiberius, *Investigation of UWB ranging in dense indoor multipath environments*, Communication systems, 2006. ICCS 2006. 10th IEEE Singapore International Conference on (2006), 1–5.

[63] E. Rosen, J. Gross, and J. Fetto (ed.), *Musculoskeletal examination, 2nd ed.*, Blackwell Science, Inc., USA, 2002.

[64] M. Porter, S. Nakagawa, J. Montufar, and J. Arango1, *Pedestrians' normal walking speed and speed when crossing a street*, Transportation Research Record: Journal of the Transportation Research Board **2002/2007** (2007), 90 – 97.

[65] M. Badaroglu, S. DAmico, V. De Heyn, C. Desset, P. Nuzzo, B. Van Poucke, P. Wambacq, A. Baschirotto, W. Dehaene, J. Ryckaert, M. Verhelst, and G. Van der Plas, *A CMOS ultra-wideband receiver for low data-rate communication*, IEEE J. Solid-State Circuits **42** (2007), no. 1, 2515–2525.

[66] T. Jia and Dong In Kim, *Analysis of channel-averaged SINR for indoor UWB rake and transmitted reference systems*, Communications, IEEE Transactions on **55** (Oct. 2007), no. 10, 2022–2032.

[67] Casey K. Kerrigan and J. A. Delisa (ed.), *Gait analysis in the science of rehabilitation*, DIANE Publishing, MD, 1998.

[68] H. Joseph (ed.), *Biomechanical basis of human movement, 3rd ed.*, Lippincott Williams and Wilkins, MD, USA, Feb. 2008.

[69] A. Chatzigeorgiou, S. Nikolaidis, G. Stephanides, K. Zotos, A. Litke, and G. Giannakides, *Energy complexity of software in embedded systems*, ACIT - Automation, Control, and Applications (2005), 483–836.

[70] S. Krishnamoorthy and A. Khouja, *Efficient power analysis of combinational circuits*, 1996 IEEE Custom Integrated Circuits Conference Proceedings, 1996, pp. 393 – 396.

[71] M. Kuhn, C. Zhang, B. Merkl, Depeng Yang, Yazhou Wang, M. Mahfouz, and A. Fathy, *High accuracy UWB localization in dense indoor environments*, Ultra-Wideband, 2008. ICUWB 2008. IEEE International Conference on, vol. 2, Sept. 2008, pp. 129–132.

[72] J. A. Lopez-Salcedo and G. Vazquez, *Waveform-independent frame-timing acquisition for UWB signals*, Signal Processing, IEEE Transactions on **55** (2007), no. 1, 279–289.

[73] S. Malik, M. Lee, V. Tiwari, and M. Fujita, *Power analysis and minimization techniques for embedded DSP software*, IEEE Trans. on Very Large Scale Integration (VLSI) Systems **5** (Mar. 1979), no. 1, 123–135.

[74] M. Verhelst et al., *Design of an energy-efficient pulsed UWB receiver*, AACD workshop, proceedings of (2006).

[75] G. MacGougan, K. O'Keefe, and R. Klukas, *Ultra-wideband ranging precision and accuracy*, Measurement Science and Technology **20** (2009), no. 9, 095105 (13pp).

[76] M. Baudoin G. Tinella, C. Belot, D. Marchaland, and D. Villegas, *System concepts dedicated to UWB transmitter*, Wireless Technology, 2005. The European Conference on (3-4 Oct. 2005), 141–144.

[77] J. L. McGinley, R. Baker, R. Wolfe, and Meg E. Morris, *The reliability of three-dimensional kinematic gait measurements: A systematic review*, Gait and Posture **29** (2009), no. 3, 360 – 369.

[78] V. Medved (ed.), *Measurement of human locomotion, 1st ed.*, CRC Press, USA, 2000.

[79] P. P. Newaskar, R. Blazquez, and A. R. Chandrakasan, *A/D precision requirements for an ultra-wideband radio receiver*, Signal Processing Systems, 2002. (SIPS '02). IEEE Workshop on (16-18 Oct. 2002), 270–275.

[80] NICT, *Nict's wideband PHY proposal part 2: MB-IR-UWB*, Tech. rep., 2009, doc: IEEE 802.15-09-0163-00-0006.

[81] I. Operan (ed.), *Ulta wideband theory and applications*, John Wiley and Sons, 2004.

[82] Optotrak, *Optotrak technical specifications*, Online: http://www.ndigital.com/optotrak-techspecs.php, 2010.

[83] Heel Pain, *Gait cycle*, heelspurs.co.uk, 2009.

[84] N. Patwari, J. N. Ash, S. Kyperountas, A. Hero, R. Moses, and N. Correal, *Locating the nodes: cooperative localization in wireless sensor networks*, Signal Processing Magazine, IEEE **22** (2005), no. 4, 54–69.

[85] T. -A. Phan, V. Krizhanovskii, S. -K. Han, S. -G. Lee, H. Oh, and N.-S. Kim, *4.7pJ/pulse 7th derivative gaussian pulse generator for impulse radio UWB*, Circuits and Systems, 2007. ISCAS 2007. IEEE International Symposium on (2007), 3043–3046.

[86] A ClydeNET project, *Biomechanics of the lower limb*, Online: http://www.gla.ac.uk/ibls/US/fab/tutorial/othrdocs/biomcont.html, 2010.

[87] M. Z. Quek and T. Q. S. Win, *Analysis of UWB transmitted-reference communication systems in dense multipath channels*, Selected Areas in Communications, IEEE Journal on **23** (Sept. 2005), no. 9, 1863–1874.

[88] Z. Knoll R. Kiss, and L. Kocsis, *Joint kinematicsnext term and spatialtemporal parameters of gait measured by an ultrasound-based system*, Gait and Posture **26** (Sept. 2004), no. 7, 611–620.

[89] T. Rappaport (ed.), *Wireless communications: Priciples and practice*, 2nd ed., Prentice Hall, Upper Saddle River, NJ, 2002.

[90] J H Reed (ed.), *An introduction to ultra wideband communication systems*, Prentice Hall, New Jersey, 2005.

[91] F. Remirez-Mireles, *On the performance of ultra wide-band signals in gaussian noise and dense multipath*, IEEE Trans. On Veh. Tech. **5** (2001), no. 50, 244–249.

[92] D. A. Rodriguez-Silva, F. Gil-Castineira, F. J. Gonzalez-Castano, R. J. Duro, F. Lopez-Pena, and J. Vales-Alonso, *Human motion tracking and gait analysis: a brief review of current sensing systems and integration with intelligent environments*, Virtual Environments, Human-Computer Interfaces and Measurement Systems, 2008. VECIMS 2008. IEEE Conference on (2008), 166–171.

[93] J. Rose and J. G. Gamble (eds.), *Human walking*, third ED., Lippincott Williams & Wilkins, Dec. 2005.

[94] J. Ryckaert, M. Verhelst, M. Badaroglu, S. D'Amico, V. De Heyn, C. Desset, P. Nuzzo, B. Van Poucke, P. Wambacq, A. Baschirotto, W. Dehaene, and G. Van der Plas, *A CMOS ultra-wideband receiver for low data-rate communication*, Solid-State Circuits, IEEE Journal of **42** (Nov. 2007), no. 11, 2515–2527.

[95] H. Hillstorm S. Barker, and W. Freedman, *A novel method of producing a repetitive dynamic signal to examine reliability and validity of gait analysis systems*, Gait and Posture **24** (Dec. 2006), no. 4, 448–452.

[96] R. Saeed, S. Khaum, B. MAli, and M. Khazani, *Performance of ultra-wideband time-of-arrival estimation enhanced with synchronization scheme*, Electrical Engineering, Electronics and Communications, ECTI Transaction on **4** (2006), no. 1, 78–84.

[97] L. Sangyoub, *Design and analysis of ulktra-wide bandwidth impulse radio receiver*, Ph.D. thesis, Southern California University, 2002.

[98] H. Shaban, M. Abou El-Nasr, and R. M. Buehrer, *Toward a highly accurate ambulatory system for clinical gait analysis via UWB radios*, IEEE Transactions on Information Technology in Biomedicine, Vol. 14, no. 2, March 2010.

[99] D. Shen, F. Lin, and W. G. Yeoh, *An analog correlator with dynamic bias control for pulse based UWB receiver in 0.18 μm CMOS technology*, Radio Frequency Integrated Circuits (RFIC) Symposium, 2006 IEEE (11-13 June 2006), 4.

[100] D. Simic, A. Jordan, Rui Tao, N. Gungl, J. Simic, M. Lang, Luong Van Ngo, and V. Brankovic, *Impulse uwb radio system architecture for body area networks*, Mobile and Wireless Communications Summit, 2007. 16th IST (1-5 July 2007), 1–5.

[101] D. Simic, A. Jordan, Rui Tao, N. Gungl, J. Simic, M. Lang, Luong Van Ngo, and V. Brankovic, *Impulse UWB radio system architecture for body area networks*, July 2007, pp. 1–5.

[102] M. K. Simon and K. S. Alouni (eds.), *Digital communication over fading channels: A unified approach to performance analysis, 1st ED.*, Wiley, NewYork, 2000.

[103] D. Soudris, K. Katis, C. Goutis, and W. Workpackage, *Lpgd a low-power design methodology/flow and its application to the modulator/demodulator (esprit 25256)*, Tech. Report LPGD/ WP1/ DUTH/D1.2R1, Duth.

[104] Springhouse (ed.), *Handbook of signs and symptoms, third edition*, Lippincott Williams and Wilkins, MD, 2005.

[105] L. Stoica and I. Oppermann, *Modelling and simulation of a non-coherent ir UWB transceiver architecture with TOA estimation*, Personal, Indoor and Mobile Radio Communications, 2006 IEEE 17th International Symposium on, Sept. 2006, pp. 1–5.

[106] L. Stoica, *Non-coherent energy detection tranceivers for ultra wideband impulse radio systems*, Ph.D. thesis, University of Oulu Finland, 2008.

[107] H. V. SURIN, *Unequal leg length*, [Online]: http://www.totaljoints.info, Oct. 2002.

[108] John Providence Health System, *Common symptoms of parkinsons disease*, Online: http://www.stjohn.org/HealthInfoLib/swArticle.aspx?3,84413, 2010.

[109] A. Taparugssanagorn, A. Rabbachin, M. Hamalainen, J. Saloranta, and J. Iinatti, *A review of channel modelling for wireless body area network in wireless medical communications*, 2008, pp. 1–5.

[110] T. Thiasiriphet, B. Schleicher, M. Leib, J. Dederer, J. Lindner, W. Menzel, and H. Schumacher, *UWB systems for biomedical diagnostics and short-range communications (UWB in medicine)*, Tech. report, UKoLoS Annual Colloquium, Ilmenau, 2008.

[111] Christopher L. Vaughan, B. L. Davis, and J. C. O. Connor, *Dynamics of human gait*, 2nd edition ed., Kiboho Publishers, Cape Town, South Africa, 1999.

[112] CL. Vaughan, *GaitCD*, CD-ROM, 1999.

[113] M. Verhelst and W. Dehaene, *Analysis of the qac IR-UWB receiver for low energy, low data-rate communication*, Circuits and Systems I: Regular Papers, IEEE Transactions on **55** (2008), no. 8, 2423 –2432.

[114] M. Verhelst, W. Vereecken, M. Steyaert, and W. Dehaene, *Architectures for low power ultra-wideband radio receivers in the 3.1-5 GHz band for data rates < 10Mbps*, Low Power Electronics and Design, 2004. ISLPED '04. Proceedings of the 2004 International Symposium on (9-11 Aug. 2004), 280–285.

[115] Vicon-BONITA, *Vicon cameras*, Online: http://www.vicon.com/products/cameras.html, 2010.

[116] Kate E. Webster, Joanne E. Wittwer, and Julian A. Feller, *Validity of the gaitrite walkway system for the measurement of averaged and individual step parameters of gait*, Gait & Posture **22** (2005), no. 4, 317 – 321.

[117] M. Weisenhorn and W. Hirt, *Robust noncoherent receiver exploiting UWB channel properties*, Ultra Wideband Systems, 2004. Joint International Workshop on (18-21 May 2004), 156–160.

[118] Wikipedia, *Running*, Online: http://en.wikipedia.org/wiki/Running, 2009.

[119] K. Y. Yazdandoost and K. S. -Pour, *Channel model for body area network (BAN)*, Tech. rep., doc: IEEE P802.15-08-0780-09-0006, April 2009.

[120] Kamya Yekeh Yazdandoost, *Channel model for body area network (BAN)*, Tech. rep., 2008, doc: IEEE P802.15-08-0780-04-0006.

[121] T. Zasowski, F. Althaus, M. Stager, A. Wittneben, and G. Troster, *UWB for noninvasive wireless body area networks: channel measurements and results*, Ultra Wideband Systems and Technologies, 2003 IEEE Conference on (16-19 Nov. 2003), 285–289.

[122] Y. P. Zhang and Q. Li, *Performance of UWB impulse radio with planar monopoles over on-human-body propagation channel for wireless body area networks*, Antennas and Propagation, IEEE Transactions on **55** (Oct. 2007), no. 10, 2907–2914.

[123] B. Zhen, H. -B. Li, and R. Kohno, *IEEE body area networks for medical applications*, Wireless Communication Systems, 2007. ISWCS 2007. 4th International Symposium on (17-19 Oct. 2007), 327–331.

[124] S. Zivanovic, A. Pavic, and P. Reynolds, *Vibration serviceability of footbridges under human-induced excitation: a literature review*, Journal of Sound and Vibration **279** (2005), no. 1-2, 1 – 74.